ΠΑΝΕΠΙΣΤΗΜΙΟ ΙΩΑΝΝΙΝΩΝ
ΣΧΟΛΗ ΘΕΤΙΚΩΝ ΕΠΙΣΤΗΜΩΝ
ΤΜΗΜΑ ΧΗΜΕΙΑΣ

ΥΒΡΙΔΙΚΑ ΥΛΙΚΑ ΒΑΣΙΣΜΕΝΑ ΣΤΟ ΓΡΑΦΕΝΙΟ ΚΑΙ ΣΧΕΤΙΚΑ ΥΛΙΚΑ ΜΕ ΜΕΤΑΛΛΙΚΕΣ ΝΑΝΟΣΥΣΤΑΔΕΣ ΓΙΑ ΕΦΑΡΜΟΓΕΣ ΜΕΤΑΤΡΟΠΗΣ ΕΝΕΡΓΕΙΑΣ

ΜΑΛΑΜΑΤΕΝΙΑ ΚΟΚΛΙΩΤΗ

ΧΗΜΙΚΟΣ ΜΗΧΑΝΙΚΟΣ Ε.Μ.Π.

ΔΙΔΑΚΤΟΡΙΚΗ ΔΙΑΤΡΙΒΗ
2019

ΠΑΝΕΠΙΣΤΗΜΙΟ ΙΩΑΝΝΙΝΩΝ
ΣΧΟΛΗ ΘΕΤΙΚΩΝ ΕΠΙΣΤΗΜΩΝ
ΤΜΗΜΑ ΧΗΜΕΙΑΣ

ΕΘΝΙΚΟ ΙΔΡΥΜΑ ΕΡΕΥΝΩΝ
ΙΝΣΤΙΤΟΥΤΟ ΘΕΩΡΗΤΙΚΗΣ ΚΑΙ ΦΥΣΙΚΗΣ ΧΗΜΕΙΑΣ

ΥΒΡΙΔΙΚΑ ΥΛΙΚΑ ΒΑΣΙΣΜΕΝΑ ΣΤΟ ΓΡΑΦΕΝΙΟ ΚΑΙ ΣΧΕΤΙΚΑ ΥΛΙΚΑ ΜΕ ΜΕΤΑΛΛΙΚΕΣ ΝΑΝΟΣΥΣΤΑΔΕΣ ΓΙΑ ΕΦΑΡΜΟΓΕΣ ΜΕΤΑΤΡΟΠΗΣ ΕΝΕΡΓΕΙΑΣ

ΜΑΛΑΜΑΤΕΝΙΑ ΚΟΚΛΙΩΤΗ
ΧΗΜΙΚΟΣ ΜΗΧΑΝΙΚΟΣ Ε.Μ.Π.

ΔΙΔΑΚΤΟΡΙΚΗ ΔΙΑΤΡΙΒΗ
2019

Ορισμός Τριμελούς Συμβουλευτικής Επιτροπής από τη Συνέλευση: 923^{A}/29-01-2016

Μέλη Τριμελούς Συμβουλευτικής Επιτροπής:

Επιβλέπων: Δημήτριος Τάσης, Επίκουρος Καθηγητής Παν/μίου Ιωαννίνων

Μέλη: Νικόλαος Ταγματάρχης, Διευθυντής Ερευνών Εθνικού Ιδρύματος Ερευνών
Μάμαντος Προδρομίδης, Καθηγητής Παν/μίου Ιωαννίνων

Ημερομηνία ορισμού θέματος: 924^{A}/26-02-2016

Θέμα: «ΥΒΡΙΔΙΚΑ ΥΛΙΚΑ ΒΑΣΙΣΜΕΝΑ ΣΤΟ ΓΡΑΦΕΝΙΟ ΚΑΙ ΣΧΕΤΙΚΑ ΥΛΙΚΑ ΜΕ ΜΕΤΑΛΛΙΚΕΣ ΝΑΝΟΣΥΣΤΑΔΕΣ ΓΙΑ ΕΦΑΡΜΟΓΕΣ ΜΕΤΑΤΡΟΠΗΣ ΕΝΕΡΓΕΙΑΣ»

ΟΡΙΣΜΟΣ ΕΠΤΑΜΕΛΟΥΣ ΕΞΕΤΑΣΤΙΚΗΣ ΕΠΙΤΡΟΠΗΣ από τη Συνέλευση: 999/17-05-2019

1. Δημήτριος Τάσης, Επίκουρος Καθηγητής Παν/μίου Ιωαννίνων
2. Νικόλαος Ταγματάρχης, Διευθυντής Ερευνών, Εθνικό Ίδρυμα Ερευνών
3. Μάμαντος Προδρομίδης, Καθηγητής Παν/μίου Ιωαννίνων
4. Άδωνις Μιχαηλίδης, Καθηγητής Παν/μίου Ιωαννίνων
5. Τριαντάφυλλος Αλμπάνης, Καθηγητής Παν/μίου Ιωαννίνων
6. Αντώνιος Ζαρκάδης, Αναπλ. Καθηγητής Παν/μίου Ιωαννίνων
7. Μιχαήλ Σίσκος, Αναπλ. Καθηγητής Παν/μίου Ιωαννίνων

Έγκριση Διδακτορικής Διατριβής με βαθμό «Άριστα» στις 04-07-2019.

Η Πρόεδρος του Τμήματος Χημείας	Η Γραμματέας του Τμήματος
Λουλούδη Μαρία, Καθηγήτρια	Ξανθή Τουτουνζόγλου

Αφιερωμένο στην οικογένειά μου

ACKNOWLEDGEMENTS

First and foremost, I would like to express my sincere gratitude to my supervisor, Dr. Nikos Tagmatarchis, Director of Research, Institute of Theoretical and Physical Chemistry, National Hellenic Research Foundation for allowing me to undertake this PhD Thesis in the first place. His constant encouragement and inspirational mentorship during the years of my PhD are highly appreciated, while he also gave me many possibilities to work with excellent collaborators. Also, I would like to thank the Institute of Theoretical and Physical Chemistry, National Hellenic Research Foundation for giving me access to the facilities. Besides my supervisor, I would like to express my appreciation to the rest of my scientific committee members; Prof. D. Tasis, and Prof. M. Prodromidis for their support and the University of Ioannina for accepting me as a PhD candidate.

Results presented in this Thesis would not have been possible without the close collaboration with friends and current members of our group, Dr. Anastasios Stergiou, Dr. Theodosis Skaltsas, Dr. Christina-Epistimi Stangel, Dr. Ruben-Canton Vitoria, Dr. Antonia Kagkoura, and Dr. Dimitris Perivoliotis. Additionally, I would like to thank Dr. S. Pispas and his group members, Dr. G. Chryssikos, and Mr. C. Tsiantos for their useful help.

The completion of this PhD Thesis would not have been possible without the valuable efforts of co-authors contributed to the publications of this dissertation. I wish to thank Dr. Kazu Suenaga, Nanomaterials Research Institute, National Institute of Advanced Industrial Science and Technology (AIST), Japan, and Dr. Mildred Quintana, Universidad Autónoma de San Luis Potosí, Mexico for TEM imaging. Special thanks also go to Dr. Carla Bittencourt, University of Mons, Belgium for her endless support, friendly atmosphere, and XPS results. Finally, part of this work was supported by an STSM Grant from the COST Action CA15107.

At last, I am indebted to my family – mum, brother, and Alex – for their never ending support and encouragement throughout this adventure; without them I would not be where I am now.

H.F.R.I. Hellenic Foundation for Research & Innovation

GSRT GENERAL SECRETARIAT FOR RESEARCH AND TECHNOLOGY

The research work was supported by the Hellenic Foundation for Research and Innovation (HFRI) and the General Secretariat for Research and Technology (GSRT), under the HFRI PhD Fellowship grant (GA. no. 93).

ΠΕΡΙΛΗΨΗ

Η απομόνωση του γραφενίου πυροδότησε το επιστημονικό ενδιαφέρον για τα δισδιάστατα υλικά, το οποίο έχει επεκταθεί προς την εξεύρεση και άλλων συγγενών υλικών όπως τα διχαλκογενίδια μετάλλων μετάπτωσης (TMDs) με κύριους εκπροσώπους τα MoS_2 και WS_2. Η παρούσα διδακτορική διατριβή αφορά στην ανάπτυξη υβριδικών υλικών με βάση το γραφένιο και τα TMDs, τα οποία συνδυάζονται με μεταλλικές νανοσυστάδες για εφαρμογές μετατροπής ενέργειας. Αρχικά, φύλλα γραφενίου τροποποιήθηκαν ομοιοπολικά με οργανικές ομάδες που φέρουν αμμωνιακά ιόντα και συνδέθηκαν μέσω υπερμοριακών αλληλεπιδράσεων με φθορίζουσες μεταλλικές νανοστάδες με βάση τον χρυσό και τον άργυρο χρησιμοποιώντας α-λιποϊκό οξύ ως συνδέτη. Ο σχηματισμός της κατάστασης των διαχωρισμένων φορτίων και η μεταφορά ενέργειας ή/και φορτίου από τις μεταλλικές νανοσυστάδες προς το γραφένιο οδήγησαν στην φωτοεπαγόμενη παραγωγή υδρογόνου, το οποίο χρησιμοποιήθηκε για την αναγωγή της 4-νιτροφαινόλης. Στη συνέχεια, μελετήθηκαν υλικά με βάση ολιγο-στρωματικά φύλλα MoS_2 και WS_2 τα οποία μέσω του φαινομένου της ιοντοβολής και της δημιουργίας πλάσματος, τροποποιήθηκαν χημικά με πρόσμιξη (doping) αζώτου και νανοσωματίδια αργύρου. Τα υβριδικά υλικά χρησιμοποιήθηκαν ως ενεργά υποστρώματα για την ανίχνευση σε χαμηλές συγκεντρώσεις αρωματικών μορίων (πολυκυκλικοί αρωματικοί υδρογονάνθρακες, όπως πυρένιο, ανθρακένιο και ναφθαλένιο) μέσω της τεχνικής της επιφανειακής ενίσχυσης της σκέδασης Raman (SERS). Η ενίσχυση SERS οφείλεται στην δημιουργία “hot spots” και των φαινομένων μεταφοράς φορτίου μεταξύ των τροποποιημένων MoS_2 και των ανιχνευθέντων ουσιών και έχει ως αποτέλεσμα την αυξημένη ευαισθησία της μεθόδου. Ακόμα, παράγωγο 1,2-διθειολάνιου προσδέθηκε ομοιοπολικά στις ατέλειες των ατόμων Mo που οφείλονται σε κενές θέσεις S και βρίσκονται στις άκρες του πλέγματος των MoS_2 φύλλων. Τα τροποποιημένα φύλλα MoS_2 αλληλεπίδρασαν ηλεκτροστατικά με φθορίζουσες μεταλλικές νανοσυστάδες μορφολογίας πυρήνα – κελύφους (core – shell) Ag@Au χρησιμοποιώντας αλβουμίνη βόειου ορού (BSA) ως συνδέτη. Στο υβριδικό υλικό που δημιουργήθηκε παρατηρήθηκαν φαινόμενα μεταφοράς ενέργειας ή/και φορτίου, τα οποία συνέβαλαν στην φωτοαποικοδόμηση της Ροδαμίνης Β μέσω της παραγωγής άκρως δραστικών ριζών. Τέλος, πραγματοποιήθηκε η ανάπτυξη ενός νέου οργανικού συνδέτη με βάση παράγωγο του αδαμαντάνιου, ο οποίος οδήγησε στην δημιουργία φθοριζουσών μεταλλικών νανοσυστάδων χρυσού. Ταυτόχρονα, το ελεύθερο άκρο του οργανικού συνδέτη έφερε άτομα άνθρακα συνδεδεμένα με διπλό δεσμό, τα οποία αλληλεπίδρασαν ομοιοπολικά μέσω της αντίδρασης “click” με φύλλα γραφενίου και MoS_2 που προηγουμένως είχαν τροποποιηθεί χημικά με ομάδες θειολών. Ο συγκεκριμένος σχεδιασμός υβριδικών υλικών ανοίγει τον δρόμο για την εφαρμογή καινοτόμων μεθόδων χημικής τροποποίησης και άλλων δισδιάστατων υλικών και την δημιουργία υβριδικών υλικών με επιθυμητές ιδιότητες σε συστήματα μετατροπής ενέργειας.

Λέξεις κλειδιά: γραφένιο, διχαλκογενίδια μετάλλων μετάπτωσης, μεταλλικές νανοσυστάδες, χημική τροποποίηση, φθορισμός, υβριδικά υλικά, μετατροπή ενέργειας

ABSTRACT

The isolation of monolayered graphene brought 2D family into the limelight extending the scientific interest to include other materials such as transition metal dichalcogenides (TMDs) with MoS_2 and WS_2 as main flatlanders. This PhD Thesis deals with the preparation of graphene and TMDs combined with fluorescent metal nanoclusters focusing on the development of hybrid materials for energy conversion applications. Firstly, graphene sheets were covalently functionalized with organic moiety bearing ammonium units and supramolecularly tethered to negatively charged α-lipoic acid-stabilized metal nanoclusters (M_{NCs}) of gold and silver. The corresponding ensemble was successfully employed as a proficient catalyst for the model reduction of 4-nitrophenol to the corresponding 4-aminophenol as proof for the photoinduced hydrogen production, while the mechanistic pathways took place upon photoillumination of the hybrid are discussed. Next, a facile way to prepare nitrogen doped TMDs (MoS_2 and WS_2) through plasma treatment, while they were simultaneously decorated with silver nanoparticles, is demonstrated. The TMD-based materials functioned as efficient surface-enhanced Raman scattering (SERS) platforms for the sensitive detection of aromatic molecules (polycyclic aromatic hydrocarbons, such as pyrene, anthracene and naphthalene). The signal enhancement is mainly due to the existence of “hot spots” and charge transfer processes between modified MoS_2 and fluorophore analyte molecules. Moreover, MoS_2 sheets were covalently functionalized with a 1,2-dithiolane derivative anchored to defected Mo atoms bearing sulfur vacancies at the edges of MoS_2. Fluorescent core – shell $Ag@Au_{NCs}$ labeled with BSA were electrostatically interacted with modified MoS_2 sheets and the obtained ensemble examined towards photodegradation of RhB. The main responsible reactive species derived from charge transfer phenomena between MoS_2 and $Ag@Au_{NCs}$ and plausible mechanistic pathways of photocatalytic decomposition of RhB are discussed. Finally, a new organic stabilizer based on a bulky adamantane moiety bearing also an 1,2-dithiolane derivative is demonstrated and employed for the synthesis of Au_{NCs} with NIR- fluorescence. Next, the C=C group of the newly synthesized ligand was exploited to covalently react with thiol-functionalized graphene and MoS_2 sheets through thiol–ene “click” reaction. The current strategy employed constitutes a general tool that is wide in scope and can, in principle, be extended to the modification of other 2D materials and/or compounds for the fabrication of hybrid schemed with tailored characteristics that today is unattainable.

Key words: graphene, transition metal dichalcogenides, metal nanoclusters, chemical functionalization, fluorescence, hybrid materials, energy conversion

Contents

Chapter 1

Graphene, transition metal dichalcogenides and metal nanoclusters

1.1 Introduction

In 21^{st} century, the pressing matters of environmental deterioration and sustainability cannot be neglected in any aspect of human activity. With growing world population, intensification of agricultural and industrial activities, contamination of air, soils and aquatic ecosystems, and global climate change, environmental issues are becoming a major concern of modern society. Currently, there is a global awareness – both from political and scientific point of view – to recognize the impact of human activities on environment and to design new technologies to mitigate associated health and environmental implications. Among the different strategies to address these environmental challenges, recent advancements in the field of nanotechnology have triggered increased interest in harnessing the unique properties of nanomaterials for environmental applications. Indeed, nanomaterials boast several properties, owing to their nanoscale dimensions, that can be exploited to design novel technologies or improve the performance of existing ones. Nanomaterials have found multiple applications in water purification, energy conversion, and contaminant sensing, and a growing amount of literature describes how nanoarchitectures may be used to address major environmental challenges.

Sticky tape could have never been regarded as the starting point of scientific breakthroughs. However, when physicists at the University of Manchester, UK, reported that they used a typical scotch tape to peel off single atomically thin sheets of carbon atoms from a chunk of graphite, it set off a revolution in materials science that is still unfolding. Graphene is the thinnest material ever made. It's 100 times stronger than steel, a better electrical and heat conductor than copper, flexible, and largely transparent. For all its great promise, graphene has drawbacks, especially its inability to act as semiconductor. Now, scientists turn their notion to the move beyond graphene by synthesizing other two-dimensional sheet-like materials that combine flexibility and transparency with electronic properties that graphene cannot reach. Transition metal dichalcogenides (TMDs) are an emerging class of 2D materials family, which mostly display semiconducting properties; a missing feature of graphene. TMDs aren't quite as thin as graphene (in MoS_2, for example, twin sheets of sulfur atoms sandwich a middle layer of molybdenum atoms), but they offer other advantages. At the few- to monolayer limit, an indirect-to-direct band gap transition occurs due to thickness-induced quantum confinement. This leads to photoluminescence signals, which can be exploited for chemical sensing and photocatalysis. These exceptional properties of 2D materials have initiated extensive efforts to use them in all fields of recent advancements, from electronic systems to biomedical devices. In the environmental field, graphene and related 2D materials have been used to develop novel materials for environmental decontamination, as building blocks for next generation water purification, and contaminant monitoring or removal. In order to improve the performance of 2D materials in these applications, various strategies have been proposed, such as functionalization and/or doping of their surface and subsequent immobilization of metal atoms in the form of nanoparticles fabricating hybrid materials. The combination of the unique properties of 2D materials and the high reactivity of fluorescent metal nanoclusters, which consist of a few to a hundred metal atoms, results in the improvement of the catalytic activity, enhancement of light absorption of graphene and TMD network, and conjugation with a variety of molecules to construct sensors.

Driven by the urgent development of such hybrid materials, this PhD Thesis presents the preparation of graphene and related 2D nanomaterials (i.e. TMDs) combined with metal nanoclusters for energy conversion applications. On this background, a series of layered-based hybrid materials with tailored interfaces were developed and characterized through complementary spectroscopic and microscopy imaging means. Anticipated results include high (photo)catalytic activity, selectivity and sensitivity, excellent stability and retention over various catalytic cycles. Moreover, the choice of 2D materials (graphene and TMDs) to be incorporated with fluorescent metal nanoclusters was decisive, as their documented performance is not well understood and exploited until now. Through attempting to uncover their mechanism and comparing them to established materials and theories, it is hoped that a clearer picture of these materials will be revealed and allow potential pitfalls for other, similar, materials to be avoided, making this work important from a scientific but also an industrial viewpoint.

1.2 Graphene

Carbon is a group IV element with a ground-state electron configuration of $1s^2 2s^2 2p^2$ and has the ability to form three different types of bonding, i.e. single, double, and triple bonds. The hybridization between 2s and 2p atomic orbitals, forming sp^n state, is responsible for creating a wide range of structures and properties in carbon-based materials. As a result of its unique bonding ability, carbon is capable of forming allotropes of any possible dimensionality ranging from 3D diamond (carbon atoms are bonded in a tetrahedral lattice arrangement) and graphite (carbon atoms are bonded in hexagonal lattice sheets) to 2D graphene, 1D nanotubes (single-walled carbon nanotubes – SWCNTs, multi-walled carbon nanotubes – MWCNTs) and, 0D fullerenes (Figure 1.1).[1-3] These allotropes together with their derivatives currently represent some of the most exciting materials available because of their unprecedented electronic, optical, mechanical, and chemical properties.

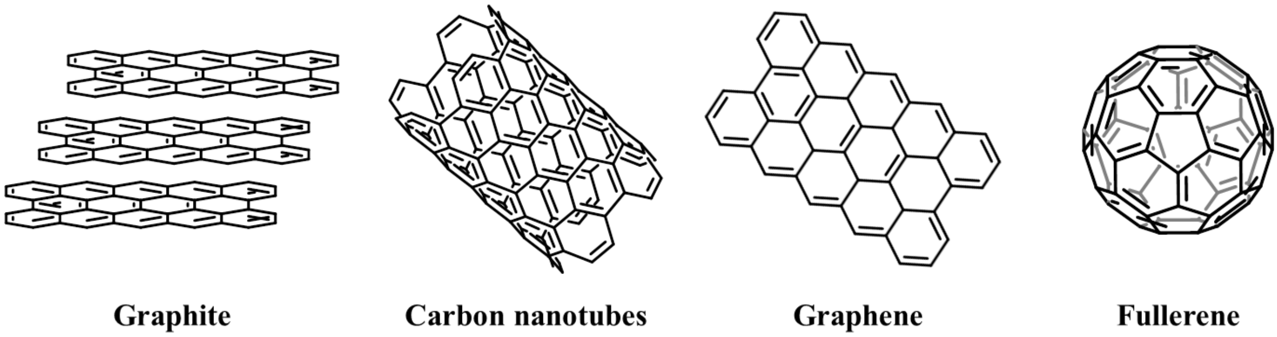

Figure 1.1 Carbon allotropes in different structures.

Graphite is the most common among the sp^2-hybridized carbon allotropes and its atoms are arranged in hexagonal lattices held together with weak van der Waals forces. Within a layer, each carbon atom is covalently bonded to three other forming a planar array of hexagons. The un-hybridized $2p_z$ orbital that accommodates the fourth electron forms a delocalized orbital of π symmetry that further stabilizes the in-plane bonds. Owing to the delocalized π band, graphite exhibits good electrical conductivity in the plane directions, while it is an insulator in the stacking direction. The individual layers of graphite are called graphene.

Graphene is a single-atom-thick planar sheet of hexagonally arrayed sp^2-bonded carbon atoms stacked in a two-dimensional honeycomb lattice. It became a hot research topic soon after its first experimental isolation in 2004, when Novoselov and coworkers[3] produced graphene flakes through "mechanically" peeling of highly oriented pyrolytic graphite employing a scotch tape. The unique 2D honeycomb structure endows graphene with many excellent physiochemical properties. These apparent merits include high thermal conductivity (5000 W m^{-1} K^{-1}),[4] high transparency (97.7%),[5] superior carrier mobility at room temperature (200 000 cm^2 V^{-1} s^{-1}),[6] good electrical conductivity (2000 S m^{-1}),[7] ability to quench fluorescence,[8] extremely high theoretical specific surface area (2630 m^2 g^{-1}),[9] excellent environmental compatibility, high mechanical strength (with a Young's modulus of 1 TPa),[10] low production cost,[11] and high adsorption capacity for organic and inorganic molecules.[12]

Graphene-based devices are expected to have a major impact in several technological fields. For example, potential electronic applications include high-frequency devices, touch screens, flexible and wearable devices, as well as ultrasensitive sensors, nano-electromechanical systems, superdense data storage, and photonic devices. In the energy storage and conversion field, applications include batteries and supercapacitors due to its property to store and transport electrical power, fuel cells, and photocatalysts. However, in the medium term, some of graphene's most appealing potential lies in its ability to transmit light as well as electricity, offering improved performance for light emitting diodes (LEDs), flexible touch screens, photodetectors, and ultrafast lasers. To move a step forward, the various developed methodologies for graphene functionalization have opened up its applications towards the biological field, such as in targeted drug delivery, imagining and diagnosis, biosensors, and hyperthermia.[13]

1.2.1 Preparation of graphene

There are various reported preparation methods of graphene including exfoliation,[14] arc-discharge[15], and chemical vapor deposition (CVD)[16]. One method for isolation of mono-layered graphene is through the mechanical exfoliation from crystalline graphite, but this is not scalable beyond a single graphene flake, making graphene with lateral dimensions on the order of tens to hundreds of micrometers. However, this method suffers from very low yield and cannot be applied for large scale synthesis. Liquid exfoliation of graphite is a straightforward method for obtaining high quality graphene. Several solvents have been reported, such as N,N-dimethylformamide (DMF), N-methylpyrrolidone (NMP), and ortho-dichlorobenzene (o-DCB).[17] Once the surface energy of the solvent is suitably controlled to be close to that of graphite, so as to surpass the thermodynamic stability of the former due to van der Waals forces, graphene can be readily exfoliated using ultrasonication. Nevertheless, the applications of this method are hindered due to the residual organic solvent on graphene surface and high energy cost during preparation. Moreover, a cathode and an anode, both with pure graphite rods, are used for the arc-discharge method, while buffer gases, such as H_2, Ar, He, NH_3, are needed for arc evaporation. As the rods are brought close together, discharge occurs resulting in the formation of plasma. When the discharge ends, the soot generated on the cathode is collected under ambient conditions.[18] The yield and purity of as-obtained graphene sheets often suffer from impurities of spherical carbon aggregates and CNTs in cathode deposit area, thus the product is mandatory to undergo another purification step.

The important large scale synthesis of graphene includes the thermal decomposition of silicon carbide and CVD growth. The formation of carbon layers is governed by the sublimation of Si in ultrahigh vacuum (UHV) at temperatures ranging from 1000 to 1500 ^{o}C, so that the remaining carbon atoms could self-assembly form graphene. However, the requirement for excessive temperature and expensive SiC wavers is not compatible with low-cost technologies. One the other hand, in a typical CVD route, a gas carbon-based precursor (e.g. CH_4, C_2H_4) is thermally decomposed and deposited on a substrate at high temperatures ranging from 1000–1600 ^{o}C. The advantage of this method is its versatility, as high quality, large size graphene sheets can be produced. However, apart from the needs of high temperatures, there are additional technical limitations for removing graphene from the growth substrate and in the scale-up of the technique. For example, transferring graphene from a metal substrate using wet etching method is likely to lead to doped and defected graphene affecting its quality.[19] As a result, CVD is still a high cost and low efficiency production method.

The most common approach to graphite exfoliation is the use of strong oxidizing agents to yield graphene oxide (GO), a hydrophilic carbon material. Although the exact structure of GO is difficult to determine, it is clear that for GO the previously contiguous aromatic lattice of graphene is interrupted by oxygen functionalities. Thus, hydroxyl or epoxy groups are introduced on the basal plane, while carbonyl and carboxylic groups are mostly present at the edges of graphene sheets (Figure 1.2). The disruption of graphene lattice is reflected in an increase in interlayer spacing from 0.335 nm for graphite to more than 0.625 nm for GO.

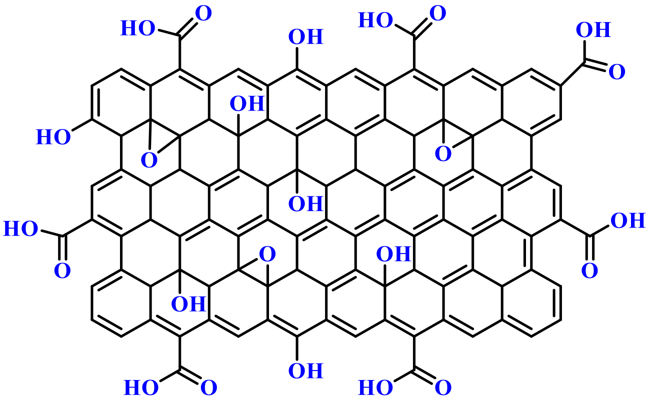

Figure 1.2 The graphene oxide structure consisting of carbon atoms and oxygen-based functional groups.

The first documented synthesis of GO is credited to Brodie in 1859.[20] Graphite was mixed with potassium chloride ($KClO_3$) and solubilized in fuming nitric acid (HNO_3) at 60 °C for 3-4 days. The elemental analysis revealed a composition of 60% C, 2% H, and 38% O and since the resulting product was dispersed in pure or alkaline water, and not in acidic media, Brodie named the material "graphic acid". Later, in 1898, Staudenmaier[20] amended Brodie's reaction by adding concentrated sulfuric acid (H_2SO_4), to increase the acidity of the mixture, and several aliquots of solid $KClO_3$ over the course of reaction. This small change in the procedure made the production of highly oxidized GO in a single reaction vessel significantly more practical. In 1958, Hummers and Offeman[21] proposed an alternative way to oxidize graphite flakes, which is the most commonly today. They mixed graphite with concentrated sulfuric acid (H_2SO_4), sodium nitrate ($NaNO_3$) and potassium permanganate ($KMnO_4$) to obtain brownish grey slurry. The suspension was diluted with water and hydrogen peroxide (H_2O_2) was added to get a higher oxidation degree. It should be noted that all three of these procedures involve the generation of highly toxic gases NO_2, N_2O_4, and/or ClO_2; the latter also being explosive. An improvement of Hummers' method was proposed by Tour's group at Rice University in 2010.[22] They substituted $NaNO_3$ with phosphoric acid (H_3PO_4) in a 9:1 mixture of concentrated H_2SO_4/H_3PO_4 and increased the amount of $KMnO_4$. This method exhibits a variety of advantages, including the higher oxidation degree of graphite and the avoidance of large exothermic phenomena or toxic gases generation, making it suitable for large scale production of GO. A comparison of the improved method with the conventional and modified Hummers' procedures can be seen in Figure 1.3.

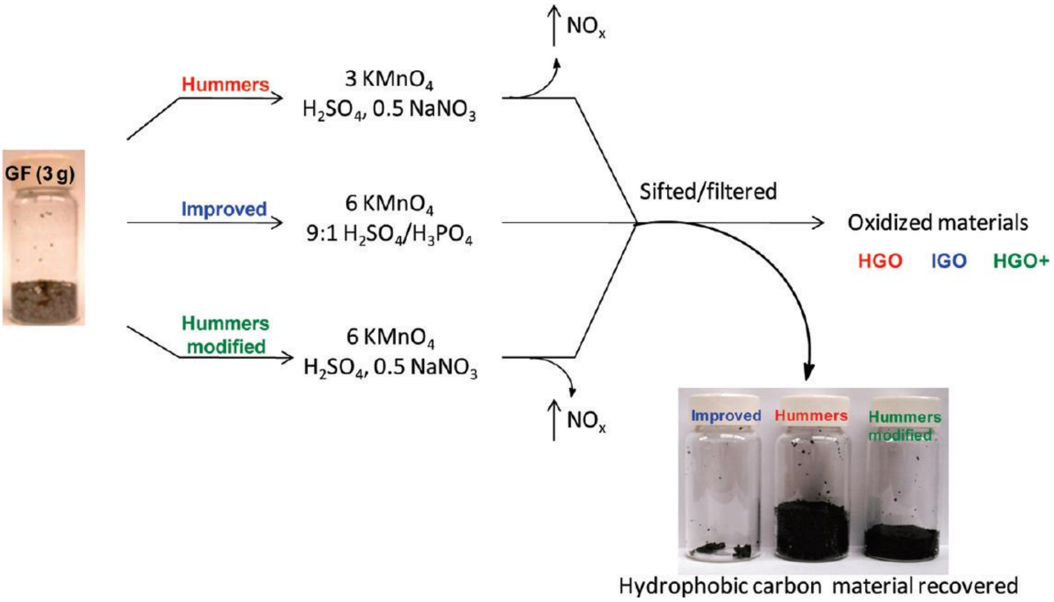

Figure 1.3 Representation of the procedures followed starting with graphite flakes (GF) through Hummers, Hummers modified and improved Hummers methods.[22]

Due to its low cost and easy processability, various attempts have been made to improve the electronic properties of GO through reduction means. The reduced GO (rGO) resembles graphene structurally and can partially restore the conductive features of perfect graphene; however, it is technologically difficult to completely eliminate all the oxygen-containing groups. The graphene derived from GO reduction generally bears some residual oxygen functional groups or structural defects such as topological vacancies and pentagon–heptagon defects, and has lower electron mobility than graphene fabricated from mechanical cleavage or CVD. Despite the partial de-oxygenation, reduced GO still yields considerable conductivity values providing a facile method for graphene-based devises.[23]

So far, various reduction methods have been used to prepare rGO and among them, chemical reduction and thermal annealing routes have been extensively applied. Chemical reduction is a solution-based route, which is regarded as the simplest and most cost-effective and can be performed at low temperature by using a wide range of reducing agents as anhydrous hydrazine (N_2H_4), sodium borohydride ($NaBH_4$), lithium aluminum hydride (LAH), hydroquinone, dimethylhydrazine, hydroxylamine hydrochloride ($H_2NOH{\cdot}HCl$), sodium hydride (NaH), urea, and sulfur-containing compounds.[24] Hydrazine is among the most used reducing agents due to its high reduction efficiency; however its chemical toxicity and introduction of nitrogen-based impurities should be thoroughly considered. For that reason, $NaBH_4$ is employed also as an environmentally friendly alternative, though with lower reducing ability than hydrazine. Thermal reduction is typically achieved under high temperatures up to 1000 ^{o}C by heating GO in inert or reducing environments such as ultra-high vacuum, H_2, Ar, NH_3, or under mild conditions by using microwave techniques. Nevertheless, the high temperature regulation is a downside of this method; the combination of both chemical and thermal reduction routes may achieve a high level of reduction efficiency. For example, the use of $NaBH_4$ and concentrated sulfuric acid combined with thermal annealing in Ar/H_2 at 1100 ^{o}C yielded rGO with high carbon content (C:O > 246).[25]

Compared with pristine graphene, the functional groups in GO can indeed give rise to remarkable structural defects. This results in some loss of electrical conductivity, which possibly affects the applicability of GO in electrically active materials and devices.[26] On the other hand, when it comes to real applications, the presence of functional groups on GO is beneficial as they can create stable and homogeneous colloidal suspensions in aqueous or polar organic solvents. This is important for further processing as these groups can serve as sites for chemical modification or functionalization of GO, which in turn can be exploited to incorporate various species through covalent or noncovalent bonds for design of novel hybrid materials. GO is therefore widely considered as a building block for novel graphene-based materials.

1.2.2 Covalent functionalization of graphene

One downside of exfoliated graphene is its high tendency to aggregate or restack forming again multilayers similar to graphite, driven by strong π-π stacking interactions and van der Waals forces. Moreover, its zero band gap property and chemical inertness put limitations in potential applications. Therefore, functionalization has to be carried out to decrease graphene hydrophobicity in polar solvents and in turn improve dispersibility and processability in organic and aqueous solutions. On this background, modification of graphene can take place either via covalent linkage of organic moieties or non-covalent interactions. The non-covalent functionalization of graphene can be achieved via π-π interactions, or through van der Waals forces, and electrostatic attractions attaching a variety of organic species on graphene through simple mixture in liquid media. Such approach is attractive as the electronic conjugated sp^2-hybridized carbon network is not perturbed, while retaining its superior intrinsic electron and thermal conductivity. In fact, π-π staking interactions are the dominating forces in supramolecular modification of graphene, as diverse planar aromatic structures (such as pyrene and porphyrin derivatives) can interact through orbital overlapping. Moreover, these interactions not only ensure the functionalization but also play an important role in the dissociation of graphenic stratums, leading gradually to a complete separation. In general, non-covalent functionalization has low stabilization energies of ~2-3 kcal/mol, indicating that the organic compounds can be easily detached from graphene sheet, which may be beneficial in bio-related applications but disadvantageous for accurate photo-electronic studies in liquid media.[27]

On the other hand, covalent modification is the most studied strategy of graphene functionalization. This is due to the fact that it causes the most substantial changes to the electrical activity of exfoliated graphene, such as the opening of zero bandgap, and allows for the introduction of a wide variety of functional groups on the graphene lattice. The main purpose is the improvement of dispersibility of graphene in common organic solvents that is usually obtained after attachment of suitable organic groups, which leads to the effective development of graphene-based devices. It is well established that the covalent grafting of molecules onto graphene gives rise to robust conjugates with energies of ~100 kcal/mol, thus facile purification methodologies for removal of excess starting materials or reaction byproducts can be adopted without any risk of desorption. Notably, GO with abundant reactive functional groups (e.g. hydroxyl, epoxy, and carboxyl acid species) provides higher dispersibility and possibility for further functionalization pathways rendering it a better candidate for modifications, in comparison to pristine graphene. However, the main drawback of covalent functionalization is the transformation of sp^2 hybridized carbon atoms into sp^3 ones, inducing defects and a sizeable loss of its electronic properties. There are various routes to covalently functionalize graphene either by employing addition or cycloaddition reactions.[28] The following subsections provide an overview of the more commonly employed covalent functionalization routes of graphene: (1) 1,3-dipolar cycloaddition reaction of *in situ* generated azomethine ylides, (2) *in situ* generated aryl diazonium salts addition, (3) addition of azides, (4) Bingel cyclopropanation addition, and (5) condensation reactions on GO.

Among the most popular covalent functionalization routes is the 1,3-dipolar cycloaddition reaction of *in situ* generated azomethine ylides. Upon thermal condensation of aldehydes and α-amino acids, fused pyrrolidine rings are cycloadded onto the skeleton of graphene sheet. In more detail, azomethine ylides are nitrogen-based 1,3-dipoles, consisting of a carbanion next to an immonium ion and can be obtained upon decarboxylation of the immonium salts derived from the condensation of α-amino acids with aldehydes or ketones (carbonyl species). Because azomethine ylides are very reactive intermediates, a fused pyrrolidine ring is immediately formed on the junction between two six-membered rings of the graphene lattice, thus inducing the transformation of sp^2 carbon atoms to sp^3 ones. The 1,3-dipolar cycloaddition reaction is very versatile, as a plethora of commercially available aldehydes and substituted α-amino acids can yield diverse graphene-based materials. The only setback is the disruption of the conjugated network of graphene upon cycloaddition reaction, resulting in lower electron conductivity values in the final hybrid.[29]

The reaction dealing with the *in situ* generation of aryl diazonium salts is by far the most widely practiced technique for the covalent introduction of aromatic species on the basal plane of graphene. The original methodology was firstly employed for the functionalization of CNTs.[30] Briefly, the diazonium salt can be *in situ* generated, by its corresponding aniline together with sodium nitrite or isoamyl nitrite. Upon heating, electron transfer from graphene to aryl diazonium salt derivative occurs, resulting in the formation of the corresponding radical aryl unit, which attacks the sp^2-hybridized carbon atoms to form covalent bonds.[31] The reaction has also shown potential as an intermediate step, allowing post-functionalization processes onto the obtained aryl-modified graphene through "click chemistry", allowing enrichment of the decoration of the resulting product.[32]

Another functionalization strategy for graphene modification is the addition of organic azides, which form aziridine adducts onto the sp^2 basal network of graphene.[33] The particular functionalization proceeds via nitrenes as generated upon the thermal or photochemical decomposition of aryl azides with subsequent N_2 release. Nitrene addition has also been used for covalently grafting polymers onto graphene lattice.[34]

The Bingel cyclopropanation reaction was firstly employed in fullerene chemistry[35] and concerns the generation of reactive carbanions from α-halo esters and their subsequent addition to carbon double bonds of graphene, followed by the elimination of halogen. The

Bingel reaction generally requires the presence of a strong base, such as 1,8-diazabicyclo[5,4,0]undec-7-ene (DBU) or sodium hydride (NaH), as a catalyst, which facilitates the carbanion formation. This strategy of covalent graphene functionalization has been widely applied thanks to the facile synthesis and variety of malonate derivatives. In fact, malonic acid allows the functionalization with different organic structures bearing hydroxyls, forming esters which are capable to reacting with graphene.[36] The chemical modification of graphene through the aforementioned addition reactions is summarized in Figure 1.4.

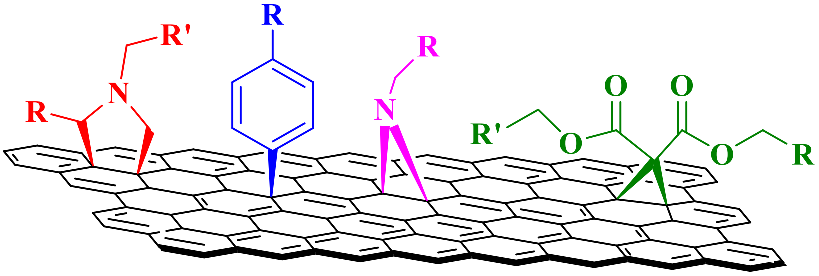

Figure 1.4 General example of chemical modification of graphene through 1,3-dipolar cycloaddition reaction (red), aryl diazonium salts addition (blue), azide addition (pink), and Bingel cycloaddition (green).

Condensation reactions constitute another category for covalent functionalization of GO. The carboxylic groups at the edges of GO can easily react with alcohols, amides or thiol organic species through covalent bond. Prior to that, the "activation" of carboxylic groups is required using active reagents such as thionyl chloride ($SOCl_2$), oxalyl chloride ($(COCl)_2$) for the formation of the corresponding acyl chlorides (GO–COCl).[37] Subsequent treatment of GO–COCl, in completely anaerobic and dry conditions, with alcohols, amines or thiols, eventually results in the formation of esters, amides or thioesters onto GO sheets (Figure 1.5). This modification route can alter the hydrophobic−hydrophilic characteristic of graphene for dispersion in different solvents and even water, a critical step that potentially leads to low-cost solution processing of graphene. Moreover, the condensation reaction does not disrupt the GO network, as the sp^2 carbons of the basal plane are not involved.

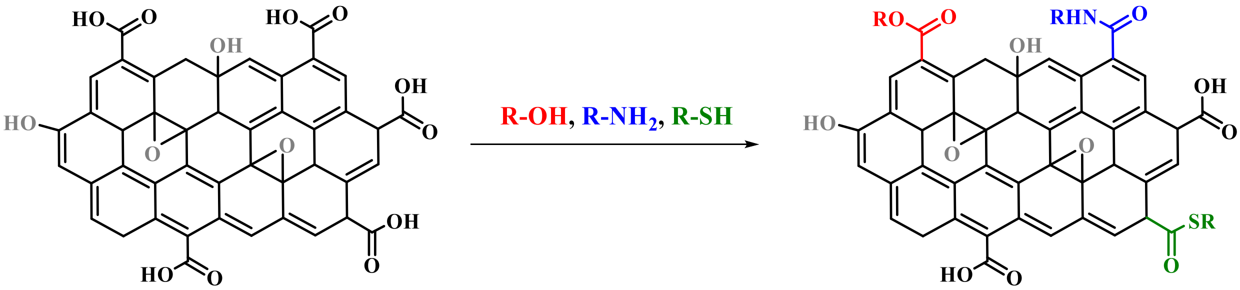

Figure 1.5 General examples of chemical modification of GO through condensation reactions with alcohols (red), amines (blue), and thiols (green).

Another concept to covalently functionalize graphene dictates the addition of organic groups on pre-modified graphene through "click" chemistry, which was firstly presented by Sharpless in 2001.[38] The synthetic appeal of "click" reactions relies upon their tolerance of water and oxygen, simple reaction conditions, and high yield. The Huisgen copper-catalyzed

1,3-dipolar azide–alkyne cycloaddition (CuAAC) has been the most employed for the modification of graphene mostly with polymers.[39-40] Generally, graphene is modified with alkyne moieties on its basal plane, while another compound carrying an azide group is required. The reaction is conducted in the presence of Cu(I) catalysts (e.g. CuI), while the addition of DBU seems to be preferred. However, the CuAAC click reaction presents an important drawback derived from the toxicity of the copper catalyst. In order to avoid the use of any toxic metal catalysts other metal-free click reactions have been developed, such as thiyl−radical approaches (thiol−ene and thiol−yne).[41-42] The thiol–ene is accomplished by the addition of a thiol-terminated organic compound directly onto the π-conjugated carbon network of graphene, while thiol−yne requires firstly the alkyne-functionalization of graphene and its coupling with thiol-functional group. These reactions possess all the desirable features of a click reaction, such as simplicity, high efficiency, no by-products and high yield, and also present an additional advantage since they can be externally-triggered by thermal (2,2′-azobis(2-methylpropionitrile) or optical initiators. The chemical modification of graphene through click-chemistry methodologies is summarized in Figure 1.6.

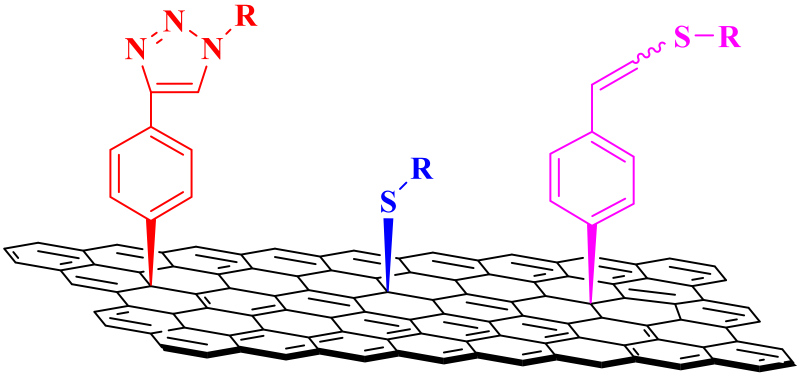

Figure 1.6 General example of chemical modification of graphene through "click" chemistry method: CuACC (red), thiol−ene (blue) and thiol−yne (pink) reactions.

1.2.3 Characterization of graphene

In order to confirm the successful functionalization of graphene, complementary spectroscopic, thermal and microscopy imaging means are normally applied. Spectroscopy techniques include Raman, and attenuated-total-reflectance infra-red (ATR-IR) spectroscopy. Further, thermal analysis includes thermogravimetric analysis (TGA) and microscopy techniques involve transmission electron microscopy (TEM) imaging.

Owning to its sensitivity to changes in the atomic structure of carbons, Raman spectroscopy is a powerful tool for monitoring changes within the lattice of graphene-based materials. Ideally, perfect exfoliated graphene exhibits two main characteristic bands, namely the G-band, due to the presence of sp^2 hybridized carbons at 1585 cm^{-1} and the second-order 2D-band at around 2700 cm^{-1}. However, in case of functionalized graphene a third band is evidenced in the Raman spectrum, the so-called D-band at around 1350 cm^{-1} assigned to the disorders of the honeycomb structure due to the introduction of defects and presence of sp^3 hybridized carbon atoms during the functionalization process. At the same time, the shape and frequency of the 2D band is sensitive to the numbers of graphene layers, while it shifts to lower wavenumbers upon modification.

The ATR-IR spectroscopy is a nondestructive technique, allowing for unraveling the functional groups of the tethered organic compounds onto graphene. Graphene has the main absorption band at ~1600 cm^{-1} attributable to C=C units; however, active IR bands can be recorded due to the presence of organic groups on modified graphene sheets, such as carbonyls (1630-1750 cm^{-1}), alkyls (2950-2850 cm^{-1}), and alcohols (3000-3300 cm^{-1}) among others. Hence, ATR-IR involves the qualitative identification of the organic constituents in graphene-modified materials.

TGA is essential for the calculation of the functionalization degree in modified graphene. Normally, graphene is thermally stable at high temperatures under inert conditions, while organic addends tend to decompose in a typical temperature range 200-550 ºC. Hence, in a thermograph of a functionalized graphene material, the loading of the organic compound onto graphene sheets can be quantitatively calculated via the following equation:

$$\text{Loading} = \frac{M_{R(\text{organic compound})} \cdot \text{mass residual}}{\text{mass loss} \cdot A_{R(\text{carbon})}}$$

M_R: molecular weight of organic compound, and A_R: atomic weight of carbon.

Moreover, microscopic techniques (TEM) are usually employed to verify the number, size and defected areas of graphene layers, while organic functional groups suffer from irradiation damage of the electron beam. TEM is usually complemented with energy dispersive X-ray (EDX) spectroscopy to identify the atomic composition not only of graphene, but also of the functional hybrid materials. Through EDX the purity of graphene-based material can be assessed.

1.3 Transition metal dichalcogenides

The great success of graphene has been followed by an equally impressive surge for the development of other 2D materials that can form atomic sheets with extraordinary properties. In particular, transition metal dichalcogenides (TMDs) have received significant attention expanding the rapidly emerging realms of 2D materials. TMDs are layered crystals with MX_2 stoichiometry, where M refers to a transition metal atom (e.g. Mo, W, Ta) and X to a chalcogen atom (S, Se, Te). Each monolayer is a three-atom-thick layered TMD, composed of a stratum of transition metal atoms sandwiched between two layers of chalcogen atoms, thus forming a X-M-X structure. The intra-layer M-X bonds are predominantly covalent in nature, whereas the sandwich layers are coupled by weak van der Waals forces allowing the crystal to readily cleave along the layer surface.[43]

Depending on the coordination environment of the transition metal and the electronic configuration, layered TMDs exhibit disparate electronic structures. The presence of unsaturated d-orbitals and chemically active edge sites results in a broad diversity of materials, including catalysts, semiconductors, semimetals, ferromagnets, and even superconductors.[44] The coordination of metal atoms in layered TMDs can be either trigonal prismatic (2H polymorph) with D_{3h} point group symmetry or octahedral O_h (1T polymorph), giving rise to semiconducting and metallic phases, respectively (Figure 1.7). Due to the combination of the different metals and chalcogens more than 60 different layered TMDs have been identified until today, each with its own set of properties spanning the full range from insulators such as HfS_2, semiconductors such as MoS_2 and WS_2 and true metals such as $NbSe_2$ and TaS_2.[43] However, the most studied, stable and commonly representative TMDs are MoS_2 and WS_2 followed by $MoSe_2$ and WSe_2. In fact, MoS_2 and WS_2 are the most investigated among the TMDs due to their economic availability and well-established obtaining processes.

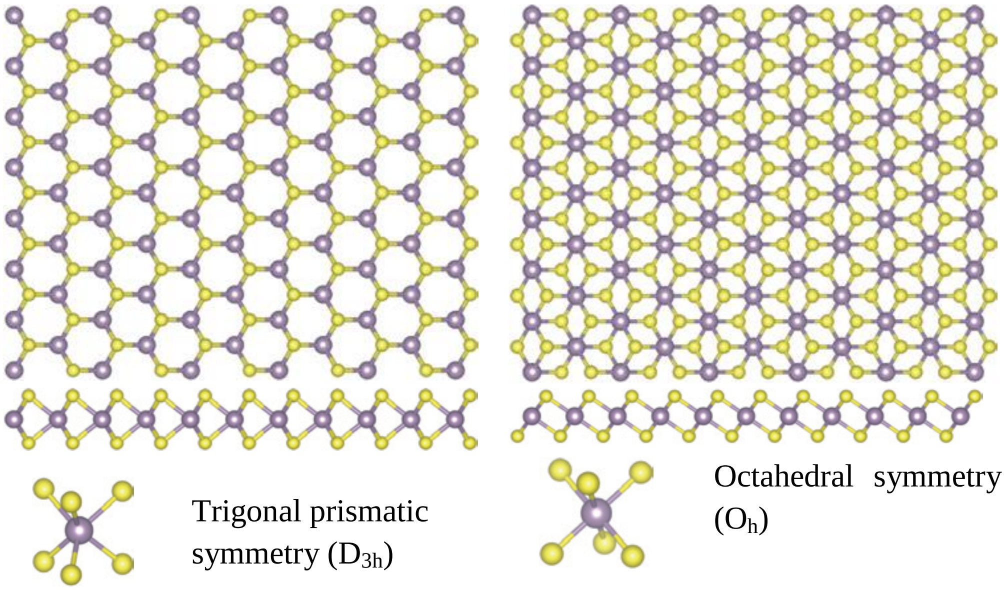

Figure 1.7 Schematic top/side view of MoS_2/WS_2 in 1T phase (left), and 2H phase (right) [43]

The emergence of the direct electronic bandgap together with the strong photoluminescence (PL), render TMDs promising candidates for a variety of opto-electronic devices, including solar cells, photo-detectors, light-emitting diodes, flexible electronics and photo-transistors.[45-46] For example, unique properties of MoS_2 include direct bandgap (~1.8 eV), good mobility (~700 $cm^2\ V^{-1}\ s^{-1}$), high current on/off ratio of ~10^7–10^8, large optical absorption and a giant PL arising from the direct bandgap (1.8 eV) in monolayer; thus, it has been studied widely for electronics and optoelectronics applications.[47-48] Alternatively, the large surface area due to their sheet-like structure makes them attractive for energy storage (supercapacitors and batteries), sensing, and photocatalytic applications. Besides having excellent optical and electronic properties, ultrathin TMDs are also characterized by a high degree of mechanical flexibility, robustness and light weight,[49] which make them ideal candidates for the fabrication of flexible, foldable and wearable/portable (opto)electronic devices.[50-51]

1.3.1 Preparation of transition metal dichalcogenides

Considerable efforts have been devoted to the synthesis of controllable, large-scale, and uniform atomic layers of diverse 2D TMDs using various bottom-up and top-down approaches, including mechanical exfoliation, chemical exfoliation, and chemical vapor deposition (CVD). CVD is still an attractive method to obtain mono- or few-layered TMDs driven by the major breakthrough that has enabled the preparation of large-area graphene. There are three main CVD techniques for preparation of TMDs: (i) co-vaporization of metal and chalcogen precursors and their decomposition, followed by deposition of TMD on a substrate material, (ii) direct sulfurization (or selenization) of metal film, and (iii) conversion of MO_3 (metal oxide) to MS_2 (metal disulfide) by sulfurization.[43, 48] These processes all have similar downsides as CVD methods with graphene, i.e. high temperatures, difficulties in transferring layers while avoiding damage to the material and scalability issues as the process is limited by the substrate. An alternative for MoS_2 has been demonstrated with a method of dip coating a surface in a precursor, ammonium thiomolybdate. This thin layer can then be thermally decomposed in the presence of sulfur to produce large area MoS_2.[52] This method is potentially much more scalable, however control of the number of MoS_2 layers is more difficult, with only tri-layer demonstrated. Furthermore, high temperatures are still required, meaning film transfer is still mandatory for many applications. As with graphene, CVD processes are best suited for high quality materials intended for electronic applications.

Due to the weak van der Walls forces between TMD stratums, it is possible to exfoliate the crystal into single layers that boast properties dramatically different from their bulk counterparts. Mechanical cleavage using the adhesive tape method yields the highest quality of monolayered TMDs. As with graphene however this process is hardly a scalable one and is limited to production of samples for property testing or lab-prototype testing. Liquid exfoliation methods are likely to be better in applications where large quantities of materials are required.

Ion-intercalation and exfoliation, which refers to “chemical exfoliation” is a common route to prepare dispersions of few to monolayered TMD nanosheets. Ion-intercalation refers to the introduction of chemical species that disrupt interlayer attraction through layer reduction and concomitant insertion of exchangeable ions into the interlayer gap. Usually, alkali metal ions or Lewis base with small radii and suitable reducing ability are employed for intercalation. The chemical intercalation of TMDs by lithium was first reported in 1970[53] and then Morrison, Frindt, and co-workers[54] demonstrated the intercalation-driven exfoliation. The typical chemical exfoliation process involves a primary reaction of bulk TMD powder with lithium-containing agents such as n-butyllithium (n-BuLi) under an inert atmosphere to allow lithium ions to insert between TMD interlayers which is accompanied by the expansion of the interlayer spacing, followed by neutralization of the intercalated materials with water (Figure 1.8). The reaction between intercalated lithium and water rapidly releases H_2 gas, which builts up adequate pressure to force the flakes kept by weak van der Waals forces apart. One intriguing feature of chemical exfoliation is the local phase rearrangement which takes place during the course of lithium intercalation, therefore changing the surface property and electronic properties accordingly. In the case of chemical exfoliation of MoS_2 employing

BuLi, bulk 2H-MoS_2 is reductively intercalated with lithium ions and this reaction results in the phase transformation from semiconducting 2H-polymorph to metallic 1T-polymorph, a structural transformation which is maintained in the final exfoliated product. Therefore, chemical exfoliation process yields the MoS_2 that contains predominantly the metallic 1T-polymorph.

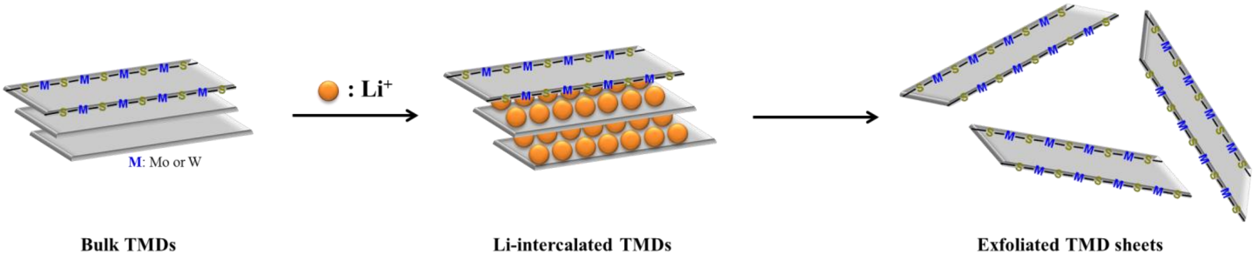

Figure 1.8. TMD exfoliation through n-butyllithium intercalation process.

The use of superacids, i.e. chlorosulfonic acid, is another liquid exfoliation method that leads principally in semiconducting TMDs.[55] In this process, chlorosulfonic acid serves as a functional intercalating agent between the layers of the TMDs with the lone of electrons of sulfur placed in the TMDs. Basal sulfur act as a weak base, which can be protonated by chlorosulfonic acid, however, without being oxidized. This fractional removal of electrons in protonated TMDs is the initial step toward exfoliation due to the development of repulsive electrostatic forces between the stratums of TMDs. Notably, deprotonation can take place in the presence of a competing base such as water· an exothermic reaction producing sulfuric acid and HCl gas, which facilitates delamination process. This methodology yields few and even monolayers of TMDs with sizes of hundreds of nanometers, while its advantage is the preservation of electronic properties of the semiconducting polytype.

Recently, the concept of liquid phase exfoliation has been developed to circumvent the limitations of the previously described approaches, which involve the use of highly flammable and explosive chemicals. Fundamentally, liquid exfoliation requires the selection of an appropriate solvent such that its surface tension to closely match the surface energy of TMDs. For MoS_2, the surface tension of NMP (40 mJ/m^2) is similar to estimated surface energies of few-layered MoS_2 (46.5 mJ/m^2).[56] Mechanical agitation via probe sonication in NMP is commonly applied, overcoming the van der Waals interactions between layers, while it is possible to stabilize the suspensions against reaggregation through London dispersion forces or polar interactions.[14] However, NMP is susceptible to sonochemical degradation during exfoliation, which leads to strong visible photoluminescence signals derived from both the degraded solvent and TMD sheets.[57] Notably, the PL spectrum of MoS_2 in NMP is dominated by the degraded solvent influencing the spectroscopic measurements. Hence, a careful consideration is needed for the selection of the appropriate exfoliation process.

1.3.2 Covalent functionalization of transition metal dichalcogenides

Another important aspect to consider is that delamination process can generate topological and structural defects on TMDs, like in case of graphene. These lattice defects affect the electronic properties of the TMD sheets, modifying the charge carrier mobility and density.[58] Although it can be considered that they could have a disadvantageous effect on material's properties, defects can be exploited for introducing novel functionalities and are regarded as the starting point for chemical functionalization of TMD materials. Defects in the form of vacancies are common in TMDs derived from liquid exfoliation process. In the case of MoS_2 prepared by micromechanical cleavage, TEM studies revealed that sulfur vacancies are the most dominant type of defects in exfoliated sheets with densities of $\sim10^{13}$ cm^{-2}, corresponding to approximately 10 sulfur vacancies over an area of 10 X 20 nm^2, while it is proved that the sulfur vacancy formation energy is lower than the formation energies of other vacancies.[59] Additionally, double sulfur vacancies were found in exfoliated nanosheets with densities in the range of $\sim10^{13}$ cm^{-2}. Besides this type of vacancies, there are also grain boundaries, dislocations, vacancies of Mo–S complexes and anti-site defects.[60]

In general, perfect TMD sheets are free of dangling bonds, and therefore it is difficult to attach functional molecules on their surfaces. Hence, functionalization of their surface is essential for many applications in order to tune or add the desired properties to the material as it has been reported that the defect sites possess high affinities toward thiol moieties. Thiol/sulfur functionalization at sulfur vacancies, which are positioned mostly at the edges, is one of the most frequently strategy to tether functional units on TMD sheets. Besenbacher and co-workers produced a fascinating set of results on CVD grown 2H-MoS_2 monolayers. [61] They demonstrated the preparation of an array of MoS_2 clusters of varying sizes (from Mo_3S_7 up to $Mo_{36}S_{102}$). These clusters exhibited different degrees of S-atom vacancies as evidenced by scanning tunneling microscopy (STM) analysis. Interestingly, STM analysis revealed that dibenzothiophene molecules interacted with MoS_2 particles, with the S-atom of the dibenzothiophene filling/healing an S vacancy. This would suggest that the S-atom of dibenzothiophene is covalently bound – and not just physisorbed – to the unsaturated Mo atoms where an S vacancy exists. The coordination site was quite open, at a corner site on a triangular particle with lateral size < 1.5 nm, presumably providing sufficient space for the thioether ligand to access the Mo atom in order to coordinate, while clusters of larger size remained unmodified. Interestingly, no examples of the thioether ligand interacting with basal plane or edge sites were reported, suggesting the availability of corner sites is essential for S-atom containing molecules to interact with MoS_2 at S-atom vacancies. Two years later, two other thiol derivatives namely (3-mercaptopropyl)trimethoxysilane and dodecanethiol were employed and selectively filled the missing sulfur atoms which were previously extracted from 2H- MoS_2 with the aid of STM tip (Figure 1.9).[62] Afterwards, the STM tip was applied again to cleave the C–S bonds of the parent molecules and restore the pristine exfoliated surface. A few years later, another study took advantage of this functionalization technique by reacting thionine (3,7-diamino-5-phenothiazinium acetate), a molecular analogue of dibenzothiophene, with liquid exfoliated 2H-MoS_2 in the presence of an ionic liquid.[63] XPS analysis provided a conclusive proof that a new S 2p feature was present in the MoS_2-thionine composite material. Importantly, this new feature was distinctly different to S 2p features observed for pristine 2H-MoS_2 and thionine suggesting that the positively charged thionine can be easily attached to the negatively charged S vacancies at the edge of MoS_2. This strongly indicates the formation of a S–Mo or S–S bond between thionine and MoS_2.

The thionine-functionalized 2H-MoS_2 was used to detect DNA, displaying a decreased electrochemical response in the presence of DNA at very low concentrations, allowing for the efficient detection of DNA in highly dilute samples.

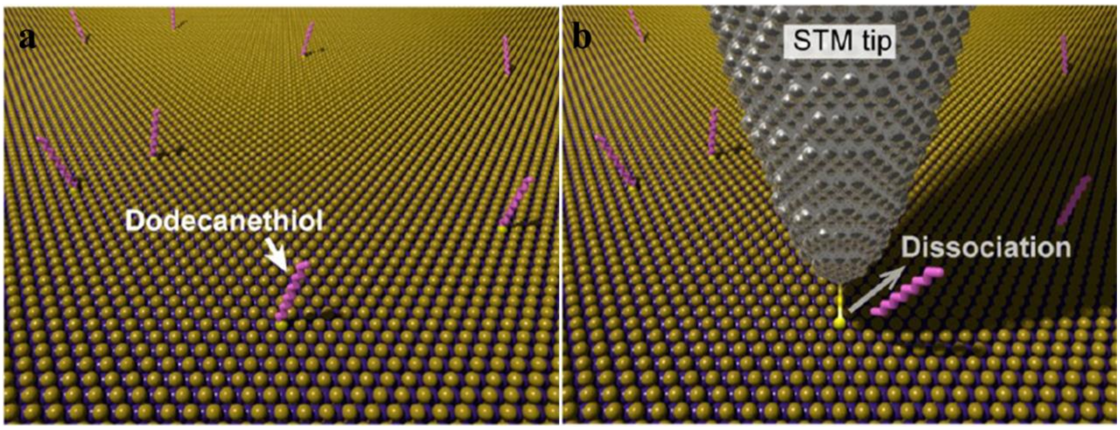

Figure 1.9 Schematic representation of STM experiments on the (a) absorption and (b) dissociation of thiol molecules, dodecanothiol, on the 2H-MoS_2 surface.[62]

Another example reporting the efficient functionalization of TMDs suggests the reaction between 1T-MoS_2 with bi-functional polyethylene glycol (PEG) ligands, which boast a thiol group at one end of the structure and the other end consists of a hydroxyl, carboxylate, or ammonium moiety.[63] Upon reaction and purification of PEG-modified MoS_2 sheets, a significant change in the zeta-potential to positive values of the TMD nanosheets was observed, indicating a change in the MoS_2 surface properties. Additionally, XPS analysis showed the presence of ether bonds in all conjugated materials, demonstrating that PEG functional groups were indeed bound to the surface of 1T-MoS_2. Furthermore, FT-IR revealed that the thiol groups reacted with the MoS_2, because the S-H band at 2563 cm^{-1} disappeared upon functionalization. The disappearance of the thiol moiety indicated the successful functionalization of MoS_2. Similarly, the functionalization of 2H-MoS_2 through reaction with organic thiols (4-mercaptophenol, thiophenol, 1-propanethiol, 1-nonanethiol, and 1-dodecanethiol) was conducted reporting the absence of S-H band in the IR spectrum, together with changes in the photoluminesce spectra of functionalized MoS_2 and in particular the characteristic emission peak was red-shifted after conjugation of thiol groups.[64] Another facile approach to synthesize organic functional group decorated MoS_2 sheets using thiol reagents as ligand was also developed. Thiol headgroups, such as mercaptopropionic acid (MPA), 2-thioglycerol (TG), and L-cysteine were used to modify 1T-MoS_2 by reaction with freshly prepared Li_xMoS_2.[65] Notably, the selection of MPA was bi-functional, as the carboxy-terminated MoS_2 was exploited for the *in situ* preparation of the corresponding polymer, i.e. poly(methylmethacrylate). Next, the negatively charged MoS_2-MPA hybrid interacted with Ag^+ ions for the growth of uniformly distributed silver nanoparticles. Analogously, the MoS_2–TG nanosheets with multiple hydroxyl groups were directly utilized to initiate ring-opening polymerization of ε-caprolactone. Hence, covalently funtionalized MoS_2 nanosheets have a high density of nucleation sites due to the presence of –COOH moieties.

The nature of groups carried by thiols may modify the properties of the hybrid material and can act as donors or acceptors via surface charge transfer. On this background, two thiol-terminated molecules containing NH_2 (i.e., 2-mercaptoethylamine) or F-containing (i.e. 1H,1H,2H,2H-perfluorodecanethiol and 2,2,2-trifluoroethanothiol) groups were covalently attached on sulfur vacancies of mechanically exfoliated MoS_2.[66] Because of the lone electron pairs of the NH_2 group, it is anticipated that the amine-terminated thiol can donate electrons to MoS_2, consequently leading to an n-doping effect. On the contrary, the high electronegativity of the fluorinated groups has the ability to withdraw electrons from MoS_2, leading to a p-doping effect in the final hybrid material. Indeed, XPS results manifested the presence of C–N and C–F bonds, while photoluminescence emission depicted a red-shift and weakening of the characteristic peak of MoS_2 in case of n-doping; opposite observations were identified in hybrids with F-containing groups due to p-doping effect. Thereafter, other organic thiols such as dithiogylcol,[67] and mercaptoundecanoic[68] were utilized to functionalize MoS_2 nanosheets offering new pathways for functionalization.

The versatility, wide applicability and variety of thiol-contaning organic molecules have undoubtedly opened up novel methodologies to functionalize TMD sheets leading to the amelioration of their physiochemical properties. However, particular consideration should be taken when it comes to the so-called “ligand conjugation” of thiol molecules to the unsaturated Mo atoms of MoS_2. A carefully conducted spectroscopic study uncovered that the reaction between organic thiols and MoS_2 nanosheets is a rather questionable way of modification, as thiols can be converted into the corresponding disulfides in a catalytic reaction activated by the presence of MoS_2, which eventually physisorb – and not covalently attach – onto the basal plane of the nanosheets.[69] Based on that, alternative strategies have already been developed employing 1,2-dithiolanes as robust thiol groups to tether to TMDs.

Recently, Canton et al. developed a novel functionalization protocol by covalently grafting 1,2-dithiolane derivatives at the S vacancies of exfoliated semiconducting MoS_2 sheets.[70] The versatility of α-lipoic acid was decisive as it allowed chemistry at the carboxylic acid and the construction of diverse schemes was possible. Two different 1,2-dithiolane organic units were used; the one with an ethylene glycol alkyl chain terminated to a butoxycarbonyl (BOC)-protected amine and the other with pyrene as an electron donor.[70] TGA analysis showed 8% loading of the organic functionalities, while HRTEM depicted the damage-free basal plane and the presence of the addend organic material at the edges. To further support the findings, electron energy loss spectroscopy (EELS) study was performed showing carbon peak signals at the edges of MoS_2 derived from the functionalization process. Additionally, XPS results revealed the disappearance of the corresponding S 2p signal attributable to “vacancy” or damaged material, indicating that the 1,2-dithiolane unit healed/filled the Mo atoms at S vacancies. Furthermore, density functional theory (DFT) modeling demonstrated that the most stable binding configuration was found for the edge functionalization rather than for the basal plane one. Similarly, the conjugation of organic molecules onto the carboxyl group of α-lipoic acid (and folic acid) was also reported for the functionalization of liquid exfoliated sheets with polyethylene glycol, which were further exploited as carriers for the anti-cancer drugs DOx, Ce6, and SN38.[71]

1.3.3 Plasma treatment of transition metal dichalcogenides

The functionalization of TMDs is an alternative way to alter their physicochemical properties by adding new functionalities in an easier and more controllable manner than wet chemistry dictates. Indeed, plasma-assisted modifications are versatile, including surface chemical functionalization, heteroatom doping, band-gap tuning, etching, and control of surface wettability, while they offer flexibility and clean experimental conditions. On this background, there are several studies reporting covalent doping of TMDs, where single atom dopants are introduced to TMD lattice through metal or chalcogen substitution, where the vacancies of TMD network exist, altering the electrical properties of the parent TMDs. For example, the use of plasma treatment has been proposed as a strategy to incorporate oxygen at the S vacancies of single-layered MoS_2, which derive from both exfoliation and bombardment process. In particular, sulfur atoms are preferentially removed from the MoS_2 sheet and oxygen atoms filled the sulfur vacancies by simultaneously oxidizing Mo atoms forming MoO_3. Markedly, MoO_3 introduced distortions in the MoS_2 lattice and acted as an insulator with great resistance properties. In another study, the oxygen plasma doping of mono-layered MoS_2 enhanced the photoluminescence signals and a red-shift of 20 nm was observed due to the defect sites introduced during plasma treatment.[72] Analogously, by using Ar and O_2 plasma treatment, a huge number of structural disorders were generated during the bombardment process altering the electronic characteristics of the flakes, which resulted in enhanced Raman signals of the fluorescent molecule of rhodamine.[73] This observation originates from the photoinduced charge transfer phenomena between rhodamine and MoS_2 and subsequent suppress of rhodamine fluorescence, which is reflected in the surface enhanced Raman scattering.

Nitrogen doping is also a popular method of plasma treatment and has been successfully applied in various materials, such as graphene.[74] Oligolayers of sol-gel grown MoS_2 sheets were functionalized with nitrogen in an *in situ* process, due to the use of molybdenum chloride and thiourea as precursors.[75] A set of characterization techniques verified the effective nitrogen doping highlighting that X-ray photoelectron spectroscopy (XPS) is one of the most critical methods to identify the covalently bonded nitrogen in MoS_2 at ~ 398 eV. Another study demonstrated that strong covalent bond between molybdenum and nitrogen atoms is achieved through chalcogen substitution of sulfur (Figure 1.10). Also, it was proved that the use of N_2 plasma induced compressive strain and p-type doping in MoS_2 without layer etching, while it enhanced the electrical properties of doped material.[76] Similar results were reported after short RF plasma treatment of CVD grown MoS_2 sheets in nitrogen.[77] Additionally, $MoSe_2$ sheets have been doped through nitrogen plasma –maybe the only report using $MoSe_2$ – demonstrating the preferential removal of Se atoms, the creation of Se vacancies and filling of those vacancies by nitrogen, as proved by a combination of characterization techniques, such as XPS and STM among them. Furthermore, other dopants have been proposed for surface modification of MoS_2 sheets, such as hydrogen,[78] fluorine,[79] and phosphorous[80]; however, with undesirable side effects, such as sample degradation and flake etching, while special handling is needed due to their high reactivity. At the same time, plasma-assisted doping and functionalization of WS_2 has not been thoroughly investigated and is an opportunity for significant future research. A notable work applied plasma fluorination on mechanically exfoliated monolayers of WS_2, showing photoluminescence enhancement and improved ability to sense n-type gases, such as NH_3.[81]

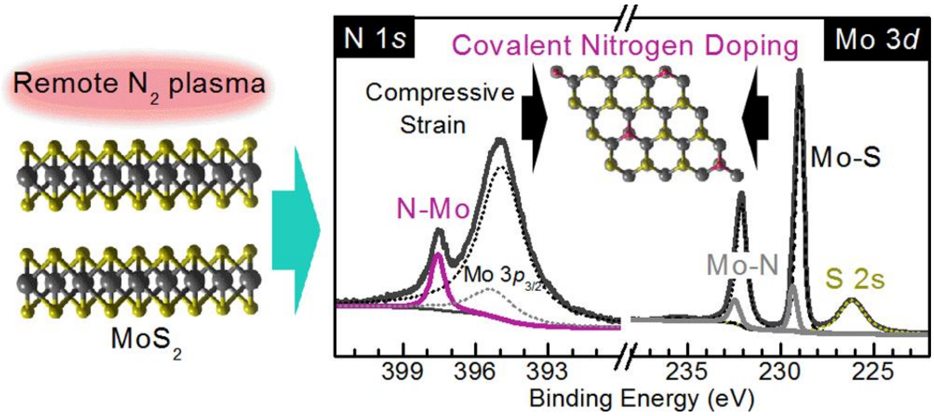

Figure 1.10 Nitrogen doping of MoS_2 through sulfur substitution. XPS spectra of N 1s and Mo 3d core levels demonstrate the nitrogen doping of MoS_2.[76]

To conclude, the use of plasma-assisted treatment of TMDs has already been proposed as an approach to functionalize their surface through application of various dopant reagents. As described below, the majority of the surface modifications are dictated by the doping of TMDs, where single atom dopants are introduced in the TMD lattice through chalcogen (sulfur) substitution. Sulfur defects are generated either naturally during the exfoliation or bombardment process due to the plasma treatment. There is also an example demonstrating the substitution of Mo by niobium (Nb) during the growth process.[82] Plasma treatment can offer a lot of merits, such as clean experimental conditions, controllable dopant concentration, variety of chemicals, solvent-free process, and high homogeneity, as compared to wet chemistry methodologies. For example, nitridation of MoS_2 was previously reported to be achieved by exposing MoS_2 to NH_3 at 750 ^oC, while no temperature regulation was needed when plasma is applied. Encouraged by the efforts on the exploration of plasma-assisted doping strategies for TMDs, the use of plasma treatment for the introduction of various species in TMD network is still an open area for scientific investigations.

1.4 Metal nanoclusters

1.4.1 Synthesis of metal nanoclusters

At the same time, metal nanoparticles constitute perhaps the most widely studied field in nanotechnology. In particular, metal nanoclusters (M_{NCs})[83-84] bridging the gap between metal atoms and nanoparticles, have become a burgeoning area of scientific interest due to their unique optical, electronic and physical properties,[85-86] along with good biocompatibility and low toxicity, contrasting their corresponding large nanoparticles. Briefly, M_{NCs} are composed of several to roughly a hundred atoms and possess dimensions comparable to the Fermi wavelength of electrons exhibiting semiconducting molecule-like properties and strong size-dependent fluorescent emission.[87-88] Although it is accepted that materials in the dimension range from 0.1 nm to 100 nm are called nanoparticles, it is recently stated that 2 nm is the core size limit for ultrafine nanoparticles to be regarded as nanoclusters.

Notably, due to their intriguing size, the novel features of M_{NCs} are of particular interest rendering them useful in diverse applications such as sensing, bioimaging, optoelectronics, catalysis, energy conversion and storage.[89-90] One of the most interesting hallmarks of M_{NCs} is their photoluminescence, as they display distinct and size-tunable electronic transitions. However, the emission mechanism of M_{NCs} has yet to be well documented, as two possible scenarios for its origin exist. First, it is suggested that photoluminescence of M_{NCs} derives from the metal core due to its inherent quantization effects. The emission in the visible region is very fast and short-lived (i.e. hundreds of fs). On the other hand, it is demonstrated that the answer lies in the particle surface, directed by the interaction between metal core and surface ligands – in that case the lifetime is long (i.e. up to μs) and near-infrared fluorescence occurs.[91] Nevertheless, the big challenge is how to controllably govern the M_{NC} size, composition, crystal structure and surface properties.[92] Minor changes in size and composition, such as the addition or removal of a single atom, can remarkably affect their performance. In the nanocluster size regime, many of the features are utterly changed, because M_{NCs} exhibit discrete electronic energy levels compared to conventional metal nanoparticles, in which surface plasmon resonance property is dominant. Specifically, in bulk metals, the conduction band has no energy gap separating it from the valence band, so electrons can move freely without suffering from any barrier. On the contrary, in the case of M_{NCs}, the band structure becomes discontinuous, broken up into energy levels. Hence, interaction with light still exists, however, similar to organic dyes, via electronic transitions between the energy levels, resulting in light absorption and emission.[93]

In general, two are the main routes for fabricating M_{NCs}: (1) reduction of metal precursors (bottom-up), and (b) etching of large metal nanoparticles, in the presence of strong stabilizers (top-down).[94] In a typical bottom-up experiment, metal cationic precursors, in the form of the corresponding metal salts, are reduced to zero valent metal atoms in a strong reducing environment (usually $NaBH_4$), while the presence of a surface ligand regulates cluster formation. Compared to large metal nanoparticles, M_{NCs} are difficult to synthesize and functionalize because they favour to aggregate due to their high surface-area-to volume ratio. The appropriate selection of stabilizer ligands plays a critical role in obtaining ultra-small M_{NCs}, as their ability to donate electrons significantly influences both their structure and fluorescence.[94] Ligands facilitate M_{NC} growth and prevent aggregation between them by keeping the cluster surfaces apart during collisions in solution.[88] Due to their strong binding properties, thiol-based passivating agents also allow purification and removal of ionic byproducts. Electrophoresis-based separation (for water soluble nanoclusters) and chromatography-based isolation (for organic soluble nanoclusters) is often applied to isolate different sized M_{NCs}; however, with low yield of each size.

The commonly used reducing agent, $NaBH_4$, is a strong one and therefore often leads to a rapid reduction process with aggregated nanoparticles; thus, it is difficult to control the degree of dispersion of the products. Sometimes, in order to create a modest reducing environment, weak reducing agents such as formic acid[95] and CO[96] are used to regulate the reduction rate. Additionally, in order to control the reduction kinetics and achieve monodispersity, other reaction conditions are also adjusted, such as the solution pH, concentration of the reducing agent, and solvent used to mediate the reaction. Moreover, M_{NCs} of different configurations such as alloy can be developed by simultaneous reduction of metal precursors and a series of Au−Ag, Au−Pt, Au− Pd, Au−Cu, Ag−Pt, Ag−Pd, Ag−Cu, Ag−Ni, and even trimetallic Au−Cu−Pd M_{NCs} have been synthesized using this method.[97]

In 2007, a kinetically controlled approach for the synthesis of $Au_{25}(SC_2H_4Ph)_{18}$ in high yield and purity was reported, while no separation or purification step was needed to obtain monodispersed crystals of such nanoclusters. This method involves strong etching phenomena of the metal core by excessive ligands and it is governed by strong interaction between metal atoms and protecting ligands (top-down route).[89] In this method, a distribution of size-mixed nanoclusters co-exist in the solution; then these nanoclusters are subjected to size focusing under appropriate conditions (e.g. temperature regulation and presence of excess ligand), under which the polydispersed nanoclusters decompose or convert into the stable size, and eventually only the most stable nanocluster in the distribution survives the "focusing" process (Figure 1.11). Hence, the size focusing methods can give rise to selective development of atomically monodispersed M_{NCs} owing to the peculiar stability of certain-sized M_{NCs}. The stabilization of M_{NC} surface by a strongly binding ligand is critical and depends also on the purification methodologies employed. Finally, the solvent extraction method is used to separate them from the reaction side products, and monodispersed M_{NCs} are obtained. In general, this method takes a relatively long time and requires complicated operation processes.

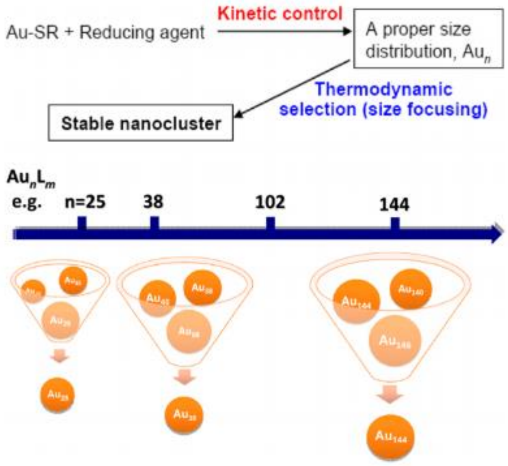

Figure 1.11 Schematic representation of size-focusing methodology[98]

One obvious advantage of employing well-defined nanoclusters in reactions lies in the fact that they can help in the understanding of the mechanism, as the compositions, structures and many other property are already known and in-depth investigations can thus be done. Another advantage is that they can find additional applications in other fields, such as sensing and photocatalysis due to their ultra-small size (less than 5 nm) and photoluminescence. The development in size-focusing methodologies has enabled the preparation of a number of size-specific nanoclusters species protected by thiolates (referred to Au_n:SR, where n is the number of gold atoms in the particle ($n < 100$)). Among them, the magic-numbered

$Au_{25}(SR)_{18}$ has been extensively investigated due to its high stability against etching and potential to participate in various catalytic applications.[99] The $Au_{25}(SR)_{18}$ structure comprises of a 13-atom Au_{13} icosahedral core and a $Au_{12}(SR)_{18}$ shell. The electronic structure of $Au_{12}(SR)_{18}$ exhibits discrete energy levels caused by the quantum-size effect. The molecular orbitals can be roughly divided into the Au-core orbitals (i.e., primarily contributed by Au_{13}) and the shell orbitals (i.e. primarily by $Au_{12}(SR)_{18}$), reflecting the geometric core – shell structure. For other types of thiolate-protected $Au_{25}(SR)_{18}$ (e.g. SR = SC_6H_{13}, $SC_{12}H_{25}$, glutathione (SG)), the same geometric structure is retained in all $Au_{25}(SR)_{18}$ regardless of the thiolate type. Moreover, all $Au_{25}(SR)_{18}$ show identical optical absorption spectrum. For larger configurations, such as $Au_{38}(SR)_{24}$, the structure comprises a bi-icosahedral Au_{23} core and six $Au_2(SR)_3$ and three $Au(SR)_2$ staple motifs for protecting the core. $Au_{144}(SR)_{60}$ is proposed to have a structure in which multiple −S(R)−Au−S(R)− oligomers cover a metal core (Au_{84}) (Figure 1.12). On the other hand, there is dependence between the type of ligand and the fluorescence property (including the emission wavelength and intensity) of fabricated M_{NCs}, as it is assumed for example that glutathione-capped Au nanoclusters present higher values of photoluminescence at 670 nm when excited at 514 nm compared to other thiol-protected Au_{NCs}. This phenomenon is attributed to the presence of electron-rich atoms within glutathione.[100-101] Considering the latter, difficulties with scaling up such methods to safely produce larger quantities of M_{NCs} do exist and should always be encountered.

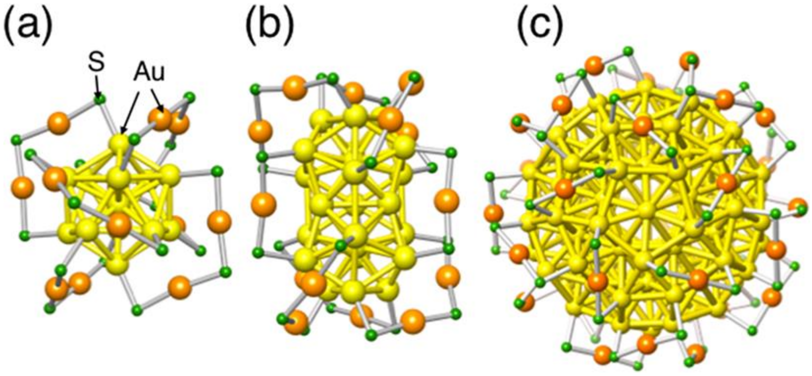

Figure 1.12 Geometrical stru ctures of representative magic $Au_n(SR)_m$ clusters: (a) $Au_{25}(SR)_{18}$, (b) $Au_{38}(SR)_{24}$, and (c) $Au_{144}(SR)_{60}$. The R groups have been omitted for simplicity.[102]

Other common strategies to obtain M_{NCs} include ligand-exchange, metal-exchange, and separation methods. The first one deals with excess addition of a new different ligand in a pre-synthesized M_{NC} solution, resulting in new stabilized M_{NCs}, while there is no change in the metal core structure. The metal-exchange method is mainly used for metal doping or constructing alloy M_{NCs}, such as $Au_{16}Ag_1$(S-Adamantane)$_{13}$ (with $Au_{18}(S\text{-}C_6H_{11})_{14}$ as the template).[103] The latter scheme is based on the isolation of monodispersed M_{NCs} using separation techniques, such as thin-layer chromatography (TLC), high-performance liquid chromatography (HPLC), polyacrylamide gel electrophoresis (PAGE), and size-exclusion chromatography (SEC).[97]

On this basis, molecular-level clusters of various metals, such as Au, Ag, Cu, Pt and Pd have steadily been developed allowing to control the structure and hence their properties.[88-89, 104] Along these lines, their luminescence property and biocompatibility have received tremendous interest in nanomedicine (bioassays of DNA/protein, bio-labeling and cellular imaging, drug delivery, and cancer therapy), and environmental monitoring and chemical sensing of harmful compounds such as hydrogen peroxide, nitrite anions, phenol groups and metal cations. Another major application field focuses on heterogeneous catalysis, due to their high specific area, and established atomic structure offering insights into the reaction/catalytic mechanisms at the atomic/molecular levels. On the other hand, there are some concerns about their stability in catalytic reactions, such as photoinduced aggregation in photocatalytic reactions and solution-phase leaching or decomposition under certain conditions. Nevertheless, M_{NCs} hold great promise in serving as a novel class of model catalysts.[98]

1.4.2. Characterization of metal nanoclusters

UV-Vis absorption spectroscopy is a powerful tool to study the optical characteristic peaks of M_{NCs}, while it assists also during their formation. Additionally, the absorption spectrum of M_{NCs} has distinct features, which can be easily obscured by impurities such as larger nanoparticles. Photoluminescence spectroscopy is also an integral part for characterization of M_{NCs}, as they exhibit intraband transitions. The maximum fluorescence intensity is usually recorded upon exciting at the maximum absorption peak, so a combination of data is necessary to unveil the optical properties of M_{NCs} in both ground and excited state. TEM is used to obtain information about the cluster morphology (size, and shape), and aggregation degree. Through EDX spectroscopy, elemental analysis can assist in the chemical composition of organic-stabilized M_{NCs}, while their purity can be assessed.

1.5 Hybrid materials based on graphene and transition metal dichalcogenides with metal nanoclusters

1.5.1 Graphene-based hybrid materials

Driven by the global environmental degradation, renewable photocatalytic solar energy conversion schemes hold great promise to be an efficient technology for removal of contaminant molecules such as organic dyes from wastewater. Hence, it is of utmost emergency to design photocatalysts that can efficiently harvest solar energy, convert it into charge carriers and allow the occurrence of controlled electron transfer reactions. Photocatalytic technology has involved rapid development and has important research significance and broad application prospects. Compared with traditional pollutant treatment technology, photocatalytic degradation technology offers many virtues: (1) it can completely decompose the pollutant or convert it to another compound useful for other industrial streams; (2) it does not cause secondary pollution; (3) the catalytic material can be used continuously, with high stability, recyclability, and low cost; (4) the reaction can be performed at ambient temperature and pressure conditions. Therefore, the decomposition of harmful pollutants governed by photocatalysis has important practical significance in energy conversion schemes.[105]

Since the discovery of the photocatalytic water splitting on TiO_2 electrodes by Fujishima and Honda in 1972, a large amount of photocatalysts have been developed for solar energy conversion and environment protection.[106] Semiconductors, such as TiO_2, CdS, and $BiVO_4$ have been largely employed, as they can absorb and harness light for chemical reactions due to their unique electronic structure composed of a filled valance band (VB) and an empty conduction band (CB).[105] At present, the principle of semiconductor photocatalytic degradation of pollutants is generally regarded as follows: when a semiconductor is photoexcited, an electron in the valence band (VB) of the semiconductor undergoes an intraband transition, producing a photogenerated electron – hole (e^{-}−h^{+}) pair. The electron – hole pair is transferred onto the semiconductor surface, where the electron is captured by dissolved oxygen to form superoxide radical anion ($O_2^{\bullet-}$), which in turn produce hydroxyl radicals ($HO^{\bullet}$) attacking the pollutant molecule. At the same time, photogenerated holes can also directly attack and decompose the dye. Photocatalytic hydrogen production via solar water splitting is another promising alternative for sustainable energy and environmental remedy issues. Its pathway mainly involves three steps: (1) electron – hole (e^{-}−h^{+}) pair generation by the photoexcited semiconductor catalyst; (2) electron and hole separation and migration onto the surface of the photocatalyst; (3) production of H_2 and O_2 by the redox reaction between H_2O and e^{-}−h^{+}. However, semiconductor photocatalysts usually suffer from low solar energy utilization and quantum efficiency. Typically, coupling with another semiconductor with matched energy levels, adding electron or hole scavengers, or combining semiconductors with other materials facilitating electron flow and charge separation are among the methods to expand light absorption. On this background, graphene-involved semiconductor photocatalysts have overhang due to their usefulness in environmental-oriented catalyst applications. Excited-state photophysical phenomena can happen between graphene and photoactive moieties, which can be exploited in energy conversion applications.

Briefly, each decay step of a photo-exited semiconductor is governed by its own rate constant and each excited state boasts its unique lifetime value. Typically, semiconductors tend to have a high recombination rate of photogenerated electron–hole pairs; however, when combined with graphene the de-activation process is not so fast, the lifetime of the excited state is sufficiently longer, hence the photo-excited electron has adequate time to travel through the π-conjugated graphene network and a stable charge-separated state is formed. In this way, the photo-excited electron can react either with dissolved oxygen or water molecules to facilitate a specific photocatalytic activity, as previously described (Figure 1.13). In the majority of the cases, the realization of a donor – acceptor system is dictated by electron and/or energy transfer processes and can be verified by electronic interactions in the ground and excited state. Both non-covalent stacking and covalent functionalization are expected to yield such observations.

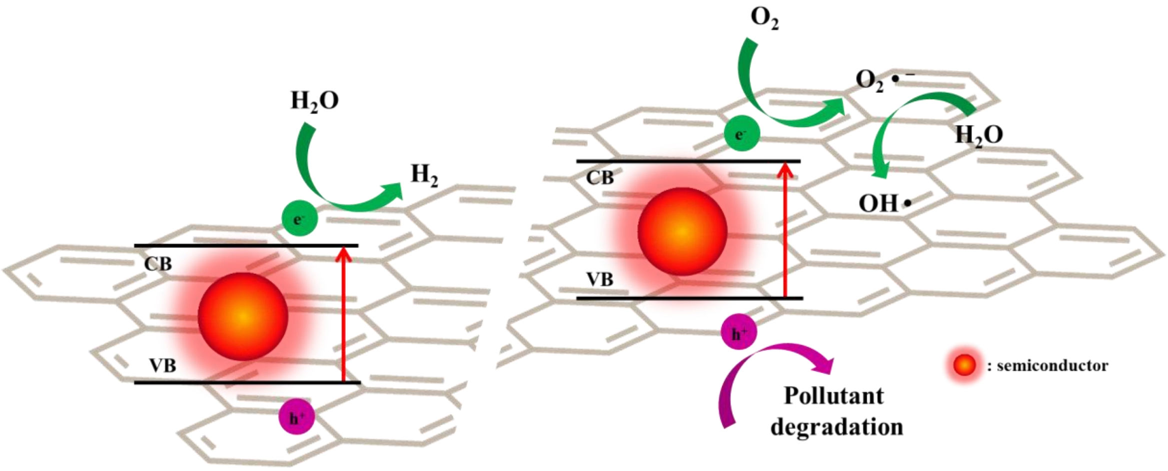

Figure 1.13 Schematic illustration of photocatalytic H_2 evolution (left) and organics degradation (right) over a graphene/semiconductor photocatalyst.

The ability of graphene to accept photogenerated electrons is ascribed to three possible mechanisms: (1) fluorescence resonance energy transfer (FRET), (2) surface energy transfer (SET), and (3) photoinduced electron transfer (PET). FRET is a mechanism describing energy transfer between a chromophore and graphene sheets. The donor chromophore, initially in its electronic excited state, may transfer energy to graphene (acceptor) through nonradiative dipole–dipole interactions. The efficiency of this energy transfer is inversely proportional to the sixth power of the distance between donor and acceptor making FRET extremely sensitive to small distances. In the process of SET, the energy transfer efficiency is inversely proportional to the fourth power of the donor – acceptor distance, making SET more efficient than FRET at relatively longer distances (20–30 nm). PET phenomenon occurs between a luminescent compound and graphene material. The quenching is a redox reaction between the excited donor and the quencher with electron transfer from the donor to the acceptor. The efficiency of the quenching decreases exponentially as the distance increases. Hence, graphene in its hybrids can not only accelerate the electron transport through its network but also promote the charge-separation state and delay the recombination of the electron–hole pair.[107] Those photo-induced electron and/or energy transfer processes can be conveniently verified by the fluorescence spectroscopy and decay, and time-resolved transient absorption spectroscopic characterizations. These measurement results provide quantitative insights, both kinetically and spectroscopically, into the nature of the interactions of graphene and photoactive molecules.

On this background, M_{NCs} have evolved as a new class of nanoparticles with unprecedented photoreactivity related to their structure, i.e. their tiny size and photoluminescence property. These M_{NCs} demonstrate a combination of benefits in photocatalytic systems: (1) their size is very small, and changing only one atom will greatly affect the nature of the cluster. Thus, M_{NCs} with predefined number and configuration of metal atoms are very necessary for the study of catalytic structure‒activity relationships; (2) in the nanoparticle regime, the interface between the metal core and protecting ligands is not well understood. In contrast, the surrounding environment of M_{NCs} is clearly established, with the amount and type of surface ligand also being precisely adjustable, which is helpful to study the surface/ interface effect;

(3) considering that organic fluorophores are susceptible to photobleaching and fluorescent semiconductor quantum dots are generally composed of toxic elements, M_{NCs} can be regarded as important photocatalytic agents; (4) profiting from the molecular purity and high uniformity, M_{NC} catalysts immobilized onto other supporting materials play a major role in bridging homogeneous and heterogeneous catalysis. They realize high activity, selectivity, stability, and recyclability at the same time. Hybrid nanostructures are particularly important in photocatalysis, because a single component catalyst might not be able to simultaneously meet the several requirements for high-performance photocatalysis (i.e., broad visible light adsorption, large specific surface area, effective electron-hole pair generation and minimum charge carrier recombination).

Indeed, the immobilization of M_{NCs} on a substrate material, particularly graphene, allows support effects, which are important in energy conversion applications. Hence, it is anticipated that nanoclusters supported onto graphene sheets, not only exploit the availability of large surface area for facile electron-transfer phenomena but also deliver better mass transport of reactants to the catalyst. Because of the tiny size of M_{NCs} and that a considerable fraction of their atoms is located on the substrate surface, these effects are likely to be more pronounced in cluster-based ensembles than in typical nanoparticle counterparts, leading not only to modification but also amelioration of their structural and electronic character. Most of the envisioned applications take advantage of the increased photoinduced charge-transfer processes occurring from the M_{NCs} to the graphene sheets. Namely, upon photoirradiation the singlet excited state of M_{NCs} is generated and charge-transfer and efficient transport takes place onto graphene. The photogenerated charge-separated state and the accumulated charges, in the form of electrons and holes that are present within these ensembles, are then exploited for the realization of energy-related applications. Graphene can form electron-conducting surfaces and channels, thus the photocatalytic activity of hybrid materials can be greatly increased, mainly owing to the effective separation of the electron−hole pairs.

Anchoring of pre-functionalized M_{NCs} onto graphene via either covalent or non-covalent means is the principal approach for the fabrication of hybrids. As for the covalent attachment of M_{NCs} on graphene, for example, pre-synthesized phosphine-protected Au_{NCs} were bound to GO, which was initially functionalized with sulfur functional groups,[108] via the displacement of one out of eight phosphine ligands decorating the Au_{NCs}, architecture due to the strong affinity of gold for the sulfur atoms. The particular approach possesses the benefit of the tight and robust incorporation of the M_{NCs} on the graphene sheets, thereby allowing more efficient interactions between the two species within the hybrid material. On the other hand in the case of non-covalent interactions, M_{NCs} protected by hydrophilic ligands can be ionized via protonation or deprotonation of the functional groups according to given pH conditions.[96, 109] In this case, the stability of the hybrid material is weaker due to the nature of the interactions developed between the two species as compared with the aforementioned covalent bonding. Commonly, negatively charged M_{NCs} interact with positively GO and the success of preparation is monitored by the alteration of the fluorescence intensity of M_{NCs} due to quenching derived from GO.[110] An alternative procedure for fabricating M_{NCs}/graphene hybrids concerns the *in situ* reduction of metal precursors and GO in a single step without using any protecting agent.[111] The major advantage of the latter as compared with the aforementioned approaches is the easier and faster synthetic protocols for the preparation of such hybrids. However, the lack of precise control on the size of M_{NCs} is a major weakness and should be kept in mind.

Of particular significance is the H_2 production from renewable resources as a future energy supply. Toward this direction, M_{NCs} based on Au and Pd were grown, immobilized on N-doped RGO and tested toward H_2 generation from formic acid.[111] The negatively charged RGO sheets were utilized not only as a platform for supporting the M_{NCs} but also as reducing agent for the M_{NCs} formation. The high surface area, large thermal stability and enhanced charge transport properties owed to the N-doped RGO sheets are important properties for aiding the growth and support of M_{NCs} as well as the catalytic activity of the hybrid material for the H_2 production from formic acid. Markedly, the catalytic activity of Au@Pd/N-doped RGO depended on the Au/Pd molar ratio. The excellent catalytic behaviour, in terms of highest H_2 evolution and time achieved, of core–shell Au@Pd in Au@Pd/N-doped RGO as compared to that owed to Au/N-doped RGO and Pd/N-doped RGO toward the H_2 generation is attributed to charge-transfer phenomena occurring between the core Au and Pd shell M_{NCs}.

Other metals such as Ru, Ir and Rh were also attached to graphene and showed catalytic activity for H_2 evolution. Ultrafine Ru_{NCs} supported on GO without any use of stabilizer, but employing tetrabutylammonium hydroxide as means for separating the exfoliated GO sheets by preventing π-π interactions between them, were prepared.[112-113] The Ru_{NCs}/GO ensembles were tested as catalyst for the methanolysis dehydrogenation of ammonia borane and found to exhibit excellent stability throughout the catalytic runs, retaining more than 73% of its initial catalytic activity after performing 15 successive catalytic cycles. In addition, the selective hydrogenation of pchloronitrobenzene to p-chloroaniline by Ru_{NCs}/RGO was demonstrated by achieving a 96% conversion.[114] In a similar fashion and taking advantage of the high surface area of graphene and its unique electric transport properties, Ir_{NCs} were synthesized in ionic liquids, without requiring particular stabilizers and with narrow size distribution, and deposited on GO.[115] The properties of Ir_{NCs}/GO were examined and proved to catalyse the hydrogenation of benzene and cyclohexene to cyclohexane. Notably, the catalyst Ir_{NCs}/GO can be re-used for over 10 consecutive hydrogenation reactions with similar activities.

The detection of compounds with harmful impact on environment has also been accomplished by M_{NCs}/graphene ensembles. The sensing of H_2O_2,[116] phenolic compounds,[117] Cu^{2+},[118] NO^{2-},[119] and Hg^{2+}[120] was achieved through employing Columbic interactions to establish electronic communication between suitably stabilized M_{NCs} (Au, and Pt) and functionalized graphene derivatives. In most of the cases, negatively charged (e.g. carboxylic moieties) M_{NCs} were electrostatically tethered to graphene bearing ammonium functional groups, while the sensing mechanism was based on the recorded fluorescence quenching of the hybrid signal upon incremental additions of under-recognition compound. Moreover, the involvement of such hybrids for the rapid and sensitive detection of molecular species with biological activity cannot be neglected. In this framework, M_{NCs}/graphene ensembles were developed and utilized as "turn-on" fluorescent probes for the detection of malignant growth, [110, 121-123] other diseases, [124-125] and drug-delivery.[126] The experimental protocol is based on the fabrication of M_{NCs} labeled with specific peptides, proteins, cell-receptor ligands or other targeting molecules and hybridization with graphene derivatives through non-covalent means. Upon addition of the target molecule in the suspension, the chemical environment of the hybrid changes, as there is strong affinity between target and ligand, resulting in the regeneration of M_{NC} fluorescence and a readout signal for successful sensing is recorded. Also, single-stranded DNA sequences have been used as stabilizers to facilitate M_{NC} growth, which then can be easily adsorbed onto GO, via π–π stacking interactions between the DNA nucleobases and the sp^2-hybridized carbons of GO. In a similar concept, when the complementary DNA sequence of the target molecule is added, a double helix DNA is formed, resulting in breakage of the M_{NCs}/GO ensemble and recovery of the fluorescence of M_{NCs} (Figure 1.14). Actually, the decreased vicinity of M_{NCs} and GO is further justified as GO binds more weakly with double-stranded DNA, since the hydrophobic bases of the DNA can efficiently be protected from GO and weaken the π–π stacking interactions.[127-129]

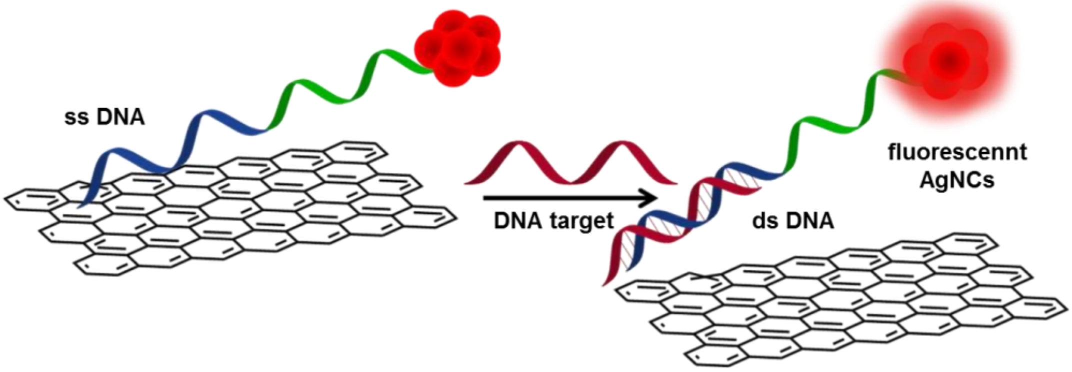

Figure 1.14 Schematic illustration of nucleic acid-protected Ag_{NCs}/GO nanohybrid response upon DNA target addition.

1.5.2 Transition metal dichalcogenide-based hybrid materials

TMDs can also be hybridized with semiconductors and enhance their photocatalytic performance in a similar way as graphene contributes. With their special 2D layered structure, TMDs can serve as effective supports to anchor semiconductor nanoparticles or even M_{NCs} on their surface, which could reduce the mobility, provide more active sites, and avoid coalescence and agglomeration of M_{NCs}. This is beneficial for keeping the activity and stability of the photocatalysts. Moreover, as in the case of graphene, the presence of TMDs can lead to enhanced charge separation and immigration resulting in higher photoactivity.

On this background, TMDs and especially MoS_2 have already been coupled with dye-labeled single-stranded DNA (ssDNA) probe,[130-132] or PEGylated quantum dots for the detection of epithelial cell adhesion molecule associated with breast cancer MCF-7 cells.[133] Interestingly, the fluorescence quenching ability of lithium-intercalated oligo-layered TiS_2, and TaS_2 sheets compared to that of MoS_2 was for the first time reported as sensing platforms for fluorescent detection of DNA, revealing that single-layer TaS_2-based sensor exhibited the best performance among the three TMD sensors.[134] The realization of the respective ensembles is governed by van der Waal forces between the two main components.

However, the immobilization of fluorescent M_{NCs} onto TMDs has not been extensively studied compared to the graphene-based hybrids, as only a handful reports can be found especially in the biological field. To this end, the fabrication of a “switch on” fluorescence biosensor was reported for the simultaneous detection of two different tumor markers (α-fetoprotein (AFP), and carcinoembryonic antigen (CEA)).[135] Firstly, dual thiolate-Au_{NCs}, i.e. green-emitting Au_{NCs} (510 nm) and red-emitting Au_{NCs} (650 nm) were covalently functionalized with AFP and CEA aptamers, respectively, and then were assembled onto MoS_2 nanosheets through van der Waals forces. The fluorescence of the dual emitting Au_{NCs} was simultaneously quenched; however, upon the addition of the target tumor markers into the suspension, green and red fluorescence signals were recorded accompanied with the releasing of the two aptamer-functionalized Au_{NCs}, due to the strong affinity of aptamers with target tumor markers. Notably, the proposed methodology was applied to distinguish between serums from hepatoma patients and healthy people, showing great selectivity. In another report, glutathione-labeled Ag_{NCs} were incorporated onto liquid-exfoliated MoS_2 sheets and the enzyme mimics potential of the hybrid was evaluated. It was found that the prepared catalyst showed a great peroxidase-like activity for decomposition of H_2O_2. Specifically, H_2O_2 could oxidize the peroxidase substrate (terephthalic acid) to yield high fluorescent 2-hydroxyterephthalic acid with a maximum photoluminescence emission at 425 nm, upon addition of the Ag_{NCs}/MoS_2 hybrid in the dispersion.[136] The electronic interactions at the excited state were verified by the fluorescence quenched peak at 652 nm attributed to pure Ag_{NCs} (excitation wavelength at 422 nm) upon addition of MoS_2 sheets. The proposed mechanism lies in the fact that MoS_2 sheets promoted effective interactions with H_2O_2 molecules due to their abundant active sites, while Ag_{NCs} facilitated electron transfer on them and improved the production of hydroxyl radicals, which were finally responsible for the oxidation of terephthalic acid. The same research group demonstrated that WS_2 sheets hybridized with BSA-stabilized Ag_{NCs} could also display remarkable peroxidase activity, when applying an identical experimental protocol.[137-138] However, in these studies despite the fabrication of the corresponding hybrid material being rationalized through TEM imaging, a detailed discussion on the coupling nature of TMDs (covalent or non-covalent interactions) with Ag_{NCs} is missing. The most important finding of these reports is focused on the fluorescence reduction of M_{NCs} when MoS_2 are present in the suspension, indicating that electronic interactions can happen between these two species. Another interesting study demonstrated improved electrocatalytic water splitting of MoS_2 when Au_{NCs} were introduced as co-catalysts.[139] The Au_{25}/MoS_2 hybrid showed improved activity towards hydrogen evolution reaction with a two-fold increased current density and lower charge transfer resistance compared to plain MoS_2. XPS analysis was implemented to unveil possible interactions between Au_{25} and MoS_2. The results revealed that that the binding energy of Mo 3d exhibited a negative shift of ~0.4 eV after introduction of nanogold, while the Au 4f binding energy showed an opposite positive shift after hybrid formation. Given the abundant defect sites of MoS_2 due to the exfoliation process, they speculate that Au_{NCs} are located on those sites and interfacial interactions between Au_{NCs} and MoS_2 can exist leading to the enhanced hydrogen production. Even though they do not demonstrate any photocatalytic activity, it is understood that improved charge transfer and electronic interactions at the Au_{NCs}/MoS_2 interface can happen (Figure 1.15). This finding is important for the performance of such hybrid materials in the energy field and might shed light on the activity of previously reported schemes.

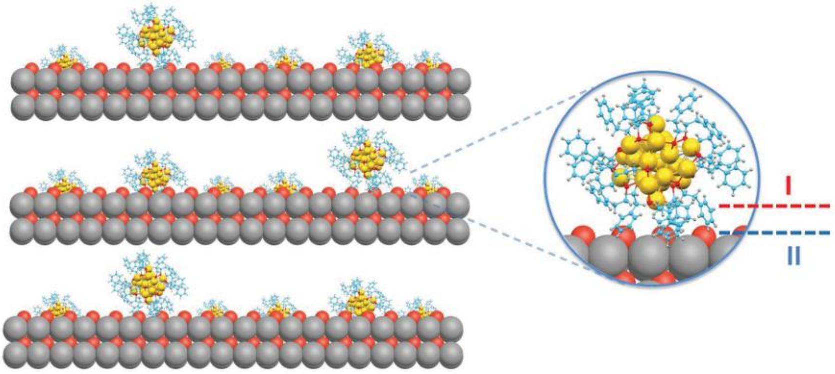

Figure 1.15 Illustration of dual interfacial effect (Interface I and II) in Au_{25}/MoS_2 composite (yellow: Au; red/orange: S; blue: C; gray: Mo).[139]

By extension, one can imagine the possibility of utilizing graphene and TMD – M_{NC} hybrids as stand-alone materials to fulfill urgent environmental concerns. Hence, there is a lot of interest in the development of such systems to accomplish the recent needs in key aspects of energy conversion applications. The expansion of graphene applications toward the creation of advanced materials can assist researchers in designing hybrids to address whole-process applications. In view of all of the above mentioned the importance of the development of such hybrids and the need for additional research in this thematic area become apparent, as a lot of research is to be further conducted in the near future. The big challenge, though, is how to controllably synthesize M_{NCs} with defined composition, and surface properties and introduce them on graphene or TMD surface.

References

1. Iijima, S.; Ichihashi, T., Single-shell carbon nanotubes of 1-nm diameter. *Nature* 1993, *363* (6430), 603-605.

2. Kroto, H. W.; Heath, J. R.; O'Brien, S. C.; Curl, R. F.; Smalley, R. E., C60: Buckminsterfullerene. *Nature* 1985, *318* (6042), 162-163.

3. Novoselov, K. S.; Geim, A. K.; Morozov, S. V.; Jiang, D.; Zhang, Y.; Dubonos, S. V.; Grigorieva, I. V.; Firsov, A. A., Electric Field Effect in Atomically Thin Carbon Films. *Science* 2004, *306* (5696), 666-669.

4. Balandin, A. A., Thermal properties of graphene and nanostructured carbon materials. *Nat. Mater.* 2011, *10*, 569-581.

5. Nair, R. R.; Blake, P.; Grigorenko, A. N.; Novoselov, K. S.; Booth, T. J.; Stauber, T.; Peres, N. M. R.; Geim, A. K., Fine Structure Constant Defines Visual Transparency of Graphene. *Science* 2008, *320* (5881), 1308.

6. Du, X.; Skachko, I.; Barker, A.; Andrei, E. Y., Approaching ballistic transport in suspended graphene. *Nat. Nanotechnol.* 2008, *3*, pages 491-495.

7. Wu, Z.-S.; Ren, W.; Gao, L.; Zhao, J.; Chen, Z.; Liu, B.; Tang, D.; Yu, B.; Jiang, C.; Cheng, H.-M., Synthesis of Graphene Sheets with High Electrical Conductivity and Good Thermal Stability by Hydrogen Arc Discharge Exfoliation. *ACS Nano* 2009, *3* (2), 411-417.

8. Bonaccorso, F.; Sun, Z.; Hasan, T.; Ferrari, A. C., Graphene photonics and optoelectronics. *Nat. Photonics* 2010, *4*, 611-622.

9. Stoller, M. D.; Park, S.; Zhu, Y.; An, J.; Ruoff, R. S., Graphene-Based Ultracapacitors. *Nano Lett.* 2008, *8* (10), 3498-3502.

10. Lee, C.; Wei, X.; Kysar, J. W.; Hone, J., Measurement of the Elastic Properties and Intrinsic Strength of Monolayer Graphene. *Science* 2008, *321* (5887), 385-388.

11. Geim, A. K.; Novoselov, K. S., The rise of graphene. *Nat. Mater.* 2007, *6*, 183-191.

12. Lazar, P.; Karlický, F.; Jurečka, P.; Kocman, M.; Otyepková, E.; Šafářová, K.; Otyepka, M., Adsorption of Small Organic Molecules on Graphene. *J. Am. Chem. Soc.* 2013, *135* (16), 6372-6377.

13. Ferrari, A. C.; Bonaccorso, F.; Fal'ko, V.; Novoselov, K. S.; Roche, S.; Bøggild, P.; Borini, S.; Koppens, F. H. L.; Palermo, V.; Pugno, N.; Garrido, J. A.; Sordan, R.; Bianco, A.; Ballerini, L.; Prato, M.; Lidorikis, E.; Kivioja, J.; Marinelli, C.; Ryhänen, T.; Morpurgo, A.; Coleman, J. N.; Nicolosi, V.; Colombo, L.; Fert, A.; Garcia-Hernandez, M.; Bachtold, A.; Schneider, G. F.; Guinea, F.; Dekker, C.; Barbone, M.; Sun, Z.; Galiotis, C.; Grigorenko, A. N.; Konstantatos, G.; Kis, A.; Katsnelson, M.; Vandersypen, L.; Loiseau, A.; Morandi, V.; Neumaier, D.; Treossi, E.; Pellegrini, V.; Polini, M.; Tredicucci, A.; Williams, G. M.; Hee Hong, B.; Ahn, J.-H.; Min Kim, J.; Zirath, H.; van Wees, B. J.; van der Zant, H.; Occhipinti, L.; Di Matteo, A.; Kinloch, I. A.; Seyller, T.; Quesnel, E.; Feng, X.; Teo, K.; Rupesinghe, N.; Hakonen, P.; Neil, S. R. T.; Tannock, Q.; Löfwander, T.; Kinaret, J., Science and technology roadmap for graphene, related two-dimensional crystals, and hybrid systems. *Nanoscale* 2015, *7* (11), 4598-4810.

14. Coleman, J. N.; Lotya, M.; O'Neill, A.; Bergin, S. D.; King, P. J.; Khan, U.; Young, K.; Gaucher, A.; De, S.; Smith, R. J.; Shvets, I. V.; Arora, S. K.; Stanton, G.; Kim, H.-Y.; Lee, K.; Kim, G. T.; Duesberg, G. S.; Hallam, T.; Boland, J. J.; Wang, J. J.; Donegan, J. F.;

Grunlan, J. C.; Moriarty, G.; Shmeliov, A.; Nicholls, R. J.; Perkins, J. M.; Grieveson, E. M.; Theuwissen, K.; McComb, D. W.; Nellist, P. D.; Nicolosi, V., Two-Dimensional Nanosheets Produced by Liquid Exfoliation of Layered Materials. *Science* 2011, *331* (6017), 568-571.

15. Qin, B., The growth mechanism of few-layer graphene in the arc discharge process. *Carbon* 2016, *102*, 494-498.

16. Obraztsov, A. N., Making graphene on a large scale. *Nat. Nanotechnol.* 2009, *4*, 212-213.

17. Skaltsas, T.; Ke, X.; Bittencourt, C.; Tagmatarchis, N., Ultrasonication Induces Oxygenated Species and Defects onto Exfoliated Graphene. *J. Phys. Chem. C* 2013, *117* (44), 23272-23278.

18. Li, N.; Wang, Z.; Zhao, K.; Shi, Z.; Gu, Z.; Xu, S., Large scale synthesis of N-doped multi-layered graphene sheets by simple arc-discharge method. *Carbon* 2010, *48* (1), 255-259.

19. Mattevi, C.; Kim, H.; Chhowalla, M., A review of chemical vapour deposition of graphene on copper. *J. Mater. Chem.* 2011, *21* (10), 3324-3334.

20. Brodie B. C.; XIII. On the atomic weight of graphite. *Philos. Trans. Royal Soc.* 1859, *149*, 249-259.

21. Hummers, W. S.; Offeman, R. E., Preparation of Graphitic Oxide. *J. Am. Chem. Soc.* 1958, *80* (6), 1339-1339.

22. Marcano, D. C.; Kosynkin, D. V.; Berlin, J. M.; Sinitskii, A.; Sun, Z.; Slesarev, A.; Alemany, L. B.; Lu, W.; Tour, J. M., Improved Synthesis of Graphene Oxide. *ACS Nano* 2010, *4* (8), 4806-4814.

23. Pei, S.; Cheng, H.-M., The reduction of graphene oxide. *Carbon* 2012, *50* (9), 3210-3228.

24. Tang, Q.; Zhou, Z.; Chen, Z., Graphene-related nanomaterials: tuning properties by functionalization. *Nanoscale* 2013, *5* (11), 4541-4583.

25. Gao, W.; Alemany, L. B.; Ci, L.; Ajayan, P. M., New insights into the structure and reduction of graphite oxide. *Nat. Chem.* 2009, *1*, 403-408.

26. Mkhoyan, K. A.; Contryman, A. W.; Silcox, J.; Stewart, D. A.; Eda, G.; Mattevi, C.; Miller, S.; Chhowalla, M., Atomic and Electronic Structure of Graphene-Oxide. *Nano Lett.* 2009, *9* (3), 1058-1063.

27. Georgakilas, V.; Tiwari, J. N.; Kemp, K. C.; Perman, J. A.; Bourlinos, A. B.; Kim, K. S.; Zboril, R., Noncovalent Functionalization of Graphene and Graphene Oxide for Energy Materials, Biosensing, Catalytic, and Biomedical Applications. *Chem. Rev.* 2016, *116* (9), 5464-5519.

28. Gong, X.; Liu, G.; Li, Y.; Yu, D. Y. W.; Teoh, W. Y., Functionalized-Graphene Composites: Fabrication and Applications in Sustainable Energy and Environment. *Chem. Mater.* 2016, *28* (22), 8082-8118.

29. Fasolino, A.; Los, J. H.; Katsnelson, M. I., Intrinsic ripples in graphene. *Nat. Mater.* 2007, *6*, 858-861.

30. Bahr, J. L.; Tour, J. M., Highly Functionalized Carbon Nanotubes Using in Situ Generated Diazonium Compounds. *Chem. Mater.* 2001, *13* (11), 3823-3824.

31. Greenwood, J.; Phan, T. H.; Fujita, Y.; Li, Z.; Ivasenko, O.; Vanderlinden, W.; Van Gorp, H.; Frederickx, W.; Lu, G.; Tahara, K.; Tobe, Y.; Uji-i, H.; Mertens, S. F. L.; De

Feyter, S., Covalent Modification of Graphene and Graphite Using Diazonium Chemistry: Tunable Grafting and Nanomanipulation. *ACS Nano* 2015, *9* (5), 5520-5535.

32. Jin, Z.; McNicholas, T. P.; Shih, C.-J.; Wang, Q. H.; Paulus, G. L. C.; Hilmer, A. J.; Shimizu, S.; Strano, M. S., Click Chemistry on Solution-Dispersed Graphene and Monolayer CVD Graphene. *Chem. Mater.* 2011, *23* (14), 3362-3370.

33. Liu, L.-H.; Yan, M., Functionalization of pristine graphene with perfluorophenyl azides. *J. Mater. Chem. A* 2011, *21* (10), 3273-3276.

34. Xu, X.; Luo, Q.; Lv, W.; Dong, Y.; Lin, Y.; Yang, Q.; Shen, A.; Pang, D.; Hu, J.; Qin, J.; Li, Z., Functionalization of Graphene Sheets by Polyacetylene: Convenient Synthesis and Enhanced Emission. *Macromol. Chem. Phys.* 2011, *212* (8), 768-773.

35. Bingel, C., Cyclopropanierung von Fullerenen. *Chem. Ber.* 1993, *126* (8), 1957-1959.

36. Jin, B.; Shen, J.; Peng, R.; Chen, C.; Zhang, Q.; Wang, X.; Chu, S., DMSO: An Efficient Catalyst for the Cyclopropanation of C_{60}, C_{70}, SWNTs, and Graphene through the Bingel Reaction. *Ind. Eng. Chem. Res.* 2015, *54* (11), 2879-2885.

37. Niyogi, S.; Bekyarova, E.; Itkis, M. E.; McWilliams, J. L.; Hamon, M. A.; Haddon, R. C., Solution Properties of Graphite and Graphene. *J. Am. Chem. Soc.* 2006, *128* (24), 7720-7721.

38. Kolb, H. C.; Finn, M. G.; Sharpless, K. B., Click Chemistry: Diverse Chemical Function from a Few Good Reactions. *Angew. Chem.* 2001, *40* (11), 2004-2021.

39. Huisgen, R., Kinetics and Mechanism of 1,3-Dipolar Cycloadditions. *Angew. Chem.* 1963, *2* (11), 633-645.

40. Ye, Y.-S.; Chen, Y.-N.; Wang, J.-S.; Rick, J.; Huang, Y.-J.; Chang, F.-C.; Hwang, B.-J., Versatile Grafting Approaches to Functionalizing Individually Dispersed Graphene Nanosheets Using RAFT Polymerization and Click Chemistry. *Chem. Mater.* 2012, *24* (15), 2987-2997.

41. Luong, N. D.; Sinh, L. H.; Johansson, L.-S.; Campell, J.; Seppälä, J., Functional Graphene by Thiol-ene Click Chemistry. *Chem. Eur. J.* 2015, *21* (8), 3183-3186.

42. Castelaín, M.; Martínez, G.; Marco, C.; Ellis, G.; Salavagione, H. J., Effect of Click-Chemistry Approaches for Graphene Modification on the Electrical, Thermal, and Mechanical Properties of Polyethylene/Graphene Nanocomposites. *Macromolecules* 2013, *46* (22), 8980-8987.

43. Chhowalla, M.; Shin, H. S.; Eda, G.; Li, L.-J.; Loh, K. P.; Zhang, H., The chemistry of two-dimensional layered transition metal dichalcogenide nanosheets. *Nat. Chem.* 2013, *5*, 263-275.

44. Ataca, C.; Şahin, H.; Ciraci, S., Stable, Single-Layer MX_2 Transition-Metal Oxides and Dichalcogenides in a Honeycomb-Like Structure. *J. Phys. Chem. C* 2012, *116* (16), 8983-8999.

45. Mak, K. F.; Lee, C.; Hone, J.; Shan, J.; Heinz, T. F., Atomically Thin MoS_2: A New Direct-Gap Semiconductor. *Phys. Rev. Lett.* 2010, *105* (13), 136805.

46. Splendiani, A.; Sun, L.; Zhang, Y.; Li, T.; Kim, J.; Chim, C.-Y.; Galli, G.; Wang, F., Emerging Photoluminescence in Monolayer MoS_2. *Nano Lett.* 2010, *10* (4), 1271-1275.

47. Bao, W.; Cai, X.; Kim, D.; Sridhara, K.; Fuhrer, M. S., High mobility ambipolar MoS_2 field-effect transistors: Substrate and dielectric effects. *Appl Phys Lett.* 2013, *102* (4), 042104.

48. Choi, W.; Choudhary, N.; Han, G. H.; Park, J.; Akinwande, D.; Lee, Y. H., Recent development of two-dimensional transition metal dichalcogenides and their applications. *Mater. Today* 2017, *20* (3), 116-130.

49. Bertolazzi, S.; Brivio, J.; Kis, A., Stretching and Breaking of Ultrathin MoS_2. *ACS Nano* 2011, *5* (12), 9703-9709.

50. Fiori, G.; Bonaccorso, F.; Iannaccone, G.; Palacios, T.; Neumaier, D.; Seabaugh, A.; Banerjee, S. K.; Colombo, L., Electronics based on two-dimensional materials. *Nat. Nanotechnol.* 2014, *9*, 768-779.

51. Cheng, R.; Jiang, S.; Chen, Y.; Liu, Y.; Weiss, N.; Cheng, H.-C.; Wu, H.; Huang, Y.; Duan, X., Few-layer molybdenum disulfide transistors and circuits for high-speed flexible electronics. *Nat Commun.* 2014, *5*, 5143.

52. Liu, K.-K.; Zhang, W.; Lee, Y.-H.; Lin, Y.-C.; Chang, M.-T.; Su, C.-Y.; Chang, C.-S.; Li, H.; Shi, Y.; Zhang, H.; Lai, C.-S.; Li, L.-J., Growth of Large-Area and Highly Crystalline MoS_2 Thin Layers on Insulating Substrates. *Nano Lett.* 2012, *12* (3), 1538-1544.

53. Acrivos, J. V.; Liang, W. Y.; Wilson, J. A.; Yoffe, A. D., Optical studies of metal-semiconductor transmutations produced by intercalation. *J. Phys. C Solid State Phys.* 1971, *4* (1), L18-L20.

54. Joensen, P.; Crozier, E. D.; Alberding, N.; Frindt, R. F., A study of single-layer and restacked MoS_2 by X-ray diffraction and X-ray absorption spectroscopy. *J. Phys. C Solid State Phys.* 1987, *20* (26), 4043-4053.

55. Pagona, G.; Bittencourt, C.; Arenal, R.; Tagmatarchis, N., Exfoliated semiconducting pure 2H-MoS_2 and 2H-WS_2 assisted by chlorosulfonic acid. *Chem. Commun.* 2015, *51* (65), 12950-12953.

56. Gaur, A. P. S.; Sahoo, S.; Ahmadi, M.; Dash, S. P.; Guinel, M. J. F.; Katiyar, R. S., Surface Energy Engineering for Tunable Wettability through Controlled Synthesis of MoS_2. *Nano Lett.* 2014, *14* (8), 4314-4321.

57. Ogilvie, S. P.; Large, M. J.; Fratta, G.; Meloni, M.; Canton-Vitoria, R.; Tagmatarchis, N.; Massuyeau, F.; Ewels, C. P.; King, A. A. K.; Dalton, A. B., Considerations for spectroscopy of liquid-exfoliated 2D materials: emerging photoluminescence of N-methyl-2-pyrrolidone. *Sci. Rep.* 2017, *7* (1), 16706.

58. Liu, D.; Guo, Y.; Fang, L.; Robertson, J., Sulfur vacancies in monolayer MoS_2 and its electrical contacts. *Appl. Phys. Lett.* 2013, *103* (18), 183113.

59. Hong, J.; Hu, Z.; Probert, M.; Li, K.; Lv, D.; Yang, X.; Gu, L.; Mao, N.; Feng, Q.; Xie, L.; Zhang, J.; Wu, D.; Zhang, Z.; Jin, C.; Ji, W.; Zhang, X.; Yuan, J.; Zhang, Z., Exploring atomic defects in molybdenum disulphide monolayers. *Nat. Commun.* 2015, *6*, 6293.

60. Bertolazzi, S.; Gobbi, M.; Zhao, Y.; Backes, C.; Samorì, P., Molecular chemistry approaches for tuning the properties of two-dimensional transition metal dichalcogenides. *Chem. Soc. Rev.* 2018, *47* (17), 6845-6888.

61. Tuxen, A.; Kibsgaard, J.; Gøbel, H.; Lægsgaard, E.; Topsøe, H.; Lauritsen, J. V.; Besenbacher, F., Size Threshold in the Dibenzothiophene Adsorption on MoS_2 Nanoclusters. *ACS Nano* 2010, *4* (8), 4677-4682.

62. Makarova, M.; Okawa, Y.; Aono, M., Selective Adsorption of Thiol Molecules at Sulfur Vacancies on MoS_2(0001), Followed by Vacancy Repair via S–C Dissociation. *J. Phys. Chem. C* 2012, *116* (42), 22411-22416.

63. Wang, T.; Zhu, R.; Zhuo, J.; Zhu, Z.; Shao, Y.; Li, M., Direct Detection of DNA below ppb Level Based on Thionin-Functionalized Layered MoS_2 Electrochemical Sensors. *Anal. Chem.* 2014, *86* (24), 12064-12069.

64. Nguyen, E. P.; Carey, B. J.; Ou, J. Z.; van Embden, J.; Gaspera, E. D.; Chrimes, A. F.; Spencer, M. J. S.; Zhuiykov, S.; Kalantar-zadeh, K.; Daeneke, T., Electronic Tuning of 2D MoS_2 through Surface Functionalization. *Adv. Mater.* 2015, *27* (40), 6225-6229.

65. Zhou, L.; He, B.; Yang, Y.; He, Y., Facile approach to surface functionalized MoS_2 nanosheets. *RSC Adv.* 2014, *4* (61), 32570-32578.

66. Sim, D. M.; Kim, M.; Yim, S.; Choi, M.-J.; Choi, J.; Yoo, S.; Jung, Y. S., Controlled Doping of Vacancy-Containing Few-Layer MoS_2 via Highly Stable Thiol-Based Molecular Chemisorption. *ACS Nano* 2015, *9* (12), 12115-12123.

67. Jiang, S.-D.; Tang, G.; Bai, Z.-M.; Wang, Y.-Y.; Hu, Y.; Song, L., Surface functionalization of MoS2 with POSS for enhancing thermal, flame-retardant and mechanical properties in PVA composites. *RSC Adv.* 2014, *4* (7), 3253-3262.

68. Kim, J.-S.; Yoo, H.-W.; Choi, H. O.; Jung, H.-T., Tunable Volatile Organic Compounds Sensor by Using Thiolated Ligand Conjugation on MoS_2. *Nano Lett.* 2014, *14* (10), 5941-5947.

69. Chen, X.; Berner, N. C.; Backes, C.; Duesberg, G. S.; McDonald, A. R., Functionalization of Two-Dimensional MoS_2: On the Reaction Between MoS_2 and Organic Thiols. *Angew. Chem.* 2016, *55* (19), 5803-5808.

70. Canton-Vitoria, R.; Sayed-Ahmad-Baraza, Y.; Pelaez-Fernandez, M.; Arenal, R.; Bittencourt, C.; Ewels, C. P.; Tagmatarchis, N., Functionalization of MoS_2 with 1,2-dithiolanes: toward donor-acceptor nanohybrids for energy conversion. *NPJ 2D Mater. Appl.* 2017, *1* (1), 13.

71. Liu, T.; Wang, C.; Gu, X.; Gong, H.; Cheng, L.; Shi, X.; Feng, L.; Sun, B.; Liu, Z., Drug Delivery with PEGylated MoS2 Nano-sheets for Combined Photothermal and Chemotherapy of Cancer. *Adv. Mater.* 2014, *26* (21), 3433-3440.

72. Kim, M. S.; Nam, G.; Park, S.; Kim, H.; Han, G. H.; Lee, J.; Dhakal, K. P.; Leem, J.-Y.; Lee, Y. H.; Kim, J., Photoluminescence wavelength variation of monolayer MoS_2 by oxygen plasma treatment. *Thin Solid Films* 2015, *590*, 318-323.

73. Sun, L.; Hu, H.; Zhan, D.; Yan, J.; Liu, L.; Teguh, J. S.; Yeow, E. K. L.; Lee, P. S.; Shen, Z., Plasma Modified MoS_2 Nanoflakes for Surface Enhanced Raman Scattering. *Small* 2014, *10* (6), 1090-1095.

74. Lv, R.; Li, Q.; Botello-Méndez, A. R.; Hayashi, T.; Wang, B.; Berkdemir, A.; Hao, Q.; Elías, A. L.; Cruz-Silva, R.; Gutiérrez, H. R.; Kim, Y. A.; Muramatsu, H.; Zhu, J.; Endo, M.; Terrones, H.; Charlier, J.-C.; Pan, M.; Terrones, M., Nitrogen-doped graphene: beyond single substitution and enhanced molecular sensing. *Sci. Rep.* 2012, *2*, 586.

75. Qin, S.; Lei, W.; Liu, D.; Chen, Y., In-situ and tunable nitrogen-doping of MoS_2 nanosheets. *Sci. Rep.* 2014, *4*, 7582.

76. Azcatl, A.; Qin, X.; Prakash, A.; Zhang, C.; Cheng, L.; Wang, Q.; Lu, N.; Kim, M. J.; Kim, J.; Cho, K.; Addou, R.; Hinkle, C. L.; Appenzeller, J.; Wallace, R. M., Covalent

Nitrogen Doping and Compressive Strain in MoS_2 by Remote N_2 Plasma Exposure. *Nano Lett.* 2016, *16* (9), 5437-5443.

77. Mishra, P.; Tangi, M.; Ng, T. K.; Hedhili, M. N.; Anjum, D. H.; Alias, M. S.; Tseng, C.-C.; Li, L.-J.; Ooi, B. S., Impact of N-plasma and Ga-irradiation on MoS_2 layer in molecular beam epitaxy. *Appl. Phys. Lett.* 2017, *110* (1), 012101.

78. Kim, Y.; Jhon, Y. I.; Park, J.; Kim, C.; Lee, S.; Jhon, Y. M., Plasma functionalization for cyclic transition between neutral and charged excitons in monolayer MoS_2. *Sci. Rep.* 2016, *6*, 21405.

79. Chen, M.; Nam, H.; Wi, S.; Ji, L.; Ren, X.; Bian, L.; Lu, S.; Liang, X., Stable few-layer MoS_2 rectifying diodes formed by plasma-assisted doping. *Appl. Phys. Lett.* 2013, *103* (14), 142110.

80. Nipane, A.; Karmakar, D.; Kaushik, N.; Karande, S.; Lodha, S., Few-Layer MoS_2 p-Type Devices Enabled by Selective Doping Using Low Energy Phosphorus Implantation. *ACS Nano* 2016, *10* (2), 2128-2137.

81. Jhon, Y. I.; Kim, Y.; Park, J.; Kim, J. H.; Lee, T.; Seo, M.; Jhon, Y. M., Significant Exciton Brightening in Monolayer Tungsten Disulfides via Fluorination: n-Type Gas Sensing Semiconductors. *Adv. Funct. Mater.* 2016, *26* (42), 7551-7559.

82. Suh, J.; Park, T.-E.; Lin, D.-Y.; Fu, D.; Park, J.; Jung, H. J.; Chen, Y.; Ko, C.; Jang, C.; Sun, Y.; Sinclair, R.; Chang, J.; Tongay, S.; Wu, J., Doping against the Native Propensity of MoS_2: Degenerate Hole Doping by Cation Substitution. *Nano Lett.* 2014, *14* (12), 6976-6982.

83. Schmid, G., The relevance of shape and size of Au_{55} clusters. *Chem. Soc. Rev.* 2008, *37* (9), 1909-1930.

84. Jin, R., Quantum sized, thiolate-protected gold nanoclusters. *Nanoscale* 2010, *2* (3), 343-362.

85. Paramanik, B.; Bain, D.; Patra, A., Making and Breaking of DNA-Metal Base Pairs: Hg^{2+} and Au Nanocluster Based Off/On Probe. *J. Phys. Chem. C* 2016, *120* (30), 17127-17135.

86. Paramanik, B.; Kundu, S.; De, G.; Patra, A., Structural evolution, photoinduced energy transfer in Au nanocluster-CdTe QD nanocomposites and amino acid sensing. *J. Mater. Chem. C* 2016, *4* (3), 486-496.

87. Diez, I.; Ras, R. H. A., Fluorescent silver nanoclusters. *Nanoscale* 2011, *3* (5), 1963-1970.

88. Wilcoxon, J. P.; Abrams, B. L., Synthesis, structure and properties of metal nanoclusters. *Chem. Soc. Rev.* 2006, *35* (11), 1162-1194.

89. Lu, Y.; Chen, W., Sub-nanometre sized metal clusters: from synthetic challenges to the unique property discoveries. *Chem. Soc. Rev.* 2012, *41* (9), 3594-3623.

90. Shang, L.; Dong, S.; Nienhaus, G. U., Ultra-small fluorescent metal nanoclusters: Synthesis and biological applications. *Nano Today* 2011, *6* (4), 401-418.

91. Yau, S. H.; Varnavski, O.; Gilbertson, J. D.; Chandler, B.; Ramakrishna, G.; Goodson, T., Ultrafast Optical Study of Small Gold Monolayer Protected Clusters: A Closer Look at Emission. *J. Phys. Chem. C* 2010, *114* (38), 15979-15985.

92. Qian, H.; Zhu, M.; Wu, Z.; Jin, R., Quantum Sized Gold Nanoclusters with Atomic Precision. *Acc. Chem. Res.* 2012, *45* (9), 1470-1479.

93. Li, J.; Zhu, J.-J.; Xu, K., Fluorescent metal nanoclusters: From synthesis to applications. *Trends Anal. Chem.* 2014, *58*, 90-98.

94. Li, Z.; Sun, Q.; Zhu, Y.; Tan, B.; Xu, Z. P.; Dou, S. X., Ultra-small fluorescent inorganic nanoparticles for bioimaging. *J. Mater. Chem. B* 2014, *2* (19), 2793-2818.

95. Chakraborty, I.; Udayabhaskararao, T.; Pradeep, T., High temperature nucleation and growth of glutathione protected ∼Ag_{75} clusters. *Chem. Commun.* 2012, *48* (54), 6788-6790.

96. Yu, Y.; Chen, X.; Yao, Q.; Yu, Y.; Yan, N.; Xie, J., Scalable and Precise Synthesis of Thiolated $Au_{10–12}$, Au_{15}, Au_{18}, and Au_{25} Nanoclusters via pH Controlled CO Reduction. *Chem. Mater.* 2013, *25* (6), 946-952.

97. Du, Y.; Sheng, H.; Astruc, D.; Zhu, M., Atomically Precise Noble Metal Nanoclusters as Efficient Catalysts: A Bridge between Structure and Properties. *Chem. Rev.* 2019. (DOI: 10.1021/acs.chemrev.8b00726)

98. Jin, R.; Zeng, C.; Zhou, M.; Chen, Y., Atomically Precise Colloidal Metal Nanoclusters and Nanoparticles: Fundamentals and Opportunities. *Chem. Rev.* 2016, *116* (18), 10346-10413.

99. Shichibu, Y.; Negishi, Y.; Tsunoyama, H.; Kanehara, M.; Teranishi, T.; Tsukuda, T., Extremely High Stability of Glutathionate-Protected Au_{25} Clusters Against Core Etching. *Small* 2007, *3* (5), 835-839.

100. Pyo, K.; Thanthirige, V. D.; Kwak, K.; Pandurangan, P.; Ramakrishna, G.; Lee, D., Ultrabright Luminescence from Gold Nanoclusters: Rigidifying the Au(I)–Thiolate Shell. *J. Am. Chem. Soc.* 2015, *137* (25), 8244-8250.

101. Wu, Z.; Jin, R., On the Ligand's Role in the Fluorescence of Gold Nanoclusters. *Nano Lett.* 2010, *10* (7), 2568-2573.

102. Zhang, Y.; Liu, S.; Lu, W.; Wang, L.; Tian, J.; Sun, X., In situ green synthesis of Au nanostructures on graphene oxide and their application for catalytic reduction of 4-nitrophenol. *Catal. Sci. Technol.* 2011, *1* (7), 1142-1144.

103. Kang, X.; Xiong, L.; Wang, S.; Pei, Y.; Zhu, M., Combining the Single-Atom Engineering and Ligand-Exchange Strategies: Obtaining the Single-Heteroatom-Doped $Au_{16}Ag_1(S\text{-}Adm)_{13}$ Nanocluster with Atomically Precise Structure. *Inorg. Chem.* 2018, *57* (1), 335-342.

104. Tyo, E. C.; Vajda, S., Catalysis by clusters with precise numbers of atoms. *Nat. Nanoyrchnol.* 2015, *10* (7), 577-588.

105. Kudo, A.; Miseki, Y., Heterogeneous photocatalyst materials for water splitting. *Chem. Soc. Rev.* 2009, *38* (1), 253-278.

106. Inoue, T.; Fujishima, A.; Konishi, S.; Honda, K., Photoelectrocatalytic reduction of carbon dioxide in aqueous suspensions of semiconductor powders. *Nature* 1979, *277* (5698), 637-638.

107. Bottari, G.; Herranz, M. Á.; Wibmer, L.; Volland, M.; Rodríguez-Pérez, L.; Guldi, D. M.; Hirsch, A.; Martín, N.; D'Souza, F.; Torres, T., Chemical functionalization and characterization of graphene-based materials. *Chem. Soc. Rev.* 2017, *46* (15), 4464-4500.

108. Bosch-Navarro, C.; Laker, Z. P. L.; Thomas, H. R.; Marsden, A. J.; Sloan, J.; Wilson, N. R.; Rourke, J. P., Covalently Binding Atomically Designed Au_9 Clusters to Chemically Modified Graphene. *Angew. Chem.* 2015, *54* (33), 9560-9563.

109. Patrick, T. K. C.; Marte van der, L.; Elleke, J. v. H.; Arjan, B.; Marcus, T. M. R.; Abraham, J. K.; Fijs, W. B. v. L.; Celso de Mello, D.; Albert, J. R. H.; Andries, M., Enhanced luminescence of Ag nanoclusters via surface modification. *Nanotechnology* 2013, *24* (7), 075703.

110. Nguyen, P.-D.; Cong, V. T.; Baek, C.; Min, J., Fabrication of peptide stabilized fluorescent gold nanocluster/graphene oxide nanocomplex and its application in turn-on detection of metalloproteinase-9. *Biosens. Bioelectron.* 2017, *89, (Part1)*, 666-672.

111. Wang, Z.-L.; Yan, J.-M.; Wang, H.-L.; Ping, Y.; Jiang, Q., Au@Pd core-shell nanoclusters growing on nitrogen-doped mildly reduced graphene oxide with enhanced catalytic performance for hydrogen generation from formic acid. *J. Mater. Chem. A* 2013, *1* (41), 12721-12725.

112. Peng, S.; Liu, J.; Zhang, J.; Wang, F., An improved preparation of graphene supported ultrafine ruthenium (0) NPs: Very active and durable catalysts for H_2 generation from methanolysis of ammonia borane. *Int. J. Hydrogen Energy* 2015, *40* (34), 10856-10866.

113. Du, C.; Ao, Q.; Cao, N.; Yang, L.; Luo, W.; Cheng, G., Facile synthesis of monodisperse ruthenium nanoparticles supported on graphene for hydrogen generation from hydrolysis of ammonia borane. *Int. J. Hydrogen Energy* 2015, *40* (18), 6180-6187.

114. Fan, G.-Y.; Huang, W.-J., Synthesis of ruthenium/reduced graphene oxide composites and application for the selective hydrogenation of halonitroaromatics. *Chin. Chem. Lett.* 2014, *25* (2), 359-363.

115. Esteban, R. M.; Schütte, K.; Brandt, P.; Marquardt, D.; Meyer, H.; Beckert, F.; Mülhaupt, R.; Kölling, H.; Janiak, C., Iridium@graphene composite nanomaterials synthesized in ionic liquid as re-usable catalysts for solvent-free hydrogenation of benzene and cyclohexene. *Nano-Structures & Nano-Objects* 2015, *2*, 11-18.

116. Chen, Y.; Shen, Y.; Sun, D.; Zhang, H.; Tian, D.; Zhang, J.; Zhu, J.-J., Fabrication of a dispersible graphene/gold nanoclusters hybrid and its potential application in electrogenerated chemiluminescence. *Chem. Commun.* 2011, *47* (42), 11733-11735.

117. Yuan, D.; Chen, S.; Yuan, R.; Zhang, J.; Zhang, W., An electrogenerated chemiluminescence sensor prepared with a graphene/multiwall carbon nanotube/gold nanocluster hybrid for the determination of phenolic compounds. *Analyst* 2013, *138* (20), 6001-6006.

118. Yang, Y.; Wu, W.; Wang, Q.; Xiao, H.; Kuang, Y.; Liu, C., Novel anodic electrochemiluminescence system of Pt nanocluster/graphene hybrids for ultrasensitive detection of Cu^{2+}. *J. Electroanal. Chem.* 2016, *772*, 73-79.

119. Xu, H.; Zhu, H.; Sun, M.; Yu, H.; Li, H.; Ma, F.; Wang, S., Graphene oxide supported gold nanoclusters for the sensitive and selective detection of nitrite ions. *Analyst* 2015, *140* (5), 1678-1685.

120. Xiaofei, W.; Ruiyi, L.; Zaijun, L.; Junkang, L.; Guangli, W.; Zhiguo, G., Synthesis of double gold nanoclusters/graphene oxide and its application as a new fluorescence probe for Hg^{2+} detection with greatly enhanced sensitivity and rapidity. *RSC Adv.* 2014, *4* (48), 24978-24985.

121. Wang, Y.; Chen, J.-T.; Yan, X.-P., Fabrication of Transferrin Functionalized Gold Nanoclusters/Graphene Oxide Nanocomposite for Turn-On Near-Infrared Fluorescent Bioimaging of Cancer Cells and Small Animals. *Anal. Chem.* 2013, *85* (4), 2529-2535.

122. Tao, Y.; Lin, Y.; Huang, Z.; Ren, J.; Qu, X., Incorporating Graphene Oxide and Gold Nanoclusters: A Synergistic Catalyst with Surprisingly High Peroxidase-Like Activity Over a Broad pH Range and its Application for Cancer Cell Detection. *Adv. Mater.* 2013, *25* (18), 2594-2599.

123. Wang, J.; Wang, X.; Wu, S.; Song, J.; Zhao, Y.; Ge, Y.; Meng, C., Fabrication of highly catalytic silver nanoclusters/graphene oxide nanocomposite as nanotag for sensitive electrochemical immunoassay. *Anal Chim Acta* 2016, *906*, 80-88.

124. Zhang, Y.; Liu, H.; Yang, Z.; Ji, S.; Wang, J.; Pang, P.; Feng, L.; Wang, H.; Wu, Z.; Yang, W., An acetylcholinesterase inhibition biosensor based on a reduced graphene oxide/silver nanocluster/chitosan nanocomposite for detection of organophosphorus pesticides. *Anal. Methods* 2015, *7* (15), 6213-6219.

125. Wang, Y.; Bai, X.; Wen, W.; Zhang, X.; Wang, S., Ultrasensitive Electrochemical Biosensor for HIV Gene Detection Based on Graphene Stabilized Gold Nanoclusters with Exonuclease Amplification. *ACS Appl. Mater. Interfaces* 2015, *7* (33), 18872-18879.

126. Wang, C.; Li, J.; Amatore, C.; Chen, Y.; Jiang, H.; Wang, X.-M., Gold Nanoclusters and Graphene Nanocomposites for Drug Delivery and Imaging of Cancer Cells. *Angew. Chem.* 2011, *50* (49), 11644-11648.

127. Tao, Y.; Lin, Y.; Huang, Z.; Ren, J.; Qu, X., DNA-templated silver nanoclusters-graphene oxide nanohybrid materials: a platform for label-free and sensitive fluorescence turn-on detection of multiple nucleic acid targets. *Analyst* 2012, *137* (11), 2588-2592.

128. Liu, X.; Wang, F.; Aizen, R.; Yehezkeli, O.; Willner, I., Graphene Oxide/Nucleic-Acid-Stabilized Silver Nanoclusters: Functional Hybrid Materials for Optical Aptamer Sensing and Multiplexed Analysis of Pathogenic DNAs. *J. Am. Chem. Soc.* 2013, *135* (32), 11832-11839.

129. Fan, D.; Zhu, J.; Liu, Y.; Wang, E.; Dong, S., Label-free and enzyme-free platform for the construction of advanced DNA logic devices based on the assembly of graphene oxide and DNA-templated AgNCs. *Nanoscale* 2016, *8* (6), 3834-3840.

130. Zhu, C.; Zeng, Z.; Li, H.; Li, F.; Fan, C.; Zhang, H., Single-Layer MoS_2-Based Nanoprobes for Homogeneous Detection of Biomolecules. *J. Am. Chem. Soc.* 2013, *135* (16), 5998-6001.

131. Ge, J.; Ou, E.-C.; Yu, R.-Q.; Chu, X., A novel aptameric nanobiosensor based on the self-assembled DNA–MoS_2 nanosheet architecture for biomolecule detection. *J. Mater. Chem. B* 2014, *2* (6), 625-628.

132. Huang, J.; Ye, L.; Gao, X.; Li, H.; Xu, J.; Li, Z., Molybdenum disulfide-based amplified fluorescence DNA detection using hybridization chain reactions. *J. Mater. Chem. B* 2015, *3* (11), 2395-2401.

133. Shi, J.; Lyu, J.; Tian, F.; Yang, M., A fluorescence turn-on biosensor based on graphene quantum dots (GQDs) and molybdenum disulfide (MoS_2) nanosheets for epithelial cell adhesion molecule (EpCAM) detection. *Biosens. Bioelectron.* 2017, *93*, 182-188.

134. Zhang, Y.; Zheng, B.; Zhu, C.; Zhang, X.; Tan, C.; Li, H.; Chen, B.; Yang, J.; Chen, J.; Huang, Y.; Wang, L.; Zhang, H., Single-Layer Transition Metal Dichalcogenide Nanosheet-Based Nanosensors for Rapid, Sensitive, and Multiplexed Detection of DNA. *Adv. Mater.* 2015, *27* (5), 935-939.

135. Xu, S.; Feng, X.; Gao, T.; Liu, G.; Mao, Y.; Lin, J.; Yu, X.; Luo, X., Aptamer induced multicoloured Au NCs-MoS_2 "switch on" fluorescence resonance energy transfer biosensor for dual color simultaneous detection of multiple tumor markers by single wavelength excitation. *Anal Chim Acta* 2017, *983*, 173-180.

136. Hassanzadeh, J.; Khataee, A.; Eskandari, H., Encapsulated cholesterol oxidase in metal-organic framework and biomimetic Ag nanocluster decorated MoS_2 nanosheets for sensitive detection of cholesterol. *Sens. Actuator B-Chem.* 2018, *259*, 402-410.

137. Khataee, A.; Haddad Irani-nezhad, M.; Hassanzadeh, J.; Woo Joo, S., Superior peroxidase mimetic activity of tungsten disulfide nanosheets/silver nanoclusters composite: Colorimetric, fluorometric and electrochemical studies. *J. Colloid Interface Sci.* 2018, *515*, 39-49.

138. Khataee, A.; Haddad Irani-nezhad, M.; Hassanzadeh, J., Improved peroxidase mimetic activity of a mixture of WS_2 nanosheets and silver nanoclusters for chemiluminescent quantification of H_2O_2 and glucose. *Microchim. Acta* 2018, *185* (3), 190.

139. Zhao, S.; Jin, R.; Song, Y.; Zhang, H.; House, S. D.; Yang, J. C.; Jin, R., Atomically Precise Gold Nanoclusters Accelerate Hydrogen Evolution over MoS_2 Nanosheets: The Dual Interfacial Effect. *Small* 2017, *13* (43), 1701519.

Chapter 2

Scope of research

To address the pressing environmental concerns, the objective of the current PhD Thesis is the development of novel hybrid materials, based on graphene and TMDs combined with photoactive components, i.e. fluorescent metal nanoclusters (M_{NCs}), which boast remarkable photophysical properties potentially suitable to be employed in energy conversion schemes. The scope of the conducted research to realize the objective is three-fold, namely to (a) incorporate M_{NCs} on suitably functionalized graphene towards hydrogen production, (b) functionalize TMDs (MoS_2, and WS_2) through nitrogen plasma treatment and decorate them with silver nanoparticles for detection polycyclic aromatic hydrocarbons via surface enhanced Raman scattering, and (c) immobilize M_{NCs} on pre-modifie MoS_2 sheets, and employ them as photocatalysts for the decomposition of Rhodamine B.

In **Chapter 3**, graphene was functionalized with ammonium units (abbreviated as *f*-G) through condensation reaction and carried positive charges. Next, the *f*-G sheets were electrostatically tethered to fluorescent water-soluble silver and gold nanoclusters stabilized by α-lipoic acid (abbreviated as Ag_{NCs} and Au_{NCs}, respectively), bearing negative charges, to form Ag_{NCs}/*f*-G and Au_{NCs}/*f*-G ensembles, respectively (Scheme 2.1). Titration assays employed to verify the effective electrostatic immobilization of both M_{NCs} onto *f*-G nanosheets, revealed the development of an isosbestic point in the electronic absorption spectrum of each M_{NC} upon incremental additions of *f*-G, thereby proving electronic communication between the two species at the ground state. Examining possible interactions at the excited state, photoluminescence measurements were performed, in which the characteristic emission band of each M_{NC} was found to decrease when titrated with *f*-G. The latter is indicative of charge-transfer phenomena, within the M_{NCs}/*f*-G ensembles that may possible yield charge-separation. Scanning transmission electron microscopy (STEM) and energy-dispersive X-ray (EDX) spectroscopy analysis were also applied to further justify the realization of the hybrid materials. Next, the M_{NCs}/*f*-G ensembles were successfully employed as proficient catalysts for the model reduction of 4-nitrophenol to the corresponding 4-aminophenol as proof for the photoinduced hydrogen production. A detailed mechanism explaining the improved photocatalytic performance of graphene-based ensemble is provided, after acknowledging all the data collected from the photophysical and kinetic studies of the catalytic reactions. Due to these processes, the newly-prepared hybrid materials are expected to find interesting applications in the energy conversion field.

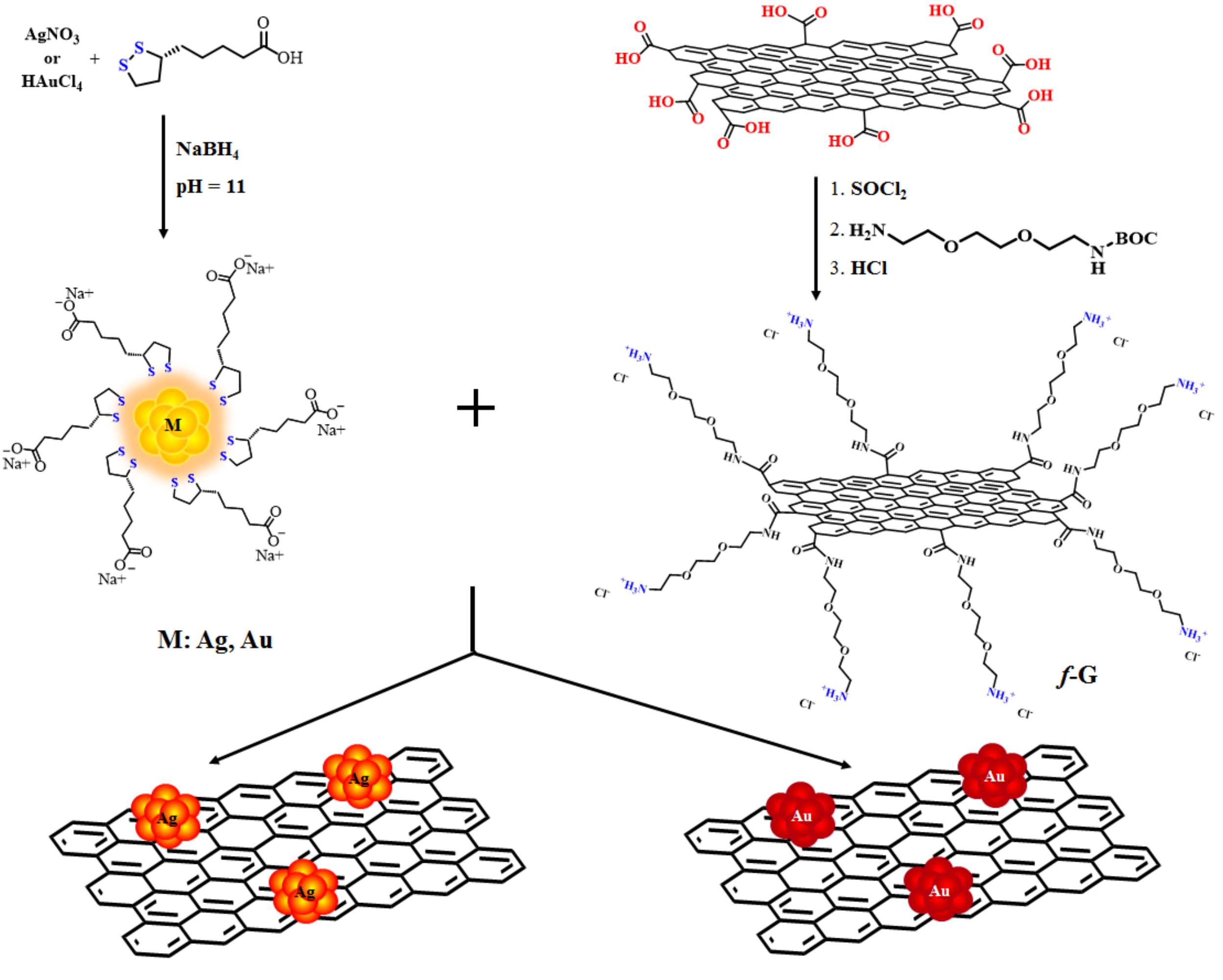

Ag_{NCs} /*f*-G ensembles

Au_{NCs} /*f*-G ensembles

Scheme 2.1 Graphene-based materials combined with Au_{NCs} and Ag_{NCs}.

In **Chapter 4**, a simple one-pot modification of few-layered MoS_2 and WS_2 sheets, employing nitrogen (N) plasma treatment and simultaneous decoration with silver nanoparticles (Ag_{NPs}), for two different plasma exposure and metal deposition times, toward the preparation of N-doped TMDs decorated with Ag_{NPs} (Scheme 2.2). The successful surface modification of TMDs was evaluated through Raman and X-ray photoelectron spectroscopy, while transmission electron microscopy imaging verified the decoration with Ag_{NPs}. Furthermore, the newly developed TMD-based hybrids were employed as surface-enhanced Raman scattering (SERS) substrates, to detect Rhodamine B (RhB) at very low concentration. Finally, considering coordination of the aromatic moieties via π−S interactions with TMDs, we accomplished the sensitive detection of polycyclic aromatic hydrocarbons such as pyrene, anthracene, and 2,3-dihydroxynaphthalene, at very low levels, by employing N-MoS_2/Ag_{NPs} as SERS substrates. The employed method offers numerous virtues, including straightforwardness, controllability, fast functionalization time, and absence of wet processes that may require additional work up procedures.

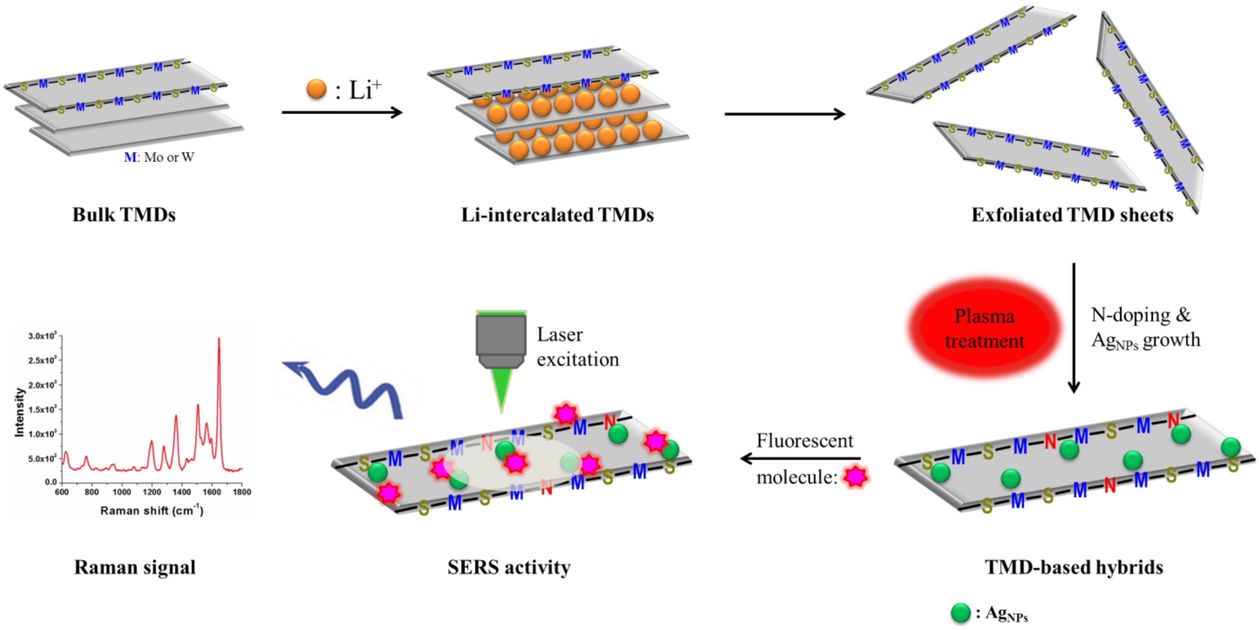

Scheme 2.2 Nitrogen doped TMD-based materials decorated with Ag nanoparticles.

In **Chapter 5**, core–shell Ag@Au_{NCs} were labeled with bovine serum albumin (BSA) bearing negative charges at alkaline media due to ionization of the carboxylic acids present in the protein. On the other hand, suitably functionalized MoS_2 nanosheets carrying positively charged ammonium moieties were prepared via reaction of exfoliated MoS_2 with a 1,2-dithiolane derivative bearing an ethylene glycol alkyl chain terminated to a butoxycarbonyl (BOC) protected amine, followed by acidic deprotection of the BOC group, and employed to form Ag@Au_{NCs}/*f*-MoS_2 ensemble via electrostatic interactions between the two species (Scheme 2.3). The successful fabrication of Ag@Au_{NCs}/*f*-MoS_2 was manifested through electronic absorption and photoluminescence spectroscopy and morphologically evaluated by high-resolution transmission electron microscopy (HRTEM) imaging. The photocatalytic properties of Ag@Au_{NCs}/*f*-MoS_2 towards the decomposition of Rhodamine B (RhB) were examined by monitoring temporal spectral changes in the absorption spectrum of the dye. Possible mechanistic pathways explaining the high photocatalytic activity of the MoS_2-based hybrid are described opening up a new era in the design of light-harvesting systems.

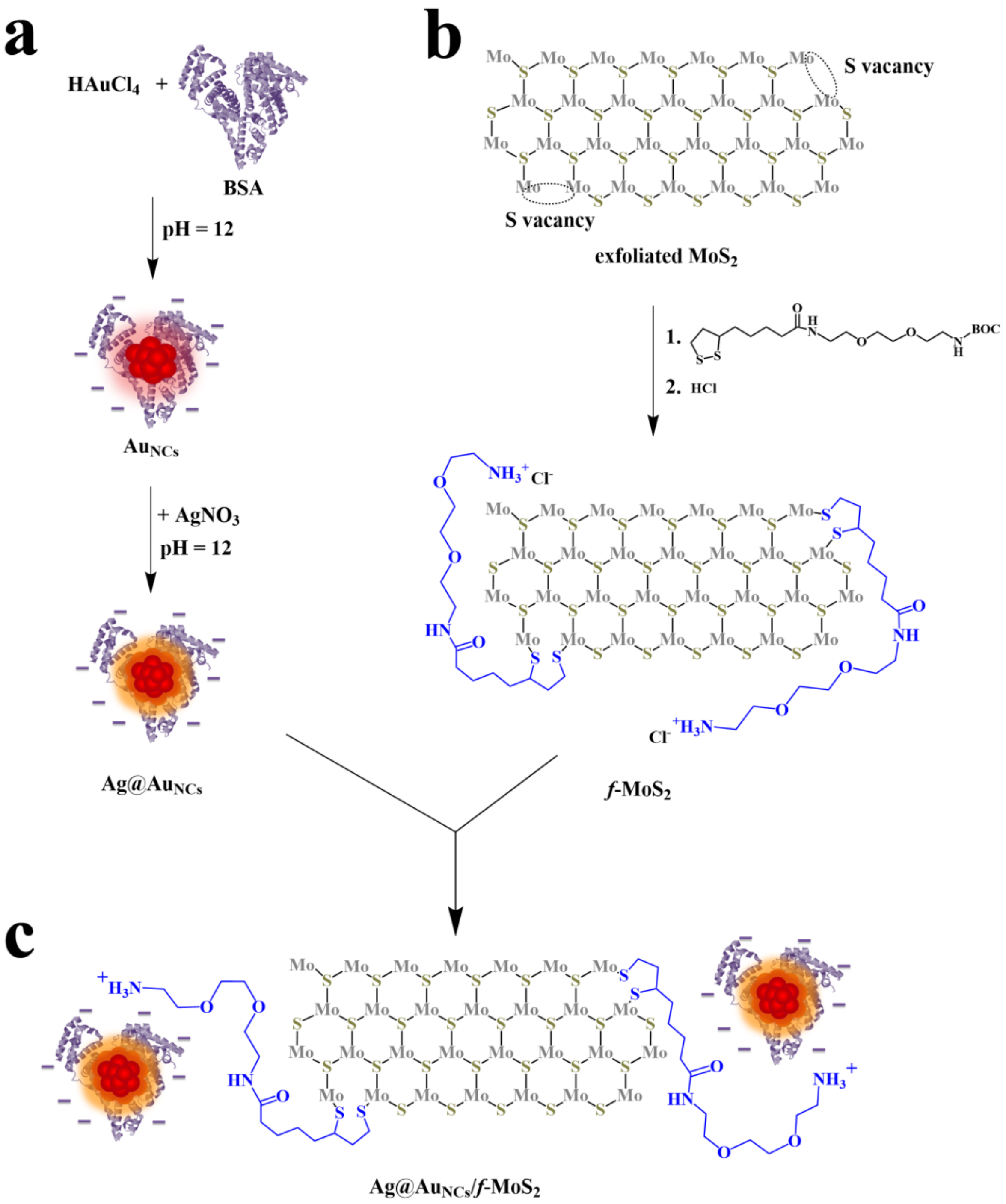

Scheme 2.3 Functionalized MoS_2 sheets combined with core–shell $Ag@Au_{NCs}$.

In **Chapter 6**, a new organic stabilizer based on a bulky adamantane moiety bearing also an 1,2-dithiolane derivative is demonstrated and employed for the synthesis of Au_{NCs} with NIR-fluorescence. Next, the C=C group of the newly synthesized ligand was exploited to covalently react with thiol-functionalized graphene and MoS_2 sheets through thiol–ene “click” reaction (Scheme 2.4 and 2.5). The successful fabrication of the hybrid materials was manifested through electronic absorption and photoluminescence spectroscopy, while ATR-IR spectroscopy and TGA assisted in the determination and quantification of the organic functionalities onto 2D sheets. The current strategy employed constitutes a general tool that is wide in scope and can, in principle, be extended to the modification of other 2D materials and/or compounds for the fabrication of hybrid schemed with tailored characteristics that today is unattainable.

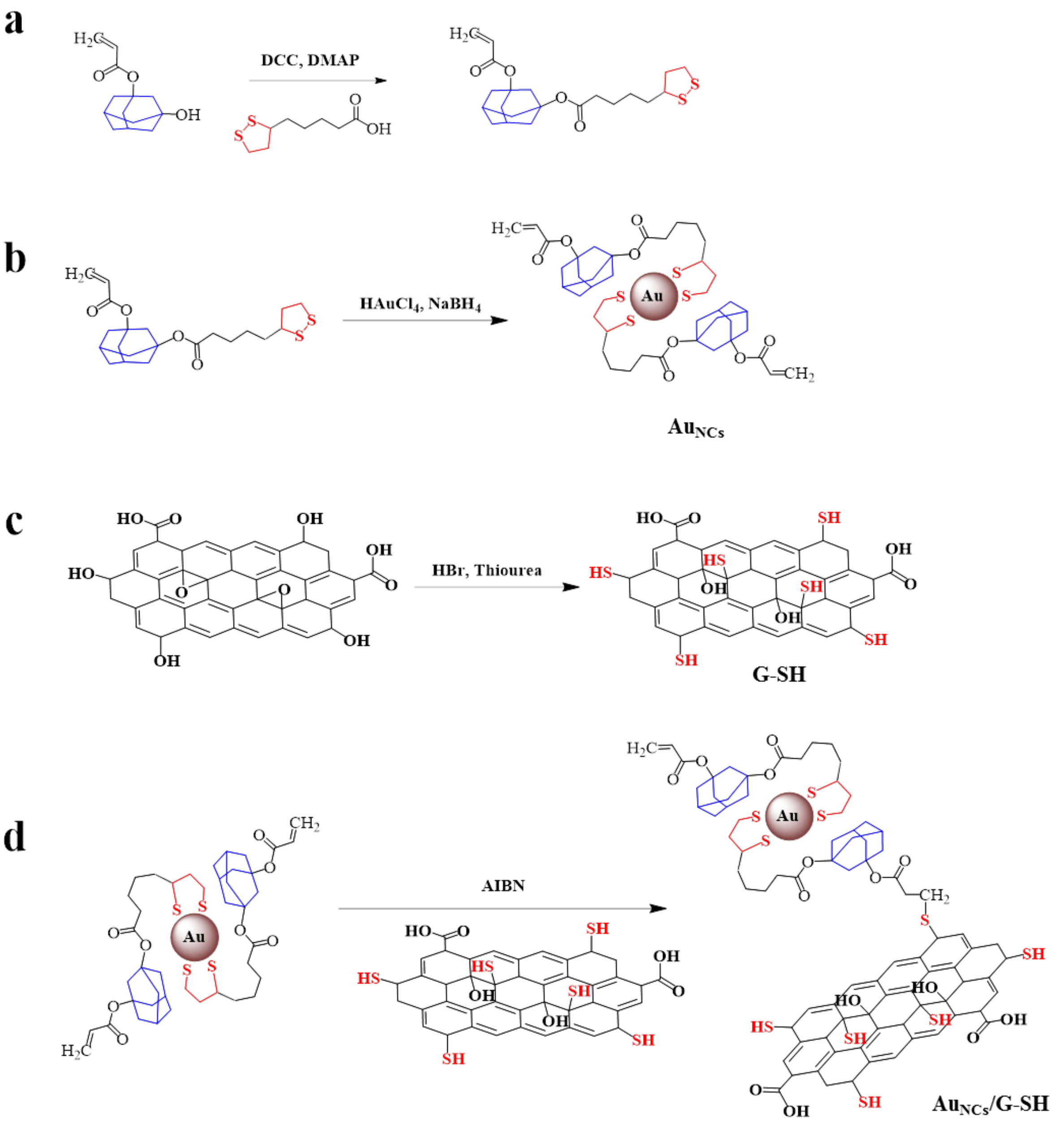

Scheme 2.4 Covalent functionalization of graphene with Au_{NCs}.

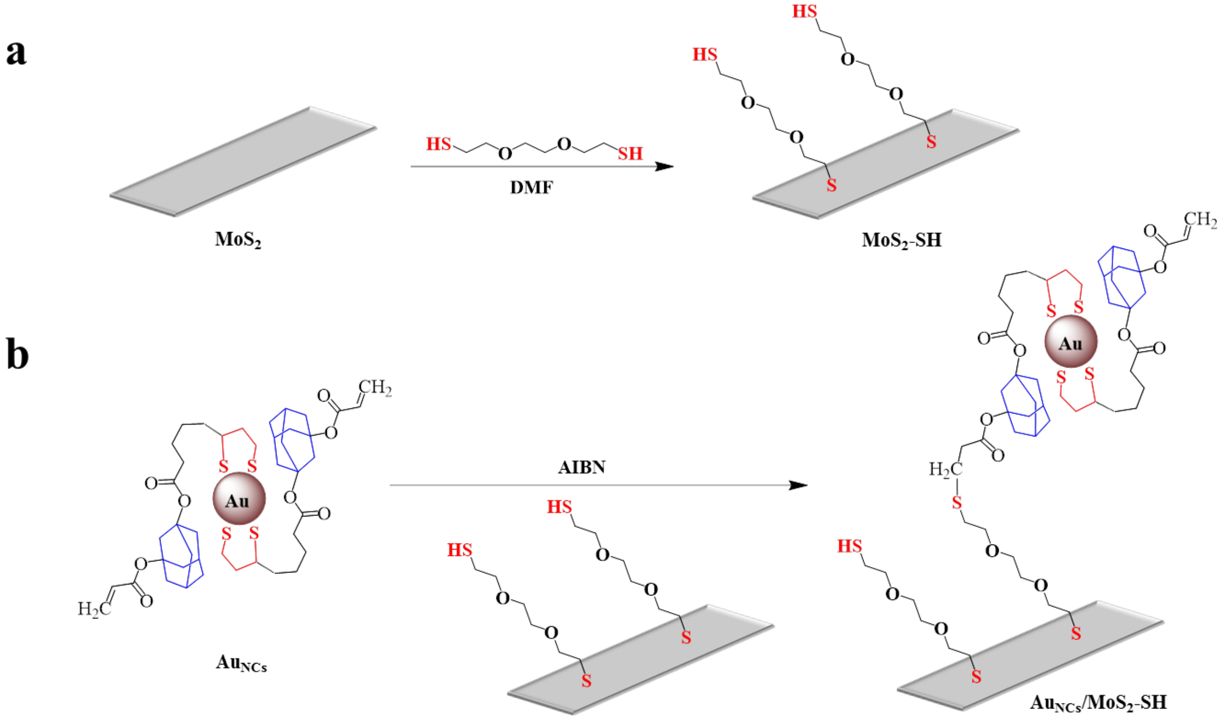

Scheme 2.5 Covalent functionalization of MoS_2 with Au_{NCs}.

Chapter 3

Metal nanocluster/graphene ensembles for managing photoinduced charge-transfer processes

Abstract

Metal nanoclusters (M_{NCs}) based on silver and gold, abbreviated as Ag_{NCs} and Au_{NCs}, respectively, were synthesized and combined with functionalized graphene, abbreviated as *f*-G, forming novel M_{NCs}/*f*-G ensembles. The preparation of M_{NCs}/*f*-G was achieved by employing attractive electrostatic interactions developed between negatively charged M_{NCs}, owed to the presence of carboxylates due to α-lipoic acid employed as stabilizer, and positively charged *f*-G, owed to the presence of ammonium units as addends. The realization of M_{NCs}/*f*-G ensembles was established via titration assays as evidenced by electronic absorption and photoluminescence spectroscopy as well as scanning transmission electron microscopy (STEM) and energy-dispersive X-ray (EDX) spectroscopy analysis. Photoinduced charge-transfer phenomena were inferred within M_{NCs}/*f*-G, attributed to the suppression of M_{NCs} photoluminescence by the presence of *f*-G. Next, the M_{NCs}/*f*-G ensembles were successfully employed as proficient catalysts for the model reduction of 4-nitrophenol to the corresponding 4-aminophenol as proof for the photoinduced hydrogen production. Particularly, the reduction kinetics decelerated by half when bare M_{NCs} were employed vs the M_{NCs}/*f*-G ensembles, highlighting the beneficial role of M_{NCs}/*f*-G to catalyse the process. Furthermore, Au_{NCs}/*f*-G displayed exceptionally higher catalytic activity both in dark and under visible light illumination conditions, which is ascribed to three synergistic mechanisms, namely, (a) hydride transfer from Au-H, (b) hydride transfer from photogenerated Au-H species, and (c) hydrogen produced by the photoreduction of water. Finally, recycling and re-employing M_{NCs}/*f*-G in successive catalytic cycles without loss of activity toward the reduction of 4-nitrophenol was achieved, thereby highlighting their wider applicability.

3.1 Introduction

Metal particles composed of several to roughly a hundred atoms with a core size less than 2 nm are known as clusters.[1-2] Nowadays, considerable research interest is devoted to them fueled by their fascinating features such as optical, electronic and physical properties,[3] which strikingly differ from the corresponding bulk materials and large nanoparticles.[4] Particularly, one of their most interesting hallmarks is photoluminescence, as they exhibit distinct and size-tunable electronic transitions. Metal nanoclusters (M_{NCs}) possess unprecedented advantages in many applications, including catalysis, imaging, medicine, optoelectronics, energy conversion and storage.[2, 5-8] Due to their unique surface electronic structures, high surface area and enhanced charge carrier mobility, M_{NCs} provide much more active sites in catalytic processes as compared to their larger counterparts, hence, it is anticipated to demonstrate enhanced activity. Conventional nanocatalysts in the form of particles are governed by polydispersity in size, while at the same time their catalytic performance is largely size dependent. Hence, in a plethora of catalytic transformations it becomes difficult to correlate the origin of the observed activity with the particle size, simply because the interpretation of results is based on the average of all particle sizes existing in the catalytic process.[9] In this regard, the well-defined particle size of M_{NCs} along with the high surface area are of great interest for catalysis, since their catalytic properties can be truly tuned on an atom-by-atom basis. Moreover, the majority of active catalysts are made of precious metals (e.g. Au, Ag), so their utility in the form of nanoclusters may have an additional substantial economic impact by decreasing the amount of precious metals required for a given catalytic reaction. Furthermore, in stark contrast with plasmonic nanoparticles, which display a continuous conduction band, nanoclusters behave as semiconductors[4] and possess sizable band-gap attributed to the quantization effect.[10] This means that upon photoexcitation their excited electronic state decays with emission of light, opposing the case of metal nanoparticles. The latter is beneficial, particularly when M_{NCs} are combined with an electron acceptor unit, leading to effective charge transfer phenomena, which can be exploited en route to enhanced photocatalytic performance.

The immobilization of M_{NCs} on a substrate material, particularly graphene, allows support effects, which are vital in many heterogeneous catalytic applications. Notably, these support effects are boosted when M_{NCs}-based materials are involved, owed to the reduced size of M_{NCs} and since a considerable amount of M_{NCs} atoms are located on the substrate surface, resulting in amelioration of their structural and electronic features. On the other hand, graphene holds an advantageous position over traditional support materials, due to its outstanding conductive network and high specific surface area, which can provide extra anchoring sites to the catalyst. The preparation, properties and applications of M_{NCs}/graphene ensembles were recently reviewed.[11] Sensing of hazardous molecules[12-15] and biomolecules,[16-19] bioimaging[20-21] and catalysis[22-23] are among the three main categories dealing with the incorporation of M_{NCs} on graphene-based materials. Particularly, sensing and bioimaging applications take advantage of photoinduced charge transfer phenomena occurring within M_{NCs}/graphene ensembles, in which the M_{NCs} upon photoillumination act as electron donors, while graphene is an excellent acceptor.

Nitroarenes, precisely nitrophenols, are non-biodegradable noxious organic pollutants, released in the aquatic system from pesticide and petrochemical industries,[24] bringing adverse high risk to the human health and the ecological system through surface, ground and drinking water contamination.[25] Hence, their selective reduction to amines, which are valuable for the manufacturing of a plethora of pharmaceuticals, i.e. analgesic and antipyretic drugs, is an urgent issue demanding efficient and cost economic catalytic pathways. In this regard, monodispersed Au_{NCs} bearing thiols with short alkyl chain lengths as stabilizers were found to catalyze with fast kinetics the reduction of 4-nitrophenol to 4-aminophenol, while also exhibiting excellent stability.[26, 27] Additionally, their unique configuration[28-29] poses less steric impedance and thus renders the catalytically active surface sites more accessible to reactants. Improved catalytic activity for the reduction of 4-nitrophenol was also reported for *N,N*-dimethylformamide-capped Au_{NCs}, in contrast to glutathione-stabilized ones.[30]

The catalytic reduction of nitro-compounds to the corresponding amines proceeds via nucleophilic attack of hydrides to the nitrogen atom in a process that takes place onto the surface of the metal catalysts. The source of the hydrides can be diverse as derived from (i) a metal salt, i.e. $NaBH_4$, (ii) the catalytic dissociation of injected hydrogen gas, and (iii) the self-evolution of hydrogen by light-driven water reduction. Particularly considering the latter, the semiconducting nature of M_{NCs} may take advantage of visible light driven processes and self-catalyze the reduction reaction of nitro-compounds by in-situ producing hydrogen/hydrides in a simpler and more economic approach, without the requirement of the presence of additional species. Hence, the model reduction reaction of 4-nitrophenol to 4-aminophenol can be employed as indirect proof for the photoinduced hydrogen production. Notably, for hydrogen evolution and the mechanism responsible concern, contrasting cases in which it is photocatalytically induced by combining graphene with organic electron donors as well as metal nanoparticles in the form of hybrid materials,[31-35] the investigation of M_{NCs}/graphene ensembles has yet to be fully assessed and still remains a challenge.

Considering the aforementioned points, the objectives of this chapter are the following (i) develop and fully characterize the M_{NCs}/graphene ensembles (M = Ag, Au), (ii) investigate the catalytic properties of the M_{NCs}/graphene ensembles for the reduction of 4-nitrophenol, and (iii) shed light on the mechanistic pathways promoting the (photo)catalytic activity. In order to achieve our aims, both Ag_{NCs} and Au_{NCs} were labeled with α-lipoic acid and bare negative charges at alkaline media owed to the presence of ionized carboxylate species. On the other hand, functionalized graphene sheets with ammonium units, carrying positive charges, were developed and employed to form Ag_{NCs}/graphene and Au_{NCs}/graphene ensembles via the exploitation of attractive electrostatic interactions between the two species. The fabrication of M_{NCs}/graphene ensembles was manifested with the aid of electronic absorption and photoluminescence spectroscopy as well as scanning transmission electron microscopy imaging. The catalytic properties of the two ensembles were examined by monitoring spectral changes in the absorption spectrum of 4-nitrophenol. Notably, considering the photoinstability of silver, the reduction of 4-nitrophenol upon visible light illumination was examined only with Au_{NCs}/graphene. Evidently, the highly reactive gold hydrides, Au-H, formed onto the surface of Au_{NCs}, within Au_{NCs}/graphene and in the presence of $NaBH_4$, are considered as key mediator to the photocatalytic performance of the ensemble. Moreover, the quenching of the photogenerated holes centered at the Au_{NCs} within

Au_{NCs}/graphene ensembles found to activate the production of hydrogen via the photoreduction of water molecules, unveiling this unique property to materials currently considered incompetent. Finally, recycling and re-employing M_{NCs}/graphene in successive catalytic cycles without loss of activity toward the reduction of 4-nitrophenol was achieved, thereby highlighting their wider applicability.

3.2 Results and discussion

3.2.1 Preparation of M_{NCs}/*f*-G ensembles

The working principle for the preparation and fabrication of the individual components constituting the Ag_{NCs}/graphene and Au_{NCs}/graphene ensembles is illustrated in Scheme 1. Particularly for the formation of Ag_{NCs}, precaution for avoiding sunlight was taken due to photosensitivity of silver. The α-lipoic acid was employed as stabilizer for both Ag_{NCs} and Au_{NCs}, which were prepared from aqueous solutions of $AgNO_3$ and $HAuCl_4$, respectively, with $NaBH_4$ acting as reducing agent in presence of NaOH for adjusting the pH at an alkaline value. Significantly, the presence of the latter was proved beneficial for attaining small-sized M_{NCs}, not only by promoting repulsive forces and avoiding aggregation during the growth of the M_{NCs}, but also by decreasing the reduction capability of $NaBH_4$ and accelerating the etching of free α-lipoic acid.[36] Markedly, at the specific alkaline conditions set (i.e. pH=11), the 1,2-dithiolane stabilizer, bearing carboxylic species, is ionized hence allowing the realization of negatively charged aqueous Ag_{NCs} and Au_{NCs}. On the other hand, oxidation of graphite flakes followed by activation of the carboxylic acid units decorating the skeleton of the graphene oxide sheets by acyl chloride, allowed to perform condensation reaction with *N*-tert-butoxycarbonyl-2,2′-(ethylenedioxy)bis-(ethylamine). The latter gave access to modified graphene sheets decorated with amine species masked with the BOC-protecting group, which was effectively cleaved by acidic treatment, furnishing water-dispersible functionalized graphene (abbreviated as *f*-G). The amino-loading of *f*-G was calculated by performing the Kaiser test and found to be 320 μmol/g. Notably, the positive charges on *f*-G, attributed to the presence of ammonium species, were exploited for interacting with the negatively charged Ag_{NCs} and Au_{NCs} via attractive Coulombic forces, allowing the fabrication of Ag_{NCs}/*f*-G and Au_{NCs}/*f*-G ensembles, respectively (Scheme 3.1).

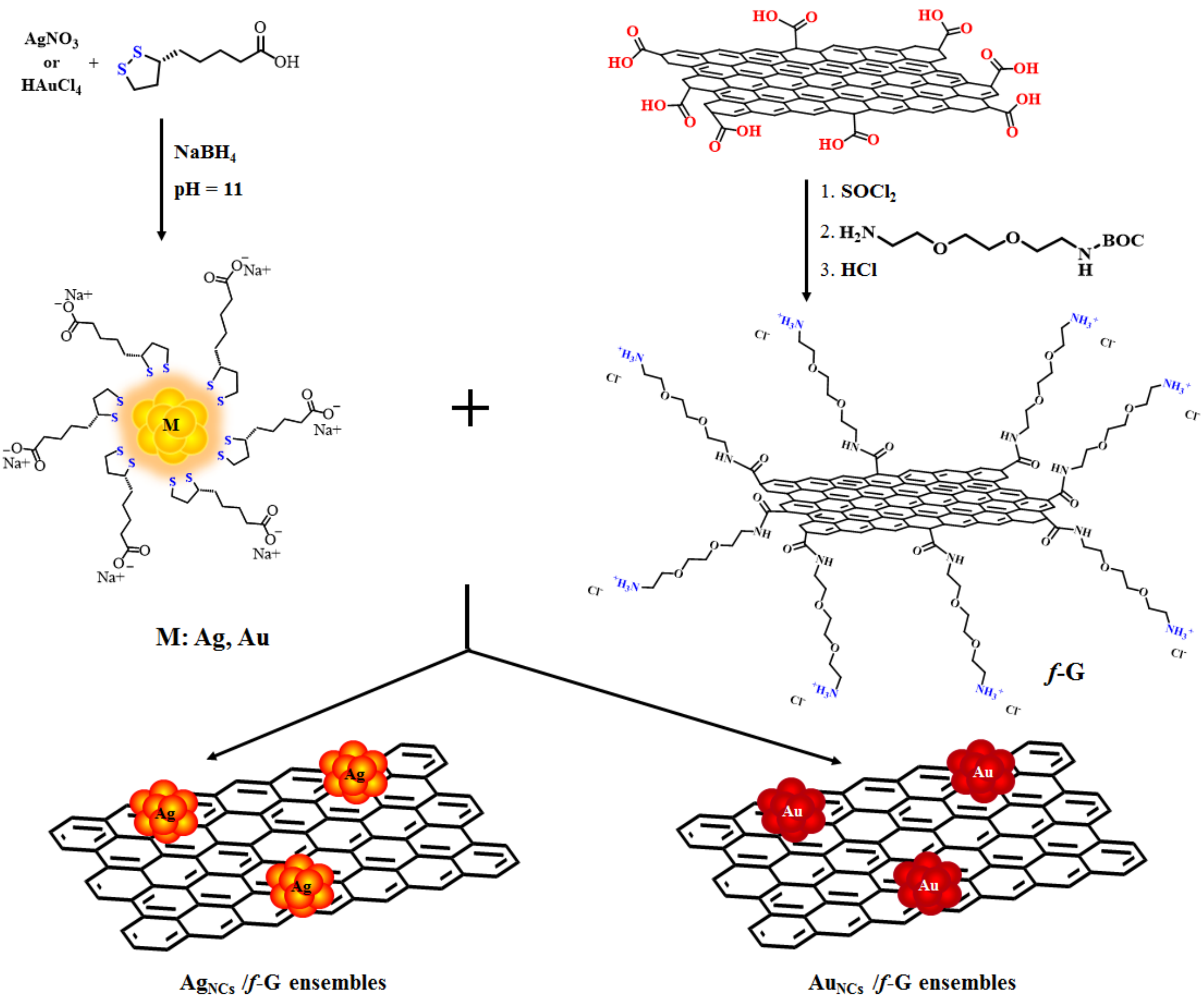

Scheme 3.1 Illustrative pathways for the preparation of Ag$_{NCs}$ and Au$_{NCs}$, ammonium functionalized graphene, *f*-G, and Ag$_{NCs}$/*f*-G and Au$_{NCs}$/*f*-G ensembles.

3.2.2 Characterization of M$_{NCs}$/*f*-G ensembles

Attenuated-total-reflectance (ATR) IR spectroscopy verified the successive transformation of GO to the *f*-G sheets. In this frame, while GO shows a strong carbonyl vibration due to the presence of carboxyl units at 1725 cm^{-1}, the BOC-functionalized graphene material displays a different and broad band at 1705 cm^{-1} arising from the carbonyl amide and BOC protecting groups. Also, strong C–H stretching and bending modes are recorded in the 2850–2960 cm^{-1} range, further demonstrating the attachment of the organic moiety onto graphene network. Notably, after treatment with HCl gas, the IR spectrum of *f*-G boasts a pronounced peak at 1660 cm^{-1} derived from the carbonyl amide of the free amine, while the disappearance of the corresponding BOC unit witnesses the successful de-protection process (Figure 3.1a). On the other hand, thermogravimetric analysis (TGA) allowed the quantitative calculation of the functionalization degree. As it can be seen, GO displayed a mass loss of about 14% in the temperature range 200–550 ^{o}C under an inert atmosphere of nitrogen due to the presence of the oxygenated functional groups and the defects generated on the carbon skeleton. For *f*-G, a mass loss of 27% was observed in the same temperature range (Figure 3.1b) attributable to the decomposition of the added organic functionalities covalently bonded on graphene, thus allowing the calculation of the number of grafted organic units onto graphene sheets as 1 per every 120 carbon atoms. Finally, the thermal decomposition of the carbon network of *f*-G proceeds up to 800 ^{o}C due to the functionalization process.

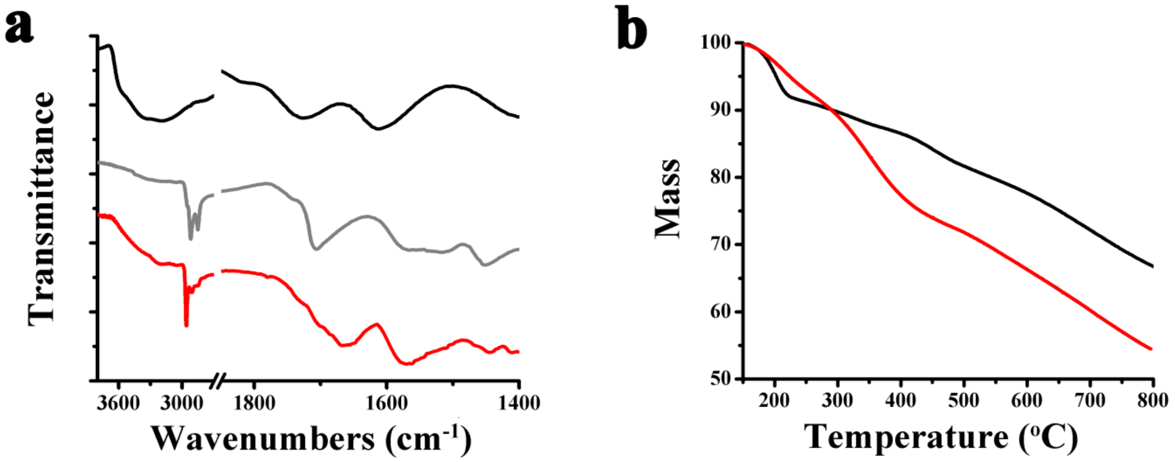

Figure 3.1 ATR-IR spectra for GO (black), BOC-modified graphene (grey), and ammonium functionalized *f*-G (red), and (b) Thermographs for GO (black) and ammonium functionalized *f*-G (red).

The morphology of Ag_{NCs}/*f*-G and Au_{NCs}/*f*-G ensembles as well as of the bare Ag_{NCs} and Au_{NCs} was imaged by scanning transmission electron microscopy (STEM) means. For the analysis, the sample was dropped onto a molybdenum microgrid coated with a holey amorphous carbon film. Evidently, round monodispersed nanoclusters with a diameter of 2.2 and 1.5 nm in average were identified by annular dark-field (ADF) STEM images, and proved to be Ag_{NCs} and Au_{NCs} by energy-dispersive X-ray spectroscopy (EDX), respectively (Figure 3.2a and b). Assuming Ag_{NCs}

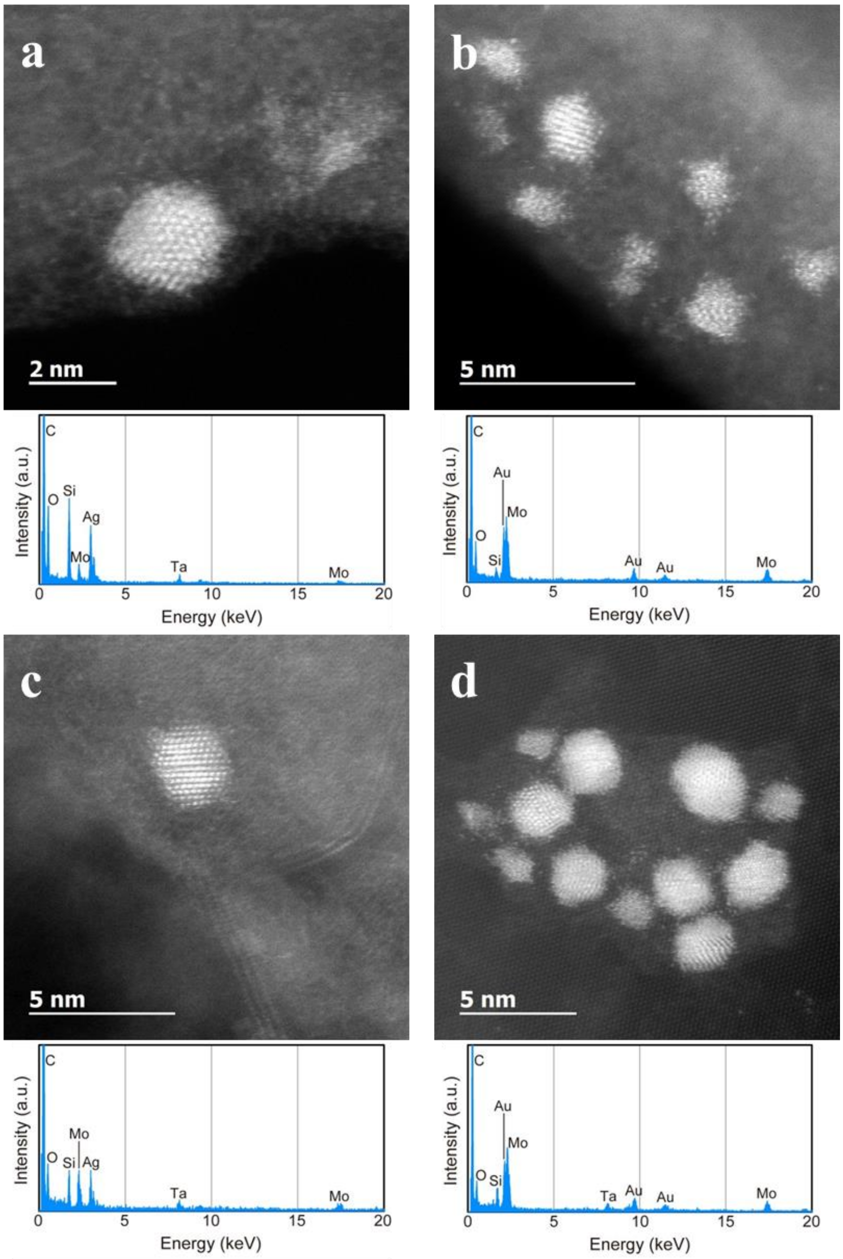

Figure 3.2 ADF-STEM images and EDX spectra of (a) $\mathrm{Ag_{NCs}}$, (b) $\mathrm{Au_{NCs}}$, (c) $\mathrm{Ag_{NCs}}$/*f*-G, and (d) $\mathrm{Au_{NCs}}$/*f*-G ensembles. EDX signals of Ta and Mo are from the materials of the specimen holder and microgrids, respectively, and that of Si is from impurity.

and $\mathrm{Au_{NCs}}$ as spherical nanocrystals with such average diameters, the numbers of atoms constituting single nanoclusters were estimated to be around $3\text{x}10^2$ and $1\text{x}10^2$, respectively. Analogously, ADF-STEM images of $\mathrm{Ag_{NCs}}$/*f*-G and $\mathrm{Au_{NCs}}$/*f*-G ensembles revealed the decoration of graphene sheets with round clusters possessing average diameters of 2.5 and 2 nm (Figure 3.2c and d), respectively. These round species imaged onto the graphene sheets found to be Ag and Au according to EDX. The estimated number of Ag and Au atoms in single nanoclusters was about $5\text{x}10^2$ and $2\text{x}10^2$, respectively, assuming spherical nanocrystals with the average diameters given above. In addition, the hexagonal lattice of multi-layered graphene domains is also visible, as shown in Figure 3.2d.

Figure 3.3a depicts the absorption and fluorescence spectra of bare Ag_{NCs}. Two distinct absorption bands were identified, with peaks located at 425 and 500 nm, which are characteristically different with the ones owed to the surface plasmon resonance absorption existing in larger silver nanoparticles, with diameter > 5 nm, in the region of 380-420 nm.[37] On the other hand, the emission spectrum of bare Ag_{NCs} showed a maximum at 675 nm upon excitation at 430 nm, in full agreement with other Ag_{NCs} stabilized with different thiolate ligands.[38] Hence, the electronic absorption and photoluminescence spectra confirm that the developed Ag_{NCs} exhibit molecular-like activity with discrete electronic transitions. Similar were the optical properties of Au_{NCs} as shown in Figure 3.3b. Evidently, the absence of the surface plasmon absorption band, which is located at around 520 nm for large gold nanoparticles,[37] signifies the successful formation of Au_{NCs}. Also, Au_{NCs} exhibit intense photoluminescence at 760 nm upon excitation at 420 nm.

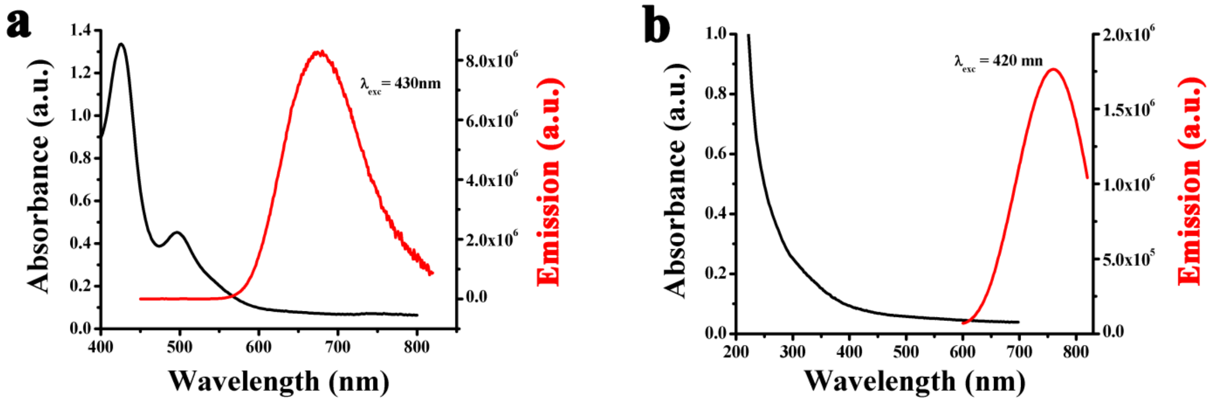

Figure 3.3 UV-Vis and photoluminescence spectra of (a) Ag_{NCs} (excitation wavelength 430 nm), and (b) Au_{NCs} (excitation wavelength 420 nm).

The effective electrostatic immobilization of Ag_{NCs} onto *f*-G en route to the preparation of Ag_{NCs}/*f*-G ensembles was realized by UV-Vis titration assays. In this frame, the development of an isosbestic point at 445 nm in the electronic absorption spectrum of Ag_{NCs} upon incremental additions of aqueous *f*-G was evident (Figure 3.4a). Furthermore, the characteristic absorption of Ag_{NCs} centered at 420 nm was gradually decreased, while the opposite trend was identified for the absorption band located at 500 nm, whereas at the same time both bands were broadened. Collectively, those observations are attributed to ground state electronic interactions between the two species within the Ag_{NCs}/*f*-G ensemble. Examining possible interactions at the excited state, photoluminescence titration measurements were performed, in which the characteristic emission of Ag_{NCs}, at 675 nm upon excitation at 430 nm, was found to gradually quench upon incremental additions of *f*-G (Figure 3.4b). The latter result manifests the presence of electron and/or energy transfer phenomena within the Ag_{NCs}/*f*-G ensembles. Analogously, titration of Au_{NCs} with *f*-G resulted on the development of an isosbestic point at 225 nm, followed by the broadening of the spectrum in the visible region (Figure 3.4c), denoting the effective formation of Au_{NCs}/*f*-G. Next, focusing on excited state properties of Au_{NCs}, photoillumination at

420 nm furnishes a strong emissive band centred at 760 nm. Initial insights into electron donor-acceptor interactions in the Au$_{NCs}$/*f*-G ensemble arose from photoluminescence assays. Fluorescence titration analyses revealed a gradual shift to higher wavelengths together with a decrease in the intensity of the Au$_{NCs}$ centred fluorescence for the various amounts of *f*-G added (Figure 3.4d). The observed fluorescence quenching in Au$_{NCs}$/*f*-G prompts to an additional decay channel from the excited state of Au$_{NCs}$ within the ensemble, namely charge and/or energy transfer.

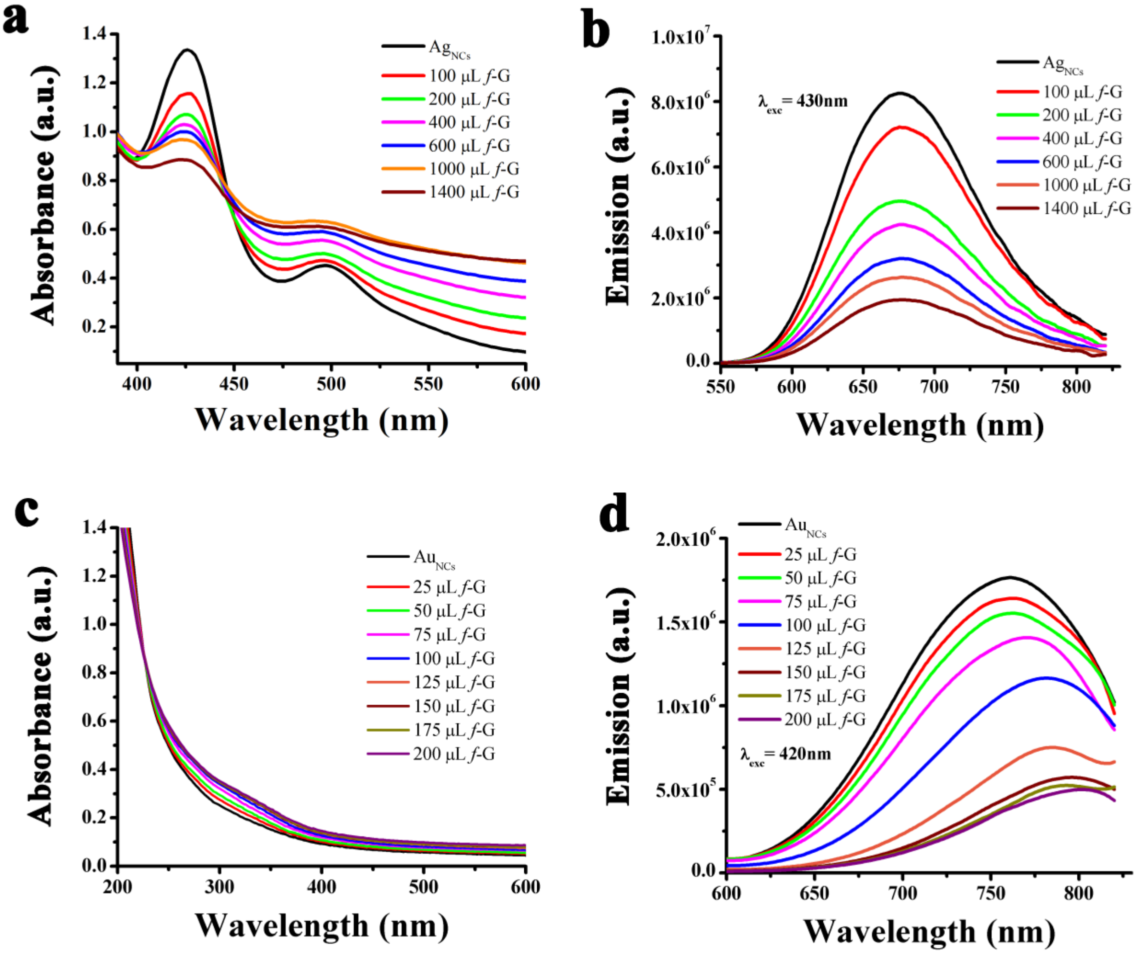

Figure 3.4 UV-Vis absorption (a and c) and photoluminescence (b and d) titration assay spectra for Ag$_{NCs}$ and Au$_{NCs}$, upon incremental additions of *f*-G.

3.2.3 Catalytic performance of M$_{NCs}$/*f*-G ensembles

Having identified the optical properties of Ag$_{NCs}$/*f*-G and Au$_{NCs}$/*f*-G ensembles and in conjunction with the unique characteristics of graphene, in terms of high surface area and charge-transport properties, the catalytic ability of Ag$_{NCs}$/*f*-G and Au$_{NCs}$/*f*-G ensembles for the reduction of 4-nitrophenol was scrutinized. The catalytic efficiencies of Ag$_{NCs}$/*f*-G and Au$_{NCs}$/*f*-G were examined and contrasted with those derived from stand-alone Ag$_{NCs}$, Au$_{NCs}$ and *f*-G to unveil differences and shed light on the mechanism of the process. The progress of the catalytic reduction reaction was monitored by UV–Vis spectroscopy as a function of the elapsed time. The first attempts to identify the formation of 4-aminophenol were negative – without observing changes in the absorption spectrum of 4-nitrophenol – demonstrating the inability of Ag_{NCs}/*f*-G or Au_{NCs}/*f*-G to catalyse the production of hydrogen from water. Nonetheless, when $NaBH_4$ was introduced as a hydride source in the reaction mixture, the success for the reduction in the absence of light was confirmed by the (a) concomitant increase in the intensity of a new absorption band at 310 nm, owed to 4-aminophenolate ions, followed by the gradual decrease of the corresponding band at 400 nm attributed to 4-nitrophenolate ions, and (b) fading of the yellow-greenish colour of the reaction mixture, which changes to colourless after the reaction was completed. Astonishingly, the reduction of 4-nitrophenol to 4-aminophenol decelerated by half when bare M_{NCs} as compared to M_{NCs}/*f*-G were employed (Figure 3.5a-d), hence, highlighting the beneficial role of graphene within the M_{NCs}/*f*-G ensembles for catalysing the reduction process. Comparing the catalytic efficiency between Ag_{NCs}/*f*-G and Au_{NCs}/*f*-G, a longer reaction time of 175 minutes (i.e. 5 times higher) was required to achieve the full reduction of 4-nitrophenol with the former ensembles (Figure 5.3b and d). Next, considering the significant photoinstability of silver, the catalytic efficiency of bare Au_{NCs} and Au_{NCs}/*f*-G ensemble was tested under visible light illumination (Figure 3.5e). Strikingly, the reaction kinetics for the transformation of 4-nitrophenolate to 4-aminophenolate was faster under photoirradiation as compared with the kinetics registered in the dark, since the complete transformation was achieved within 12 min by Au_{NCs}/*f*-G (Figure 3.5f) as compared to the 30 min required in the absence of light (Figure 3.5d). The latter corroborates the beneficial role of Au for the reduction of 4-nitrophenol under photocatalytic conditions, while the function of *f*-G as efficient electron and/or energy transfer mediator was also demonstrated.

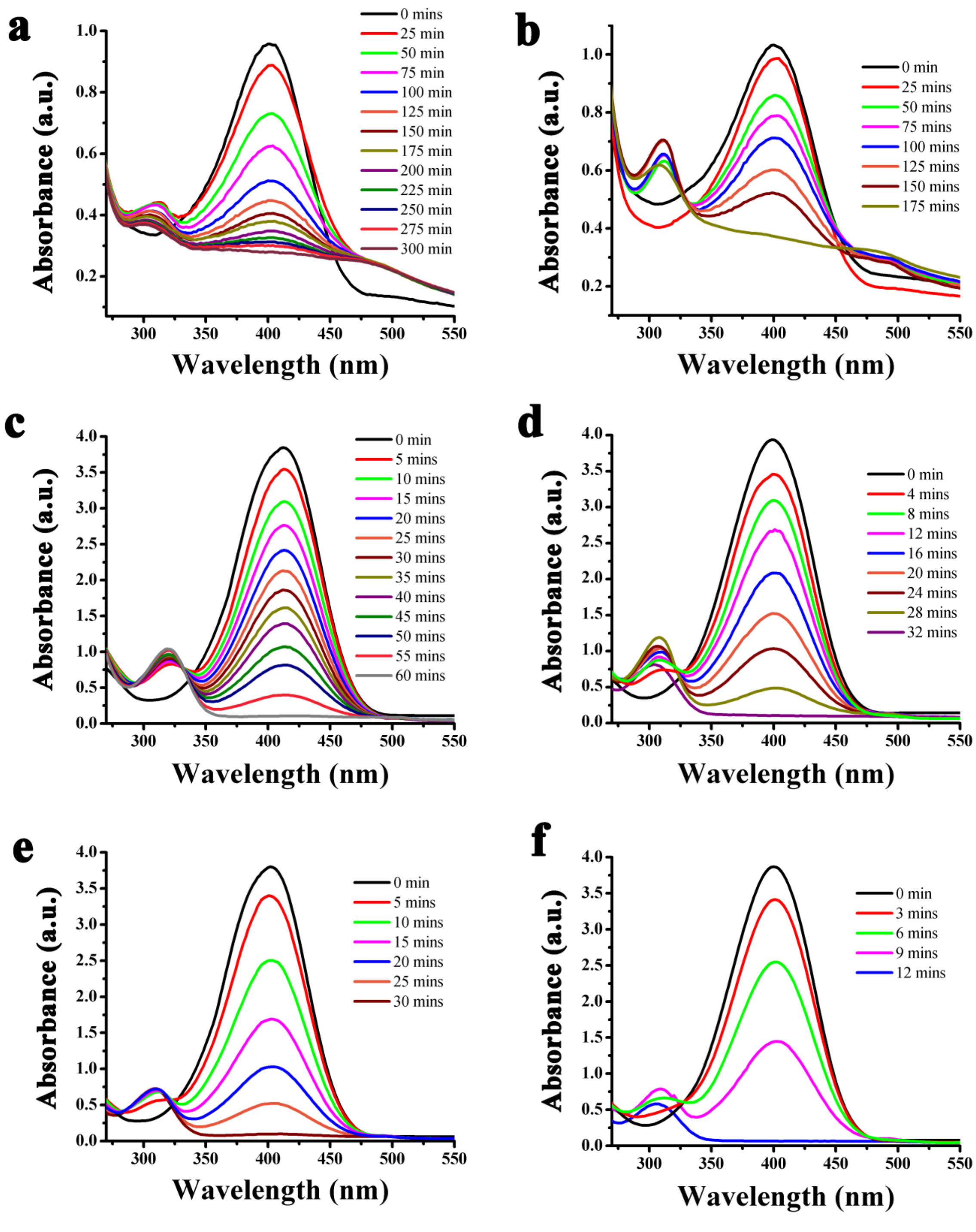

Figure 3.5 Evolution of UV-Vis absorption spectra for the reduction of 4-nitrophenol catalysed by (a) Ag_{NCs}, (b) Ag_{NCs}/*f*-G ensembles, (c) Au_{NCs}, and (d) Au_{NCs}/*f*-G ensembles, in H_2O containing $NaBH_4$ under dark conditions. Upon visible light illumination, the reduction of 4-nitrophenol proceeds with faster kinetics as depicted in the corresponding UV-Vis absorption spectra in the presence of (e) Au_{NCs}, and (f) Au_{NCs}/*f*-G ensembles.

Since industrial applications highly demand catalysts to be easily separable, stable and reusable without diminishing their catalytic activities, recyclability assays for M_{NCs}/*f*-G were performed. In this context, after completing the first run of the reduction of 4-nitrophenol, the Au_{NCs}/*f*-G or Ag_{NCs}/*f*-G catalyst, was retrieved by filtration and reused in a consecutive catalytic cycle. More than 15 cycles were performed for Au_{NCs}/*f*-G and Ag_{NCs}/*f*-G, both in dark and under light illumination for the former ensemble, without observing significant changes in the reaction time and activity. Notably, performing blank assays (a) in the absence of Au_{NCs}/*f*-G or Ag_{NCs}/*f*-G as catalyst, (b) in the absence of Au_{NCs} or Ag_{NCs} and the presence of only *f*-G, and (c) in the absence of $NaBH_4$ and the presence of Au_{NCs}/*f*-G or Ag_{NCs}/*f*-G, the UV-Vis spectrum of 4-nitrophenolate ion (or 4-nitrophenol for the third blank assay) was always acquired unaltered, thereby ascertaining the significance of M_{NCs}/*f*-G ensembles for catalyzing the reduction of 4-nitrophenol.

3.2.4 Mechanism for the reduction of 4-nitrophenol by Au_{NCs}/*f*-G ensembles

Materials based on gold metallic nanoparticles (Au_{NPs}) or semiconducting clusters (Au_{NCs}) participate in a variety of catalytic transformations under homo- or heterogeneous conditions. Whereas it is established that in general M_{NCs}-based materials boast photocatalytic activity towards redox reactions, the mechanisms promoting those processes remain still largely elusive. The catalytic activity observed in Au_{NCs}/*f*-G ensembles can be rationalized by the existing knowledge based on Au_{NPs}.[39] A key difference between metallic Au_{NPs} and semiconducting Au_{NCs} is the oxidation state of Au atoms. In Au_{NPs} the population of Au^0 atoms dominates the Au^+ cations and is responsible for the metallic character of these particles. In contrast to Au_{NPs}, the density of Au^+ species within Au_{NCs} is increased and comparable with the loading of Au^0 resulting to semiconducting behavior.[40-42] Markedly, variations in the Au^0/Au^+ ratio depend on the size of the clusters and the employed stabilizer. On the other hand, Au^+ species in the presence of a hydride (H^-) source, such as $NaBH_4$, readily form reactive Au-H intermediates (Scheme 3.2a), via dissociation of the B-H bond, thereby, acting as hydride transfer agents and catalyzing the reduction of 4-nitrophenol to the corresponding amine. As presented in Figure 3.5c, Au_{NCs} efficiently catalyze the reduction of 4-nitrophenol in the absence of light. Thus, according to the aforementioned discussion, the latter reaction proceeds via three hydride addition steps by Au-H intermediates, according to Scheme 3.2b. After each hydride attack to the nitro-species, the Au^+ is regenerated and completes the catalytic cycle, hence, being able to form a new Au-H species. The Au_{NCs}/*f*-G ensembles, developed upon electrostatic attractive interactions between the negatively charged Au_{NCs} and the positively charged *f*-G, showed a 2-fold increase in catalytic performance (cf. Figure 3.5d), attributed to the presence of *f*-G, which offers a high specific surface support, hence, allowing a fine distribution of the Au_{NCs} onto the carbon network and subsequently a superior dispersion of the aromatic nitro-species onto the graphene sheets via π-π interactions. Therefore, Au_{NCs}/*f*-G brings together the substrate and the reactive Au-H sites in the catalytic cycle, thus, benefits favorable reduction reaction. Similar phenomena exist also for Ag_{NCs} and Ag_{NCs}/*f*-G, when operating under dark conditions.

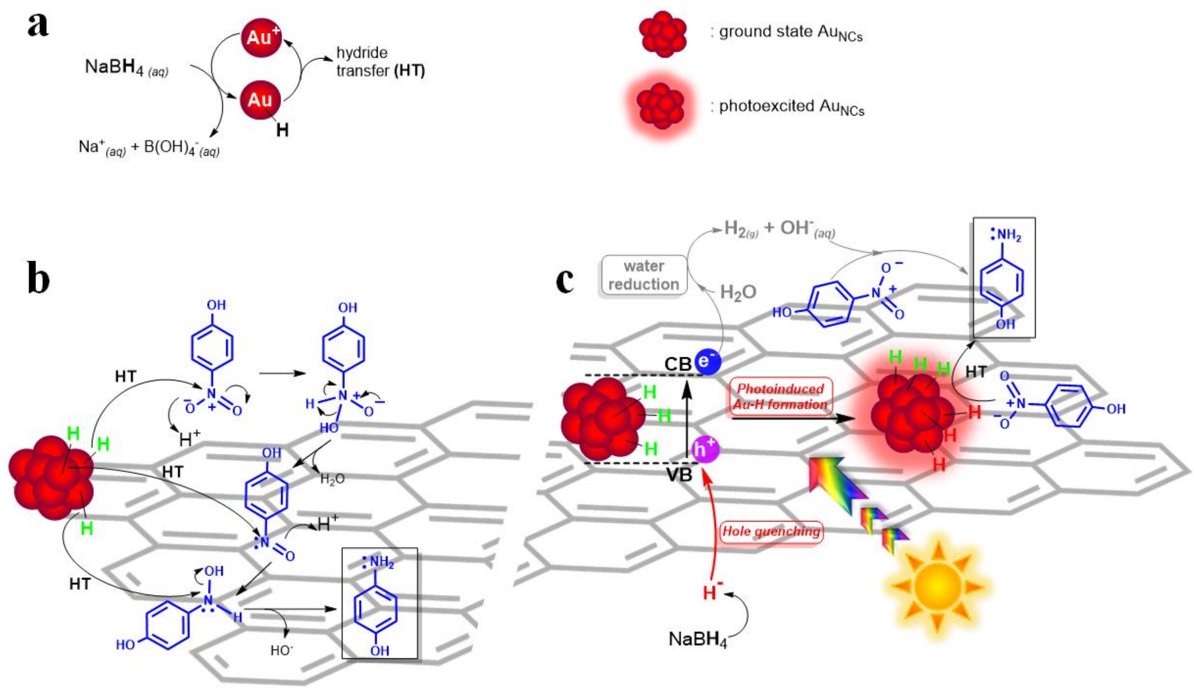

Scheme 3.2 (a) Formation of the reactive Au-H species onto the surface of Au$_{NCs}$. Reduction of 4-nitrophenol to the corresponding amine catalyzed by the Au$_{NCs}$/*f*-G ensembles via (b) hydride transfer from Au-H (green) species, operating under dark condition, and (c) synergistically promoted by (i) hydride transfer from Au-H (green) as well as photoinduced Au-H (red) species, and (ii) hydrogen evolved by transfer of electrons to water.

Next, examining for the first time the role of visible light irradiation on the catalytic performance of Au$_{NCs}$/*f*-G toward the reduction of 4-nitrophenol, the acceleration of the reduction reaction (cf. Figure 3.5e-f), which is strongly related to the photophysical properties of the semiconducting Au$_{NCs}$ species, is observed. In more detail, as it is illustrated in Scheme 3.2c, photoillumination of Au$_{NCs}$ initially yields an electron-hole pair. The holes (h^+) are effectively quenched by the hydrides (H^-) arising from the B-H bond dissociation across the Au$_{NCs}$ as described earlier. The injection of hydrides into the valence band of Au$_{NCs}$ boosts the formation of new Au-H intermediates, and therefore increases the density of the catalytic sites on the surface of the clusters, resulting to differences detected in the enhanced catalytic performance for the reduction of 4-nitrophenol in the presence vs the absence of light irradiation within Au$_{NCs}$/*f*-G (cf. Figure 3.5d and f). The conductive sp^2 sites of *f*-G, which efficiently stabilize the photogenerated holes within the Au$_{NCs}$, assist the injection of hydrides to the valence band of Au$_{NCs}$ and therefore promote the faster formation of Au-H species. Markedly, the quenching of the photogenerated holes by the highly reactive hydrides populates the valence band, hence, delaying the recombination of the electron-hole pair. Additionally, the photogenerated electrons may also follow a third channel, resulting in the reduction of water molecules present in the catalytic system, as it is demonstrated in Scheme 3.2c. Particularly the latter process is of great significance in terms of enabling the production of hydrogen from water mediated by Au$_{NCs}$, for which up to now are incompetent. Concluding, three possible pathways synergistically cooperate to the transformation of 4-

nitrophenol to 4-aminophenol by Au_{NCs}/*f*-G, namely, (a) hydride transfer from Au-H (both in the presence and absence of light), (b) hydride transfer from photogenerated Au-H, and (c) hydrogen generated by photoreduction of water. Currently, restrictions in adequate scale production of such nanocatalysts limit the realization of qualitative and quantitative techniques capable of clarifying all the intermediate products of the photocatalytic reaction. Furthermore, sophisticated instrumentation needs to be applied to distinguish the hydrogen gas evolving via the B-H bond cleavage and that from the photoinduced water reduction in the presence of Au_{NCs}/*f*-G ensembles. Nevertheless, we have attempted to produce evidence for the proposed quenching mechanism of the photogenerated holes by the hydrides derived from the dissociation of $NaBH_4$ onto the surface of Au_{NCs}. In a typical photoluminescence experiment of Au_{NCs}/*f*-G, the emission of Au_{NCs} is quenched by a factor depending on the quantity of the added *f*-G. According to the proposed mechanisms under visible light irradiation, the addition of $NaBH_4$ should quench the photogenerated holes of Au_{NCs} resulting to the total suppression of their emission, since recombination of the photogenerated charges is inhibited. Actually, the emission spectra recorded for bare Au_{NCs} and those supported on graphene sheets, namely Au_{NCs}/*f*-G, in the presence of $NaBH_4$ reveal the expected total emission quenching (Figure 3.6).

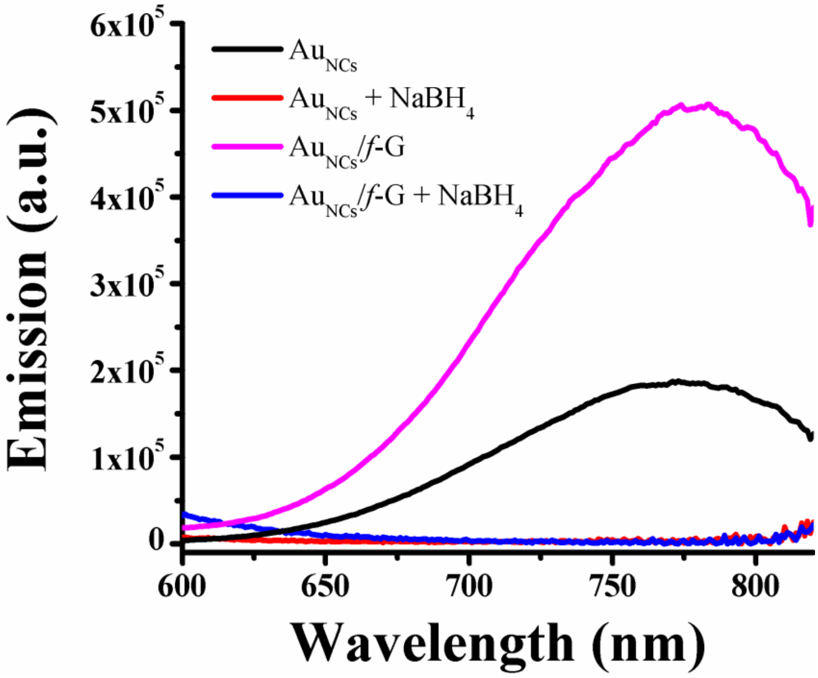

Figure 3.6 Photoluminescence spectra of Au_{NCs} (black) and Au_{NCs}/*f*-G ensembles (pink) with and without $NaBH_4$ (red and blue), respectively. For the acquisition of the spectrum for Au_{NCs}/*f*-G ensemble (pink) an additional 100 μL Au_{NCs} was added to the stock quenched dispersion.

The described photocatalytic activity should be also strongly dependent on the available catalytic sites and therefore a zero-order kinetics is expected, namely the reaction rate should be independent from the concentration of 4-nitrophenol and $NaBH_4$. It is noteworthy that the kinetic plots versus the reactions time, both in the absence and presence of light irradiation, for bare Au_{NCs} and Au_{NCs}/*f*-G, demonstrate a clear zero-order curve (Figure 3.7). In this work, the Au loading is not higher than 3% w/w based on 4-nitrophenol, allowing the recognition of this well zero-order kinetics of the catalytic reaction, which is unfamiliar in literature (Table 3.1), where the Au/4-nitrophenol w/w ratio varies from high (14%) to extremely high (12000%) values and meet first and quasi-first order kinetics.

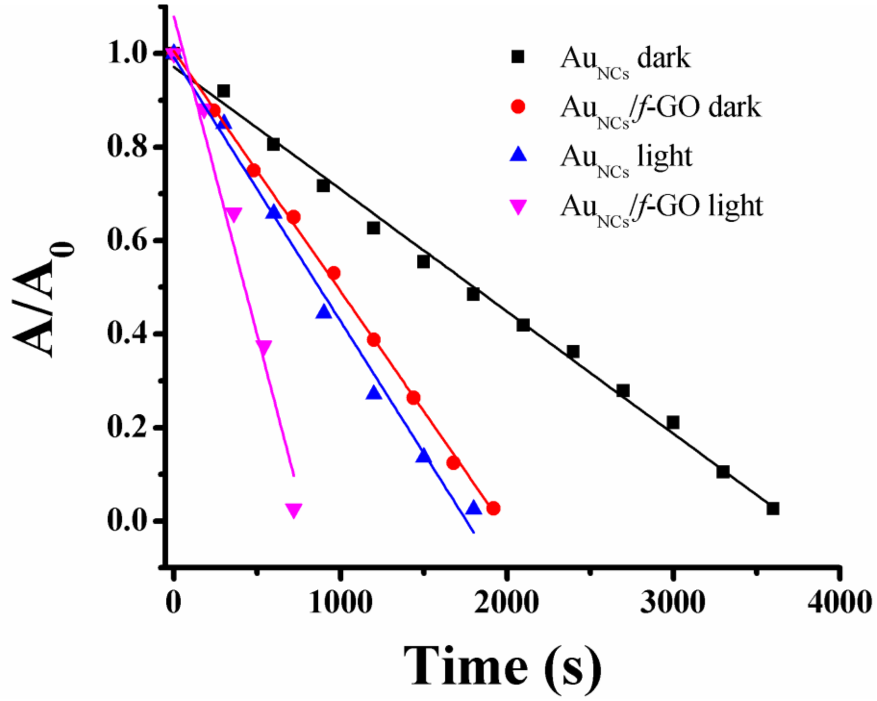

Figure 3.7 Kinetics for the reduction of 4-nitrophenol to 4-aminophenol, in the presence of bare Au_{NCs} (black, blue) and Au_{NCs}/*f*-G (red, green) in the dark and under visible light illumination conditions, respectively, as monitored from the nitrophenol peak at 400 nm.

Table 3.1 Collective data known in literature for Au/graphene-based catalysts for the reduction of 4-nitrophenol (4-NP) to 4-animophenol in the absence and presence of light irradiation.

Reference	**Metal Content**	**Graphene Content**	**$NaBH_4$ quantity**	**4-NP**	**4-NP/Au (% w/w)**	**Photo catalysis**	**Mechanism**	**Time (min)**	**k (s^{-1})**
This work	0.003 mg Au	0.012 mg	10 mg	0.1 mg	3%	YES	Zero-order	12	$6.0\text{x}10^{-4\ a}$
This work	0.003 mg Au	0.012 mg	10 mg	0.1 mg	3%	NO	Zero-order	32	$1.4\text{x}10^{-3\ a}$
J. Mater. Chem. 2012, 22, 8426-8430.	0.024 mg Au	0.076 mg	0.076 mg	0.039 mg	61%	NO	Pseudo-first	12	$3.17\text{x}10^{-3}$
Catal. Sci. Technol. 2011, 1, 1142-1144.	0.14 mg Au	-	6.05 mg	0.97 mg	14%	NO	Pseudo-first	27	0.002
Catal. Sci. Technol. 2011, 1, 1142-1144.	0.14 mg Au	0.5 mg	6.05 mg	0.97 mg	14%	NO	Pseudo-first	18	0.003
ACS Appl. Mater. Interfaces 2012, 4, 5472-5482.	12 mg AuNPs	1.32 g	18.915 mg	0.0974 mg	12320%	NO	Pseudo-first	5	$0.14\text{x}10^{-3}$
RSC Adv. 2016,6, 35945-35951.	0.5 mg Au	2.8 mg	0.1135 mg	0.21 mg	238%	NO	Pseudo-first	7	$9.87\text{x}10^{-3}$
RSC Adv. 2016,6, 64028-64038.	4.78 mg Au	-	47 mg	0.347 mg	1377%	NO	Pseudo-first	39	N/A
RSC Adv. 2016,6, 64028-64038.	4.78 mg Au	25 mg	47 mg	0.347 mg	1377%	NO	Pseudo-first	18	0.003
Pol. J. Chem. Tech. 2016, 18 (4), 47-55.	8 mg Au	8 mg	7.566 mg	0.417 mg	1918%	NO	Pseudo-first	50	$0.4\text{x}10^{-3}$
Pol. J. Chem. Tech. 2016, 18 (4), 47-55.	8 mg Ag	8 mg	7.566 mg	0.417 mg	1918%	NO	Pseudo-first	50	$0.7\text{x}10^{-3}$
Appl. Surf. Sci. 2016, 389, 1050-1055.	1.64 mg Au + 0.89 mg Ag	-	0.075 mg	1.95 mg	130%	NO	Pseudo-first	6	$3.47\text{x}10^{-3}$
Appl. Surf. Sci. 2016, 389, 1050-1055.	1.64 mg Au + 0.89 mg Ag	0.83 mg	0.075 mg	1.95 mg	130%	NO	Pseudo-first	6	$6.83\text{x}10^{-3}$

[a] The reaction rate coefficient is expressed in M s^{-1}.

3.4 Conclusions

Summarizing, innovative materials composed of metal nanoclusters based on Ag and Au immobilized onto functionalized graphene sheets forming M_{NCs}/*f*-G ensembles were successfully synthesized and characterized. Notably, we took advantage of the optical features of M_{NCs} to impart photoluminescence and facile surface tailorability bearing sensitive to pH –COOH units as parts of α-lipoic acid employed as stabilizer for the formation of the metal nanoclusters. On the other hand, graphene sheets decorated with positively charged ammonium units were prepared following standard chemical transformations. Hence, at alkaline pH conditions, the negatively ionized M_{NCs} were efficiently attracted via Coulombic forces by the positively charged *f*-G. Titration assays monitored by absorption and photoluminescence verified the effective realisation of M_{NCs}/*f*-G ensembles. The photoinduced donor-acceptor function of the M_{NCs}/*f*-G materials was deduced attributed to the quenching of M_{NCs} photoluminescence by the presence of *f*-G, which designated the development of charge electron and/or energy transfer phenomena between the two components. Markedly, for the first time, both Ag_{NCs}/*f*-G and Au_{NCs}/*f*-G ensembles were successfully employed as proficient catalysts for the reduction of 4-nitrophenol to the corresponding 4-aminophenol. Particularly, Au_{NCs}/*f*-G displayed exceptionally higher catalytic activity both in dark and under light irradiation conditions in comparison to Ag_{NCs}/*f*-G. The use of M_{NCs}/*f*-G ensembles as (photo)catalysts for the reduction of 4-nitrophenol possesses several merits: (a) the ease to monitor the progression of the reaction as a function of time, by employing electronic absorption spectroscopy assays, with the advantage of lacking overlapping of absorption peaks owed to M_{NCs}, (b) the facile procedure for the preparation of M_{NCs}/*f*-G ensembles and the meagre quantity of metal precursor employed, rendering the catalytic system inexpensive, and (c) the recovery and re-employment of M_{NCs}/*f*-G in subsequent catalytic cycles with the same efficiency.

Finally, the deep understanding on the mechanisms taking place in the presence and absence of light illumination is critical for the engineering of such M_{NCs}/*f*-G ensembles and related devices. Particularly, acknowledging the data collected from the photophysical and kinetic studies of the catalytic reactions, we ascribe the enhanced photocatalytic activity of Au_{NCs}/*f*-G to three synergistic mechanisms, namely, (a) hydride transfer from Au-H, (b) hydride transfer from photogenerated Au-H species, and (c) hydrogen produced by the photoreduction of water. The high specific surface area of *f*-G benefits the fine distribution of Au_{NCs} onto the graphene network and subsequently a superior dispersion of the aromatic nitro-compound onto the graphene sheets through π-π interactions is realized. Moreover, the conductive sp^2 sites of *f*-G efficiently stabilize the photogenerated holes within the Au_{NCs} and assist the formation of photoinduced Au-H species. At this point, it should be noted that photoinduced electrons generated by Au_{NCs} may be efficiently transferred to *f*-G, within the Au_{NCs}/*f*-G ensembles, before employed for reducing water and evolve hydrogen.

It is expected that the deeper understanding of the quenching mechanism of the photogenerated holes within Au_{NCs} will prompt to identify pathways leading to the production of hydrogen by pristine or supported Au_{NCs}. Considering that organic fluorophores are susceptible to photobleaching and fluorescent semiconductor quantum dots are generally composed of toxic elements, the utility of M_{NCs}/*f*-G is of great importance. Without a doubt, M_{NCs}/*f*-G as photocatalysts can pave the way for further advancing this nascent class of materials towards the detection of a variety of chemical analytes and other technological explorations.

3.3 Experimental section

3.3.1 General

All solvents and reagents were purchased from Aldrich and used without further purification unless otherwise stated. Thermogravimetric analysis was performed using a TGA Q500 V20.2 Build 27 instrument by TA in a nitrogen (purity >99.999%) inert atmosphere at a heating rate of 10 ^{o}C/min. Mid-infrared spectra in the region 500−4500 cm^{-1} were obtained on a Fourier transform IR spectrometer (Equinox 55 from Bruker Optics) equipped with a single reflection diamond ATR accessory (DuraSamp1IR II by SensIR Technologies). Steady state electronic absorption spectra were recorded on a Perkin-Elmer (Lambda 19) UV–Vis spectrophotometer. Steady state emission spectra were recorded on a Fluorolog-3 JobinYvon-Spex spectrofluorometer (model GL3-21). The light source used was a 500 W Xenon lamp, which was positioned 20 cm away from the reactor. Scanning transmission electron microscopy (STEM) analysis was performed on a JEOL JEM-2100F electron microscope equipped with double JEOL Delta spherical aberration correctors operated at an electron accelerating voltage of 60 kV. For the analysis, the samples were dropped onto a molybdenum microgrid coated with a holey amorphous carbon film. Energy dispersive X-ray spectroscopy (EDX) measurements were carried out using double JEOL Centurio detectors installed to the electron microscope.

3.3.2 Synthesis of M_{NCs}

Ag_{NCs}. The preparation of Ag_{NCs} was based on previously reported methods.[38, 43-44] In a typical experiment, α-lipoic acid (19 mg, 0.09 mmol) was dissolved in HPLC grade H_2O (14 mL) were placed into a flask. Subsequently, $NaBH_4$ (7.0 mg, 0.18 mmol) was added dropwise under stirring until the solution became transparent (15 min). Afterwards, aqueous $AgNO_3$ (700 μL, 25 mM) was added into the reaction mixture while stirring and the solution turned into dark red. To this mixture, an excess of a freshly prepared aqueous $NaBH_4$ (10 mg to 2 mL water) was added dropwise and a dark brown solution developed. The flask was wrapped with aluminium foil to minimize the influence of light. A bright orange solution obtained after 4-5 hours stirring at room temperature, indicating the completion of the Ag_{NCs} growth. The as-prepared Ag_{NCs} were stored in dark.

Au$_{NCs}$. The preparation of Au$_{NCs}$ was adapted from previously described procedures.[42, 45] Typically, α-lipoic acid (6.2 mg, 30 μmol) was dissolved in HPLC grade H_2O (20 mL), in which the pH was previously adjusted to 11 with aqueous NaOH (1M). Then, addition of an aqueous $HAuCl_4$ (4.2 mg in 200 μL water) was followed and the reaction was stirred until the reaction mixture became colourless. Afterwards, a freshly prepared aqueous $NaBH_4$ (0.8 mg to 400 μL water) was added dropwise and the solution color immediately turned into brown. The reaction proceeded for 16 h at RT and the solution colour changed from dark brown into pale brown indicating the effective growth of Au$_{NCs}$.

3.3.3 Functionalization of graphene

Initially, graphite powder was oxidized following a modified Hummers and Offeman's method.[46] Then, oxidized graphene (20 mg) was activated by treatment with $SOCl_2$ (6 mL) at 70 ^oC for 24 hours under nitrogen atmosphere. After that period, the excess $SOCl_2$ was evaporated under reduced pressure and the remaining solid was washed with dry THF under nitrogen to remove residual $SOCl_2$. Afterwards, *N*-tert-butoxycarbonyl-2,2′-(ethylenedioxy)bis-(ethylamine) (300 mg) was added in dry THF (5 mL) and the reaction mixture was refluxed for 3 days. After that period, the reaction mixture was filtered over a PTFE membrane filter (0.2 μm pore size) and extensively washed with CH_2Cl_2 for several times to remove organic residues and dried at room temperature overnight under vacuum. Next, the material was dispersed in dry CH_2Cl_2 and treated with gaseous HCl to cleave the *N*-tert-butoxycarbonyl moieties and liberate free amine units. After a period of 24 hours, the solvent was evaporated to dryness and the solid material was washed with CH_2Cl_2 and dried to yield water-dispersible *f*-G.

3.3.4 Preparation of M$_{NCs}$/*f*-G ensembles

An aqueous solution of M$_{NCs}$was titrated with aqueous *f*-G (1 mg/mL) and the formation of Ag$_{NCs}$/*f*-G and Au$_{NCs}$/*f*-G ensembles was verified by electronic absorption and fluorescence emission spectroscopy assays.

3.3.5 Catalytic reduction of 4-nitrophenol

In a typical experiment, 4-nitrophenol (20 μL, 3.6 mM), 42 μL Au$_{NCs}$/*f*-G (5:2 volume ratio) were dissolved in 3 mL water and excess $NaBH_4$ (10 mg) was introduced to the quartz cuvette under stirring. The progress of the reaction was monitored by UV-Vis absorption at different time intervals.

References

1. Jin, R., Quantum sized, thiolate-protected gold nanoclusters. *Nanoscale* **2010,** *2* (3), 343-362.
2. Lu, Y.; Chen, W., Sub-nanometre sized metal clusters: from synthetic challenges to the unique property discoveries. *Chem. Soc. Rev.* **2012,** *41* (9), 3594-3623.
3. Schmid, G., The relevance of shape and size of Au_{55} clusters. *Chem. Soc. Rev.* **2008,** *37* (9), 1909-1930.
4. Corma, A.; Concepción, P.; Serna, P., A Different Reaction Pathway for the Reduction of Aromatic Nitro Compounds on Gold Catalysts. *Angew. Chem.* **2007,** *46* (38), 7266-7269.
5. Shang, L.; Dong, S.; Nienhaus, G. U., Ultra-small fluorescent metal nanoclusters: Synthesis and biological applications. *Nano Today* **2011,** *6* (4), 401-418.
6. Chen, Y.-S.; Kamat, P. V., Glutathione-Capped Gold Nanoclusters as Photosensitizers. Visible Light-Induced Hydrogen Generation in Neutral Water. *J. Am. Chem. Soc.* **2014,** *136* (16), 6075-6082.
7. Fang, J.; Zhang, B.; Yao, Q.; Yang, Y.; Xie, J.; Yan, N., Recent advances in the synthesis and catalytic applications of ligand-protected, atomically precise metal nanoclusters. *Coord. Chem. Rev.* **2016,** *322*, 1-29.
8. Luo, Z.; Zheng, K.; Xie, J., Engineering ultrasmall water-soluble gold and silver nanoclusters for biomedical applications. *Chem. Commun.* **2014,** *50* (40), 5143-5155.
9. Li, G.; Jin, R., Atomically Precise Gold Nanoclusters as New Model Catalysts. *Acc. Chem. Res.* **2013,** *46* (8), 1749-1758.
10. Xu, H.; Suslick, K. S., Water-Soluble Fluorescent Silver Nanoclusters. *Adv. Mater.* **2010,** *22* (10), 1078-1082.
11. Koklioti, M. A.; Tagmatarchis, N., Hybrids of Metal Nanoclusters and Graphene-Based Materials: Preparation, Properties and Applications. *ChemNanoMat* **2016,** *2* (12), 1065-1072.
12. Chen, Y.; Shen, Y.; Sun, D.; Zhang, H.; Tian, D.; Zhang, J.; Zhu, J.-J., Fabrication of a dispersible graphene/gold nanoclusters hybrid and its potential application in electrogenerated chemiluminescence. *Chem. Commun.* **2011,** *47* (42), 11733-11735.
13. Yuan, D.; Chen, S.; Yuan, R.; Zhang, J.; Zhang, W., An electrogenerated chemiluminescence sensor prepared with a graphene/multiwall carbon nanotube/gold nanocluster hybrid for the determination of phenolic compounds. *Analyst* **2013,** *138* (20), 6001-6006.
14. Xu, H.; Zhu, H.; Sun, M.; Yu, H.; Li, H.; Ma, F.; Wang, S., Graphene oxide supported gold nanoclusters for the sensitive and selective detection of nitrite ions. *Analyst* **2015,** *140* (5), 1678-1685.
15. Xiaofei, W.; Ruiyi, L.; Zaijun, L.; Junkang, L.; Guangli, W.; Zhiguo, G., Synthesis of double gold nanoclusters/graphene oxide and its application as a new fluorescence probe for Hg^{2+} detection with greatly enhanced sensitivity and rapidity. *RSC Adv.* **2014,** *4* (48), 24978-24985.

16. Nguyen, P.-D.; Cong, V. T.; Baek, C.; Min, J., Fabrication of peptide stabilized fluorescent gold nanocluster/graphene oxide nanocomplex and its application in turn-on detection of metalloproteinase-9. *Biosens. Bioelectron.* **2017,** *89, Part 1,* 666-672.

17. Wang, C.; Li, J.; Amatore, C.; Chen, Y.; Jiang, H.; Wang, X.-M., Gold Nanoclusters and Graphene Nanocomposites for Drug Delivery and Imaging of Cancer Cells. *Angew. Chem.* **2011,** *50* (49), 11644-11648.

18. Fan, D.; Zhu, J.; Liu, Y.; Wang, E.; Dong, S., Label-free and enzyme-free platform for the construction of advanced DNA logic devices based on the assembly of graphene oxide and DNA-templated AgNCs. *Nanoscale* **2016,** *8* (6), 3834-3840.

19. Liu, X.; Wang, F.; Aizen, R.; Yehezkeli, O.; Willner, I., Graphene Oxide/Nucleic-Acid-Stabilized Silver Nanoclusters: Functional Hybrid Materials for Optical Aptamer Sensing and Multiplexed Analysis of Pathogenic DNAs. *J. Am. Chem. Soc.* **2013,** *135* (32), 11832-11839.

20. Wang, Y.; Chen, J.-T.; Yan, X.-P., Fabrication of Transferrin Functionalized Gold Nanoclusters/Graphene Oxide Nanocomposite for Turn-On Near-Infrared Fluorescent Bioimaging of Cancer Cells and Small Animals. *Anal. Chem.* **2013,** *85* (4), 2529-2535.

21. Tao, Y.; Lin, Y.; Huang, Z.; Ren, J.; Qu, X., DNA-templated silver nanoclusters-graphene oxide nanohybrid materials: a platform for label-free and sensitive fluorescence turn-on detection of multiple nucleic acid targets. *Analyst* **2012,** *137* (11), 2588-2592.

22. Wang, Z.-L.; Yan, J.-M.; Wang, H.-L.; Ping, Y.; Jiang, Q., Au@Pd core-shell nanoclusters growing on nitrogen-doped mildly reduced graphene oxide with enhanced catalytic performance for hydrogen generation from formic acid. ***J****. Mater. Chem. A* **2013,** *1* (41), 12721-12725.

23. Peng, S.; Liu, J.; Zhang, J.; Wang, F., An improved preparation of graphene supported ultrafine ruthenium (0) NPs: Very active and durable catalysts for H_2 generation from methanolysis of ammonia borane. *Int. J. Hydrogen Energy* **2015,** *40* (34), 10856-10866.

24. Yi, S.; Zhuang, W.-Q.; Wu, B.; Tay, S. T.-L.; Tay, J.-H., Biodegradation of p-Nitrophenol by Aerobic Granules in a Sequencing Batch Reactor. *Environ. Sci. Technol.* **2006,** *40* (7), 2396-2401.

25. Sun, S.-P.; Lemley, A. T., p-Nitrophenol degradation by a heterogeneous Fenton-like reaction on nano-magnetite: Process optimization, kinetics, and degradation pathways. *J. Mol. Catal. A: Chem.* **2011,** *349* (1–2), 71-79.

26. Li, J.; Nasaruddin, R. R.; Feng, Y.; Yang, J.; Yan, N.; Xie, J., Tuning the Accessibility and Activity of $Au_{25}(SR)_{18}$ Nanocluster Catalysts through Ligand Engineering. *Chem. Eur. J.* **2016,** *22* (42), 14816-14820.

27. Shivhare, A.; Ambrose, S. J.; Zhang, H.; Purves, R. W.; Scott, R. W. J., Stable and recyclable Au_{25} clusters for the reduction of 4-nitrophenol. *Chem. Commun.* **2013,** *49* (3), 276-278.

28. Qian, H.; Zhu, M.; Wu, Z.; Jin, R., Quantum Sized Gold Nanoclusters with Atomic Precision. *Acc. Chem. Res.* **2012,** *45* (9), 1470-1479.

29. Li, M.-B.; Tian, S.-K.; Wu, Z.; Jin, R., Peeling the Core–Shell Au_{25} Nanocluster by Reverse Ligand-Exchange. *Chem. Mater.* **2016,** *28* (4), 1022-1025.

30. Yamamoto, H.; Yano, H.; Kouchi, H.; Obora, Y.; Arakawa, R.; Kawasaki, H., N,N-Dimethylformamide-stabilized gold nanoclusters as a catalyst for the reduction of 4-nitrophenol. *Nanoscale* **2012,** *4* (14), 4148-4154.

31. Stergiou, A.; Tagmatarchis, N., Fluorene–Perylene Diimide Arrays onto Graphene Sheets for Photocatalysis. *ACS Appl. Mater. Interfaces* **2016,** *8* (33), 21576-21584.

32. Li, J.; Liu, C.-y.; Liu, Y., Au/graphene hydrogel: synthesis, characterization and its use for catalytic reduction of 4-nitrophenol. *J. Mater. Chem. A* **2012,** *22* (17), 8426-8430.

33. Zhang, M.; Lu, X.; Wang, H.-Y.; Liu, X.; Qin, Y.; Zhang, P.; Guo, Z.-X., Porous gold nanoparticle/graphene oxide composite as efficient catalysts for reduction of 4-nitrophenol. *RSC Adv.* **2016,** *6* (42), 35945-35951.

34. Adhikari, B.; Biswas, A.; Banerjee, A., Graphene Oxide-Based Hydrogels to Make Metal Nanoparticle-Containing Reduced Graphene Oxide-Based Functional Hybrid Hydrogels. *ACS Appl. Mater. Interfaces* **2012,** *4* (10), 5472-5482.

35. Cao, X.; Yan, S.; Hu, F.; Wang, J.; Wan, Y.; Sun, B.; Xiao, Z., Reduced graphene oxide/gold nanoparticle aerogel for catalytic reduction of 4-nitrophenol. *RSC Adv.* **2016,** *6* (68), 64028-64038.

36. Yang, J.; Xia, N.; Wang, X.; Liu, X.; Xu, A.; Wu, Z.; Luo, Z., One-pot one-cluster synthesis of fluorescent and bio-compatible Ag_{14} nanoclusters for cancer cell imaging. *Nanoscale* **2015,** *7* (44), 18464-18470.

37. Ristig, S.; Prymak, O.; Loza, K.; Gocyla, M.; Meyer-Zaika, W.; Heggen, M.; Raabe, D.; Epple, M., Nanostructure of wet-chemically prepared, polymer-stabilized silver-gold nanoalloys (6 nm) over the entire composition range. *J. Mater. Chem. B* **2015,** *3* (23), 4654-4662.

38. Chen, W.-T.; Hsu, Y.-J.; Kamat, P. V., Realizing Visible Photoactivity of Metal Nanoparticles: Excited-State Behavior and Electron-Transfer Properties of Silver (Ag_8) Clusters. *J. Phys. Chem. Lett* **2012,** *3* (17), 2493-2499.

39. Stratakis, M.; Garcia, H., Catalysis by Supported Gold Nanoparticles: Beyond Aerobic Oxidative Processes. *Chem. Rev.* **2012,** *112* (8), 4469-4506.

40. Stamplecoskie, K. G.; Chen, Y.-S.; Kamat, P. V., Excited-State Behavior of Luminescent Glutathione-Protected Gold Clusters. *J. Phys. Chem. C* **2014,** *118* (2), 1370-1376.

41. Zhou, C.; Sun, C.; Yu, M.; Qin, Y.; Wang, J.; Kim, M.; Zheng, J., Luminescent Gold Nanoparticles with Mixed Valence States Generated from Dissociation of Polymeric Au(I) Thiolates. *J. Phys. Chem. C* **2010,** *114* (17), 7727-7732.

42. Shang, L.; Azadfar, N.; Stockmar, F.; Send, W.; Trouillet, V.; Bruns, M.; Gerthsen, D.; Nienhaus, G. U., One-Pot Synthesis of Near-Infrared Fluorescent Gold Clusters for Cellular Fluorescence Lifetime Imaging. *Small* **2011,** *7* (18), 2614-2620.

43. Patrick, T. K. C.; Marte van der, L.; Elleke, J. v. H.; Arjan, B.; Marcus, T. M. R.; Abraham, J. K.; Fijs, W. B. v. L.; Celso de Mello, D.; Albert, J. R. H.; Andries, M., Enhanced luminescence of Ag nanoclusters via surface modification. *Nanotechnology* **2013,** *24* (7), 075703.

44. Adhikari, B.; Banerjee, A., Facile Synthesis of Water-Soluble Fluorescent Silver Nanoclusters and Hg^{II} Sensing. *Chem. Mater.* **2010,** *22* (15), 4364-4371.

45. Wang, T.; Wang, D.; Padelford, J. W.; Jiang, J.; Wang, G., Near-Infrared Electrogenerated Chemiluminescence from Aqueous Soluble Lipoic Acid Au Nanoclusters. *J. Am. Chem. Soc.* **2016,** *138* (20), 6380-6383.

46. Hummers, W. S.; Offeman, R. E., Preparation of Graphitic Oxide. *J. Am. Chem. Soc.* **1958,** *80* (6), 1339-1339.

Chapter 4

Silver nanoparticle/transition metal dichalcogenide hybrids as surface enhanced Raman scattering platforms

Abstract

The modification of transition metal dichalcogenides (TMDs), incorporating nitrogen doping and silver nanoparticles (Ag_{NPs}) decoration on the skeleton of exfoliated MoS_2 and WS_2 was accomplished. The preparation of N-doped and Ag_{NPs} decorated TMDs involved an one-pot treatment procedure in a vacuum sputtering chamber under nitrogen plasma conditions and in the presence of a silver cathode as the source. Two different deposition times, 5 and 10 s, respectively, were applied to obtain N-doped with Ag_{NPs} decorated MoS_2 and WS_2 hybrids, abbreviated as N5-MoS_2/Ag_{NPs}, N10-MoS_2/Ag_{NPs}, N5-WS_2/Ag_{NPs} and N10-WS_2/Ag_{NPs}, respectively, for each functionalization time. The successful incorporation of nitrogen as dopant within the lattice of exfoliated MoS_2 and WS_2 as well as the deposition of Ag_{NPs} on their surface, yielding N-MoS_2/Ag_{NPs} and N-WS_2/Ag_{NPs}, was manifested through extensive X-ray photoelectron spectroscopy measurements. The observation of peaks at ~398 eV derived from covalently bonded nitrogen and the evolution of a doublet of peaks at ~370 eV guaranteed the presence of Ag_{NPs} in the modified TMDs. Also, the morphology of N-MoS_2/Ag_{NPs} and N-WS_2/Ag_{NPs} was examined by transmission electron microscopy, which proved that silver deposition resulted in nanoparticles growth, rather than creation of a continuous metal film on the TMD sheets. Next, the newly developed hybrid materials were attested as efficient surface enhanced Raman scattering (SERS) platforms by achieving the detection of Rhodamine B (RhB). Markedly, N10-MoS_2/Ag_{NPs} showed the highest sensitivity for detecting RhB at concentration as low as 10^{-9} M. Charge-transfer interactions between RhB and the modified TMDs, together with the polarized character of the system causing dipole-dipole coupling interactions, were determined as the main mechanisms to induce the Raman scattering enhancement. Finally, polycyclic aromatic hydrocarbons such as pyrene, anthracene and 2,3-dihydroxy naphthalene, coordinated via π-S interactions with N-MoS_2/Ag_{NPs}, were screened with high sensitivity and reproducibility. These findings highlight the excellent functionality of the newly developed N-MoS_2/Ag_{NPs} and N-WS_2/Ag_{NPs} hybrid materials as SERS substrates for sensing widespread organic and environmental pollutants as well as carcinogen and mutagen species.

4.1 Introduction

Transition metal dichalcogenides (TMDs) are at the forefront of the current research investigations of 2D layered materials beyond graphene, especially for energy applications.[1-3] Their attractiveness has become increasingly apparent, as they are undoubtedly about to have their own share of extraordinary capabilities, contrasting those of their bulk counterparts and complementing those of graphene. Molybdenum and tungsten disulfide, MoS_2 and WS_2, respectively, are typical examples of TMDs with structural properties similar to graphene – atomic layered structure – and unique chemical and optoelectronical attributes.[4] Various methodologies for exfoliating TMDs from the bulk powder have already been developed, mainly based on wet chemistry approaches that give access to mass production of material suitable for basic research and proof-of-concept studies. In this frame, liquid exfoliation assisted by sonication,[5-9] either in the presence or absence of intercalant species, is considered among the most applied routes for obtaining few-layered TMD sheets. However, in order to fully harness their potential, chemical functionalization[10-13] is an absolute necessity for opening up unique opportunities and broaden their applications. Especially, interfacing delaminated layers of TMDs with surface adatoms, for example metal nanoparticles, is anticipated to pave the way for their establishment in rational applications, from which chemical sensing through Raman enhancement signal is considered among the most exciting ones.[14-16]

Raman spectroscopy is one of the most powerful and ultrasensitive techniques for materials structural characterization. However, application of Raman spectroscopy meets constraints due to weak Raman scattering and highly fluorescent signals, particularly when examining organic molecules.[17] Nevertheless, in recent years, the development of the surface-enhanced Raman scattering (SERS) technique, in which the Raman signal is enhanced by several orders of magnitude when metal nanoparticles are adsorbed onto roughened surfaces,[15] has received significant attention. Subsequently, the expansion of SERS boosted the applicability of the spectroscopic technique, especially as a nanoscale tool for bioanalysis, owed to the unique vibrational fingerprints of analytes.[16-18]

Recently, TMDs started to appear as SERS platforms[18] that would promote stable physicochemical tethering of aromatic molecules onto their surface and facilitate interlayer charge transfer phenomena, however, with modest enhancement for organic species.[19-21] In order to improve the SERS effect, TMDs need to be modified, for example by hybridization with metal nanoparticles to take advantage of their surface plasmon properties by generating "hot spots",[22-24] while additional effort should be undertaken to control the size, crystallinity and shape of the nanoparticles. Furthermore, TMD layers can reduce additional signals by isolating the metal nanoparticles from the fluorophore analyte molecules, which in turn enhances the uniformity of SERS signals and detection efficiency. In addition, TMDs can act as shielding materials against oxidation and photobleaching of metal nanoparticles, hence endowing the hybrid system with exceptional stability and long lifetime performance.

However, only few synthetic strategies have been employed for the fabrication of TMD-based SERS substrates ranging from simple wet chemistry procedures[25-28] to sophisticated ones, involving micropatterning guided by laser beam.[19, 29-30] These experimental procedures require chemical reduction of a metal precursor and pre-processing of TMDs to activate their otherwise inert surface. Particularly for the cases employing chemical methods, although they possess some merits, such as low cost and high throughput, they dictate the existence of metal salts and strong reducing agents. Hence, additional chemical reagents are required, which may bring byproducts in the reaction mixture, entail extra purification steps, involve solubility compatibility experiments and cause toxicity and contamination. On the other hand, processes which implicate relatively high laser power may increase the surface activity of TMDs, albeit with high cost and extra effort. In addition, due to the strong heating effect of the continuous laser, they unavoidably cause detrimental thermal oxidation[30] and phase transition of semiconducting 2H-MoS_2 to metallic 1T-MoS_2.[31-32] Alternatively, oxygen and argon plasma treated MoS_2 sheets have been also examined, in which the creation of structural disorders, local dipoles and roughened surface due to the bombardment process resulted in enhanced SERS phenomena on MoS_2 surface.[33] Based on the aforementioned points, the preparation of robust sensing platforms with TMD-based species still remains a daunting challenge. In this chapter, the fabrication of such platforms free of complex, multi-step and tedious methodologies is presented. Furthermore, the development of modified TMDs, which simultaneously incorporate dopant species and metal nanoparticles on their structure, for improved performance as SERS substrates is investigated.

Several processes to etch the surfaces of TMDs, grow nanoparticles on them and/or even alter their surface chemistry, employ various kinds of plasma technology. In addition, plasma exposure offers flexibility in terms of dopant species and metal nanoparticles that are incorporated within the structure of TMDs, while at the same time ensures clean experimental conditions. Herein, we report – for the first time – a simple one-pot modification of few-layered MoS_2 and WS_2 sheets, employing nitrogen plasma treatment and simultaneous decoration with silver nanoparticles (Ag_{NPs}), for two different plasma exposure and metal deposition times, toward the preparation of N-doped and with Ag_{NPs} decorated TMDs. The employed method offers numerous virtues over the previously reported studies, including straightforwardness, controllability, fast functionalization time, and absence of wet processes that may require additional work up procedures. The successful surface modification of TMDs was evaluated through Raman and X-ray photoelectron spectroscopy (XPS), while transmission electron microscopy (TEM) imaging verified the decoration with Ag_{NPs}. Furthermore, the newly developed N-MoS_2/Ag_{NPs} and N-WS_2/Ag_{NPs} hybrids were employed as SERS substrates, according to Scheme 4.1, to detect Rhodamine B (RhB) at very low concentration. Markedly, it was found that the SERS efficiency, by observing clearly all RhB Raman active bands, depends on both doping and deposition time as well as the type of TMD employed as substrate. Charge-transfer phenomena witnessed between RhB and the modified TMDs, along with the polarized character of the hybrid system, causing dipole-dipole coupling interactions, were ascribed for the enhancement of the Raman signal acquired. Finally, considering the coordination of aromatic moieties via π-S interactions with TMDs, we accomplished the sensitive detection of polycyclic aromatic hydrocarbons such as pyrene, anthracene and 2,3-dihydroxy naphthalene, at very low levels, by employing N-MoS_2/Ag_{NPs} as SERS substrate.

4.2 Results and discussion

4.2.1 Modification of TMDs as SERS substrates

Initially, organolithium chemistry was employed to exfoliate the TMDs from the bulk. Following simple and well-established procedures, MoS_2 and WS_2 powders were treated with *N*-butyl lithium.[34] This process operates by intercalating lithium cations to MoS_2 and WS_2, weakening interlayer spacing, thereby resulting to single and mostly few-layered MoS_2 and WS_2 sheets. The as-exfoliated MoS_2 and WS_2 formed stable dispersions in *N*,*N*-dimethyl formamide and methanol, allowing easy handling and manipulation. In the following step, to boost the electronic properties of MoS_2 and WS_2, modification of the surface was accomplished by interfacing the TMDs with nitrogen and silver nanoparticles, by treating them in a conventional vacuum sputtering chamber under nitrogen plasma conditions and in the presence of a silver cathode as the source. An one-pot treatment procedure was applied for two different deposition times, 5 and 10 s, respectively, to obtain N-doped and with Ag_{NPs} decorated MoS_2 and WS_2 hybrids, abbreviated as N5-MoS_2/Ag_{NPs}, N10-MoS_2/Ag_{NPs}, N5-WS_2/Ag_{NPs} and N10-WS_2/Ag_{NPs}, respectively, for each functionalization time.

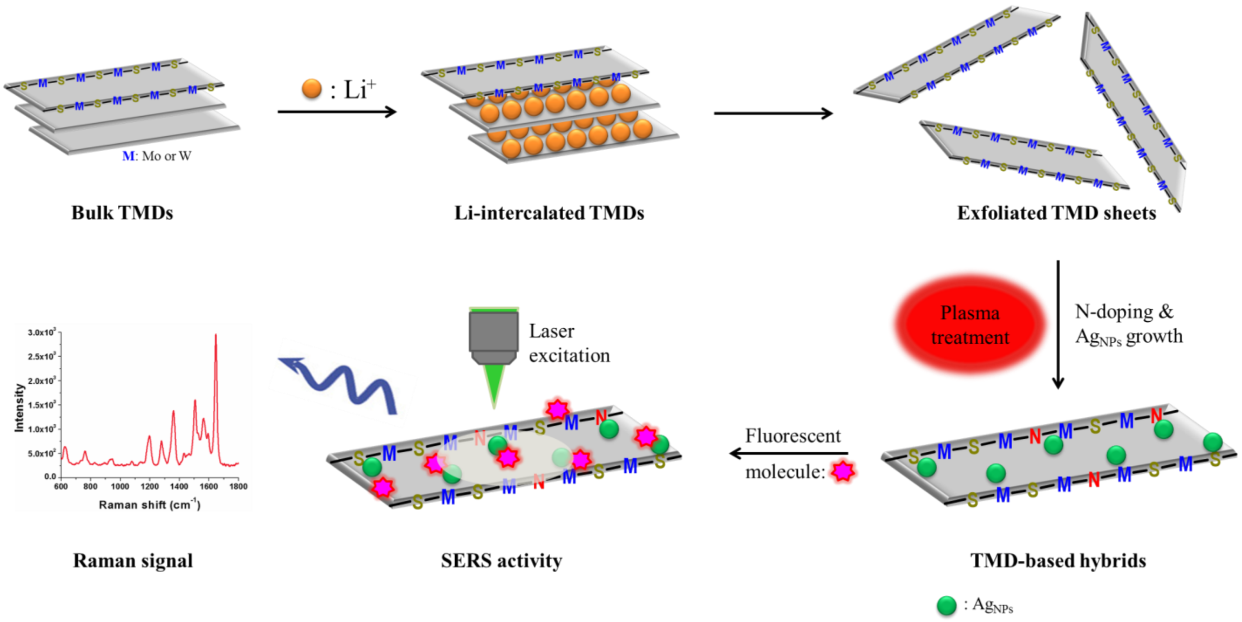

Scheme 4.1. Illustrative representation for the preparation of N-doped and decorated with Ag_{NPs} TMDs and their application as SERS substrates.

4.2.2 Characterization of modified TMDs as SERS Substrates

Raman spectroscopy was firstly applied to provide meaningful information on the atomic structural arrangement of the as-exfoliated MoS_2 and WS_2 sheets. The Raman spectrum of bulk MoS_2 at 633 nm excitation is dominated by three characteristic bands at 376, 402 and 450 cm^{-1} (Figure 4.1a). These bands are attributed to the in-plane E^1_{2g} mode (376 cm^{-1}) derived from opposite vibrations of two S atoms with respect to Mo atom, the A_{1g} mode (402 cm^{-1}) associated with the out-of-plane vibration of S atoms, and the second-order Raman scattering 2LA(M) mode (450 cm^{-1}).[35] The frequency difference between the A_{1g} and E^1_{2g} modes found to be 22 cm^{-1}, reduced by 4 cm^{-1} as compared to the value observed for the bulk material (ca. 26 cm^{-1}), demonstrates the successful exfoliation and the existence of few-layered MoS_2.[6, 36] Notably, the presence of two new bands centred at 178 and 224 cm^{-1}, further justified the formation of the 1T-MoS_2 phase in the exfoliated material (Figure 4.1a).[37] Additionally, the FWHM of the A_{1g} mode increased from 9 cm^{-1} for the bulk material to 14 cm^{-1} for the exfoliated few-layered MoS_2 sheets, as van der Waals interactions weaken after exfoliation, causing band broadening. On the other hand, the FWHM of E^1_{2g} was practically remained unaltered. Although further analysis goes beyond the scope of the current work, the latter results are in full agreement with previous reports,[38] and attributed to dielectric screening of long range Coulomb interactions.[39] Evidently, the intensity of 2LA(M) increased in the exfoliated material, which is attributed to the creation of more sulfur vacancies sheets due to the delamination process.[40] Similarly for exfoliated WS_2, strong Raman bands centred at 349 and 417 cm^{-1} corresponding to the E^1_{2g} and A_{1g} modes, respectively, were also apparent (Figure 4.1b). The relative peak distance also decreased from 68.5 to 63.4 cm^{-1}, as moving from bulk to exfoliated WS_2, highlights the effective generation of 1T-WS_2 crystals. The FWHM values for E^1_{2g} and A_{1g} were calculated to be 13 and 12 cm^{-1}, respectively, for both bulk and exfoliated WS_2, although a decrease in the ratio of the intensity of E^1_{2g} to A_{1g} was reported and ascribed to the weak interlayered interactions after exfoliation.

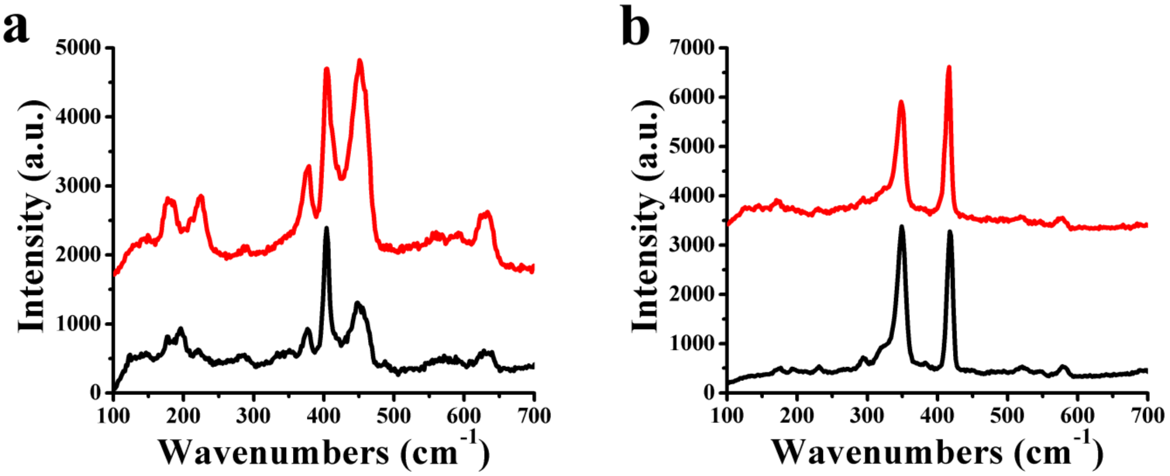

Figure 4.1 Raman spectra (633 nm) for (a) exfoliated MoS_2 (red) as compared to bulk material (black), and (b) exfoliated WS_2 (red) as compared to bulk material (black).

Detailed surface characterization for exfoliated MoS_2 was conveyed by XPS studies. From the high-resolution XPS deconvoluted spectra for Mo 3d orbitals, peaks at 231.2 and 228.2 eV (Figure 4.2a), corresponding to the binding energies of $3d_{3/2}$ and $3d_{5/2}$ orbitals for Mo^{4+}, respectively, were observed.[41-42] The S 2s spectrum shows a peak at 225.6 eV, while the S 2p one is resolved into two components located at 162.6 and 161.4 eV (Figure 4.2b), owed to $2p_{1/2}$ and $2p_{3/2}$ orbitals of saturated divalent sulfur, respectively. As far as the XPS of exfoliated WS_2 is concerned, peaks due to the presence of W^{4+} $5p_{3/2}$, $4f_{5/2}$ and $4f_{7/2}$ orbitals were identified at 37.9, 34.5 and 32.3 eV (Figure 4.2c), respectively, in agreement with previous observations.[43] Additionally, peaks at 163.5 and 162.3 eV in the S 2p spectrum

(Figure 4.2d) are ascribed to the $2p_{1/2}$ and $2p_{3/2}$ orbitals of divalent sulfide ions (S^{2-}) in WS_2, respectively.[44]

The successful incorporation of nitrogen as dopant within the lattice of exfoliated MoS_2 and WS_2 as well as the deposition of Ag_{NPs} on their surface, yielding N5-MoS_2/Ag_{NPs}, N10-MoS_2/Ag_{NPs}, N5-WS_2/Ag_{NPs} and N10-WS_2/Ag_{NPs} hybrids, was also probed by XPS, as nicely demonstrated on the corresponding survey spectra (Figure 4.2e and f). Obvious differences are identified between XPS spectra of exfoliated and modified TMDs. In modified TMDs, the emergence of two new peaks – one located at ~398 eV, attributed to the chemical identity of nitrogen, and a doublet one at ~370 eV, associated with Ag_{NPs}, were evident. In both N-MoS_2/Ag_{NPs} and N-WS_2/Ag_{NPs} hybrids, longer plasma treatment time, i.e. 10 s, resulted in the development of more intense and prominent peaks. To further justify our statements, XPS core level spectra were also collected. More precisely, nitrogen plasma exposure for 5 and 10 s resulted in the emergence of a low intensity peak at 398.5 eV in the N 1s region confirming the presence of nitrogen doping (Figure 4.2g). It should be underlined that the Mo $3p_{3/2}$ overlaps with the N 1s region, as evidenced by the peak attributed to MoS_2 at 394.8 eV. Additionally, nitrogen did not show any reactivity with sulfur, as no S–N bonding was detected in the S 2p region. Hence, the favorable development of a covalent bond between Mo and N is clearly revealed, signifying that nitrogen preferentially substitutes sulfur atoms from the MoS_2 skeleton. As for N 1s region spectra of WS_2, longer plasma treatment time, i.e. 10 s, resulted in the development of a more distinct peak at 396.8 eV, as evidenced in Figure 4.2h, compared to that acquired upon 5 s deposition. Overall, a controllable nitrogen concentration could be realized at the applied plasma exposure conditions. On the other hand, the evolution of a doublet of peaks located at 373.8 and 367.0 eV attributed to Ag 3d states, owed to $3d_{3/2}$ and $3d_{5/2}$ orbitals, respectively (Figure 4.2i and j), verifies the deposition of Ag_{NPs} on the surface of N-doped MoS_2 and WS_2. Again, longer deposition time, i.e. 10 vs 5 s, resulted in the development of more pronounced peaks for silver on the XPS spectra for N-MoS_2/Ag_{NPs} and N-WS_2/Ag_{NPs}. Then, for proving that the Ag 3d signals are due to Ag_{NPs} and not simply to bulk Ag, a reference measurement was conducted, derived from 5 s deposition of silver onto silicon substrate. Evidently, the emergence of sharp peaks attributed to bulk silver were recorded (Appendix, Figure S4.1), contrasting the evolution of broad peaks identified at ~370 eV for N-MoS_2/Ag_{NPs} and N-WS_2/Ag_{NPs} hybrids, hence, proving the deposition of silver in the form of nanoparticles instead of bulk[45] onto N-doped MoS_2 and WS_2. The atomic % concentration for nitrogen and silver was calculated and presented in Table 4.1 for N-MoS_2/Ag_{NPs} and N-WS_2/Ag_{NPs} hybrid materials at the different doping and deposition times.

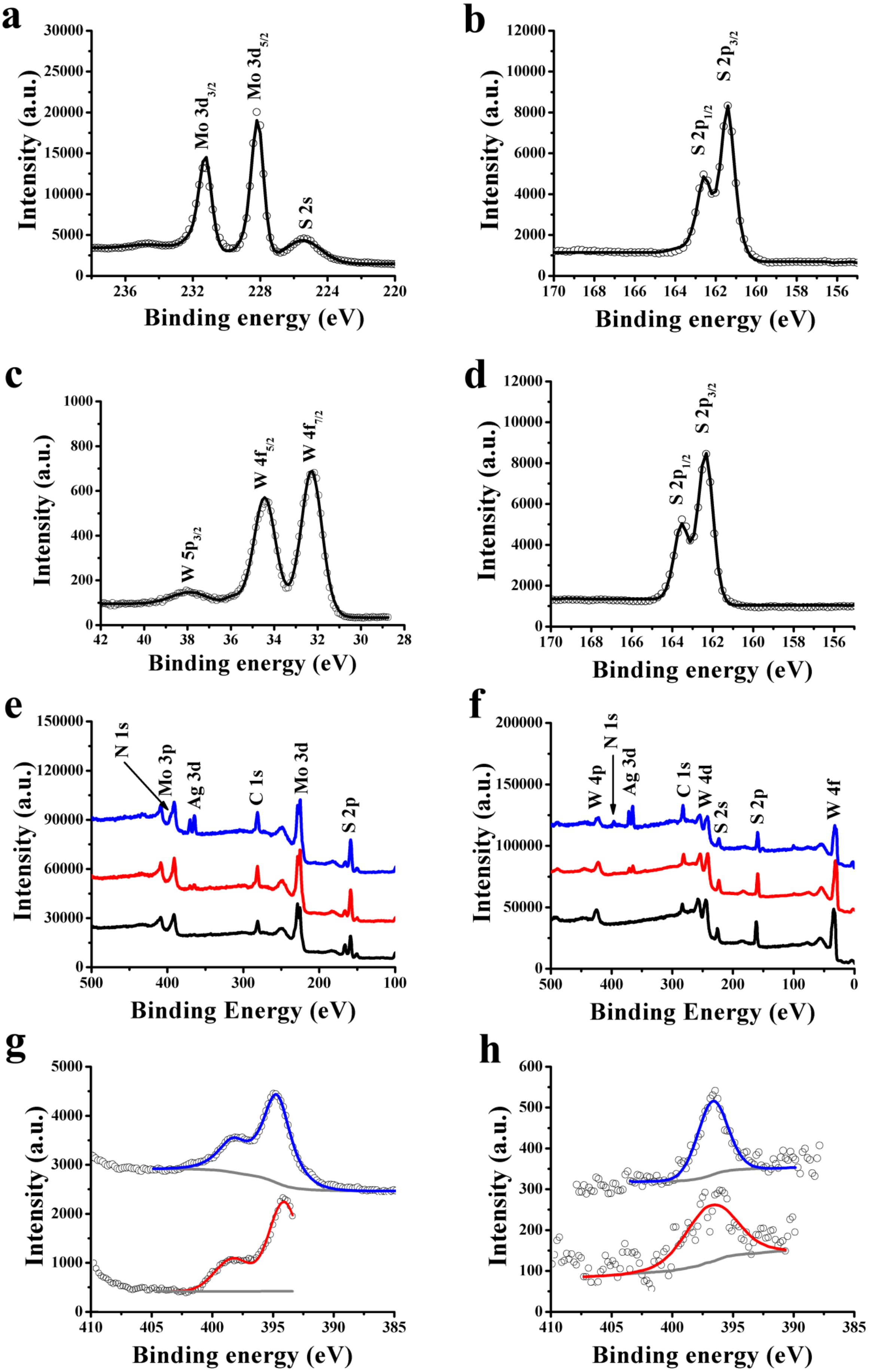
a
Intensity (a.u.)
Binding energy (eV)
Mo 3d$_{3/2}$
Mo 3d$_{5/2}$
S 2s
30000
25000
20000
15000
10000
5000
0
236
232
228
224
220
b
Intensity (a.u.)
Binding energy (eV)
S 2p$_{1/2}$
S 2p$_{3/2}$
12000
10000
8000
6000
4000
2000
0
170
168
166
164
162
160
158
156
c
Intensity (a.u.)
Binding energy (eV)
W 5p$_{3/2}$
W 4f$_{5/2}$
W 4f$_{7/2}$
1000
800
600
400
200
0
42
40
38
36
34
32
30
28
d
Intensity (a.u.)
Binding energy (eV)
S 2p$_{1/2}$
S 2p$_{3/2}$
12000
10000
8000
6000
4000
2000
0
170
168
166
164
162
160
158
156
e
Intensity (a.u.)
Binding Energy (eV)
N 1s
Mo 3p
Ag 3d
C 1s
Mo 3d
S 2p
150000
120000
90000
60000
30000
0
500
400
300
200
100
f
Intensity (a.u.)
Binding Energy (eV)
W 4p
N 1s
Ag 3d
C 1s
W 4d
S 2s
S 2p
W 4f
200000
150000
100000
50000
0
500
400
300
200
100
0
g
Intensity (a.u.)
Binding energy (eV)
5000
4000
3000
2000
1000
0
410
405
400
395
390
385
h
Intensity (a.u.)
Binding energy (eV)
600
500
400
300
200
100
0
410
405
400
395
390
385

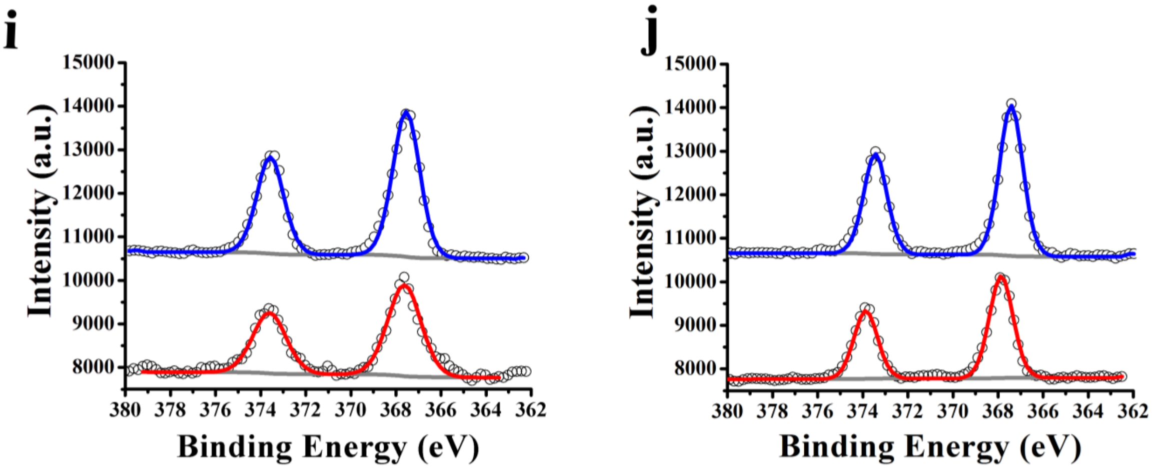

Figure 4.2 Deconvoluted XPS core level peak regions for exfoliated MoS$_2$ (a) Mo 3d and S 2s, and (b) S 2p, and for exfoliated WS$_2$ (c) W 5p and 4f, and (d) S 2p. Survey XPS for (e) exfoliated MoS$_2$ (black), N5-MoS$_2$/Ag$_{NPs}$ (red) and N10-MoS$_2$/Ag$_{NPs}$ (blue), and (f) exfoliated WS$_2$ (black), N5-WS$_2$/Ag$_{NPs}$ (red) and N10-WS$_2$/Ag$_{NPs}$ (blue). N1s core level peak regions for (g) N5-MoS$_2$/Ag$_{NPs}$ (red) and N10-MoS$_2$/Ag$_{NPs}$ (blue), and (h) N5-WS$_2$/Ag$_{NPs}$ (red) and N10-WS$_2$/Ag$_{NPs}$ (blue). Ag 3d core level spectra for (i) N5-MoS$_2$/Ag$_{NPs}$ (red) and N10-MoS$_2$/Ag$_{NPs}$ (blue), and (j) N5-WS$_2$/Ag$_{NPs}$ (red) and N10-WS$_2$/Ag$_{NPs}$ (blue).

Table 4.1. Atomic concentration percentage of nitrogen and silver for the various N-MoS$_2$/Ag$_{NPs}$ and N-WS$_2$/Ag$_{NPs}$ hybrid materials, as obtained by XPS data.

Material	N (%)	Ag (%)
N5-MoS$_2$/Ag$_{NPs}$	5.5	1.5
N10-MoS$_2$/Ag$_{NPs}$	8.0	6.0
N5-WS$_2$/Ag$_{NPs}$	4.0	2.5
N10-WS$_2$/Ag$_{NPs}$	7.5	8.0

Further justification for the successful incorporation of Ag$_{NPs}$ on the TMD surface was provided by electronic absorption spectroscopy. In the UV-Vis spectra of N5-MoS$_2$/Ag$_{NPs}$ and N10-MoS$_2$/Ag$_{NPs}$ (Figure 4.3a), a broad band centered at 420 nm due to the presence of Ag$_{NPs}$, overlapped to some extent with the absorption of MoS$_2$, was identified. For N5-WS$_2$/Ag$_{NPs}$ and N10-WS$_2$/Ag$_{NPs}$, a broad absorption band in the visible region (450-540 nm) was similarly discernable (Figure 4.3b).

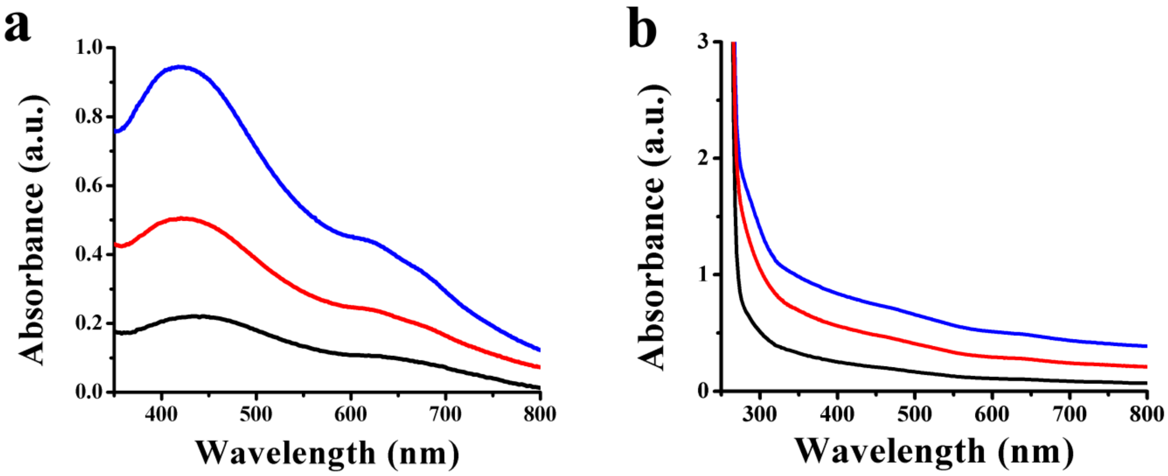

Figure 4.3 Absorption spectra for (a) MoS_2 (black), N5-MoS_2/Ag_{NPs} (red) and N10-MoS_2/Ag_{NPs} (blue), and (b) WS_2 (black), N5-WS_2/Ag_{NPs} (red) and N10-WS_2/Ag_{NPs} (blue), obtained in DMF.

The morphology of N-MoS_2/Ag_{NPs} and N-WS_2/Ag_{NPs} hybrids was examined by TEM, so as to prove that silver deposition resulted in nanoparticle growth rather than the creation of a continuous film on TMD sheets. As shown in the Appendix (Figure S4.2a and b), flakes of exfoliated MoS_2 and WS_2 were imaged and the different layers were clearly observed. Focusing on N-MoS_2/Ag_{NPs} and N-WS_2/Ag_{NPs} hybrid materials, TEM imaging revealed the decoration of the TMD sheets with Ag_{NPs} as round dark objects (Figure 4.4). By comparing the amount of Ag_{NPs} decorating the surface of N-doped TMDs, it is clear that the more time treated the exfoliated MoS_2 and WS_2, the larger the amount of Ag_{NPs} deposited (*cf.* Table 4.1). The size distribution of Ag_{NPs} was determined by measuring several of those (~ 50 Ag_{NPs}) in TEM images. The Ag_{NPs} average diameter in N-MoS_2/Ag_{NPs} was found to be 3.44 ± 0.21 nm (Figure 4.4a and b), while they display clear lattice fringes with interplanar spacing of 0.32 nm, as shown in the inset of Figure 3b. In N-WS_2/Ag_{NPs}, the average diameter of Ag_{NPs} was found to be slightly smaller, 2.2 ± 0.69 nm (Figure 4.4c and d).

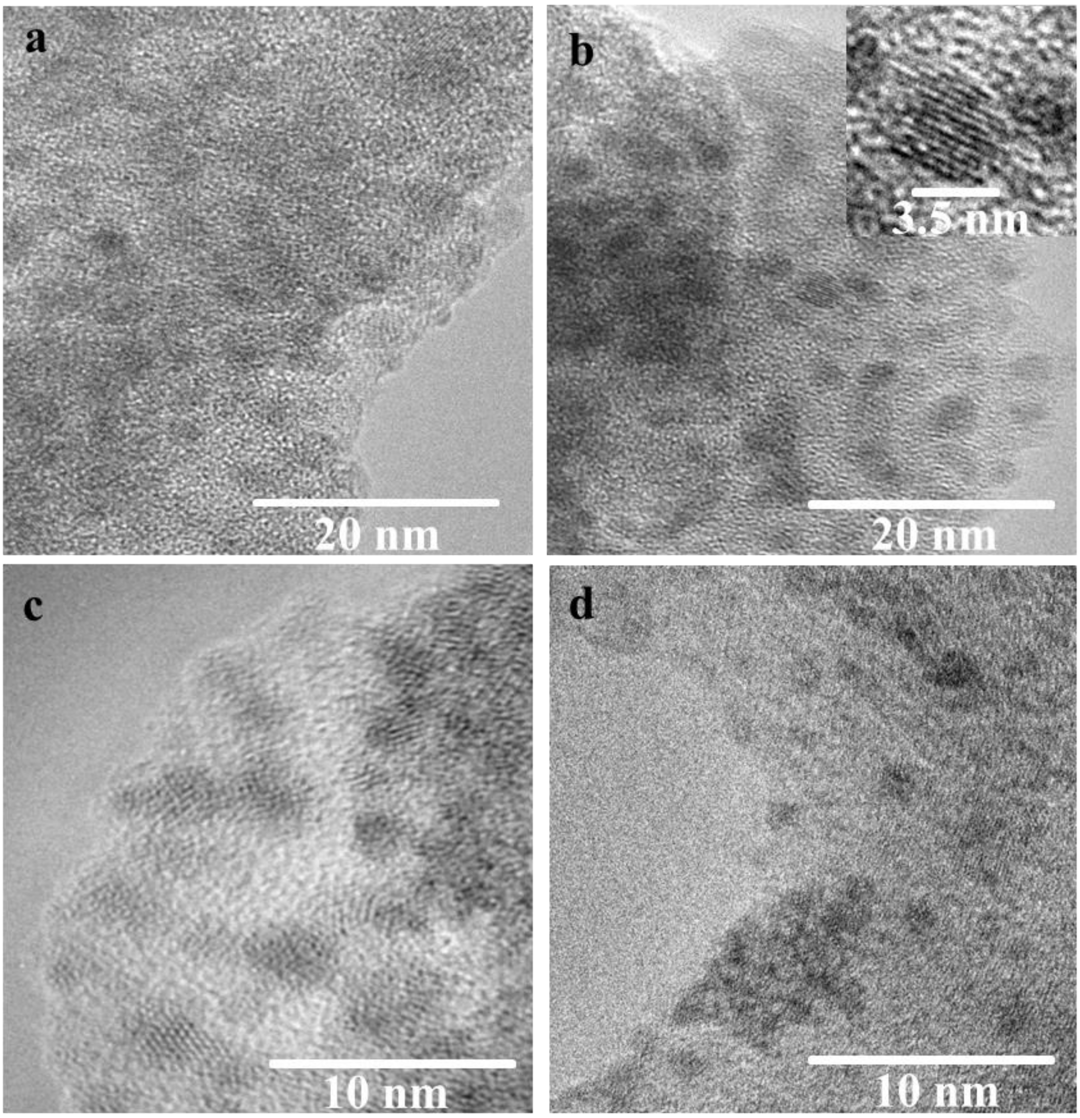

Figure 4.4 Representative TEM images for (a) N5-MoS_2/Ag_{NPs}, (b) N10-MoS_2/Ag_{NPs}. Inset: Lattice fringes of Ag_{NPs}, (c) N5-WS_2/Ag_{NPs}, and (d) N10-WS_2/Ag_{NPs}.

4.2.3 SERS evaluation

Having successfully fabricated in a controlled fashion N-MoS_2/Ag_{NPs} and N-WS_2/Ag_{NPs} and sufficiently characterized all the hybrid materials with spectroscopic and imaging means, we turn our notion to investigate their function as SERS substrates for molecular sensing. Rhodamine B (RhB) was selected to be a model analyte as a highly employed Raman probe molecule. Depositing the hybrids onto Si wafers and dipping them into aqueous RhB resulted to effective association of RhB with TMDs via multiple π-S interactions. For comparison reasons, RhB was also drop-casted onto bare Si as well as onto exfoliated MoS_2 and WS_2 (i.e. non-modified) substrates for Raman signal detection. When the Raman spectrum of the dye adsorbed on the Si substrate was collected, only strong fluorescent background due to RhB was observed (Appendix, Figure S4.3). When collecting Raman spectra from RhB deposited onto as-exfoliated MoS_2 and WS_2 substrates, partial bands with too low intensity started to appear (Figure 4.5a and 4.5b). In sharp contrast, when SERS measurements were performed employing the modified nanostructures obtained upon shorter plasma period, namely, N5-MoS_2/Ag_{NPs} and N5-WS_2/Ag_{NPs}, clear and distinct bands with high intensity and strong signal-to-noise ratio were observed. For comparison reasons, we also conducted the same measurement on Si substrate coated with silver nanoparticles (Appendix, Figure S4.3), however only strong fluorescent was recorded and a very low intensity band at 1648 cm^{-1} was merely detected. Hence, it is underlined that only 5 s exposure of exfoliated MoS_2 and WS_2 at plasma conditions was more than enough to successfully unfold the Raman spectrum of RhB. The latter showcases the capability of lightly modified TMDs as efficient SERS substrates, without undergoing any sophisticated and time-consuming functionalization process. Evidently, the characteristic Raman modes of RhB were undoubtedly visible and more pronounced when the plasma treatment period for the fabrication of the substrates increased, by employing in the measurement the N10-MoS_2/Ag_{NPs} and N10-WS_2/Ag_{NPs} substrates. Specifically, the Raman spectrum of RhB, by employing any of the types of modified TMDs, shows distinct modes at 625 cm^{-1} (C–C–C ring in plane bending), 760 cm^{-1} (C–H out of plane bending), 943 cm^{-1} (C–H stretching), 1195 cm^{-1} (C–H in plane bending), 1278 cm^{-1} (C–O–C stretching), 1360, 1505, 1563, 1648 cm^{-1} (aromatic C–C stretching) and 1594 cm^{-1} (C=C stretching), in full agreement with previous reports. [46-47] Focusing on the 1648 cm^{-1} band, the SERS signal was enhanced by 8 times for the 10 s plasma treated substrates as opposed to the 5 s ones. This emphasizes the importance and influence of the amount of nitrogen-doping and silver-deposition onto TMDs on the Raman enhancement of the fabricated SERS substrates for detecting RhB.

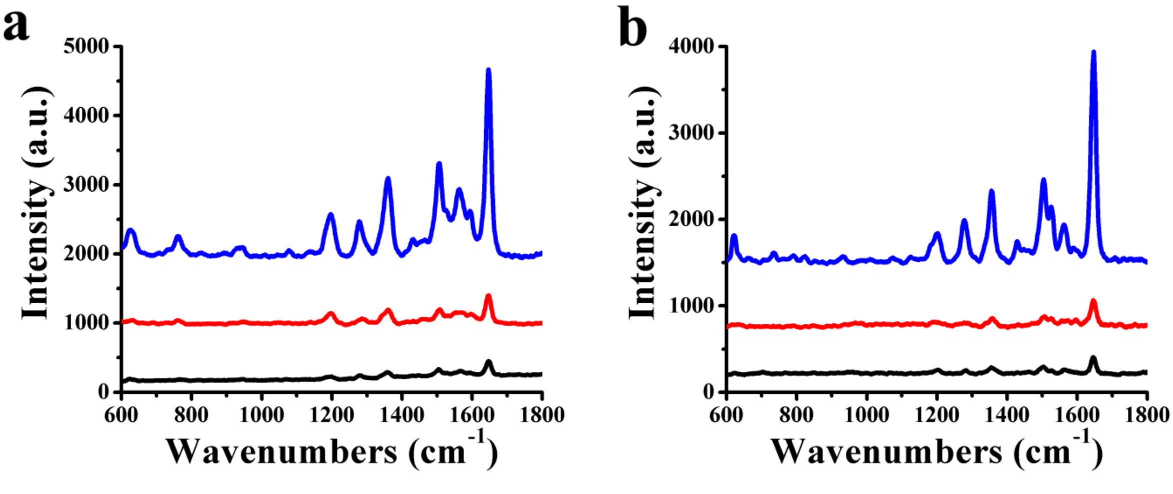

Figure 4.5 SERS spectra (514 nm) of aqueous RhB (10^{-5} M) on (a) exfoliated MoS_2 (black), N5-MoS_2/Ag_{NPs} (red) and N10-MoS_2/Ag_{NPs} (blue) substrates, and (b) exfoliated WS_2 (black) N5-WS_2/Ag_{NPs} (red) and N10-WS_2/Ag_{NPs} (blue) substrates.

In order to optimize the performance of N-MoS_2/Ag_{NPs} and N-WS_2/Ag_{NPs} as efficient SERS substrates and uncover the sensitivity of the method, SERS spectra were collected after depositing different concentrations of RhB onto N10-MoS_2/Ag_{NPs} and N10-WS_2/Ag_{NPs}. In this frame, aqueous RhB solutions with varied concentration from 10^{-5} down to 10^{-9} M were screened, revealing clearly visible Raman modes at a concentration level as low as 10^{-9} M, based on the employment of the N10-MoS_2/Ag_{NPs} substrate (Figure 4.6a). With N10-

WS_2/Ag_{NPs}, the detection level of RhB was lower, as very low intensity bands were observed upon decreasing the RhB concentration from 10^{-5} to 10^{-6} M. At lower concentration (i.e. 10^{-7} M), the Raman spectrum was hardly detected, as only the band at 1648 cm^{-1} can be observed at an extremely low intensity (Figure 4.6b). To quantify the SERS activity of N10-MoS_2/Ag_{NPs}, the enhancement factor (EF) was calculated by comparing the intensity of a single molecule SERS signal with that from the respective exfoliated, using the following equation[48-49] :

$$EF= \frac{I_{SERS}}{I_{EXF}} \times \frac{C_{EXF}}{C_{SERS}}$$

where C_{EXF} and C_{SERS} is the concentration of RhB on exfoliated MoS_2 and modified N10-MoS_2/Ag_{NPs}, respectively. Considering the two more dominant bands, located at 1648 and 1360 cm^{-1}, the relevant calculations are summarized in Table 4.2. The EF was calculated to be 8×10^3 and 1.1×10^4 using the bands at 1648 and 1360 cm^{-1}, respectively. The average EF reaches the value of 10^4, which is even higher or comparable with that of other reported TMD-based SERS substrates.[20, 25, 30, 50-52] Though, direct comparison of EF values to elucidate the SERS activity is rather uncertain because numerous assumptions and underestimations are taken into account for its calculation, leading to false conclusions. In fact, for the calculation of EF the concentration of the analyte, the penetration depth of the laser together with its excitation wavelength, the reference band, the exposure time of the sample at the laser, the density of the nanoparticles and the existence of the substrate are some of the factors taken into account.[53] However, not all of those parameters are fully described in the various assays reported, so as a direct comparison between SERS performances among different or similar systems can be rather ambiguous. Nevertheless, the current results showcase the strong EF obtained with the N-TMDs/Ag_{NPs} providing reliable SERS signals, even though they have yet to be fully optimized. In addition, the detection limit for RhB by employing the N10-MoS_2/Ag_{NPs} material, found to be as low as 10^{-9} M. The latter value is comparable or even superior as compared to previously reported works employing TMD-based materials[25, 28, 30, 52, 54] and in agreement with detection limits reported for other nanostructures based on silver as SERS substrates.[55-58] Although there has been reported higher detection limit for RhB,[26, 59] it should be emphasized that the currently developed method involving simultaneous incorporation of nitrogen and deposition of silver nanoparticles on TMDs has just initiated to tap into the application of these matrices as active SERS substrates.

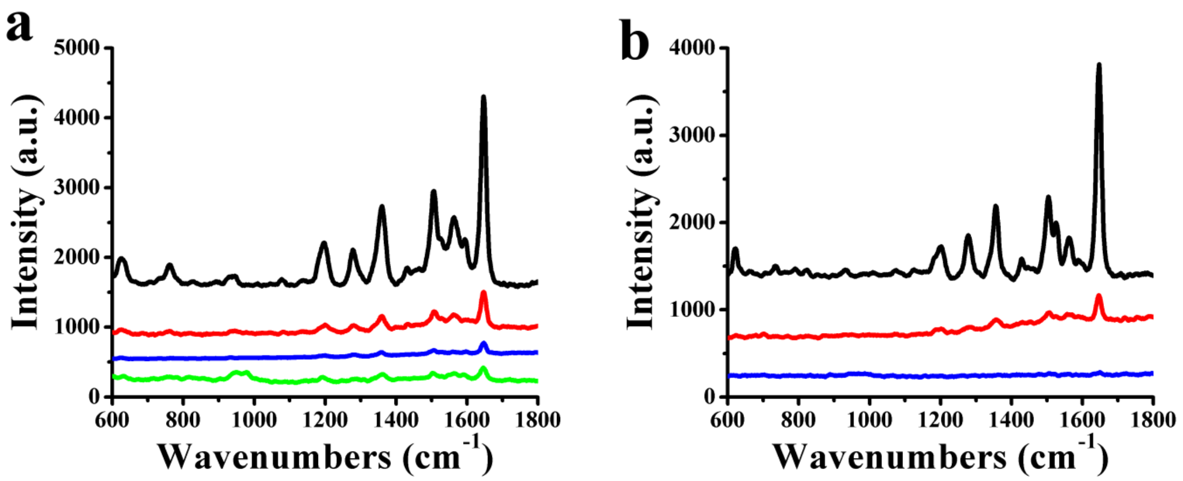

Figure 4.6 SERS spectra (514 nm) of aqueous RhB at 10^{-5} M (black), 10^{-6} M (red), 10^{-7} M (blue) and 10^{-9} M (green) on (a) N10-MoS_2/Ag_{NPs}, and (b) N10-WS_2/Ag_{NPs} substrates.

Table 4.2 Parameters for the calculation of enhancement factor (EF).

Material	RhB (mol·L^{-1})	Relative intensity (a.u.)		EF	
N-MoS_2/Ag_{NPs}	10^{-9}	153 [a]	100 [b]	8×10^{3} [a]	1.1×10^{4} [b]
MoS_2	10^{-5}	191 [a]	89 [b]		

[a] at the 1648 cm^{-1} mode

[b] at the 1360 cm^{-1} mode

The core idea of this chapter is to employ suitably modified TMDs as SERS substrates. Since the SERS effect generally depends on the presence of “hot spots” owed to nanoparticles and considering the inert surface of TMDs, we specifically designed a novel approach, never tested before, for preparing double-modified TMDs. Particularly, we successfully achieved the simultaneous incorporation of nitrogen within the lattice of TMDs as dopant and decoration of the lattice with Ag_{NPs}, in an one-pot procedure, through nitrogen plasma treatment and silver evaporation. Markedly, N-doping of TMDs is beneficial itself, since such doping contributes to roughening of the otherwise inert surface of TMDs, providing grafting capability and acting as nucleation site for the uniform distribution of Ag_{NPs}. Moreover, with the simultaneous deposition of nitrogen and introduction of silver, we achieved minimization of the precursors quantities employed, while we abandon wet chemistry processes that may have been employed for purification and isolation of the modified TMDs. Therefore, the synthesis of single-modified MoS_2 materials, by only incorporating N-dopants or only loading Ag_{NPs} was disregarded. Nevertheless, N-MoS_2 and MoS_2/Ag_{NPs} were prepared and their SERS efficiency was examined and found to be considerably smaller as compared with the one achieved when N-MoS_2/Ag_{NPs} was employed (Figure 4.7). The latter result highlights the great advantage of the double-modified MoS_2 over the single-modified one as SERS substrate. This itself is a major finding, which can be further elaborated, advanced and/or optimized in future studies, by employing not only different amounts of N and Ag_{NPs} but also other elements for doping and/or other metals for depositing diverse nanoparticles on the TMDs to achieve even higher detection limits.

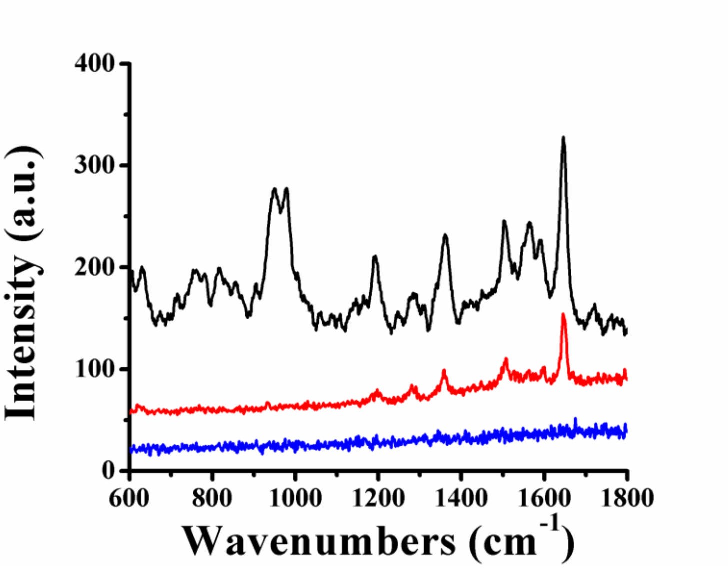

Figure 4.7 SERS spectra (514 nm) of aqueous 10^{-9} M RhB on N-MoS_2 (blue), MoS_2/Ag_{NPs} (red) and N10-MoS_2/Ag_{NPs} (black) substrates.

Although the basis of SERS has yet to be fully understood, it may be ascribed to two possible pathways, namely, the electromagnetic and the chemical mechanism. The electromagnetic mechanism is due to the enhancement of the local electromagnetic field of metal substrates as associated with the surface plasmon resonance (resulting to a factor of 10^4–10^8 enhancement),[20] while the chemical mechanism is based on charge transfer processes developed between the organic molecule to be detected and the substrate (resulting to a factor of 10–10^2 enhancement).[60] In the current study, the combination of N-doped two-dimensional TMDs as SERS substrates, where charge-transfer phenomena with organic dyes prevail,[13, 19-20] incorporating metallic silver nanoparticles, benefits the function of the hybrid materials as efficient SERS platforms from both mechanisms.[20, 25, 33, 54] In more detail, steady-state photoluminescence assays revealed that the strong emission of RhB, located at 570 nm upon photoexcitation at 490 nm, was quenched in the presence of N-MoS_2/Ag_{NPs} and N-WS_2/Ag_{NPs} (Figure 4.8). Hence, transduction of electron and/or energy from the singlet excited state of RhB to the N-doped TMDs takes place, implying that the latter act as electron acceptors. Similar phenomena were observed when RhB interacted with as-exfoliated MoS_2 and WS_2, though the photoluminescence quenching of RhB was smaller, suggesting stronger n-type behavior for the N-doped TMDs, thereby resulting in higher SERS by N-MoS_2/Ag_{NPs} and N-WS_2/Ag_{NPs}. These charge-transfer interactions between RhB and the modified TMDs, together with the polarized character of the system, owed to the different electron affinity of the transition metal and the chalcogen atoms within the layered structure of the hybrids causing dipole-dipole coupling interactions, induce Raman scattering enhancement.[20, 33, 54] In addition, the plasma treatment of TMDs changed the local surface properties and chemistry of TMDs by simultaneously introducing N-doping and depositing Ag_{NPs} onto the surface of MoS_2 and WS_2, while also etching and roughening the edges and introducing defects, where

RhB can coordinate via π-S interactions, creating local dipoles which further enhance Raman scattering signals. Furthermore, the optimized conditions employed for silver plasma deposition resulted to the controlled decoration of N-doped TMDs with Ag_{NPs} of tiny size, avoiding the formation of bigger Ag_{NPs} aggregates, which may have created a thick film onto TMDs minimizing and/or vanishing the active surface. The "hot spots" created on N-doped TMDs due to Ag_{NPs}, locally enhance the electric field[61] due to the collective oscillations of the conduction electrons inside the structure of the hybrid, thus the Raman scattering phenomenon is consequently improved. Hence, equivalent contribution also derives from the enhancement of the local electromagnetic field, which originates from the strong localized surface plasmon resonances at Ag_{NPs}. Overall, synergetic effects based on surface modification of TMDs by changing the local surface properties, which resulted in greater charge-transfer interactions, dipole-dipole coupling interactions and local electromagnetic fields enhanced around Ag_{NPs}, work in tandem to justify the excellent SERS effect of modified TMDs for the detection of RhB at a concentration level as low as 10^{-9} M, particularly when employing N10-MoS_2/Ag_{NPs} as substrate. A possible explanation for the lower sensitivity found for N10-WS_2/Ag_{NPs} might be ascribed to the higher atomic concentration of silver on WS_2, despite employing the same period for the plasma exposure, causing locally high density of Ag_{NPs} aggregations, which may reach saturation, hence hampering the creation of "hot spots".

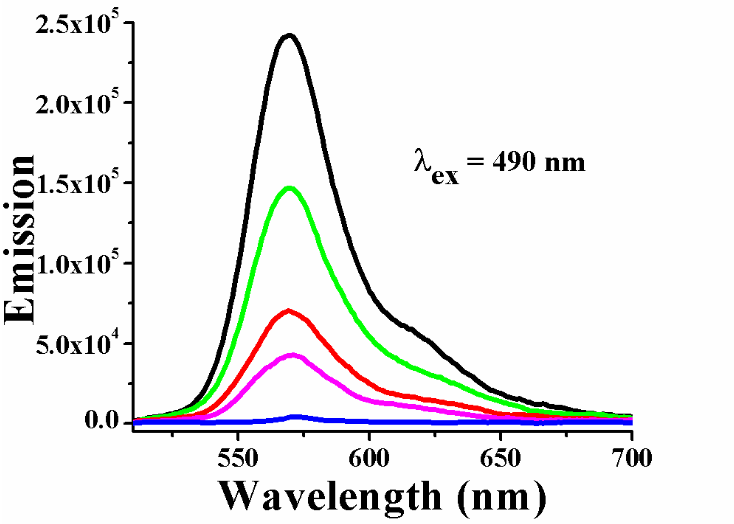

Figure 4.8 Photoluminescence spectra (490 nm) of RhB (black) and RhB after the addition of MoS_2 (red), WS_2 (green), N10-MoS_2/Ag_{NPs} (blue) and N10-WS_2/Ag_{NPs} (pink), respectively. For the acquisition of the spectra, 4 μL of a stock methanol solution of RhB (10^{-3} M) were added to a dispersion of N10-MoS_2/Ag_{NPs} and N10-WS_2/Ag_{NPs}, respectively.

4.2.4 Sensing Polycyclic Aromatic Hydrocarbons

Considering the coordination of aromatic moieties via π-S interactions with TMDs, we applied the N10-MoS_2/Ag_{NPs} hybrid as substrate for the sensitive recognition at very low levels of polycyclic aromatic hydrocarbons. The latter are not only regarded as widespread organic pollutants in the atmosphere but also known to be highly carcinogen and mutagen species[62] and therefore their highly-sensitive in-situ detection is attracted extensive attention nowadays. To this end and having evaluated the activity of N10-MoS_2/Ag_{NPs} as SERS substrate with RhB, the potential application of the former as meaningful sensor for pyrene, anthracence and 2,3-dihydroxy naphthalene was investigated. In general, the bulk Raman spectra of those polyaromatics are governed by strong fluorescence background, making impossible the detection of characteristic Raman signals. Figure 4.9 displays the SERS spectra of the examined polycyclic aromatic hydrocarbons at a concentration level of 10^{-5} M. In all cases, the detection of the polycyclic aromatic hydrocarbons, as well as the sensing of RhB, retained at the same level, proving the reproducibility of the measurements for all hybrids as SERS substrates. In the SERS spectrum of pyrene, seven distinctive modes at 407, 592, 1241, 1406, 1592, 1627, and 1643 cm^{-1} were easily identified, while similarly SERS of anthracene and 2,3-dihydroxy naphthalene revealed distinctive bands at 752, 1006, 1183, 1402 and 1557 cm^{-1} and at 448, 750, 1363, 1412, 1488 and 1585 cm^{-1}, respectively. Although the assignment of those bands is beyond the scope of the work, in general, they can be divided into three main regions: (a) bands below 550 cm^{-1}, which are attributed to C–C out-of-plane bending vibrations, (b) bands at 600–1000 cm^{-1} which are associated with C–H out-of-plane bending and at 1000–1300 cm^{-1}, which are related to C–H in-plane bending and rocking, and (c) bands at 1300–1650 cm^{-1}, which are due to aromatic C–C stretching.[63] For comparison, SERS spectra were collected on a Si substrate after performing silver nanoparticles deposition on it (Appendix, Figure S4.4). High fluorescence background and absence of the detection of characteristic bands owed to pyrene and anthracene were revealed, while only some very low intensity bands due to 2,3-dihydroxy naphthalene were recorded.

To the best of our knowledge, this is the first application of 2D TMDs, specifically N-doped MoS_2 simultaneously decorated with Ag_{NPs}, as effective SERS platform for the sensitive detection of polycyclic aromatic hydrocarbons. To further highlight the impact of the current work, it should be noted that the SERS detection of polycyclic aromatic hydrocarbons by other substrates requires special modification methodologies of metal nanoparticles to ensure effective communication between the substrate and the analyte, as the aromatic rings exhibit low affinity for metals.[64-68] However, herein, π-S interactions with TMDs were exploited and by extension, the SERS application of TMDs as analytical, environmental and biomedical sensors can certainly be envisioned. In fact, upon optimization the sensing efficiency may be further improved to reach or surpass the one registered for RhB and bring the N-doped decorated with Ag_{NPs} TMDs in the frontline as 2D SERS substrates.

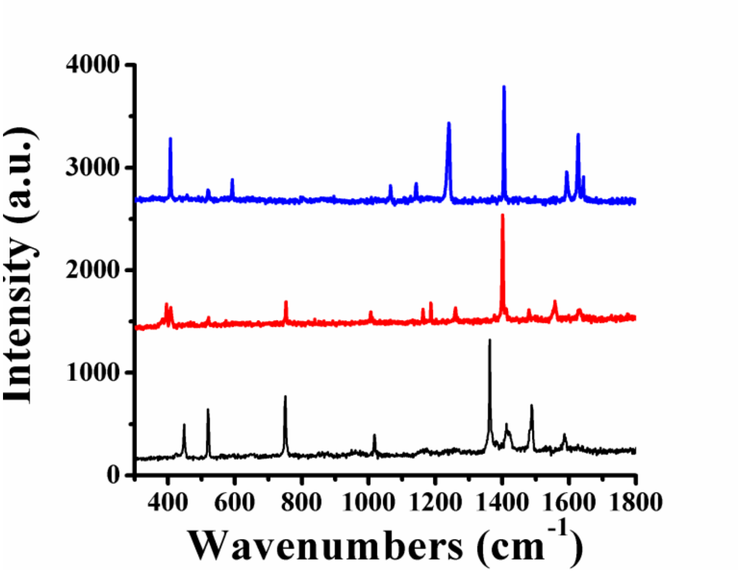

Figure 4.9 SERS spectra (514 nm) of pyrene (blue), anthracene (red) and 2,3-dihydroxy naphthalene (black) at 10^{-5} M deposited onto N10-MoS_2/Ag_{NPs} substrate.

4.3 Conclusions

The one-pot preparation of N-doped and decorated with Ag_{NPs} MoS_2 and WS_2 nanosheets via a facile and effective strategy was accomplished. Precisely, treatment of exfoliated MoS_2 and WS_2 with nitrogen plasma and in the presence of a silver cathode as source in a vacuum sputtering chamber, for 5 and 10 s deposition time, allowed the realization of N5-MoS_2/Ag_{NPs}, N10-MoS_2/Ag_{NPs}, N5-WS_2/Ag_{NPs} and N10-WS_2/Ag_{NPs}. Markedly, N-doping of TMDs was beneficial, since such doping contributes to roughening of the otherwise inert surface of TMDs, providing grafting capability and acting as nucleation site for the uniform distribution of Ag_{NPs}. Hence, controllable concentration of nitrogen dopant was realized and the size of Ag_{NPs} was gradually regulated. Additionally, with the simultaneous deposition of nitrogen and introduction of silver, minimization of the precursors quantities employed was achieved, while wet chemistry processes that may have been employed for purification and isolation of the modified TMDs were abandoned. Comprehensive characterization of the newly prepared N-MoS_2/Ag_{NPs} and N-WS_2/Ag_{NPs} hybrid materials was performed by Raman and XPS, while the morphology was imaged with the aid of TEM. Next, the newly developed hybrid materials were attested as efficient SERS platforms and the effective detection of RhB was accomplished. Notably, it was proved that the SERS of RhB, with N-MoS_2/Ag_{NPs} and N-WS_2/Ag_{NPs}, depends not only on the doping and deposition time induced by plasma exposure, but also on the type of the TMD. The N10-MoS_2/Ag_{NPs} showed the highest sensitivity for RhB at concentration as low as 10^{-9} M by clearly observing all Raman active modes. The efficient SERS effect was rationalized and attributed to both chemical and electromagnetic mechanisms. Charge-transfer phenomena, dipole-dipole coupling interactions and local electromagnetic fields around Ag_{NPs} within N-MoS_2/Ag_{NPs} led synergistically to the enhancement of the Raman scattering. Finally, polycyclic aromatic hydrocarbons such as pyrene, anthracene and 2,3-dihydroxy naphthalene were coordinated via π-S interactions with

N10-MoS_2/Ag_{NPs} and screened with high sensitivity and reproducibility. To conclude, this is a proof-of-concept study examining a set of two different TMD-based hybrid materials in terms of the amount of N-doping and Ag_{NPs} loading on MoS_2 and WS_2 as a function of plasma treatment and metal deposition period. The results revealed better performance/efficiency as SERS substrate for the modified material with the higher content of N and Ag_{NPs} for detecting Rhodamine B at very low concentration, while also applied to sense polycyclic aromatic hydrocarbons. All in all, our findings highlight the excellent functionality and applicability of the newly developed materials N-MoS_2/Ag_{NPs} and N-WS_2/Ag_{NPs} as SERS substrates for sensing widespread organic and environmental pollutants as well as carcinogen and mutagen species. We anticipate that this study benefits future potential applications of TMD materials, as well as their hybrid structures, for environmental pollution monitoring, ultrasensitive biological sensing and defense and security applications.

4.4 Experimental Section

4.4.1 General

All solvents and reagents were purchased from Aldrich and used without further purification unless otherwise stated. Steady state electronic absorption spectra were recorded on a Perkin-Elmer (Lambda 19) UV–Vis spectrophotometer, while Raman characterization was carried out at room temperature with a Renishaw confocal spectrometer using Ar – Laser at 514 and 633 nm. The evaluation of sample composition was conducted by X-ray photoelectron spectroscopy using a VERSAPROBE PHI 5000 from Physical Electronics, equipped with a monochromatic Al Kα X-ray source. The X-ray photoelectron spectra were collected at the take-off angle of 45° with respect to the electron energy analyzer operated in the CAE (constant analyzer energy) mode. For the survey and the high-resolution detail spectra, the pass energies were respectively, 50 eV and 20 eV. For the compensation of built-up charge on the sample surface during the measurements, a dual beam charge neutralization composed of an electron gun (≈1 eV) and an Ar ion gun (≤10 eV) was used. Binding energies are all referred to the C1s at 284.6 eV. Atomic concentration percentages were determined by XPS data using CasaXPS software. Transmission electron microscopy images were acquired on a TEM JEOL JEM-2100, using an accelerating voltage of 200 kV. The instrument is equipped with an EDS-SDD detector of 80 mm^2 area for chemical analysis. Samples were prepared by drop casting of stable dispersions onto a TEM grid (300 mesh, cooper, Lacey Carbon Film LC300-CU). Steady state emission spectra were recorded on a Fluorolog-3 JobinYvon-Spex spectrofluorometer (model GL3-21).

4.4.2 Exfoliation of TMDs

N-butyl lithium (5 mL) was added to bulk MoS_2 powder (1 g) and the mixture was stirred at 65 ^oC under N_2 atmosphere for 3 days. In the resulting solid material, distilled water was carefully added at 0 ^oC under vigorous stirring, until the completion of the exothermic reaction. The resultant dispersion was washed three times with hexane (50 mL) to remove byproducts, then transferred to a beaker and sonicated at 60 ^oC for 30 minutes. The material was left overnight to settle and the exfoliated TMDs were obtained from the supernatant. In the final step, the dispersion was filtered over PTFE filter (pore size 0.1 μm) and washed several times with water, methanol and dichloromethane. The solid residue was dried to obtain 200 mg of exfoliated MoS_2. The same experimental procedure was followed for obtaining exfoliated WS_2 sheets.

4.4.3 Functionalization of TMDs

The exfoliated TMDs were introduced in a conventional pulsed DC magnetron sputtering chamber with base pressure at about $4 \cdot 10^{-6}$ mbar. Doping with nitrogen was performed by exposing the exfoliated material in the presence of a reactive gas (N_2) mixed with the conventional sputtering gas (Ar). Simultaneously, Ag_{NPs} were plasma deposited on the exfoliated TMDs using a silver cathode as a source. The following functionalization parameters were used in all experiments: mean power, $P = 40$ W; gas flux, $\Phi = 20$ sccm ($\Phi_{Ar} = 2$ sccm and $\Phi_{N2} = 18$ sccm); working pressure, $P_w = 30$ mTorr; functionalization time, $t = 5$ and 10 s.

4.4.4 Preparation of SERS Substrates

A stock aqueous solution (10^{-3} M) of Rhodamine B (RhB) was prepared and stored in a cold place. Upon dilution, solutions of different RhB concentrations ranging from 10^{-5} to 10^{-9} M were prepared from the stock solution. Exfoliated and functionalized TMDs deposited onto Si wafers were immersed into the aqueous RhB and dried under nitrogen flow, before subjecting them to SERS measurements. The same procedure was followed for the deposition of the polycyclic aromatic hydrocarbons, by employing acetone stock solutions (10^{-5} M) of pyrene, anthracence and 2,3-dihydroxy naphthalene in each case.

4.5 Appendix

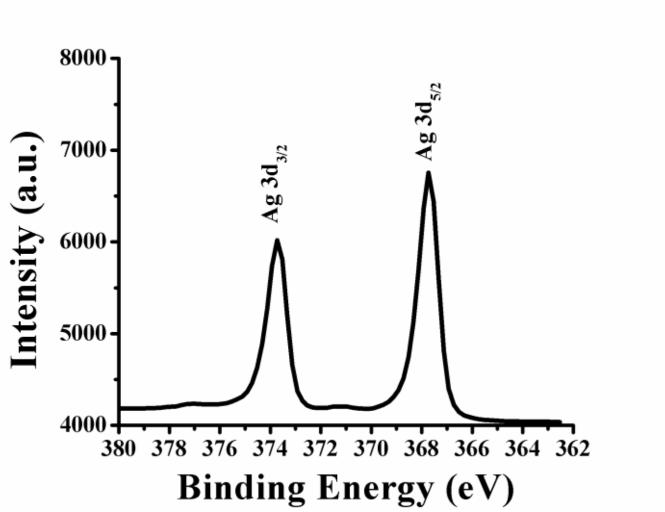

Figure S4.1 XPS core level peak regions for Ag 3d, after 5 s deposition onto a Si wafer.

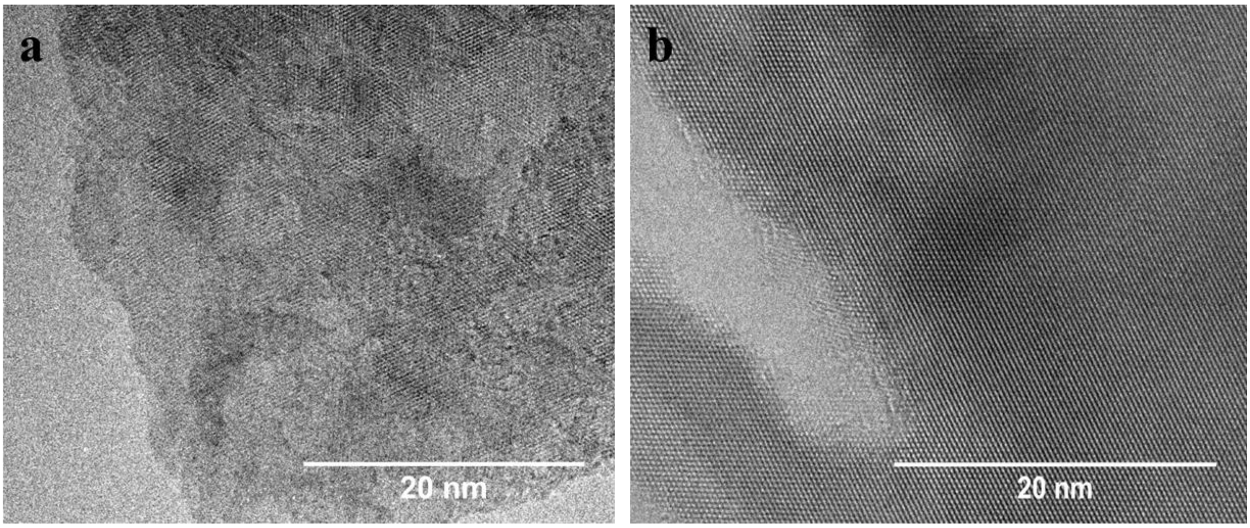

Figure S4.2 Representative TEM images for as-exfoliated (a) MoS_2, and (b) WS_2.

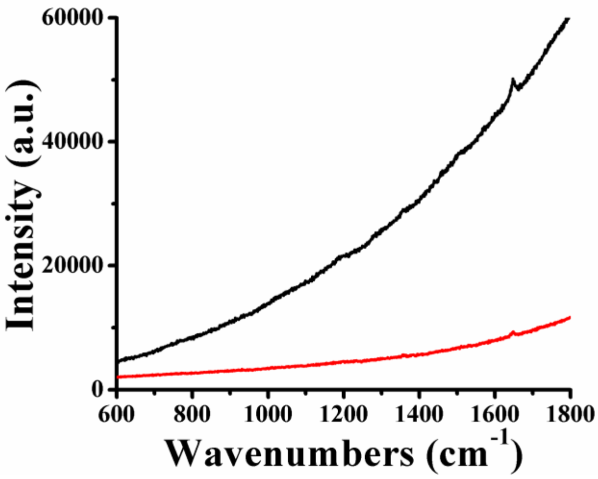

Figure S4.3 Raman spectra (514 nm) of RhB on Si wafer before (black) and after silver nanoparticles deposition (red).

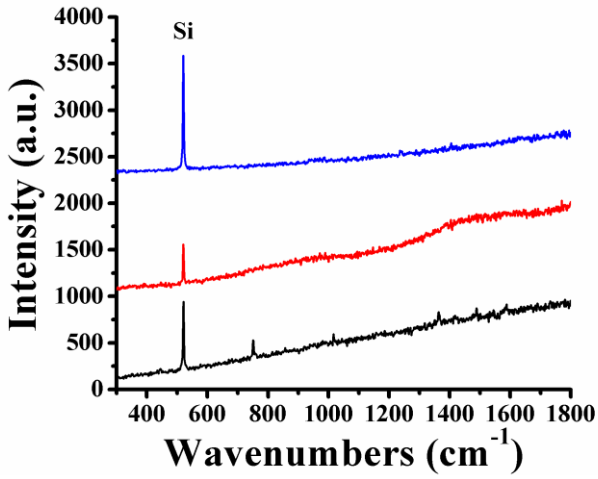

Figure S4.4 SERS spectra (514 nm) of 10^{-5} M pyrene (blue), anthracene (red) and 2,3-dihydroxy napthalene (black), on Si substrate after silver nanoparticles deposition.

References

1. Huang, X.; Zeng, Z.; Zhang, H., Metal dichalcogenide nanosheets: preparation, properties and applications. *Chem. Soc. Rev.***2013,** *42* (5), 1934-1946.

2. Pumera, M.; Sofer, Z.; Ambrosi, A., Layered transition metal dichalcogenides for electrochemical energy generation and storage. *J. Mater. Chem. A* **2014,** *2* (24), 8981-8987.

3. Perivoliotis, D. K.; Tagmatarchis, N., Recent advancements in metal-based hybrid electrocatalysts supported on graphene and related 2D materials for the oxygen reduction reaction. *Carbon* **2017,** *118*, 493-510.

4. Wang, Q. H.; Kalantar-Zadeh, K.; Kis, A.; Coleman, J. N.; Strano, M. S., Electronics and optoelectronics of two-dimensional transition metal dichalcogenides. *Nat. Nanotechnol.* **2012,** *7*, 699-712.

5. Zheng, J.; Zhang, H.; Dong, S.; Liu, Y.; Tai Nai, C.; Suk Shin, H.; Young Jeong, H.; Liu, B.; Ping Loh, K., High yield exfoliation of two-dimensional chalcogenides using sodium naphthalenide. *Nat. Commun.* **2014,** *5*, 2995.

6. Pagona, G.; Bittencourt, C.; Arenal, R.; Tagmatarchis, N., Exfoliated semiconducting pure 2H-MoS_2 and 2H-WS_2 assisted by chlorosulfonic acid. *Chem. Commun.* **2015,** *51* (65), 12950-12953.

7. Yao, Y.; Tolentino, L.; Yang, Z.; Song, X.; Zhang, W.; Chen, Y.; Wong, C. p., High-Concentration Aqueous Dispersions of MoS_2. *Adv. Funct. Mater.* **2013,** *23* (28), 3577-3583.

8. Eda, G.; Yamaguchi, H.; Voiry, D.; Fujita, T.; Chen, M.; Chhowalla, M., Photoluminescence from Chemically Exfoliated MoS_2. *Nano Lett.* **2011,** *11* (12), 5111-5116.

9. Coleman, J. N.; Lotya, M.; O'Neill, A.; Bergin, S. D.; King, P. J.; Khan, U.; Young, K.; Gaucher, A.; De, S.; Smith, R. J.; Shvets, I. V.; Arora, S. K.; Stanton, G.; Kim, H.-Y.; Lee, K.; Kim, G. T.; Duesberg, G. S.; Hallam, T.; Boland, J. J.; Wang, J. J.; Donegan, J. F.; Grunlan, J. C.; Moriarty, G.; Shmeliov, A.; Nicholls, R. J.; Perkins, J. M.; Grieveson, E. M.; Theuwissen, K.; McComb, D. W.; Nellist, P. D.; Nicolosi, V., Two-Dimensional Nanosheets Produced by Liquid Exfoliation of Layered Materials. *Science* **2011,** *331* (6017), 568-571.

10. Chen, X.; McDonald Aidan, R., Functionalization of Two-Dimensional Transition-Metal Dichalcogenides. *Adv. Mater.* **2016,** *28* (27), 5738-5746.

11. Voiry, D.; Goswami, A.; Kappera, R.; Silva, C. d. C. C. e.; Kaplan, D.; Fujita, T.; Chen, M.; Asefa, T.; Chhowalla, M., Covalent functionalization of monolayered transition metal dichalcogenides by phase engineering. *Nat. Chem.* **2014,** *7*, 45.

12. Knirsch, K. C.; Berner, N. C.; Nerl, H. C.; Cucinotta, C. S.; Gholamvand, Z.; McEvoy, N.; Wang, Z.; Abramovic, I.; Vecera, P.; Halik, M.; Sanvito, S.; Duesberg, G. S.; Nicolosi, V.; Hauke, F.; Hirsch, A.; Coleman, J. N.; Backes, C., Basal-Plane Functionalization of Chemically Exfoliated Molybdenum Disulfide by Diazonium Salts. *ACS Nano* **2015,** *9* (6), 6018-6030.

13. Canton-Vitoria, R.; Sayed-Ahmad-Baraza, Y.; Pelaez-Fernandez, M.; Arenal, R.; Bittencourt, C.; Ewels, C. P.; Tagmatarchis, N., Functionalization of MoS_2 with 1,2-dithiolanes: toward donor-acceptor nanohybrids for energy conversion. *npj 2D Mater. Appl.* **2017,** *1* (1), 13.

14. Zuccaro, L.; Kern, K.; Balasubramanian, K., Identifying Chemical Functionalization on Individual Carbon Nanotubes and Graphene by Local Vibrational Fingerprinting. *ACS Nano* **2015,** *9* (3), 3314-3323.

15. Deng, Z.; Chen, M.; Wu, L., Novel Method to Fabricate SiO_2/Ag Composite Spheres and Their Catalytic, Surface-Enhanced Raman Scattering Properties. *J. Phys. Chem. C* **2007,** *111* (31), 11692-11698.

16. Shang, B.; Wang, Y.; Yang, P.; Peng, B.; Deng, Z., Synthesis of superhydrophobic polydopamine-Ag microbowl/nanoparticle array substrates for highly sensitive, durable and reproducible surface-enhanced Raman scattering detection. *Sens. Actuators, B* **2018,** *255*, 995-1005.

17. Xie, L.; Ling, X.; Fang, Y.; Zhang, J.; Liu, Z., Graphene as a Substrate To Suppress Fluorescence in Resonance Raman Spectroscopy. *J. Am. Chem. Soc.***2009,** *131* (29), 9890-9891.

18. Kannan, P. K.; Late, D. J.; Morgan, H.; Rout, C. S., Recent developments in 2D layered inorganic nanomaterials for sensing. *Nanoscale* **2015,** *7* (32), 13293-13312.

19. Lee, Y.; Kim, H.; Lee, J.; Yu, S. H.; Hwang, E.; Lee, C.; Ahn, J.-H.; Cho, J. H., Enhanced Raman Scattering of Rhodamine 6G Films on Two-Dimensional Transition Metal Dichalcogenides Correlated to Photoinduced Charge Transfer. *Chem. Mater.* **2016,** *28* (1), 180-187.

20. Ling, X.; Fang, W.; Lee, Y.-H.; Araujo, P. T.; Zhang, X.; Rodriguez-Nieva, J. F.; Lin, Y.; Zhang, J.; Kong, J.; Dresselhaus, M. S., Raman Enhancement Effect on Two-Dimensional Layered Materials: Graphene, h-BN and MoS_2. *Nano Lett.* **2014,** *14* (6), 3033-3040.

21. Muehlethaler, C.; Considine, C. R.; Menon, V.; Lin, W.-C.; Lee, Y.-H.; Lombardi, J. R., Ultrahigh Raman Enhancement on Monolayer MoS_2. *ACS Photonics* **2016,** *3* (7), 1164-1169.

22. Li, X.; Zhu, J.; Wei, B., Hybrid nanostructures of metal/two-dimensional nanomaterials for plasmon-enhanced applications. *Chem. Soc. Rev.* **2016,** *45* (11), 3145-3187.

23. Jain, P. K.; Huang, X.; El-Sayed, I. H.; El-Sayed, M. A., Review of Some Interesting Surface Plasmon Resonance-enhanced Properties of Noble Metal Nanoparticles and Their Applications to Biosystems. *Plasmonics* **2007,** *2* (3), 107-118.

24. Chen, H.; Shao, L.; Li, Q.; Wang, J., Gold nanorods and their plasmonic properties. *Chem. Soc. Rev.* **2013,** *42* (7), 2679-2724.

25. Su, S.; Zhang, C.; Yuwen, L.; Chao, J.; Zuo, X.; Liu, X.; Song, C.; Fan, C.; Wang, L., Creating SERS Hot Spots on MoS_2 Nanosheets with in Situ Grown Gold Nanoparticles. *ACS Appl. Mater. Interfaces* **2014,** *6* (21), 18735-18741.

26. Singha, S. S.; Nandi, D.; Singha, A., Tuning the photoluminescence and ultrasensitive trace detection properties of few-layer MoS_2 by decoration with gold nanoparticles. *RSC Adv.* **2015,** *5* (31), 24188-24193.

27. Zhao, J.; Zhang, Z.; Yang, S.; Zheng, H.; Li, Y., Facile synthesis of MoS_2 nanosheet-silver nanoparticles composite for surface enhanced Raman scattering and electrochemical activity. *J. Alloys Compd.* **2013,** *559*, 87-91.

28. Li, Z.; Jiang, S.; Xu, S.; Zhang, C.; Qiu, H.; Li, C.; Sheng, Y.; Huo, Y.; Yang, C.; Man, B., Few-layer MoS_2-encapsulated Cu nanoparticle hybrids fabricated by two-step annealing process for surface enhanced Raman scattering. *Sens. Actuators, B* **2016,** *230*, 645-652.

29. Zhang, D.; Wu, Y.-C.; Yang, M.; Liu, X.; Coileáin, C. Ó.; Abid, M.; Abid, M.; Wang, J.-J.; Shvets, I.; Xu, H.; Chun, B. S.; Liu, H.; Wu, H.-C., Surface enhanced Raman scattering of monolayer MX_2 with metallic nano particles. *Sci. Rep.* **2016,** *6*, 30320.

30. Lu, J.; Lu, J. H.; Liu, H.; Liu, B.; Gong, L.; Tok, E. S.; Loh, K. P.; Sow, C. H., Microlandscaping of Au Nanoparticles on Few-Layer MoS_2 Films for Chemical Sensing. *Small* **2015,** *11* (15), 1792-1800.

31. Kretschmer, S.; Komsa, H.-P.; Bøggild, P.; Krasheninnikov, A. V., Structural Transformations in Two-Dimensional Transition-Metal Dichalcogenide MoS_2 under an Electron Beam: Insights from First-Principles Calculations. *J. Phys. Chem. Lett* **2017,** *8* (13), 3061-3067.

32. Gao, G.; Jiao, Y.; Ma, F.; Jiao, Y.; Waclawik, E.; Du, A., Charge Mediated Semiconducting-to-Metallic Phase Transition in Molybdenum Disulfide Monolayer and Hydrogen Evolution Reaction in New 1T′ Phase. *J. Phys. Chem. C* **2015,** *119* (23), 13124-13128.

33. Sun, L.; Hu, H.; Zhan, D.; Yan, J.; Liu, L.; Teguh Jefri, S.; Yeow Edwin, K. L.; Lee Pooi, S.; Shen, Z., Plasma Modified MoS_2 Nanoflakes for Surface Enhanced Raman Scattering. *Small* **2014,** *10* (6), 1090-1095.

34. Zeng, Z.; Yin, Z.; Huang, X.; Li, H.; He, Q.; Lu, G.; Boey, F.; Zhang, H., Single-Layer Semiconducting Nanosheets: High-Yield Preparation and Device Fabrication. *Angew. Chem.* **2011,** *50* (47), 11093-11097.

35. Deng, Y.; Chen, M.; Zhang, J.; Wang, Z.; Huang, W.; Zhao, Y.; Nshimiyimana, J. P.; Hu, X.; Chi, X.; Hou, G.; Zhang, X.; Guo, Y.; Sun, L., Thickness-dependent morphologies of Ag on n-layer MoS_2 and its surface-enhanced Raman scattering. *Nano Res.* **2016,** *9* (6), 1682-1688.

36. Li, H.; Zhang, Q.; Yap Chin Chong, R.; Tay Beng, K.; Edwin Teo Hang, T.; Olivier, A.; Baillargeat, D., From Bulk to Monolayer MoS_2: Evolution of Raman Scattering. *Adv. Funct. Mater.* **2012,** *22* (7), 1385-1390.

37. Wu, M.; Zhan, J.; Wu, K.; Li, Z.; Wang, L.; Geng, B.; Wang, L.; Pan, D., Metallic 1T MoS_2 nanosheet arrays vertically grown on activated carbon fiber cloth for enhanced Li-ion storage performance. *J. Mater. Chem. A* **2017,** *5* (27), 14061-14069.

38. Chakraborty, B.; Matte, H. S. S. R.; Sood, A. K.; Rao, C. N. R., Layer-dependent resonant Raman scattering of a few layer MoS_2. *J. Raman Spectrosc.* **2012,** *44* (1), 92-96.

39. Lee, C.; Yan, H.; Brus, L. E.; Heinz, T. F.; Hone, J.; Ryu, S., Anomalous Lattice Vibrations of Single- and Few-Layer MoS_2. *ACS Nano* **2010,** *4* (5), 2695-2700.

40. Bae, S.; Sugiyama, N.; Matsuo, T.; Raebiger, H.; Shudo, K.-i.; Ohno, K., Defect-Induced Vibration Modes of Ar^+-Irradiated MoS_2. *Phys. Rev. Appl.* **2017,** *7* (2), 024001.

41. Acerce, M.; Voiry, D.; Chhowalla, M., Metallic 1T phase MoS_2 nanosheets as supercapacitor electrode materials. *Nat. Nanotechnol.* **2015,** *10*, 313–318.

42. Ding, Q.; Meng, F.; English, C. R.; Cabán-Acevedo, M.; Shearer, M. J.; Liang, D.; Daniel, A. S.; Hamers, R. J.; Jin, S., Efficient Photoelectrochemical Hydrogen Generation

Using Heterostructures of Si and Chemically Exfoliated Metallic MoS_2. *J. Am. Chem. Soc.***2014,** *136* (24), 8504-8507.

43. Mahler, B.; Hoepfner, V.; Liao, K.; Ozin, G. A., Colloidal Synthesis of 1T-WS_2 and 2H-WS_2 Nanosheets: Applications for Photocatalytic Hydrogen Evolution. *J. Am. Chem. Soc.***2014,** *136* (40), 14121-14127.

44. Loh, T. A. J.; Chua, D. H. C., Origin of Hybrid 1T- and 2H-WS_2 Ultrathin Layers by Pulsed Laser Deposition. *J. Phys. Chem. C* **2015,** *119* (49), 27496-27504.

45. Boyen, H. G.; Ethirajan, A.; Kästle, G.; Weigl, F.; Ziemann, P.; Schmid, G.; Garnier, M. G.; Büttner, M.; Oelhafen, P., Alloy Formation of Supported Gold Nanoparticles at Their Transition from Clusters to Solids: Does Size Matter? *Phys. Rev. Lett.* **2005,** *94* (1), 016804.

46. Michaels, A. M.; Nirmal, M.; Brus, L. E., Surface Enhanced Raman Spectroscopy of Individual Rhodamine 6G Molecules on Large Ag Nanocrystals. *J. Am. Chem. Soc.***1999,** *121* (43), 9932-9939.

47. Liu, X.; Shao, Y.; Tang, Y.; Yao, K.-F., Highly Uniform and Reproducible Surface Enhanced Raman Scattering on Air-stable Metallic Glassy Nanowire Array. *Sci. Rep.* **2014,** *4*, 5835.

48. He, Y.; Su, S.; Xu, T.; Zhong, Y.; Zapien, J. A.; Li, J.; Fan, C.; Lee, S.-T., Silicon nanowires-based highly-efficient SERS-active platform for ultrasensitive DNA detection. *Nano Today* **2011,** *6* (2), 122-130.

49. Chang, C.-C.; Yang, K.-H.; Liu, Y.-C.; Hsu, T.-C.; Mai, F.-D., Surface-Enhanced Raman Scattering-Active Au/SiO_2 Nanocomposites Prepared Using Sonoelectrochemical Pulse Deposition Methods. *ACS Appl. Mater. Interfaces* **2012,** *4* (9), 4700-4707.

50. Li, J.; Zhang, W.; Lei, H.; Li, B., Ag nanowire/nanoparticle-decorated MoS_2 monolayers for surface-enhanced Raman scattering applications. *Nano Res.* **2018,** *11* (4), 2181-2189.

51. Zheng, Z.; Cong, S.; Gong, W.; Xuan, J.; Li, G.; Lu, W.; Geng, F.; Zhao, Z., Semiconductor SERS enhancement enabled by oxygen incorporation. *Nat. Commun.* **2017,** *8* (1), 1993.

52. Shorie, M.; Kumar, V.; Kaur, H.; Singh, K.; Tomer, V. K.; Sabherwal, P., Plasmonic DNA hotspots made from tungsten disulfide nanosheets and gold nanoparticles for ultrasensitive aptamer-based SERS detection of myoglobin. *Microchim. Acta* **2018,** *185* (3), 158.

53. Le Ru, E. C.; Blackie, E.; Meyer, M.; Etchegoin, P. G., Surface Enhanced Raman Scattering Enhancement Factors: A Comprehensive Study. *J. Phys. Chem. C* **2007,** *111* (37), 13794-13803.

54. Zuo, P.; Jiang, L.; Li, X.; Li, B.; Xu, Y.; Shi, X.; Ran, P.; Ma, T.; Li, D.; Qu, L.; Lu, Y.; Grigoropoulos, C. P., Shape-Controllable Gold Nanoparticle–MoS_2 Hybrids Prepared by Tuning Edge-Active Sites and Surface Structures of MoS_2 via Temporally Shaped Femtosecond Pulses. *ACS Appl. Mater. Interfaces* **2017,** *9* (8), 7447-7455.

55. Stamplecoskie, K. G.; Scaiano, J. C.; Tiwari, V. S.; Anis, H., Optimal Size of Silver Nanoparticles for Surface-Enhanced Raman Spectroscopy. *J. Phys. Chem. C* **2011,** *115* (5), 1403-1409.

56. Ciou, S.-H.; Cao, Y.-W.; Huang, H.-C.; Su, D.-Y.; Huang, C.-L., SERS Enhancement Factors Studies of Silver Nanoprism and Spherical Nanoparticle Colloids in The Presence of Bromide Ions. *J. Phys. Chem. C* **2009,** *113* (22), 9520-9525.

57. Fan, W.; Lee, Y. H.; Pedireddy, S.; Zhang, Q.; Liu, T.; Ling, X. Y., Graphene oxide and shape-controlled silver nanoparticle hybrids for ultrasensitive single-particle surface-enhanced Raman scattering (SERS) sensing. *Nanoscale* **2014,** *6* (9), 4843-4851.

58. Lu, G.; Li, H.; Liusman, C.; Yin, Z.; Wu, S.; Zhang, H., Surface enhanced Raman scattering of Ag or Au nanoparticle-decorated reduced graphene oxide for detection of aromatic molecules. *Chem. Sci.* **2011,** *2* (9), 1817-1821.

59. Zuo, P.; Jiang, L.; Li, X.; Li, B.; Ran, P.; Li, X.; Qu, L.; Lu, Y., Metal (Ag, Pt)–MoS_2 Hybrids Greenly Prepared Through Photochemical Reduction of Femtosecond Laser Pulses for SERS and HER. *ACS Sustainable Chem. Eng.* **2018,** *6* (6), 7704-7714.

60. Campion, A.; Kambhampati, P., Surface-enhanced Raman scattering. *Chem. Soc. Rev.***1998,** *27* (4), 241-250.

61. Wang, X.; Li, M.; Meng, L.; Lin, K.; Feng, J.; Huang, T.; Yang, Z.; Ren, B., Probing the Location of Hot Spots by Surface-Enhanced Raman Spectroscopy: Toward Uniform Substrates. *ACS Nano* **2014,** *8* (1), 528-536.

62. Conney, A. H., Induction of Microsomal Enzymes by Foreign Chemicals and Carcinogenesis by Polycyclic Aromatic Hydrocarbons: G. H. A. Clowes Memorial Lecture. *Cancer Res.* **1982,** *42* (12), 4875-4917.

63. Long, D. A. Infrared and Raman characteristic group frequencies. Tables and charts George Socrates John Wiley and Sons, Ltd, Chichester, Third Edition, 2001. *J. Raman Spectrosc.* 2004, *35*, 905−905.

64. Guerrini, L.; Garcia-Ramos, J. V.; Domingo, C.; Sanchez-Cortes, S. Sensing Polycyclic Aromatic Hydrocarbons with Dithiocarbamate-Functionalized Ag Nanoparticles by Surface-Enhanced Raman Scattering. *Anal. Chem.* **2009**, *81*, 953−960.

65. Xie, Y.; Wang, X.; Han, X.; Song, W.; Ruan, W.; Liu, J.; Zhao, B.; Ozaki, Y. Selective SERS Detection of Each Polycyclic Aromatic Hydrocarbon (PAH) in a Mixture of Five Kinds of PAHs. *J. Raman Spectrosc.* **2011**, *42*, 945−950.

66. Gu, X.; Tian, S.; Zhou, Q.; Adkins, J.; Gu, Z.; Li, X.; Zheng, J. SERS Detection of Polycyclic Aromatic Hydrocarbons on a Bowl-Shaped Silver Cavity Substrate. *RSC Adv.* **2013**, *3*, 25989−25996.

67. Kwon, Y. H.; Sowoidnich, K.; Schmidt, H.; Kronfeldt, H. D. Application of Calixarene to High Active Surface-Enhanced Raman Scattering (SERS) Substrates Suitable for In Situ Detection of Polycyclic Aromatic Hydrocarbons (PAHs) in Seawater. *J. Raman Spectrosc.* **2012**, *43*, 1003−1009.

68. Jiang, M.; Qian, Z.; Zhou, X.; Xin, X.; Wu, J.; Chen, C.; Zhang, G.; Xu, G.; Cheng, Y. CTAB Micelles Assisted rGO-AgNP Hybrids for SERS Detection of Polycyclic Aromatic Hydrocarbons. Phys. *Chem. Chem. Phys.* **2015**, *17*, 21158−21163.

Chapter 5

Metal nanocluster/MoS$_2$ ensembles for managing electronic processes in photocatalysis

Abstract

Metal nanoclusters (M$_{NCs}$) based on gold as core and silver as shell, abbreviated as Ag@Au$_{NCs}$, were electrostatically associated with functionalized semiconducting MoS$_2$ nanosheets, abbreviated as *f*-MoS$_2$. The realization of the Ag@Au$_{NCs}$/*f*-MoS$_2$ ensemble was manifested by UV-Vis and photoluminescence titration assays, while its morphology was evidenced by high-angle annular dark-field STEM imaging coupled with EDX analyses. Photoinduced intra-ensemble charge-transfer phenomena were witnessed and attributed to the suppression and concomitant shift of Ag@Au$_{NC}$ photoluminescence by incremental additions of *f*-MoS$_2$. The Ag@Au$_{NCs}$/*f*-MoS$_2$ was employed as RhB photodegradation catalyst for wastewater purification from organic pollutant dyes. The production of highly oxidant radicals from the photogenerated electron-hole pairs within Ag@Au$_{NCs}$/*f*-MoS$_2$ were found to be the main reactive species, while the holes left on Ag@Au$_{NCs}$ attacked RhB, as evidenced by the disappearance of the characteristic absorption band. The photocatalytic reaction by the ensemble followed fast kinetics as compared with bare Ag@Au$_{NCs}$ or individual Au$_{NCs}$ and Ag$_{NCs}$.

5.1 Introduction

Ultra-small metal particles in the size regime of 1-3 nm, so-called metal nanoclusters (M_{NCs}), have reached blooming attention due to their intriguing characteristics such as optical, electronic and physical properties, as already examined in Chapter 3.[1-2] Particularly, their strong photoluminescence together with the good biocompatibility and low toxicity offer bonus potentials in diverse applications.[3-4] Therefore, M_{NCs} can have a considerable role in photocatalysis and solar energy conversion schemes due to the high surface-to-volume ratio, unique surface electronic properties and enhanced charge carrier mobility. Such features provide M_{NCs} with rich active sites vital for catalytic processes as compared with the larger metal nanoparticles.[5] Indeed, M_{NCs} have been employed in photocatalytic redox schemes, such as water splitting and oxidative pollutants degradation, when supported onto graphene and TiO_2.[6-9] In these systems, photogenerated electrons from M_{NCs} are transferred to the supporting material, thereby inducing charge-separation and retarding charge recombination. Those separated charges, holes on M_{NCs} and electrons on supporting materials, can be efficiently employed to either reduce water molecules or generate highly oxidative species attacking and decomposing organic contaminant moieties. For example, glutathione labeled Au_{NCs} attached on mesoscopic TiO_2 when employed as sensitizer in photoelectrochemical water splitting, produced great photocurrent activity under visible light excitation, comparable to that of CdS quantum dots, and injection of photogenerated electrons on TiO_2.[10-11] As we previously shown, upon incorporation of aqueous Au_{NCs} on properly functionalized graphene sheets, the photoreduction of 4-nitrophenol to the corresponding 4-aminophenol was accomplished.[7] The reaction proceeds via hydride transfer from photogenerated Au-H and hydrogen produced by the photoreduction of water, with exceptionally high kinetics. The previous result was attributed not only to photoinduced electron transfer from Au_{NCs} to graphene sheets, which were employed for the reduction of water and hydrogen production, but also to presence of conductive sp^2 sites on graphene stabilizing the formation of photoinduced Au-H.

Combining the unique physicochemical and electronic characteristics of individual M_{NCs}, improved and/or novel properties are evolved in bimetallic core-shell type $M^1@M^2_{NCs}$ due to interactions between the two metallic electronic states. Hence, core-shell $M^1@M^2_{NCs}$ are anticipated to function as promising alternative photocatalysts. For instance, when combining Au_{NCs} with Ag_{NCs} new surface and optical features can be developed between the two different metal elements, bringing remarkable properties into play. In prominent examples, core-shell $Ag@Au_{NCs}$ were employed for the selective chemical sensing of heavy metals (e.g. Cu^{2+}, Hg^{2+}, Al^{3+})[12-15] and hydrogen peroxide.[16] Consequently, $Ag@Au_{NCs}$ are at the forefront of current research investigations for developing alternative fluorescent agents that boast both the desirable optical characteristics of Au_{NCs} and Ag_{NCs}. However, the stability of M_{NCs} under *in situ* photoirradiation conditions still remains a bottleneck for their rational application in photocatalytic systems.[17]

On the other hand, transition metal dichalcogenides (TMDs) have sparked tremendous research interest due to their exceptional structural and optoelectronic properties.[18]

Molybdenum disulfide MoS_2 is a prototypical TMD composed of a stratum of molybdenum atom sandwiched between two planes of sulfur atoms.[19-20] Delaminated MoS_2 can be obtained by exfoliation (mechanical or chemical) of the bulk counterpart yielding semiconducting or metallic nanosheets depending on the exfoliating moieties involved.[21-26] However, considering the limited solubility of MoS_2, which handicaps effective handling and manipulation in liquid media, functionalization and formation of hybrid structures is important to enhance their versatility. The latter point can be addressed by chemical modification of exfoliated MoS_2,[27-30] which at the same time tailors the electronic properties of TMDs by tuning the charge-carrier density.[31] Equally, defects provide a safe avenue to modify the optoelectronic properties of MoS_2, particularly when considering that defects can be naturally introduced during the exfoliation process. On this background, a facile and straightforward functionalization route involves reaction with 1,2-dithiolane derivatives possessing high binding affinity for Mo atoms located at the edges with S vacancies.[32-34]

Driven by global environmental degradation, renewable photocatalytic solar energy conversion schemes hold great promise to be an efficient technology for removal of contaminant molecules such as organic dyes from wastewater. Hence, the design of new photocatalysts that can efficiently harvest solar energy, convert it into charge carriers and allow the occurrence of controlled electron transfer reactions is necessary. Ultimately, in donor-acceptor ensembles, such processes enable the generation of highly reactive species, via the efficient reduction of dioxygen by the presence of accumulated electrons at the acceptor site. Considering all the above points, $M^1@M^2_{NCs}$ and TMDs, as two of the most promising nanomaterials in the energy field, each one with unique characteristics and properties, coalesced en route to the realization of novel donor-acceptor ensembles. Specifically, aqueous semiconductor core-shell $Ag@Au_{NCs}$ were combined with functionalized semiconducting MoS_2 nanosheets, abbreviated as f-MoS_2, to yield $Ag@Au_{NCs}/f$-MoS_2, which were subsequently examined as photocatalyst for the degradation of rhodamine B (RhB). To achieve the aims of the current study, we initially hypothesize that the bimetallic core-shell $Ag@Au_{NCs}$ are anticipated to demonstrate enhanced catalytic activity as compared with the monometallic counterparts, as synergistic effects such as strong fluorescent emission and stability can be exploited. Herein, core-shell $Ag@Au_{NCs}$ were labeled with bovine serum albumin (BSA) protein bearing negative charges at alkaline media due to ionization of the carboxylic acids present in the protein. Notably, the applied synthesis procedure for $Ag@Au_{NCs}$ is an environmentally friendly method since the protocol involves aqueous media and the absence of any toxic stabilizing and/or reducing agent. On the other hand, functionalized MoS_2 sheets carrying positively charged ammonium moieties were prepared via reaction of exfoliated MoS_2 with a 1,2-dithiolane derivative bearing an ethylene glycol alkyl chain terminated to a butoxycarbonyl (BOC) protected amine, followed by acidic deprotection of the BOC group, and employed to form $Ag@Au_{NCs}/f$-MoS_2 ensembles via electrostatic interactions between the two species. The successful fabrication of $Ag@Au_{NCs}/f$-MoS_2 was manifested through electronic absorption and photoluminescence spectroscopy and morphologically evaluated by high-resolution transmission electron microscopy (HRTEM) imaging. The photocatalytic properties of $Ag@Au_{NCs}/f$-MoS_2 towards the decomposition of RhB were examined by monitoring temporal spectral changes in the absorption spectrum of the dye. The photodegradation of RhB by Ag@Au$_{NCs}$/*f*-MoS$_2$ follows fast kinetics as compared to that on bare Ag@Au$_{NCs}$ or individual Au$_{NCs}$ and Ag$_{NCs}$ unveiling the important role of MoS$_2$ as substrate for the catalytic reaction. Furthermore, charge-transfer phenomena were witnessed to occur within Ag@Au$_{NCs}$/*f*-MoS$_2$, with the production of highly oxidant radicals being responsible for the photocatalytic degradation of RhB, while on an additional path, photogenerated holes on Ag@Au$_{NCs}$ can also directly attack and degrade the dye.

5.2 Results and discussion

5.2.1 Preparation of Ag@Au$_{NCs}$/*f*-MoS$_2$ ensembles

Core-shell Ag@Au$_{NCs}$ were prepared employing BSA as stabilizer and aqueous chlorauric acid as precursor for the formation of the core (Scheme 5.1a). BSA was employed as stabilizer for the preparation of Ag@Au$_{NCs}$ considering its beneficial role as a “protective cage effect” avoiding photobleaching phenomena.[35] In parallel, BSA acts as reducing agent preventing the use of additional reducing species (e.g. NaBH$_4$), which could involve an extra step of purification. In addition, Au$_{NCs}$ were selected as core since they form stable and robust particles of uniform size, facilitating the growth of Ag$_{NCs}$ on top of them in a controllable approach.[36] Briefly, under vigorous stirring of aqueous chlorauric acid and BSA, the reaction mixture turned into dark yellow, attributed to the reduction of Au^{3+} to Au^{1+} of most of the gold atoms, due to the reducing and stabilizing abilities of BSA. Then, the pH adjusted to an alkaline value (pH=12) upon addition of aqueous NaOH and the reaction mixture was heated. During that period, the color changed from dark yellow to bright red, indicating the reduction of gold atoms from Au^{1+} to Au^0 forming Au$_{NCs}$.[37] In the next step, the obtained Au$_{NCs}$ were used as core to prepare a shell of silver nanoclusters, by employing aqueous AgNO$_3$ as precursor. The addition of silver shell resulted firstly in the darkening of the reaction mixture from red to brownish, indicating the reduction of silver ions, and finally to bright orange witnessing the formation of Ag@Au$_{NCs}$, emitting intense red luminescence under UV light. The BSA protein, containing several aminoacids such as cysteine, serine, threonine, acted both as reducing and capping agents for the stabilization of Ag@Au$_{NCs}$. Especially, gold and silver ions can be reduced quite easily from a thermodynamic point of view. Unfolding of the BSA protein facilitates the reduction process, while regulation of temperature slightly above room temperature gave BSA the required amphiphilic behavior necessary for the surface activity to produce shape-directing effects in aqueous media. High concentration of BSA facilitated the formation of small stable fluorescent nanoclusters, whereas a lower one resulted in the growth of large non-fluorescent nanoparticles. Although further analysis is beyond the scope of the current work, it should be noted that, hydroxyl units in serine and threonine act as reducing agents, while cysteine (sulfhydryl groups) offers coordination to the gold surface.[38] The addition of NaOH increased the pH value, which is vital for enhancing the reducing ability of BSA for both gold and silver ions.[37, 39] Markedly, at the specific alkaline conditions set (i.e. pH=12), the BSA was ionized, hence, allowing the realization of negatively charged aqueous Ag@Au$_{NCs}$.

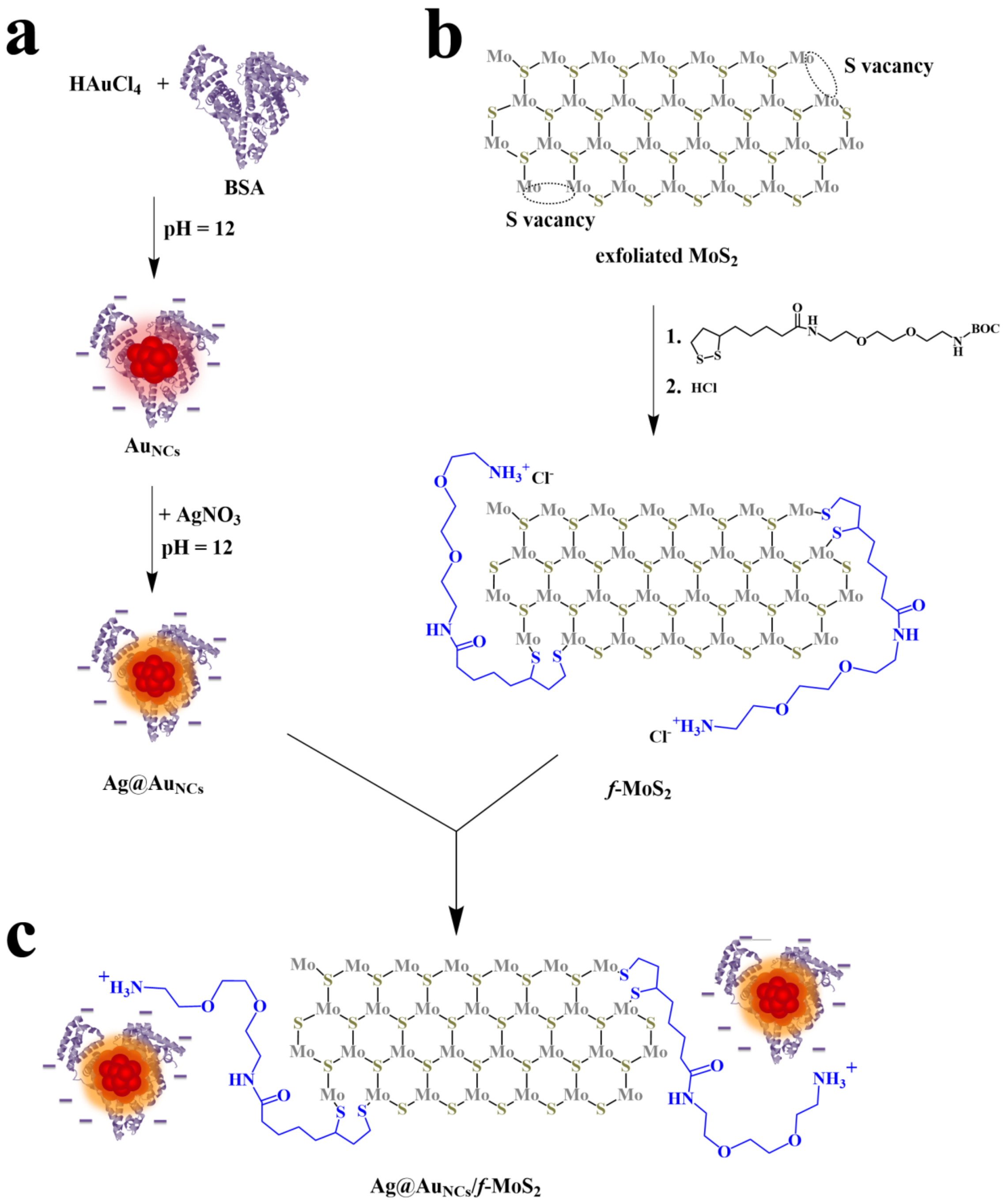

Scheme 5.1 Schematic illustration of the synthesis protocol leading to the formation of (a) Ag@Au$_{NCs}$, (b) functionalized *f*-MoS$_2$, and (c) Ag@Au$_{NCs}$/*f*-MoS$_2$ ensemble.

In parallel, chlorosulfonic acid assisted the exfoliation of MoS_2 from the bulk in the form of semiconducting nanosheets.[21] Afterwards, treatment of exfoliated MoS_2 with 1,2-dithiolane-based tert-butyl carbamate (BOC) derivative afforded BOC-modified MoS_2 based on the high binding affinity of 1,2-dithiolanes for the Mo atoms.[32] Filtration of the reaction mixture over a PTFE membrane and extensive washing of the solid product on top of the filter with dichloromethane aided the removal of unbound organic species. In the next step, the BOC-protecting group was effectively cleaved by acid treatment, which gave access to modified MoS_2 sheets decorated with ammonium species, furnishing water-soluble functionalized

MoS_2 (abbreviated as *f*-MoS_2), according to Scheme 5.1b. Next, the hybrid material was fabricated by incorporating the *f*-MoS_2 to Ag@Au_{NCs}. Notably, the positive charges on *f*-MoS_2, derived from the presence of ammonium species, were exploited for interacting with the negatively charged Ag@Au_{NCs} via attractive Coulombic forces, allowing the fabrication of the Ag@Au_{NCs}/*f*-MoS_2 ensemble (Scheme 5.1c).

5.2.2 Characterization of Ag@Au_{NCs}/*f*-MoS_2 ensembles

Attenuated-total-reflectance IR spectroscopy verified the successful functionalization of MoS_2 sheets. In the BOC-modified MoS_2, strong C–H vibrational modes were registered in the region 2840–2960 cm^{-1} owed to the alkyl chain of the addend. Furthermore, the presence of bands at 1645 and 1707 cm^{-1} was attributed to the carbonyl amide and BOC protecting units, respectively (Figure 5.1a).[40] Notably, the latter one became absent in the IR spectrum of *f*-MoS_2, witnessing the successful BOC de-protection process.

Next, Raman spectroscopy was used to provide essential information on the functionalization process of MoS_2. Upon resonantly excited MoS_2 at 633 nm, a number of additional modes were recorded, as compared with measurements under off-resonance conditions at 514 nm, due to strong electron-phonon coupling interactions. Four dominant Raman active modes, namely, A_{1g}-LA(M), E^1_{2g}, A_{1g} and 2LA(M) at 178, 380, 403 and 450 cm^{-1}, respectively, were clearly evident in both exfoliated MoS_2 and *f*-MoS_2. The E^1_{2g} and A_{1g} bands exhibit significant dependence on the thickness of MoS_2 stratums, while their frequency difference, ca. 23 cm^{-1}, highlights the existence of few-layered MoS_2.[41] The 2LA(M) vibration mode results from the resonance Raman scattering and is related to the S vacancies.[42] Comparing the two Raman spectra of exfoliated

MoS_2 and *f*-MoS_2, the intensity ratio of A_{1g}/2LA(M) is considerably higher in *f*-MoS_2, implying the suppression of 2LA(M) band for *f*-MoS_2, which is another evidence for the effective modification due to the elimination of S vacancies owed to functionalization (Figure 5.1b).[30, 43] Furthermore, it is worth noting the absence of bands due to metallic MoS_2 polytype so-called J_1, J_2 and J_3 at 150, 225 and 325 cm^{-1}, respectively, ensuring that semiconducting is the predominant phase in the employed MoS_2-based materials.

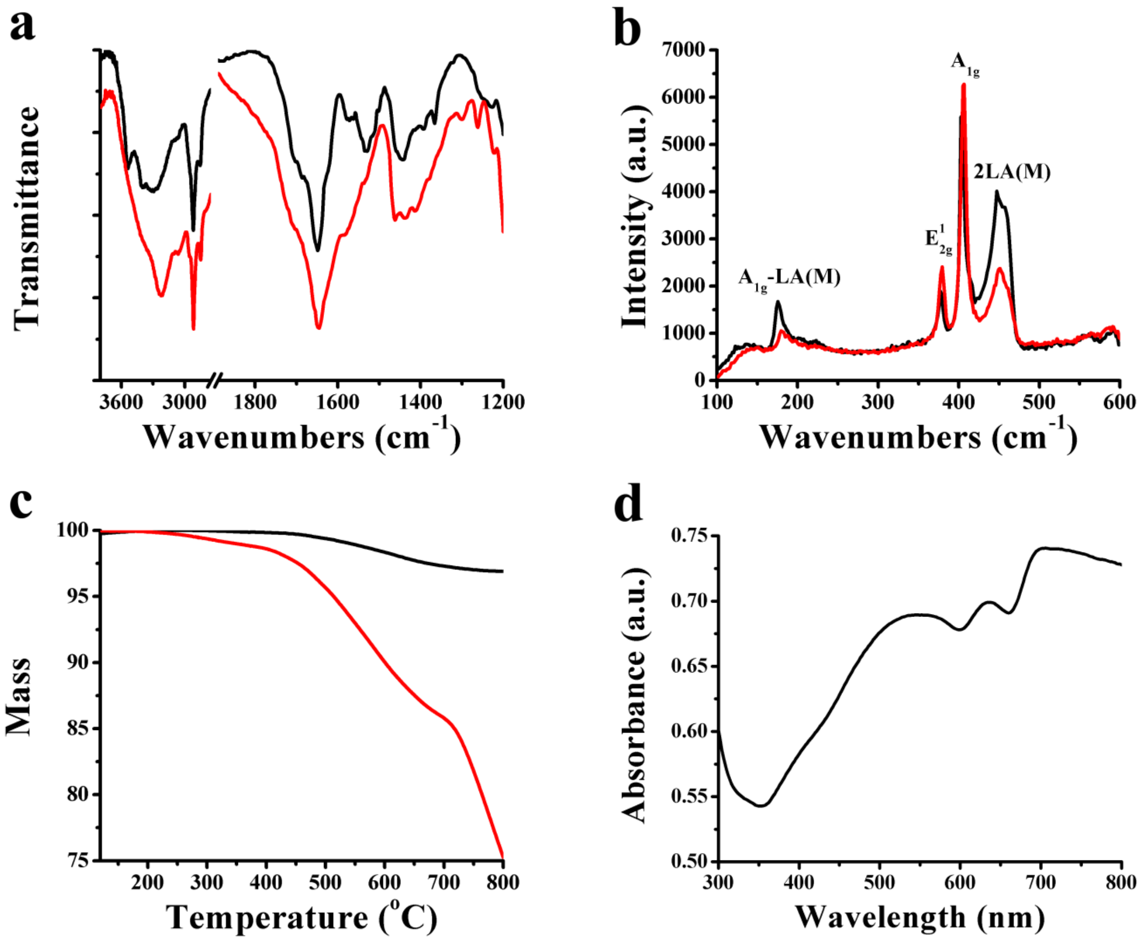

Figure 5.1 (a) ATR-IR spectra for BOC-modified MoS_2 (black) and ammonium functionalized *f*-MoS_2 (red). (b) Raman spectra (633 nm) for exfoliated MoS_2 (black) and ammonium functionalized *f*-MoS_2 (red). (c) Thermographs for exfoliated MoS_2 (black) and ammonium functionalized *f*-MoS_2 (red). (d) UV-Vis electronic absorption spectrum for exfoliated MoS_2 (black), obtained in dimethylformamide.

Thermogravimetric analysis (TGA) assisted in the quantitative calculation of the functionalization degree. Exfoliated MoS_2 sheets are thermally stable up to 800 ^oC under nitrogen atmosphere, whereas *f*-MoS_2 exhibited a mass loss of about 6% in the temperature range 200-500 ^oC (Figure 5.1c). Such mass loss is attributed to the thermal decomposition of the covalently bonded organic functionalities onto *f*-MoS_2.

The UV-Vis spectrum shows the characteristic excitonic transitions of the semiconducting phase of MoS_2 sheets, appearing at 690 and 630 nm, followed by direct transition from the valence to the conduction band at 500 and 400 nm (Figure 5.1d).[44] These transitions were also present in the absorption spectrum of *f*-MoS_2. A continuous absorption throughout the visible region was also evident and owed to the high transparency of MoS_2.

The morphology and elemental composition of the $Ag@Au_{NCs}$/*f*-MoS_2 ensemble was examined by HRTEM imaging and energy dispersive X-ray (EDX) mapping and spectroscopy analysis and compared with those allocated to $Ag@Au_{NCs}$, Ag_{NCs} and Au_{NCs}. A representative TEM image of $Ag@Au_{NCs}$/*f*-MoS_2, shown in Figure 5.2a, revealed uniform distribution of round-shaped $Ag@Au_{NCs}$ immobilized on *f*-MoS_2. Based on EDX analysis, the chemical composition of Ag@Au$_{\text{NCs}}$/*f*-MoS$_2$ was found to be Ag (2.98 keV), Au (2.12 and 9.7 keV), Mo (2.29 keV), S (2.30 keV), together with C (0.27 keV), O (0.52 keV) and N (0.39 keV) due to their presence in the organic addend on *f*-MoS$_2$ (Figure 5.2b). Furthermore, to acquire deeper insight on the Ag@Au$_{\text{NCs}}$/*f*-MoS$_2$, high-angle annular dark-field scanning TEM (HAADF-STEM) imaging coupled with EDX mapping was performed. The representative HAADF-STEM image shown in Figure 2c confirms the presence of round-shaped Ag@Au$_{\text{NCs}}$ with an average diameter of 3-4 nm on *f*-MoS$_2$ sheets, while EDX mapping revealed a core-shell structure with a Au-rich core (~ 2-3 nm) and a Ag shell (~ 1-2 nm), according to Figure 5.2d and e. Additional HAADF-STEM-EDX elemental mapping also manifested the existence of all chemical components of the Ag@Au$_{\text{NCs}}$/*f*-MoS$_2$ ensemble (Appendix, Figure S5.1). For the reference materials, Ag@Au$_{\text{NCs}}$, Au$_{\text{NCs}}$ and Ag$_{\text{NCs}}$, similar TEM images were acquired and found to possess round morphology with a mean diameter distribution of around 3, 2 and 2-5 nm, respectively (Appendix, Figure S5.2-4).

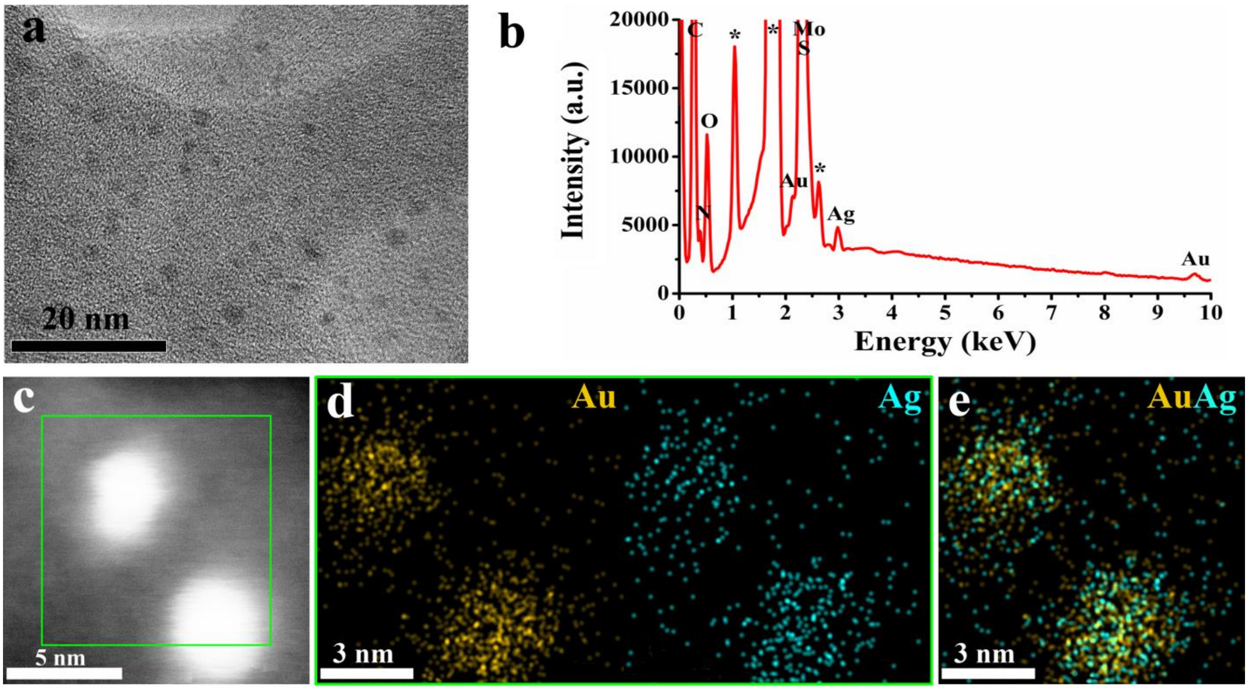

Figure 5.2 Representative (a) TEM image and (b) EDX spectrum of the Ag@Au$_{\text{NCs}}$/*f*-MoS$_2$ ensemble (peaks denoted with * are due to Na, Cl, and Si that come as impurity and from the sample holder). (c) HAADF-STEM image, and (d, e) EDX elemental mapping and overlay, respectively, for Au and Ag, of Ag@Au$_{\text{NCs}}$/*f*-MoS$_2$.

Moving on the wet phase examination for the formation of Ag@Au$_{\text{NCs}}$/*f*-MoS$_2$, electronic absorption and photoluminescence titration assays were conducted. The UV-Vis spectrum of aqueous Ag@Au$_{\text{NCs}}$ showed no distinguishable features in the visible region (Figure 5.3), in agreement with previous reports.[45] Apparently, the absence of a plasmonic band confirmed the formation of nanoclusters instead of large nanoparticles, which boast absorption in the region of 380-420 nm for silver nanoparticles and around 520 nm for gold ones.[3] For comparison reasons, the synthesis of individual Au$_{\text{NCs}}$ and Ag$_{\text{NCs}}$ was accomplished and the corresponding spectroscopic data are presented in the Appendix, Figure S5.5a and b, respectively. Our conception was to take advantage of the positive charges on *f*-MoS$_2$, originated from the presence of ammonium units, to tether with the negatively charged Ag@Au$_{NCs}$, owed to the presence of ionized BSA, via attractive Coulombic forces, allowing the realization of Ag@Au$_{NCs}$/*f*-MoS$_2$ hybrid. Based on UV-Vis titration assays, the development of an isosbestic point at 305 nm in the electronic absorption spectrum of Ag@Au$_{NCs}$, upon incremental additions

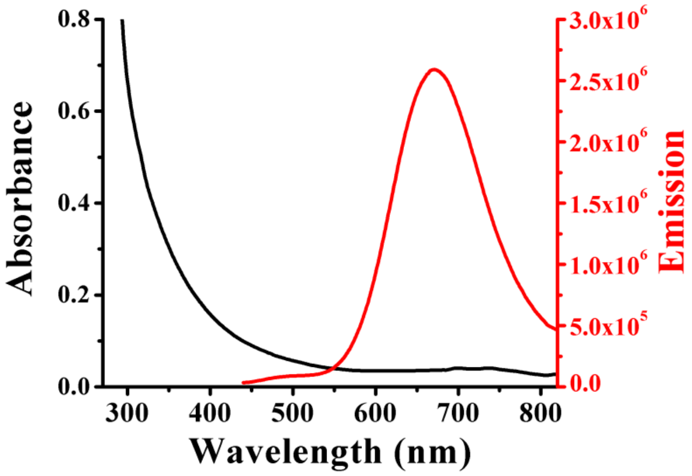

Figure 5.3 UV-Vis and photoluminescence spectra of Ag@Au$_{NCs}$ (excitation wavelength 420 nm).

of aqueous *f*-MoS$_2$, was manifested (Figure 5.4a), highlighting not only the successful formation of Ag@Au$_{NCs}$/*f*-MoS$_2$ but also the development of ground-state interactions between the individual species of the ensemble. Subtraction of the MoS$_2$ absorption background allowed a clear observation of the titration effects – please note that MoS$_2$ nanosheets show only characteristic bands beyond 400 nm. Particularly, the effect of *f*-MoS$_2$ additions on the Ag@Au$_{NCs}$ spectrum in UV-Vis titration assays without subtracting the corresponding MoS$_2$ bands is depicted in the Appendix, Figure S5.6. Similar isosbestic points were developed for Au$_{NCs}$/*f*-MoS$_2$ and Ag$_{NCs}$/*f*-MoS$_2$ at 320 and 520 nm, respectively, for exactly the same reasons (Appendix, Figure S5.7).

Examining possible interactions at the excited state, photoluminescence titration measurements were conducted. The characteristic emission of Ag@Au$_{NCs}$ at 670 nm upon excitation at 420 nm gradually quenched upon cumulative additions of *f*-MoS$_2$ (Figure 5.4b). Notably, fluorescence titration analyses revealed an intense shift to higher wavelengths from 670 to 705 nm (i.e. 35 nm red shift) together with a gradual decrease and broadening of the corresponding intensity of the Ag@Au$_{NCs}$ centred fluorescence for the various amounts of *f*-MoS$_2$ added. The considerable quenching of photoluminescence prompts to an additional decay channel, which occurs from the photoexcited state of Ag@Au$_{NCs}$ and is indicative of charge and/or energy transfer processes existing within the ensemble.

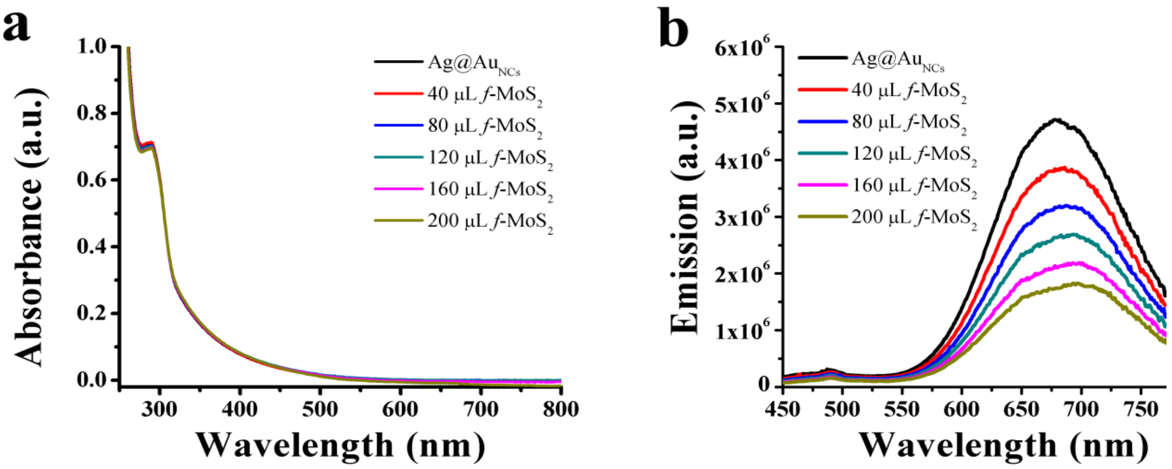

Figure 5.4 (a) UV-Vis absorption and (b) photoluminescence titration assay spectra for Ag@Au$_{NCs}$, upon incremental additions of *f*-MoS$_2$, obtained at λ_{exc} 420 nm.

5.2.3 Catalytic activity of Ag@Au$_{NCs}$/*f*-MoS$_2$

After the optical properties of Ag@Au$_{NCs}$/*f*-MoS$_2$ were successfully ascertained and interpreted by electronic absorption and fluorescence emission spectroscopy, the catalytic performance towards the degradation of Rhodamine B (RhB) under visible light (> 400 nm) irradiation was assessed. Briefly, a catalytic amount of Ag@Au$_{NCs}$/*f*-MoS$_2$ was added to aqueous RhB and the reaction mixture was stirred continuously in the dark for 60 minutes to establish an adsorption-desorption equilibrium among the ensemble and the dye. After that period, the system was brought into visible light irradiation and the progress of the catalytic reaction was monitored by UV-Vis spectroscopy as a function of the elapsed time. In order to shed light on the mechanism of the degradation process, the photocatalytic activity of Ag@Au$_{NCs}$/*f*-MoS$_2$ was investigated in the presence of oxygen and compared to that of bare Ag@Au$_{NCs}$ as well as individual Au$_{NCs}$ and Ag$_{NCs}$.

5.2.4 Photocatalytic degradation

The photodegradation of RhB was scrutinized upon the addition of catalytic amounts of Ag@Au$_{NCs}$/*f*-MoS$_2$ in the presence of oxygen, by following absorption spectral changes at the characteristic band of RhB centered at 554 nm. Initially, the effect of light illumination in the absence of Ag@Au$_{NCs}$/*f*-MoS$_2$ as catalyst on the degradation of RhB was examined. To this end, a blank experiment was performed by light irradiating an aqueous RhB solution and monitoring the UV-Vis spectrum of RhB. Evidently, no changes were observed in the absorption spectrum of RhB (Appendix, Figure S5.8), proving that light illumination is not sufficient itself to degrade RhB. Similarly negative was the result from an additional blank experiment performed in the presence of only *f*-MoS$_2$ (i.e. without any Ag@Au$_{NCs}$), namely, the UV-Vis spectrum of RhB remained practically unaltered. Continuing with reference assays, when a catalytic amount of bare Ag@Au$_{NCs}$ was used, the characteristic absorption band of RhB progressively decreased as a function of elapsed time, indicating decomposition of RhB. Simultaneously, the absorption band blue-shifted by 12 nm, giving rise to ca. 70%

degradation of RhB after 180 minutes of irradiation (Figure 5.5a). Strikingly on the other hand, when the same catalytic amount of Ag@Au$_{NCs}$/*f*-MoS$_2$ was employed, higher degradation kinetics for RhB were manifested (Figure 5.4b). In more detail, utilization of Ag@Au$_{NCs}$/*f*-MoS$_2$ resulted in nearly quantitatively degradation of RhB (> 85%), within 100 minutes, which was slightly more than the half period in comparison to the one registered for Ag@Au$_{NCs}$. Moreover, when Au$_{NCs}$ and Ag$_{NCs}$ were examined, around 60 and 50 % degradation of RhB was observed, respectively, after 210 minutes of light illumination (Supporting Information, Figure S5.9).

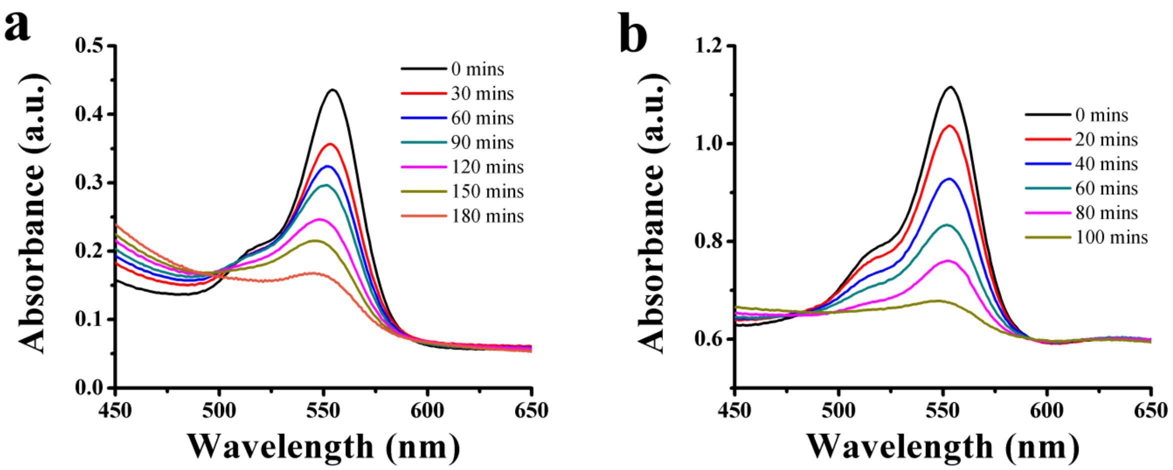

Figure 5.5 Evolution of UV-Vis absorption spectra for the decomposition of RhB by (a) Ag@Au$_{NCs}$, and, (b) Ag@Au$_{NCs}$/*f*-MoS$_2$ ensemble upon visible light illumination. The photo-degradation proceeds with faster kinetics as depicted in the corresponding UV-Vis absorption spectra in the presence of Ag@Au$_{NCs}$/*f*-MoS$_2$ ensemble.

In addition, the light irradiation had to continue up to 300 minutes to correspondingly reach 75 and 62 % degradation of RhB, with Au$_{NCs}$ and Ag$_{NCs}$. At this point, it should be underlined that the kinetic plots vs the irradiation time, for Ag@Au$_{NCs}$, Ag@Au$_{NCs}$/*f*-MoS$_2$, bare Au$_{NCs}$ and Ag$_{NCs}$, demonstrated a clear zero-order curve meaning that the photodegradation process is independent from the concentration of RhB (Figure 5.6).

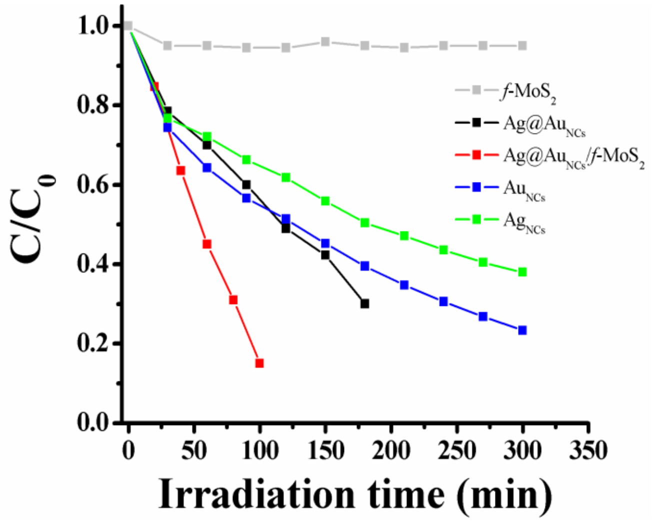

Figure 5.6 Temporal course of the photocatalytic degradation of aqueous RhB in the presence of *f*-MoS_2 (grey), Ag@Au_{NCs} (black), Ag@Au_{NCs}/*f*-MoS_2 (red), bare Au_{NCs} (blue) and Ag_{NCs} (green), under visible light illumination.

Recycling by filtration and re-employing Ag@Au_{NCs}/*f*-MoS_2 in consecutive photocatalytic cycles gave similar results, without observing any loss of activity toward RhB degradation. In fact, the absence of noteworthy changes in the reaction time and activity even after subjecting Ag@Au_{NCs}/*f*-MoS_2 in five subsequent photocatalytic cycles, showcases the high stability and broad applicability of Ag@Au_{NCs}/*f*-MoS_2 for the decomposition of RhB.

Generally, RhB is de-ethylated in a stepwise manner, i.e., ethyl groups are detached one by one, resulting in a gradual shift of the maximum absorption band of RhB towards the blue region of the electromagnetic spectrum. In fact, de-ethylation of the *N,N,N′,N′*-tetraethylated rhodamine molecule leads to its major absorption band shifted towards the blue region, e.g. *N,N,N′*-tri-ethylated rhodamine absorbs at 539 nm, *N,N′*-di-ethylated rhodamine absorbs at 522 nm, *N*-ethylated rhodamine absorbs at 510 nm, and rhodamine absorbs at 498 nm.[46] Although it is beyond the scope of the current work to examine the nature of the possible degradation mechanism/products of RhB, it is evident that photocatalysis in the presence of Ag_{NCs} led to a *N,N,N′*-triethylated degraded material, whereas Au_{NCs} contributed mostly to degradation with slightly higher kinetics. Instead, when bare Ag@Au_{NCs} was employed, the combination of the two metals in core-shell structure considerably improved the photocatalytic reaction performance in terms of the degradation rate. Considering all the above, the fast kinetics are attributed to the existence of gold, while silver rises the transformation/decomposition capability. Remarkably, the degradation efficiency of RhB driven by visible light reached the highest value when the Ag@Au_{NCs}/*f*-MoS_2 ensemble was employed, revealing *f*-MoS_2 as key mediator during the photocatalytic performance – see below for detailed analysis.

5.2.4 Photodegradation mechanism of RhB

It is well known that oxygen free radicals $O_2^{\bullet -}$, hydroxyl and hydroperoxyl radicals ($HO^{\bullet}$ and $HOO^{\bullet}$, respectively), and photoinduced holes are high oxidants, which can initiate the degradation process of organic chromophores. Therefore, in order to identify and confirm the responsible species accountable for the photodegradation of RhB, additional trapping experiments were conducted by employing tert-butyl alcohol (TBA), p-benzoquinone (p-BQ) and sodium oxalate (SO) as scavengers for $HO^{\bullet}$/ $HOO^{\bullet}$, $O_2^{\bullet-}$ and holes, respectively.[47] In more detail, addition of tert-butyl alcohol, which is oxidized by capturing $HO^{\bullet}$/ $HOO^{\bullet}$, inhibited the RhB degradation by Ag@Au$_{NCs}$/*f*-MoS$_2$ (Figure 5.7), revealing that $HO^{\bullet}$/ $HOO^{\bullet}$ played the most important role in the photodegradation process. Next, upon addition of p-benzoquinone, which traps $O_2{\bullet}^-$ via a simple electron-transfer process, in the aqueous RhB dispersion, the degradation rate was also inhibited, though to a lesser degree as compared with the case of tert-butyl alcohol. The same was also true after the addition of sodium oxalate in aqueous RhB, namely, the photogenerated holes were effectively scavenged proving that they hold their own share in the degradation rate. Overall, compared to the total absence of any scavengers, in which >85% degradation in 100 minutes was observed, one can realize that the deceleration of photodegradation activity is in the order of TBA (80%) > p-BQ (60%), SO (60%) (Figure 5.7). The latter highlights the synergistic effect of $HO^{\bullet}$/ $HOO^{\bullet}$ and $O_2{\bullet}^-$ as reactive oxidants together with the presence of photogenerated holes towards RhB photodegradation.

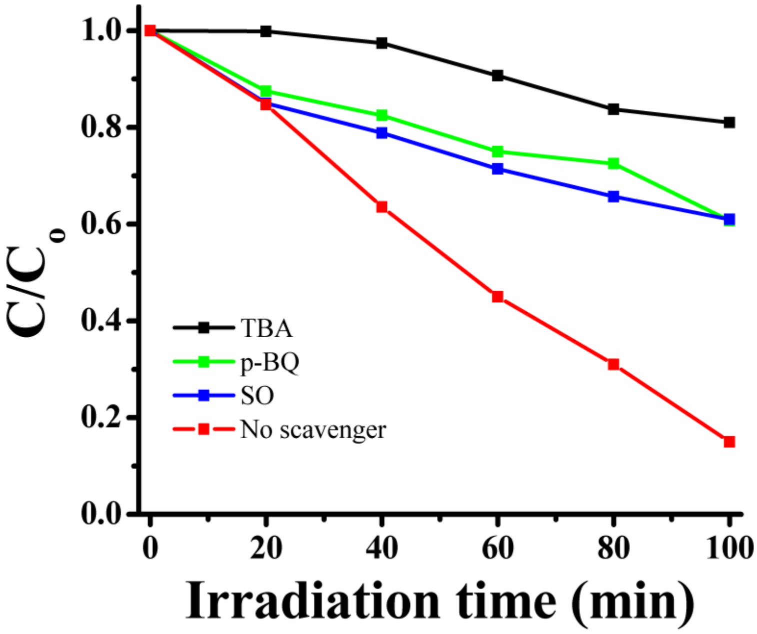

Figure 5.7 Kinetic plots for the photocatalytic degradation of aqueous RhB by Ag@Au$_{NCs}$/*f*-MoS$_2$ in the presence of TBA (black), p-BQ (green) and SO (blue) as scavengers and in the absence of any scavenger (red).

Based on the aforementioned results, a proposed mechanism for RhB degradation is described. Considering the existence of a deactivation pathway from photoexcited Ag@Au$_{NCs}$ within the Ag@Au$_{NCs}$/*f*-MoS$_2$ ensemble, rationalized by the observed photoluminescence quenching (*cf.* Figure 5.4b), the high photocatalytic efficiency observed for the degradation of RhB in the presence of oxygen is attributed to the effective charge-separation within Ag@Au$_{NCs}$/*f*-MoS$_2$. The presence of *f*-MoS$_2$ in the ensemble permits high flow of electrons, derived from photoexcited Ag@Au$_{NCs}$, while delaying the charge-recombination of the photogenerated holes and electrons within Ag@Au$_{NCs}$/*f*-MoS$_2$ as compared to bare Ag@Au$_{NCs}$. As an immediate result, acceleration of the catalytic reaction kinetics occurs. Then, molecular oxygen is reduced by those electrons, yielding superoxide radical ions, which in turn produce hydroxyl radicals as highly reactive species responsible for attacking and decomposing RhB according to the processes shown in Scheme 5.2. On an additional path, photogenerated holes on Ag@Au$_{NCs}$ can also directly attack and decompose RhB.

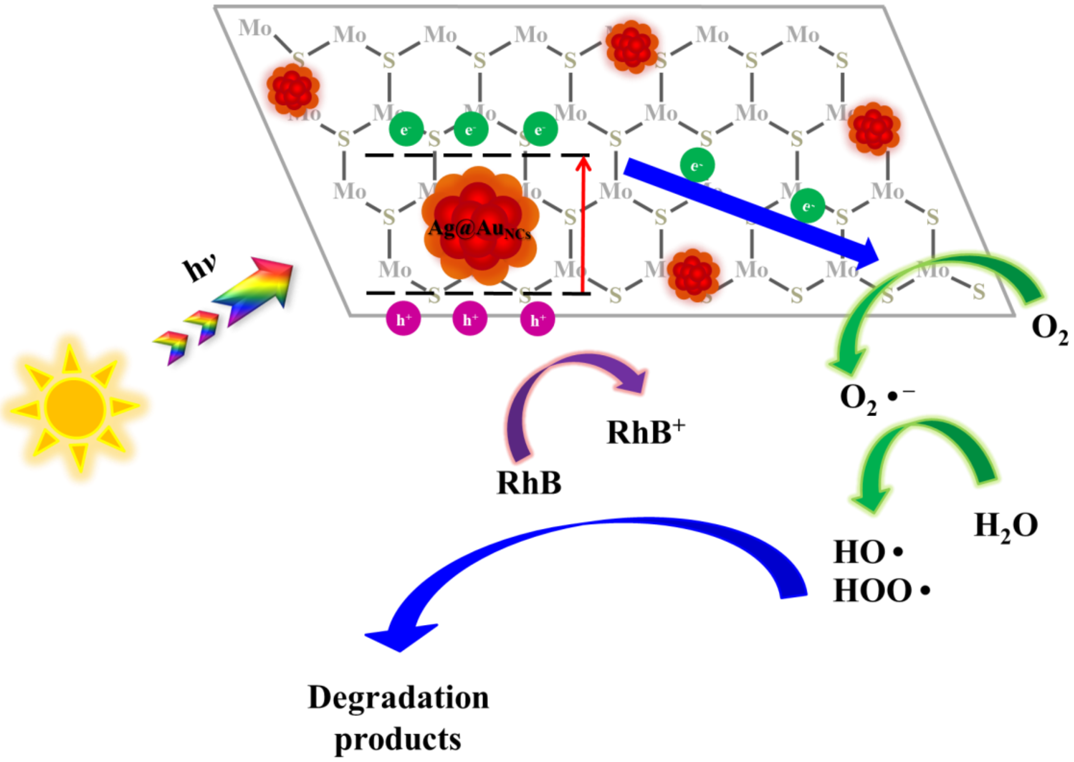

Scheme 5.2 Illustration of the mechanism of photocatalytic degradation of RhB over Ag@Au$_{NCs}$/*f*-MoS$_2$ ensemble.

5.3 Conclusions

In summary, innovative hybrid materials composed of core-shell metal nanoclusters based on Au core and Ag shell, electrostatically associated with ammonium functionalized MoS$_2$ nanosheets yielding Ag@Au$_{NCs}$/*f*-MoS$_2$ ensembles, were successfully developed. Importantly, Ag@Au$_{NCs}$ were stabilized by BSA, which is an effective protective agent, avoiding the addition of strong reducing species. Moreover, the cage effect of the protein stabilized the clusters and enhanced their optical properties reducing photobleaching. The core-shell Ag@Au$_{NCs}$ structure offered bonus potentials from both the preparation point of view and the photophysical features of the nanoclusters. First of all, the synthesis of bare Ag$_{NCs}$ is rather demanding mostly due to aggregation phenomena. On the other hand, Au$_{NCs}$ can form stable particles of uniform particle size, hence facilitating the growth of Ag$_{NCs}$ on top of them in a controllable manner. Secondly, the formation of Ag@Au$_{NCs}$ resulted in significant fluorescence enhancement, due to strong electronic coupling between Au and Ag, facilitating the development of photoinduced electron transfer processes and resulting in high catalytic activity. In parallel, semiconducting MoS_2 were decorated with positively charged ammonium units, which drastically improve the dispersibility and enhance the colloidal stability of the modified nanosheets in water.

Coulombic attractive interactions between positively charged functionalized MoS_2 and $Ag@Au_{NCs}$ bearing negative charges allowed the fabrication of the $Ag@Au_{NCs}/f\text{-}MoS_2$ ensemble as certified by electronic absorption and fluorescence emission titration assays. Quenching of the fluorescence emission of $Ag@Au_{NCs}$ by the presence of $f\text{-}MoS_2$ revealed the development of electron/energy transfer phenomena between the two components within the ensemble. Notably, $Ag@Au_{NCs}/f\text{-}MoS_2$ was successfully employed as photocatalyst for the degradation of RhB demonstrating exceptionally high catalytic capabilities (> 85%) within 100 minutes of illumination, compared to bare $Ag@Au_{NCs}$ which exhibited activity up to 70% after 180 minutes of irradiation. Moreover, when individual Au_{NCs} and Ag_{NCs} were examined, less activity was registered, around 60 and 50 % respectively, after 210 minutes of light illumination. The mechanism behind the photocatalytic function of $Ag@Au_{NCs}/f\text{-}MoS_2$ involves the production of highly reactive hydroxyl, which derive via superoxide radical ions via reduction of oxygen from charge-separated photogenerated electrons. Additionally, the holes left on $Ag@Au_{NCs}$ attack RhB molecules until its total degradation, as evidenced by the decolorization of the bright magenta solution and disappearance of the characteristic absorption at 554 nm.

By extension, one can imagine that the performance of $M^1@M^2_{NCs}/MoS_2$ hybrids holds a lot of virtues for their establishment in photocatalytic applications. Indeed, MoS_2 sheets are currently receiving a lot of interest from both scientific and industrial sectors, although their applicability is emerging, time is needed to unfold all the potential benefits and limitations. At the same time, $M^1@M^2_{NCs}$ can efficiently participate in photoredox catalytic applications, although strategies should be applied to substitute precious metals with others of reduced cost, but of the same optical characteristics. Without a doubt integration of MoS_2 and/or other transition metal dichalcogenide materials with $M^1@M^2_{NCs}$ opens up a new era in the design of light-harvesting systems and this field of research promises to grow in the coming years.

5.4 Experimental Section

5.4.1 General

All solvents and reagents were purchased from Aldrich and used without further purification unless otherwise stated. Mid-infrared spectra in the region 500−4500 cm^{-1} were obtained on a Fourier transform IR spectrometer (Equinox 55 from Bruker Optics) equipped with a single reflection diamond ATR accessory (DuraSamp1IR II by SensIR Technologies). Micro-Raman scattering measurements were performed at room temperature in the backscattering geometry using a RENISHAW inVia Raman microscope equipped with a CCD camera and a Leica microscope. As an excitation source the Coherent HeNe laser at 633 nm was used for characterizing the Raman signatures of MoS_2 sheets with and without functionalization. The laser spot was focused on the sample surface using a long working distance 50x objective. Measurements were taken with 20 seconds of exposure time upon one accumulation with 10% laser power (~1 mW) and dispersed by 1200 mm^{-1} in air under ambient conditions. Raman spectra were collected on numerous spots on the sample and recorded with Peltier cooled CCD camera. The data were collected and analyzed with Renishaw Wire and Origin software. Thermogravimetric analysis was performed using a TGA Q500 V20.2 Build 27 instrument by TA in a nitrogen (purity >99.999%) inert atmosphere. Steady state UV–Vis electronic absorption spectra were recorded on a Perkin-Elmer (Lambda 19) UV–Vis-NIR spectrophotometer. Steady state emission spectra were recorded on a Fluorolog-3 Jobin Yvon-Spex spectro-fluorometer (model GL3-21). Transmission electron microscopy images were acquired on a TEM JEOL JEM-2100, using an accelerating voltage of 200 kV. The instrument is equipped with an Energy Dispersive X-Ray Spectrometer, EDS, with a 50 mm^2 detector of 0.28sr of solid angle. HAADF-STEM Z contrast imaging and EDS mapping were performed using a FEI-TITAN 300 kV equipped with an X-Ray detector EDAX. Samples were prepared by drop casting of stable dispersions onto a TEM grid (300 mesh, cooper, Lacey Carbon Film LC300-CU). Additional EDX spectroscopy was performed on a FE-SEM (model JSM-7610F) equipped with an EDAX (X-ACT, Oxford Instrument) on samples deposited on a silicon substrate.

5.4.2 Synthesis of core-shell $Ag@Au_{NCs}$

The preparation of $Ag@Au_{NCs}$ was based on previously reported methods.[45] In a typical synthetic procedure, an aqueous solution of $HAuCl_4$ (20 mg, 5 mL) was added to aqueous bovine serum albumin (10 mM, 5 mL, 37 ^oC) under vigorous stirring for preparing the core. The pH of the solution was adjusted to 12 by adding aqueous NaOH (0.5 mL, 1M). A bright red solution was obtained after 14 hours of magnetic stirring at 37 ^oC, indicating the completion of the Au_{NCs} growth. Afterwards, to the as-prepared Au_{NCs} solution, aqueous solution of $AgNO_3$ (2.5 mL, 10 mM) was added. The reaction proceeded for 24 hours at 37 ^oC and the solution colour changed from red to bright orange, indicating the effective growth of $Ag@Au_{NCs}$. The as-prepared $Ag@Au_{NCs}$ solution was stored in the fridge.

5.4.3 Synthesis of Au_{NCs} and Ag_{NCs}

Synthesis of Au_{NCs} was based on the previously described approach, while the synthesis of Ag_{NCs} was adapted from the literature.[48] Briefly, aqueous solution of $AgNO_3$ (2 mL, 10 mM) was added to aqueous solution of BSA (2 mL, 0.05 g/mL) under vigorous stirring. Next, aqueous solution of NaOH (110 μL, 1.0 M) was added into the reaction mixture, followed by drop-wise addition of aqueous solution of $NaBH_4$ (150 μL, 10 mM). Immediately, the solution color changed from colorless to reddish brown indicating the formation of Ag_{NCs}, which were collected 1 h later.

5.4.4 Preparation of exfoliated MoS_2

The exfoliated semiconducting MoS_2 sheets were prepared based on a previously described procedure.[21] Briefly, chlorosulfonic acid (5 mL) was added to bulk MoS_2 powder (200 mg) and the mixture was bath sonicated for 3 h. In the resultant solid material, distilled water was carefully added at 0 °C under vigorous stirring, until the completion of the exothermic reaction. Next, the resultant dispersion was filtered over a PTFE filter (pore size 0.1 μm) and washed several times with dichloromethane and methanol. Before the filter was completely dried, the solid residue was transferred to a beaker, NMP (200 mL) was added and the mixture was probe sonicated (1 h, 35% amplitude, 0 °C). The dispersion was left overnight to settle and the exfoliated MoS_2 were obtained from the supernatant. The solid residue washed with dichloromethane and dried to obtain exfoliated MoS_2.

5.4.5 Functionalization of MoS_2

The covalent functionalization of semiconducting MoS_2 sheets was conducted by employing 1,2-dithiolane units bearing an ethylene glycol alkyl chain terminated to a butoxycarbonyl (BOC)-protected amine.[32] In brief, exfoliated MoS_2 (20 mg) and 1,2-dithiolane derivative (20 mg) were stirred in dimethylformamide (10 mL) at 70 °C for 3 days. In the next step, the reaction mixture was filtered through a PTFE filter (pore size 0.1 μm), the solid material was thoroughly washed with dichloromethane to remove organic residues and finally collected as a dispersion in dichloromethane. Afterwards, the BOC modified MoS_2 material was treated with gaseous HCl to cleave the BOC protecting group and liberate free amine units on the modified MoS_2. After a period of 24 h, the solvent was evaporated to dryness and the solid material was washed with dichloromethane and dried to yield water-dispersible ammonium functionalized MoS_2 sheets. The amino-loading of functionalized MoS_2 was calculated by performing the Kaiser test and found to be 50 μmol/g.

5.4.6 Preparation of $Ag@Au_{NCs}/f\text{-}MoS_2$ ensembles

An aqueous solution (3 mL) of $Ag@Au_{NCs}$ (50 μL) was titrated with aqueous $f\text{-}MoS_2$ (1 mg/mL) and the formation of $Ag@Au_{NCs}/f\text{-}MoS_2$ ensemble was verified by electronic absorption and fluorescence emission spectroscopic assays.

5.4.7 Photocatalytic degradation of Rhodamine B

The degradation of aqueous RhB was carried out in glassware surrounded by a circulating water jacket for cooling. To ensure that illumination was only by visible light, an aqueous solution of $NaNO_2$ (1.0 M) was used as a UV cut-off filter ensuring. The light source used was a 500 W Xenon lamp, which was positioned 20 cm away from the reactor. In a typical experiment, 250 μL of $Ag@Au_{NCs}/f\text{-}MoS_2$ (1:4 volume ratio of the two components) and RhB (9.75 μL, 10^{-3} M) were dissolved in 3 mL water and the mixture was stirred for 1 h in the dark to achieve a suitable adsorption-desorption equilibrium of the dye on the surface of the photocatalyst. After the equilibration period, the mixture was irradiated under the presence of oxygen. At given irradiation time intervals, the reaction mixture was sampled and separated by centrifugation (4.2 rpm, 5 min). The presence of RhB was determined by monitoring changes in the characteristic absorption band for RhB centred at 554 nm.

5.4.8 Trapping experiments for degradation of Rhodamine B

Trapping experiments were conducted to investigate the active species generated during the photocatalytic process; TBA (300 μL), p-BQ (0.3 mg) and SO (0.3 mg) were used as scavengers for $HO^{\bullet}$/ $HOO^{\bullet}$, $O_2^{\bullet-}$ and holes, respectively. In a typical experiment, each scavenger and RhB (9.75 μL, 10^{-3} M) were dissolved in 3 mL water and the solution was irradiated under the presence of oxygen. At given irradiation time intervals, the presence of RhB was determined by monitoring changes in the characteristic absorption band at 554 nm.

5.5 Appendix

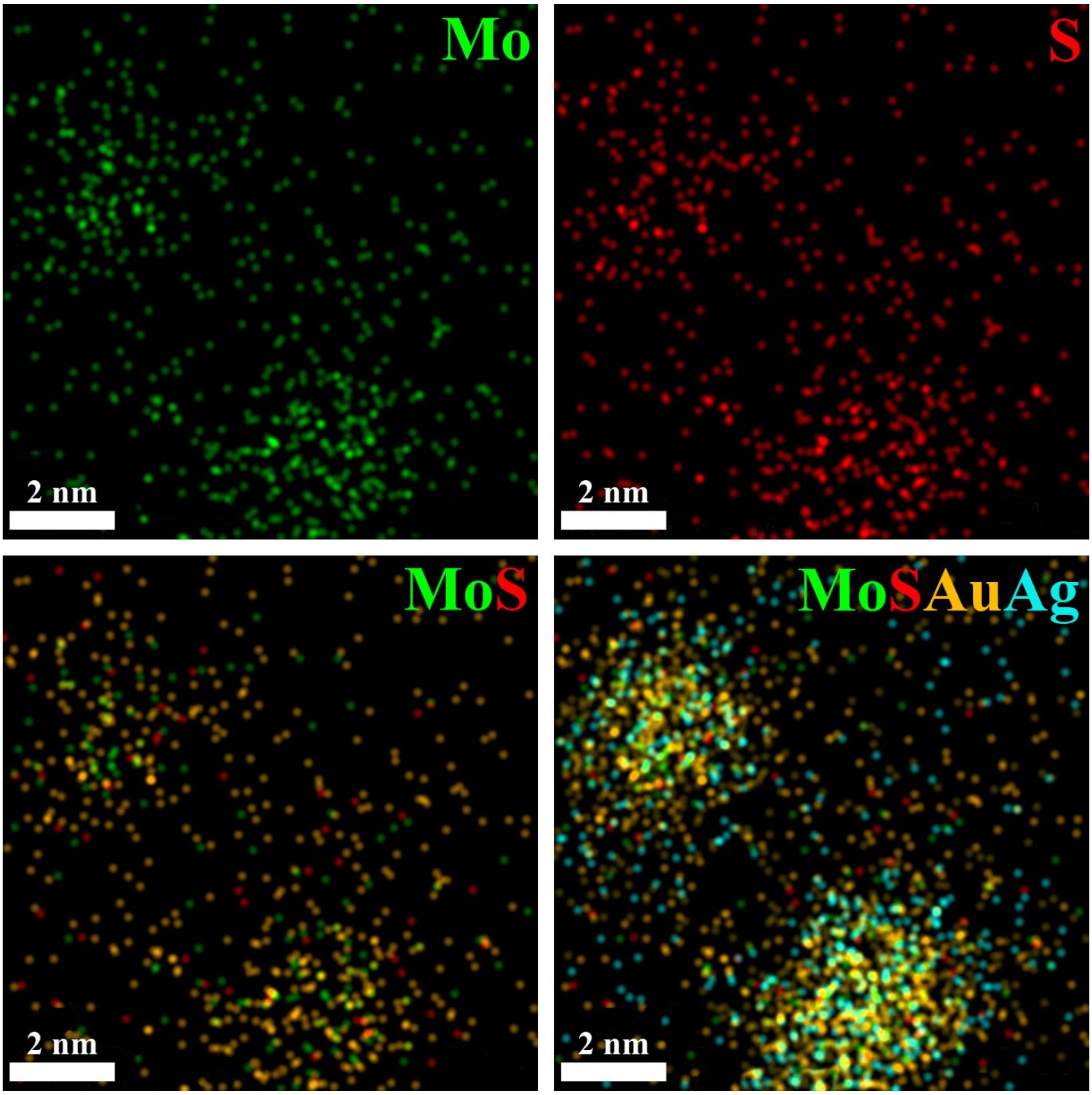

Figure S5.1 Representative HAADF-STEM-EDX mapping for the Ag@Au$_{NCs}$/f-MoS$_2$ ensemble.

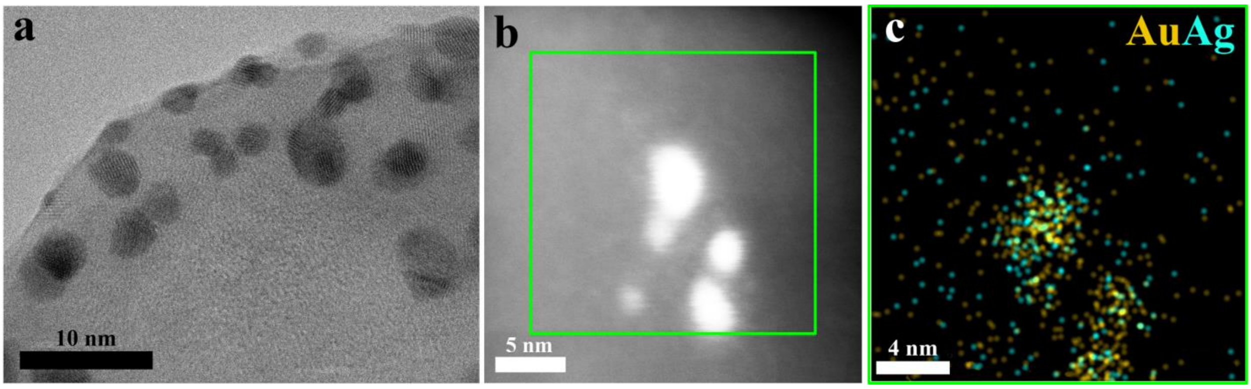

Figure S5.2 Representative (a) TEM image, (b) HAADF-STEM image, and (c) EDX elemental mapping for Ag@Au$_{NCs}$.

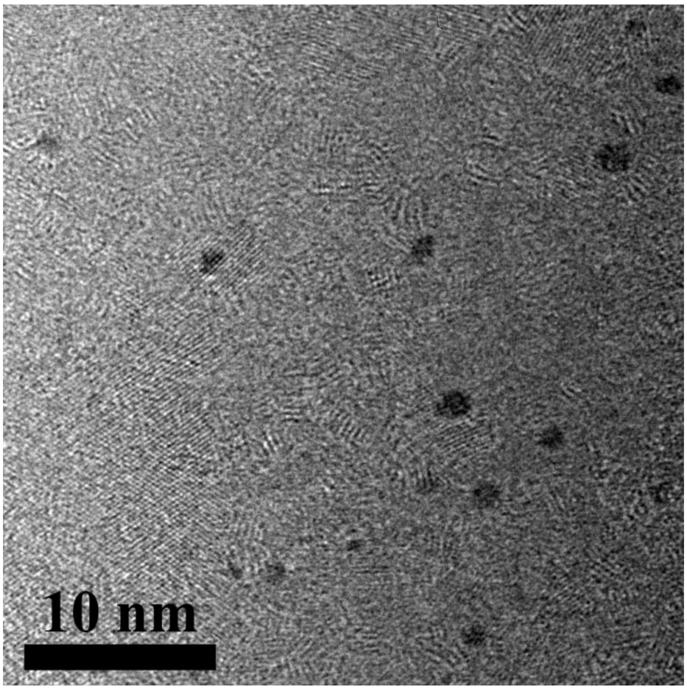

Figure S5.3 Representative TEM image for Au$_{NCs}$.

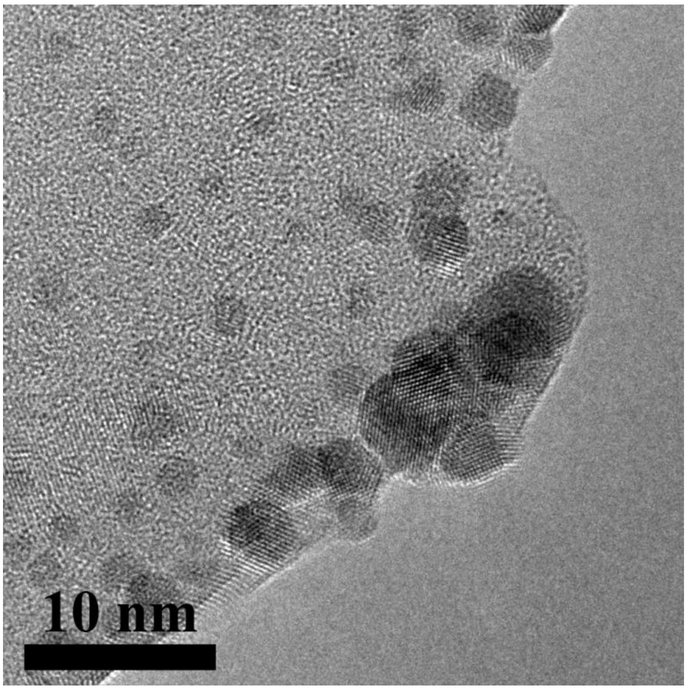

Figure S5.4 Representative TEM image for Ag$_{NCs}$.

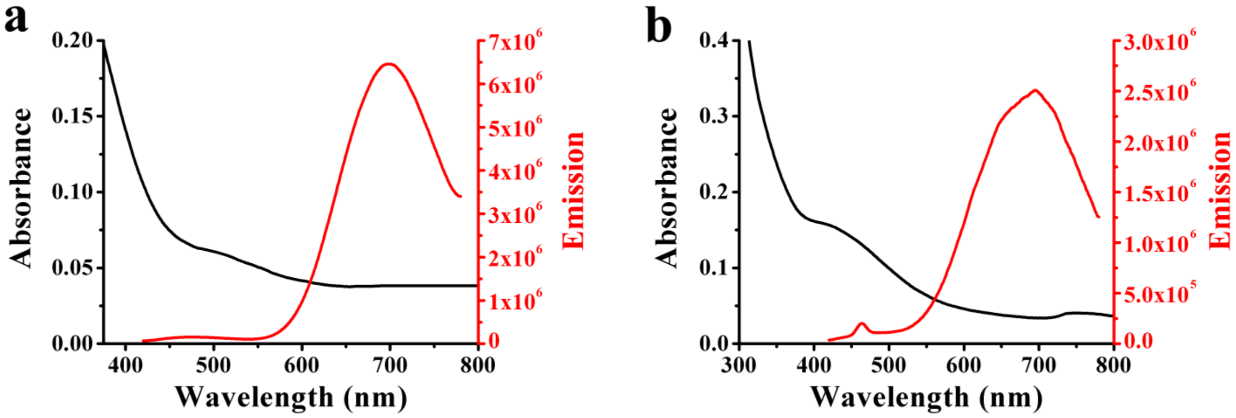

Figure S5.5 UV-Vis and photoluminescence (excitation wavelength 400 nm) spectra for (a) Au$_{NCs}$ and (b) Ag$_{NCs}$.

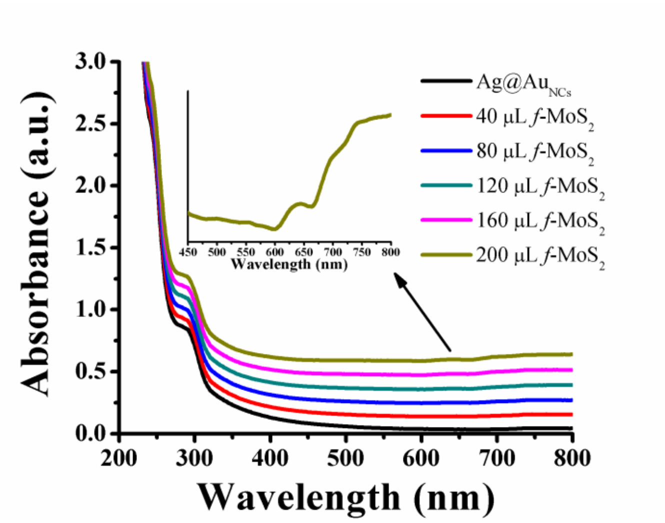

Figure S5.6 UV-Vis titration assay spectra for Ag@Au$_{NCs}$, upon incremental additions of f-MoS$_2$ (without subtraction of MoS$_2$ absorption bands). Inset: Enlargement of the 450-800 nm region of the f-MoS$_2$ material.

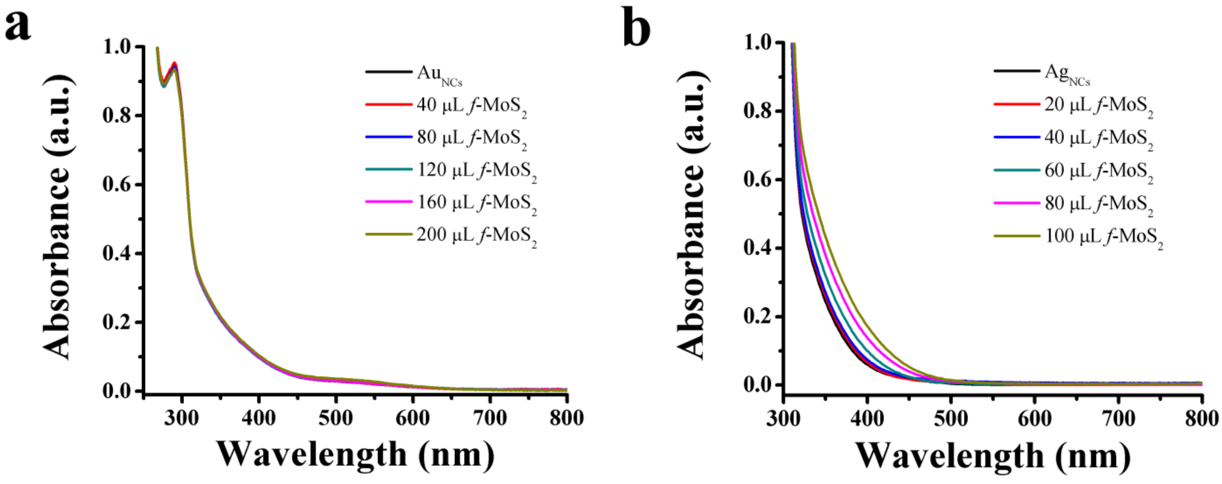

Figure S5.7 UV-Vis absorption titration assay spectra for (a) Au$_{NCs}$ and, (b) Ag$_{NCs}$, upon incremental additions of f-MoS$_2$.

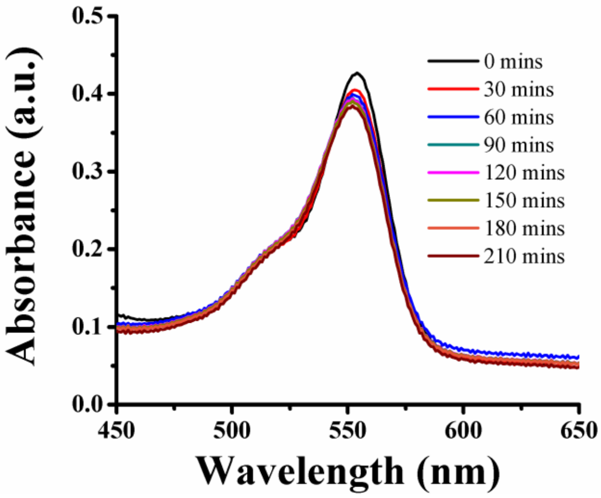

Figure S5.8 UV-Vis absorption spectra of aqueous RhB under light illumination.

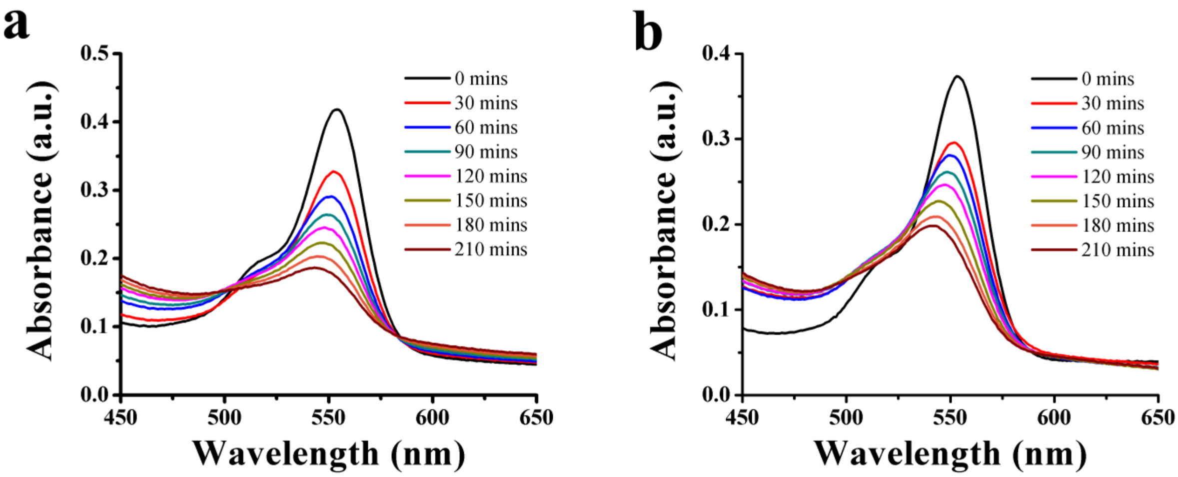

Figure S5.9 Evolution of UV-Vis absorption spectra for the decomposition of RhB by (a) Au_{NCs}, and, (b) Ag_{NCs} upon visible light illumination.

References

1. Lu, Y.; Chen, W., Sub-nanometre sized metal clusters: from synthetic challenges to the unique property discoveries. *Chem. Soc. Rev.* **2012,** *41* (9), 3594-3623.

2. Schmid, G., The relevance of shape and size of Au_{55} clusters. *Chem. Soc. Rev.* **2008,** *37* (9), 1909-1930.

3. Jin, R.; Zeng, C.; Zhou, M.; Chen, Y., Atomically Precise Colloidal Metal Nanoclusters and Nanoparticles: Fundamentals and Opportunities. *Chem. Rev.* **2016,** *116* (18), 10346-10413.

4. Shang, L.; Dong, S.; Nienhaus, G. U., Ultra-small fluorescent metal nanoclusters: Synthesis and biological applications. *Nano Today* **2011,** *6* (4), 401-418.

5. Li, G.; Jin, R., Atomically Precise Gold Nanoclusters as New Model Catalysts. *Acc. Chem. Res.* **2013,** *46* (8), 1749-1758.

6. Koklioti, M. A.; Tagmatarchis, N., Hybrids of Metal Nanoclusters and Graphene-Based Materials: Preparation, Properties and Applications. *ChemNanoMat* **2016,** *2* (12), 1065-1072.

7. Koklioti, M. A.; Skaltsas, T.; Sato, Y.; Suenaga, K.; Stergiou, A.; Tagmatarchis, N., Mechanistic insights into the photocatalytic properties of metal nanocluster/graphene ensembles. Examining the role of visible light in the reduction of 4-nitrophenol. *Nanoscale* **2017,** *9* (27), 9685-9692.

8. Xiao, F.-X.; Hung, S.-F.; Miao, J.; Wang, H.-Y.; Yang, H.; Liu, B., Metal-Cluster-Decorated TiO_2 Nanotube Arrays: A Composite Heterostructure toward Versatile Photocatalytic and Photoelectrochemical Applications. *Small* **2014,** *11* (5), 554-567.

9. Yu, C.; Li, G.; Kumar, S.; Kawasaki, H.; Jin, R., Stable $Au_{25}(SR)_{18}/TiO_2$ Composite Nanostructure with Enhanced Visible Light Photocatalytic Activity. *J. Phys. Chem. Lett.* **2013,** *4* (17), 2847-2852.

10. Chen, Y.-S.; Choi, H.; Kamat, P. V., Metal-Cluster-Sensitized Solar Cells. A New Class of Thiolated Gold Sensitizers Delivering Efficiency Greater Than 2%. *J. Am. Chem. Soc.***2013,** *135* (24), 8822-8825.

11. Abbas, M. A.; Kim, T.-Y.; Lee, S. U.; Kang, Y. S.; Bang, J. H., Exploring Interfacial Events in Gold-Nanocluster-Sensitized Solar Cells: Insights into the Effects of the Cluster Size and Electrolyte on Solar Cell Performance. *J. Am. Chem. Soc.***2016,** *138* (1), 390-401.

12. Liu, H.; Zhang, X.; Wu, X.; Jiang, L.; Burda, C.; Zhu, J.-J., Rapid sonochemical synthesis of highly luminescent non-toxic AuNCs and Au@AgNCs and Cu (II) sensing. *Chem. Commun.* **2011,** *47* (14), 4237-4239.

13. Guha, S.; Roy, S.; Banerjee, A., Fluorescent Au@Ag Core–Shell Nanoparticles with Controlled Shell Thickness and Hg^{II} Sensing. *Langmuir* **2011,** *27* (21), 13198-13205.

14. Zhang, N.; Si, Y.; Sun, Z.; Chen, L.; Li, R.; Qiao, Y.; Wang, H., Rapid, Selective, and Ultrasensitive Fluorimetric Analysis of Mercury and Copper Levels in Blood Using Bimetallic Gold–Silver Nanoclusters with “Silver Effect”-Enhanced Red Fluorescence. *Anal. Chem.* **2014,** *86* (23), 11714-11721.

15. Zhou, T.-y.; Lin, L.-p.; Rong, M.-c.; Jiang, Y.-q.; Chen, X., Silver–Gold Alloy Nanoclusters as a Fluorescence-Enhanced Probe for Aluminum Ion Sensing. *Anal. Chem.* **2013,** *85* (20), 9839-9844.

16. Guan, G.; Cai, Y.; Liu, S.; Yu, H.; Bai, S.; Cheng, Y.; Tang, T.; Bharathi, M. S.; Zhang, Y.-W.; Han, M.-Y., High-Level Incorporation of Silver in Gold Nanoclusters: Fluorescence Redshift upon Interaction with Hydrogen Peroxide and Fluorescence Enhancement with Herbicide. *Chem. Eur. J.* **2015,** *22* (5), 1675-1681.

17. Weng, B.; Lu, K.-Q.; Tang, Z.; Chen, H. M.; Xu, Y.-J., Stabilizing ultrasmall Au clusters for enhanced photoredox catalysis. *Nat. Commun.* **2018,** *9* (1), 1543.

18. Wang, Q. H.; Kalantar-Zadeh, K.; Kis, A.; Coleman, J. N.; Strano, M. S., Electronics and optoelectronics of two-dimensional transition metal dichalcogenides. *Nat. Nanotechnol.* **2012,** *7*, 699.

19. Duong, D. L.; Yun, S. J.; Lee, Y. H., van der Waals Layered Materials: Opportunities and Challenges. *ACS Nano* **2017,** *11* (12), 11803-11830.

20. Miró, P.; Audiffred, M.; Heine, T., An atlas of two-dimensional materials. *Chem. Soc. Rev.* **2014,** *43* (18), 6537-6554.

21. Pagona, G.; Bittencourt, C.; Arenal, R.; Tagmatarchis, N., Exfoliated semiconducting pure 2H-MoS_2 and 2H-WS_2 assisted by chlorosulfonic acid. *Chem. Commun.* **2015,** *51* (65), 12950-12953.

22. Grayfer, E. D.; Kozlova, M. N.; Fedorov, V. E., Colloidal 2D nanosheets of MoS_2 and other transition metal dichalcogenides through liquid-phase exfoliation. *Adv. Colloid Interface Sci.* **2017,** *245*, 40-61.

23. Tao, H.; Zhang, Y.; Gao, Y.; Sun, Z.; Yan, C.; Texter, J., Scalable exfoliation and dispersion of two-dimensional materials – an update. *Phys. Chem. Chem. Phys.* **2017,** *19* (2), 921-960.

24. Niu, L.; Coleman, J. N.; Zhang, H.; Shin, H.; Chhowalla, M.; Zheng, Z., Production of Two-Dimensional Nanomaterials via Liquid-Based Direct Exfoliation. *Small* **2015,** *12* (3), 272-293.

25. Zhang, X.; Lai, Z.; Tan, C.; Zhang, H., Solution-Processed Two-Dimensional MoS_2 Nanosheets: Preparation, Hybridization, and Applications. *Angew. Chem.* **2016,** *55* (31), 8816-8838.

26. Fan, X.; Xu, P.; Li, Y. C.; Zhou, D.; Sun, Y.; Nguyen, M. A. T.; Terrones, M.; Mallouk, T. E., Controlled Exfoliation of MoS_2 Crystals into Trilayer Nanosheets. *J. Am. Chem. Soc.* **2016,** *138* (15), 5143-5149.

27. Bertolazzi, S.; Gobbi, M.; Zhao, Y.; Backes, C.; Samorì, P., Molecular chemistry approaches for tuning the properties of two-dimensional transition metal dichalcogenides. *Chem. Soc. Rev.* **2018**, *47*, 6845–6888.

28. Chen, X.; McDonald, A. R., Functionalization of Two-Dimensional Transition-Metal Dichalcogenides. *Adv. Mater.* **2016,** *28* (27), 5738-5746.

29. Voiry, D.; Goswami, A.; Kappera, R.; Silva, C. d. C. C. e.; Kaplan, D.; Fujita, T.; Chen, M.; Asefa, T.; Chhowalla, M., Covalent functionalization of monolayered transition metal dichalcogenides by phase engineering. *Nat. Chem.* **2014,** *7*, 45–49.

30. Knirsch, K. C.; Berner, N. C.; Nerl, H. C.; Cucinotta, C. S.; Gholamvand, Z.; McEvoy, N.; Wang, Z.; Abramovic, I.; Vecera, P.; Halik, M.; Sanvito, S.; Duesberg, G. S.; Nicolosi, V.; Hauke, F.; Hirsch, A.; Coleman, J. N.; Backes, C., Basal-Plane Functionalization of Chemically Exfoliated Molybdenum Disulfide by Diazonium Salts. *ACS Nano* **2015,** *9* (6), 6018-6030.

31. Ryder, C. R.; Wood, J. D.; Wells, S. A.; Hersam, M. C., Chemically Tailoring Semiconducting Two-Dimensional Transition Metal Dichalcogenides and Black Phosphorus. *ACS Nano* **2016,** *10* (4), 3900-3917.

32. Canton-Vitoria, R.; Sayed-Ahmad-Baraza, Y.; Pelaez-Fernandez, M.; Arenal, R.; Bittencourt, C.; Ewels, C. P.; Tagmatarchis, N., Functionalization of MoS_2 with 1,2-dithiolanes: toward donor-acceptor nanohybrids for energy conversion. *NPJ 2D Mater. Appl.* **2017,** *1* (1), 13.

33. Canton-Vitoria, R.; Vallan, L.; Urriolabeitia, E.; Benito, A. M.; Maser, W. K.; Tagmatarchis, N., Electronic Interactions in Illuminated Carbon Dot/MoS_2 Ensembles and Electrocatalytic Activity towards Hydrogen Evolution. *Chem. Eur. J.* **2018,** *24* (41), 10468-10474.

34. Canton-Vitoria, R.; Stangel, C.; Tagmatarchis, N., Electrostatic Association of Ammonium-Functionalized Layered-Transition-Metal Dichalcogenides with an Anionic Porphyrin. *ACS Appl. Mater. Interfaces* **2018,** *10* (28), 23476-23480.

35. Mathew, A.; Sajanlal, P. R.; Pradeep, T., A fifteen atom silver cluster confined in bovine serum albumin. *J. Mater. Chem.* **2011,** *21* (30), 11205-11212.

36. Jin, R., Atomically precise metal nanoclusters: stable sizes and optical properties. *Nanoscale* **2015,** *7* (5), 1549-1565.

37. Zhang, P.; Yang, X. X.; Wang, Y.; Zhao, N. W.; Xiong, Z. H.; Huang, C. Z., Rapid synthesis of highly luminescent and stable Au_{20} nanoclusters for active tumor-targeted imaging in vitro and in vivo. *Nanoscale* **2014,** *6* (4), 2261-2269.

38. Au, L.; Lim, B.; Colletti, P.; Jun, Y. S.; Xia, Y., Synthesis of Gold Microplates Using Bovine Serum Albumin as a Reductant and a Stabilizer. *Chem. Asian J.* **2009,** *5* (1), 123-129.

39. Govindaraju, S.; Ankireddy, S. R.; Viswanath, B.; Kim, J.; Yun, K., Fluorescent Gold Nanoclusters for Selective Detection of Dopamine in Cerebrospinal fluid. *Sci. Rep.* **2017,** *7,* 40298.

40. Long, D. A. Infrared and Raman characteristic group frequencies. Tables and charts George Socrates John Wiley and Sons, Ltd, Chichester, Third Edition, 2001. *J. Raman Spectrosc.* 2004, *35*, *905−905.*

41. Li, H.; Zhang, Q.; Yap Chin Chong, R.; Tay Beng, K.; Edwin Teo Hang, T.; Olivier, A.; Baillargeat, D., From Bulk to Monolayer MoS_2: Evolution of Raman Scattering. *Adv. Funct. Mater.* **2012,** *22* (7), 1385-1390.

42. Bae, S.; Sugiyama, N.; Matsuo, T.; Raebiger, H.; Shudo, K.-i.; Ohno, K., Defect-Induced Vibration Modes of Ar^+-Irradiated MoS_2. *Phys. Rev. Appl.* **2017,** *7* (2), 024001.

43. Benson, E. E.; Zhang, H.; Schuman, S. A.; Nanayakkara, S. U.; Bronstein, N. D.; Ferrere, S.; Blackburn, J. L.; Miller, E. M., Balancing the Hydrogen Evolution Reaction, Surface Energetics, and Stability of Metallic MoS_2 Nanosheets via Covalent Functionalization. *J. Am. Chem. Soc.* **2018,** *140* (1), 441-450.

44. Eda, G.; Yamaguchi, H.; Voiry, D.; Fujita, T.; Chen, M.; Chhowalla, M., Photoluminescence from Chemically Exfoliated MoS_2. *Nano Lett.* **2011,** *11* (12), 5111-5116.

45. Wang, Z.-X.; Zheng, C.-L.; Ding, S.-N., Label-free detection of sulfide ions based on fluorescence quenching of unmodified core-shell Au@Ag nanoclusters. *RSC Adv.* **2014,** *4* (19), 9825-9829.

46. Watanabe, T.; Takizawa, T.; Honda, K., Photocatalysis through excitation of adsorbates. 1. Highly efficient N-deethylation of rhodamine B adsorbed to cadmium sulfide. *J. Phys. Chem.* **1977,** *81* (19), 1845-1851.

47. Zou, J.-P.; Ma, J.; Luo, J.-M.; Yu, J.; He, J.; Meng, Y.; Luo, Z.; Bao, S.-K.; Liu, H.-L.; Luo, S.-L.; Luo, X.-B.; Chen, T.-C.; Suib, S. L., Fabrication of novel heterostructured few layered WS_2-Bi_2WO_6/$Bi_{3.84}W_{0.16}O_{6.24}$ composites with enhanced photocatalytic performance. *Appl. Catal. B* **2015,** *179*, 220-228.

48. Yu, Y.; Geng, J.; Ong Edward Yong, X.; Chellappan, V.; Tan Yen, N., Bovine Serum Albulmin Protein-Templated Silver Nanocluster (BSA-Ag_{13}): An Effective Singlet Oxygen Generator for Photodynamic Cancer Therapy. *Adv. Healthc. Mater.* **2016,** *5* (19), 2528-2535.

Chapter 6

Au nanocluster/2D material hybrids

Abstract

Controlling the architecture and properties through structure–directing agents is a versatile approach for next generation 2D-based materials. However, the lack of rigid organic entities which facilitate multi-functional roles in the fabrication of hybrid materials requires the development of novel methodologies. To this end, a new organic stabilizer based on a bulky adamantane moiety bearing also an 1,2-dithiolane derivative is demonstrated and employed for the synthesis of Au_{NCs} with NIR- fluorescence. Next, the C=C group of the newly synthesized ligand was exploited to covalently react with thiol-functionalized graphene and MoS_2 sheets through thiol–ene “click” reaction. The current strategy employed constitutes a general tool that is wide in scope and can, in principle, be extended to the modification of other 2D materials and/or compounds for the fabrication of hybrid schemes with tailored characteristics that today is unattainable.

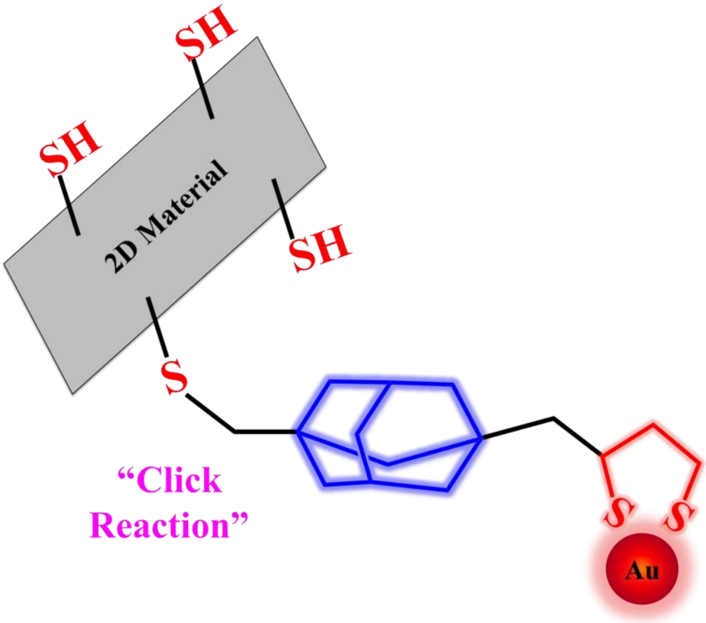

6.1 Introduction

Metal nanoparticles stabilized by organic ligands have spurred the scientific interest in the past decades due to their remarkable properties.[1] The nature (i.e. structure, properties) of surface-capping agent is decisive not only in preventing nanoparticles from aggregation but also in regulating their size, morphology, and physicochemical properties for applications, including, catalysis, medicine, and environmental remediation.[2-4] An important issue though is how the structure and chemical properties of the organic ligand-stabilizer affect the features of nanoparticles, as for example specific growth protocols may lead to the formation of the so-called metal nanoclusters with intriguing photophysical properties.[5] To this end, bulky stabilizers are employed because they tend to decrease the particle size and form clusters of specific architecture due to steric reasons, while the presence of a thiol moiety is usually a prerequisite to facilitate metal affinity.[6] Phosphine molecules are commonly employed as bulky stabilizers for nanoparticle/nanoclusters formation, while mixed thiolate/phosphine protected Au_{NCs} are also reported.[2, 7] Moreover, amino acid derivatives, such as glutathione and bovine serum albumin, are routinely employed for nanocluster formation, which are soluble in aqueous media.[8-9] In addition to ligand bulkiness, many other factors, such as metal to ligand ratio, type of reducing agent, manner of addition and mixing, reaction time and temperature influence the particle size and morphology.

Adamantane is a cycloaliphatic hydrocarbon, whose derivatives such as adamantanethiolate, and 1-adamantanecarboxylic acid have been applied to synthesize monodispersed nanoparticles.[10-11] Adamantane meets the requirements for nanocluster growth not only due to its bulky spherical shape, but also rigidity, solubility in organic solvents, while adamantane derivatives can be further functionalized allowing the realization of multifunctional hybrid materials with defined structure and targeted performance.

The pressing matter of environmental deterioration dictates the development of alternative materials and undoubtedly 2D material systems, such as graphene and TMD-based materials have already proved their superiority over energy conversion devices. However, in order to study their potential in applications, functionalization is mandatory to suppress the tendency over aggregation and enable dispersibility in organic solvents. Click chemistry reactions have been successfully employed to the field of polymers[12] and more recently to carbon nanostructures including carbon nanotubes[13] and graphene.[14-15] The characteristics of click chemistry are among others, high efficiency, absence of side products and easy purification, leading to the preparation of new, otherwise unattainable functionalized materials. In particular, the copper catalyzed azide−alkyne cycloaddition (CuAAC) has been the most employed for the modification of graphene.[16-17] However, the CuAAC click reaction presents an important drawback derived from the toxicity of the copper catalyst. In order to avoid the use of any toxic metal catalysts other metal-free click reactions have been developed, such as the thiol−ene and thiol−yne ones.[18-21] Thiol–ene reaction possesses many desirable features, such as simplicity, high efficiency, no by-products and high yield, and also present an additional virtue since it can be externally-triggered by thermal initiator. Both click chemistry reactions and adamantane derivatives open up an innovative avenue to controllably design hybrid materials that fulfill specific urgent demands.

On this background, one can imagine adamantane to function as an sp^3–carbon building block molecule facilitating both nanocluster formation and covalent attachment of 2D materials to construct a novel donor – acceptor hybrid material for energy conversion applications. In this work, we exploited the features of 1-acryloyloxy-3-hydroxyadamantane, an adamantine derivative that boasts two functional units, namely –OH and C=C groups. Nevertheless, those standalone moieties cannot initiate either particle growth or interactions without pre-functionalization. To move a step forward, the hydroxyl moiety was capable of reacting with the carboxyl unit of α-lipoic acid through a well-established esterification process to furnish 3-(acryloyloxy)adamantan-1-yl 5-((R)-1,2-dithiolan-3-yl)pentanoate (**1**), while at the same time, the free 1,2-dithiolane group of α-lipoic acid could establish robust attachment of sulfur onto gold atoms. Hence, the fabrication of a newly developed organic stabilizer with cage-structure, high metal affinity, and improved solubility was realized for Au_{NC} formation with near-infrared luminescence. The bulkiness of adamantane may also be beneficial for preventing clusters from photobleaching – a phenomenon which handicaps nanocluster applicability. On the other hand, the C=C entity of the adamantane derivative can be harnessed to covalently interact with thiol-modified 2D materials (graphene, and TMDs) through thiol–ene click chemistry means, en route the fabrication of a robust hybrid materials with interesting photophysical properties.

6.2 Results and discussion

The working principle for the fabrication of Au_{NCs}/2D-material ensembles is based on the decisive choice of the adamantine derivative, which possesses a bi-functional role boasting a hydroxyl group attached on one end and a carbon-carbon double bond on the other. Firstly, we exploited the –OH group to react with a suitable carboxyl acid, i.e. α-lipoic acid, through a typical condensation reaction. Despite the yield being low due to adamantane steric hindrance, the 1,2-dithiolane group facilitated the growth of stable Au_{NCs}, while simultaneously the bulkiness of adamantane derivate offered bonus potentials for their robustness and solubility in organic solvents (i.e. THF, DMF, CH_2Cl_2, $CHCl_3$). To date, most of the studied metal nanoclusters are dissolved in aqueous media, while usually phase transfer procedures assisted by chemical agents like tetraoctylammonium bromide are prerequisite for their transfer from aqueous to organic phase. In such kind of processes, the separation between catalyst and particle components could require cumbersome and laborious efforts, while the possibility of emulsion formation, nanoparticle collapse, or solubility issues cannot be neglected. Secondly, the presence of the terminal C=C offers an effective avenue for post functionalization scenarios through a thiol–ene “click” reaction. On this background, we conceived the idea to prepare functionalized graphene and MoS_2 sheets with thiol functional groups. Oxidation of graphite flakes followed by bromination yielded the corresponding brominated species. Afterwards, addition of excess of thiourea resulted in the transformation of brominated species to isothiouronium salt. Subsequent addition of NaOH resulted in the quaternization of ammonium units and realization of thiol-functionalized graphene, abbreviated as G-SH. On the other hand, MoS_2 sheets were covalently functionalized using a di-thiol moiety, abbreviated as MoS_2-GH, by exploiting the S vacancies generated during exfoliation process. Afterwards, the covalent coupling of Au_{NCs} with G-SH and MoS_2-GH for the development of respective hybrids was based on typical thiol–ene "click" reaction between the C=C unit of the newly synthesized organic stabilizer and thiol groups attached on 2D materials. The realization of the hybrid material was a straightforward procedure, as only the temperature regulation and addition of thermal initiator (AIBN) were required (Scheme 6.1 and 6.2).

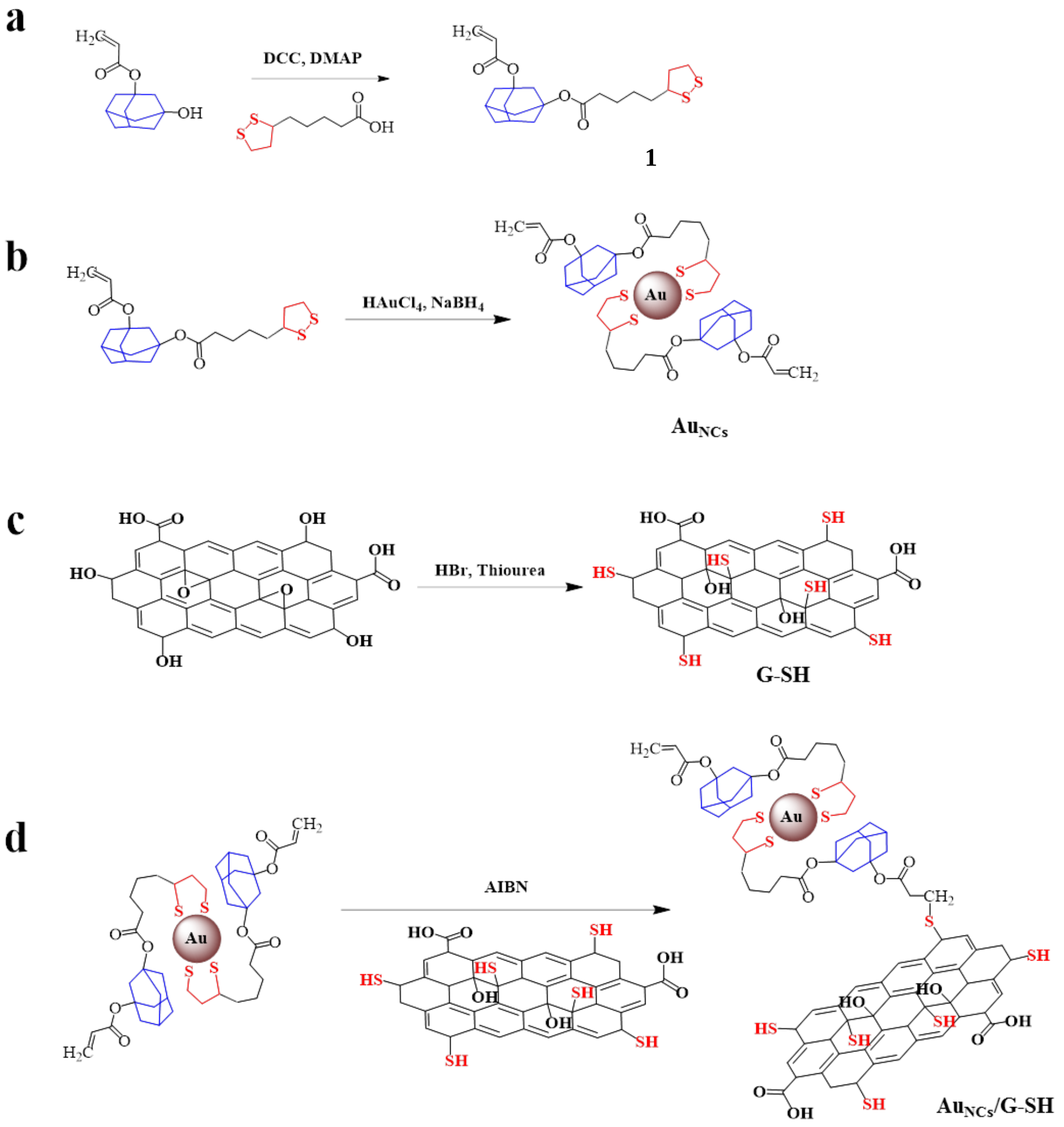

Scheme 6.1 Schematic illustration of the synthesis procedure of (a) adamantane derivative 1, (b) Au_{NCs}, and preparation of (c) thiol-functionalized graphene, G-SH, and (d) Au_{NCs}/G-SH ensemble.

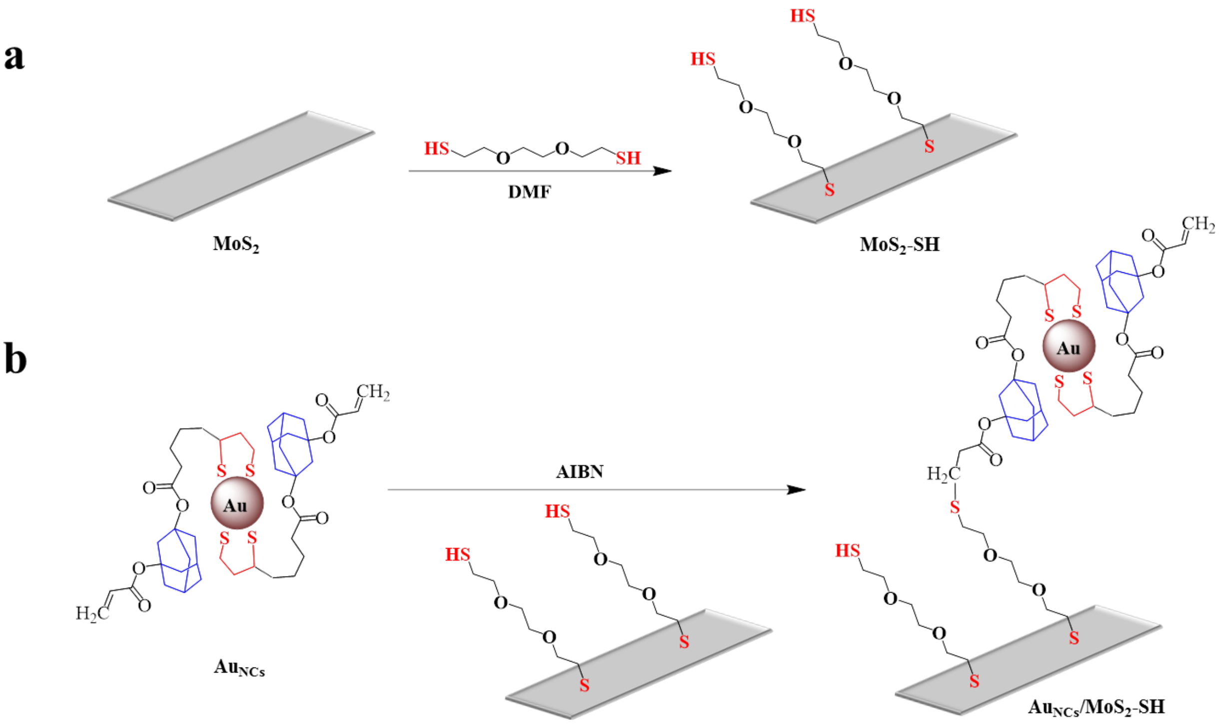

Scheme 6.2 Schematic illustration of the preparation procedure of (a) MoS_2-SH, (b) Au_{NCs}/MoS_2-SH hybrid.

6.2.1 Characterization of adamantane derivative 1

The structure of the newly developed adamantane-based derivative **1**, to be employed as stabilizer for the preparation of Au_{NCs}, was fully justified based on ^{1}H and ^{13}C NMR and IR spectroscopy and further confirmed by mass spectrometry. Briefly, the ^{1}H NMR spectrum of **1** contains the characteristic peaks derived from both adamantane and α-lipoic acid; however, the triplet at 2.38 ppm assigned to the proton next to the carboxyl group of α-lipoic acid is shifted to 2.23 ppm, which is indicative of the ester formation. Additionally, the three representative peaks belonging to the vinylic proton signals of 1-acryloyloxy-3-hydroxyadamantane found intact and slightly shifted to higher magnetic field (Figure S6.1). Moreover, the ^{13}C NMR spectrum confirmed the structure of **1**, as the emergence of two signals due to the carbonyl carbons were recorded; one at 165 ppm attributable to the ester group of the adamantane derivative and a second new one at 172.5 ppm, which arises from the newly derived carbonyl moiety due to the esterification process. The double bonded carbon atoms present two signals at 129.7 and 130 ppm, while the two quaternary carbon atoms near the oxygen moieties found at 80.6 and 80.9 ppm. In the 28-55 ppm region of the ^{13}C NMR spectrum the presence of 15 sp^3 hybridized carbon atoms is identified (Figure S6.2).

Attenuated-total-reflectance (ATR) IR spectroscopy also gave meaningful information for the condensation reaction and formation of adamantane derivative **1**. In this frame, the carbonyl band of α-lipoic acid at 1688 cm^{-1} is shifted to higher wavenumbers, i.e. appearing at 1720 cm^{-1}, due to the ester carbonyl formation of the adamantane derivative. Lastly, the disappearance of the stretching vibration of O–H at 3390–3350 cm^{-1} is an additional proof that the adamantine-based organic compound is free of starting material (Figure 6.1a). Final proof for the structure of adamantane-based compound **1** derived by registering the $(M+H_2O)^+$ peak at 428 amu via ESI-MS mass spectrometry. (Figure S6.3).

6.2.2 Characterization of G-SH

Firstly, ATR-IR spectra were recorded to specify the functional groups on the graphene-based materials. Typical IR bands corresponding to O–H stretching vibration (broad shoulder at 3420 cm^{-1}), C=O carbonyl stretching vibration (1720 cm^{-1}), and C=C in-plane stretching mode (1620 cm^{-1}) are observed in case of GO. Vibrations of C–O of different species mainly epoxy and hydroxyl groups are present in the range of 1300 and 850 cm^{-1} and we found distinct signals at about 1260, 1215, 1050 and 845 cm^{-1}. However, after treatment with HBr and thiourea, the C–O region became poor. The signals at about 1415 cm^{-1} correspond to O–H deformation vibrations from carboxylic groups (Figure 6.1b).

Further spectroscopic analysis through Raman shown the two characteristic peaks of graphene-based materials; the D band at ~1350 cm^{-1} ascribed to the presence of structural defects in sp^2-hybridized carbon network and the G band at ~1600 cm^{-1} associated with the in-plane vibration of the sp^2 C–C bonds. The ratio of peak intensities for D and G bands (I_D/I_G) reflects the extent of defects on graphene materials, in which GO and G-SH showed values of 0.85 and 1.00, respectively. The slightly higher degree of defective carbon atoms on G-SH is expected for graphene-based materials that have undergone reduction or functionalization treatments. Moreover, a red shift of ~10 cm^{-1} is detected in the G band of G-SH spectrum as compared to GO, indicative of graphene n-type doping (Figure 6.1c).

Thermogravimetric analysis also gave important information on the functionalization degree of graphene. As it can be seen, GO displayed a mass loss of about 14% in the temperature range 200–550 ^oC under an inert atmosphere of nitrogen due to the presence of the oxygenated functional groups and the defects generated on the carbon skeleton. On the contrary, the G-SH exhibited a mass loss of 10% at 200–450 ^oC, demonstrating higher thermal stability than GO, due to the elimination of oxygen functionalities on carbon network, as a result of the thermally induced thiolation reaction (Figure 6.1d).

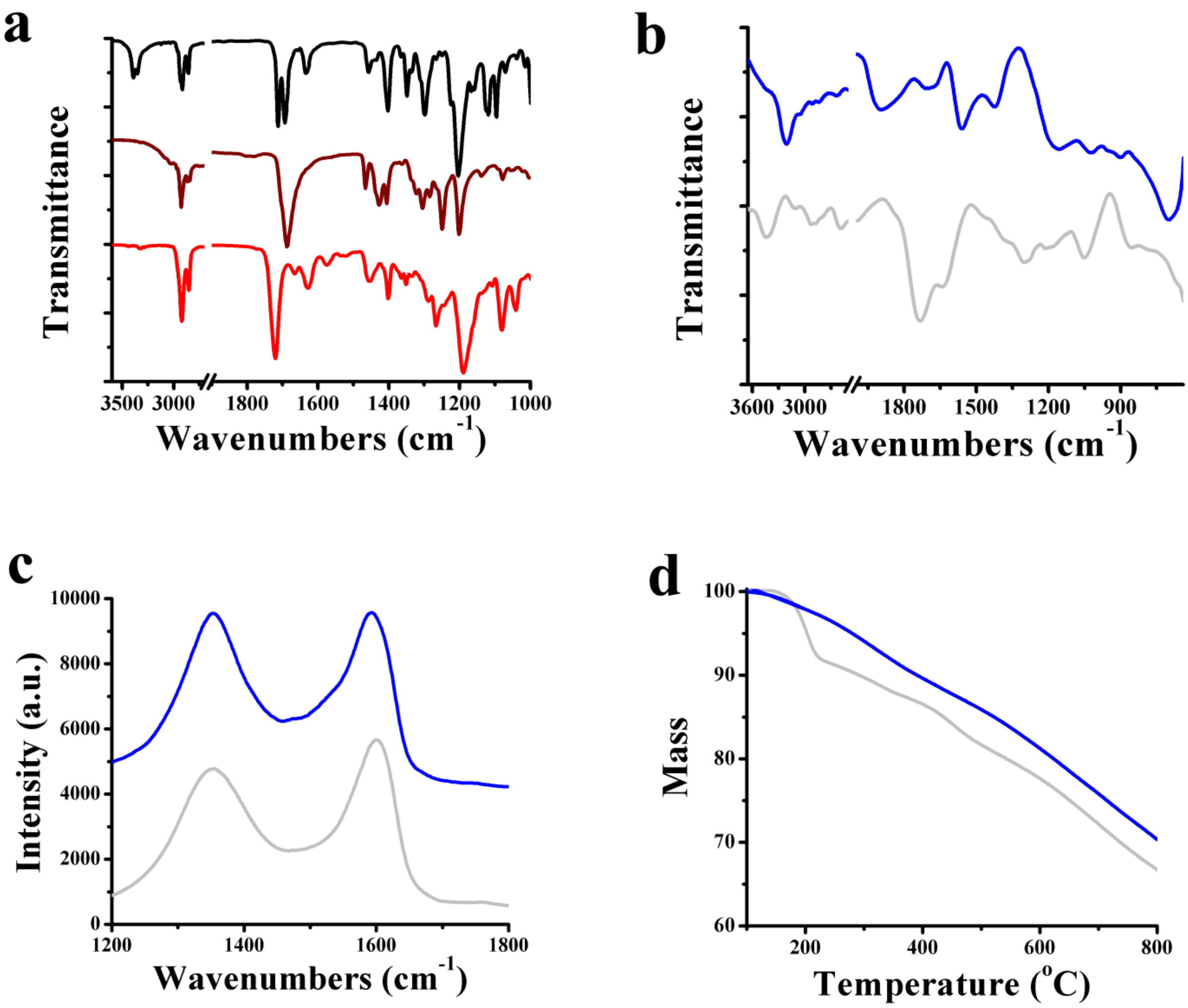

Figure 6.1 (a) ATR-IR spectra for 1-acryloyloxy-3-hydroxyadamantane (black), α-lipoic acid (wine red), and adamantane derivative 1 (red). (b) ATR-IR spectra for G-SH (blue), and GO (grey). (c) Raman spectra for G-SH (blue), and GO (grey). Thermographs for G-SH (blue), and GO (grey).

6.2.3 Characterization of MoS_2-SH

Analogously, IR spectroscopy gave valuable information on the functionalization of MoS_2 with 2,2′-(ethylenedioxy)diethanethiol moiety. The IR spectrum of MoS_2-SH is largely similar to that of the 2,2′-(ethylenedioxy)diethanethiol, while there is a shift to the right for C–S peak at 1088 cm^{-1}. Considering the Raman, the suppression of 2LA(M) band for MoS_2-SH is another evidence for the effective functionalization due to the elimination of S vacancies. In the TGA, MoS_2-SH exhibited a mass loss of about 8% in the temperature range 180-300 ^{o}C, due to the thermal decomposition of the covalently bonded organic functionality onto MoS_2 sheets.

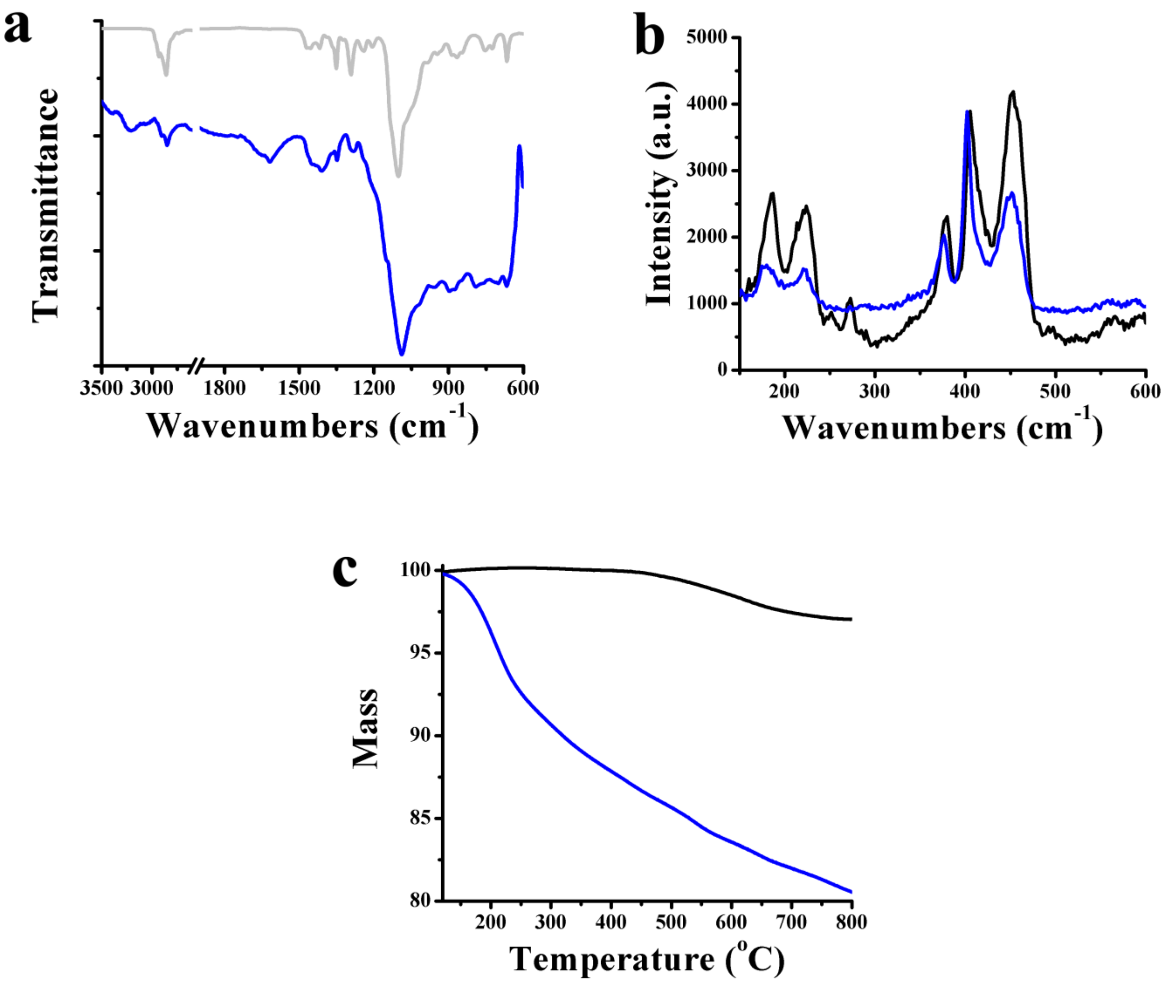

Figure 6.2 (a) ATR-IR spectra for 2,2′-(ethylenedioxy)diethanethiol (black), and MoS_2-SH (blue). (b) Raman spectra for MoS_2 (black), and MoS_2-SH (blue). Thermographs for MoS_2 (black), and MoS_2-SH (blue).

6.2.4 Characterization of Au_{NCs}

The absorption spectrum of Au_{NCs} is almost featureless without any plasmonic band, which is typical of nanocluster growth. Moreover, a slope-change in the range 300 – 400 nm is observed and centered at ~340 nm, which may be ascribed to the 1,2-dithiolane unit of the organic ligand (Figure 6.3a). Next, the NIR luminescence of Au_{NCs} at 795 nm upon exciting at 420 nm is characteristic and driven by their tiny size (generally consisting of fewer than ∼100 Au atoms) (Figure 6.3b). The bulky stabilizer hinders the formation of large particles, thus interesting photophysical phenomena are happening.

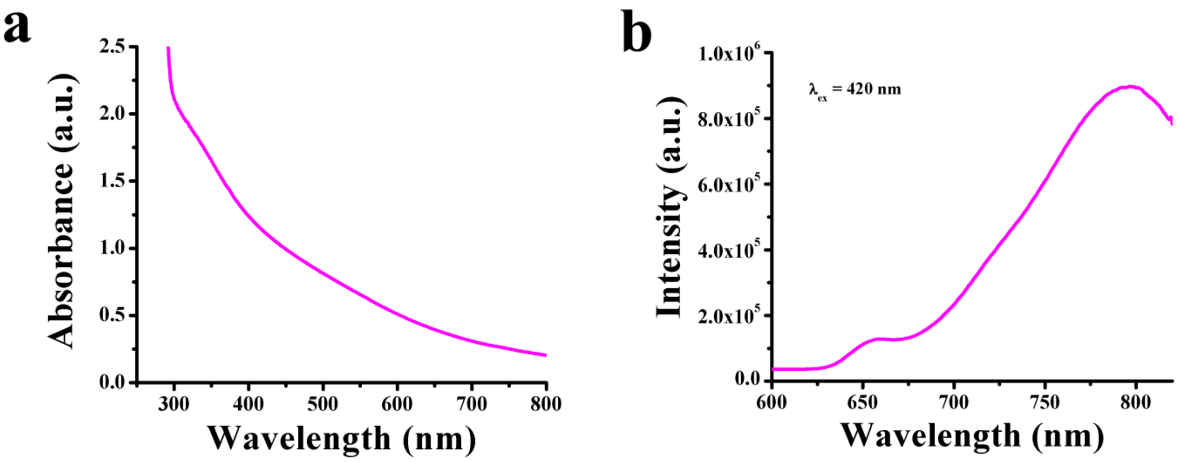

Figure 6.3 (a) UV-Vis and (b) photoluminescence spectra of Au$_{NCs}$ (excitation wavelength 420 nm).

6.2.5 Characterization of Au$_{NCs}$/G-SH

After ascertaining the spectroscopic and thermal characteristics of the individual components in G-SH and Au$_{NCs}$, we moved on the realization of the Au$_{NCs}$/G-SH ensemble through thiol–ene click reaction. The initial screening of the successful fabrication of the ensemble is based on IR results. On this background, the first signal is the emergence of two bands centred at 2920 and 2850 cm^{-1} associated with C–H stretching vibrations, which are absent in G-SH and originate from the covalent grafting of **1** onto graphene sheets (Figure 6.4a). Additionally, the sharp peak located at 1727 cm^{-1} is slightly shifted and belongs to the carboxyl unit of the newly-synthesized ligand. Arguably, both GO and G-SH boast IR bands at 1720 cm^{-1}; however they display more broad features. Moreover, the region at 1300–980 cm^{-1} is now enriched with organic moieties derived from the organic ligand, as compared to the IR spectrum of G-SH which was featureless in the same range. TGA provided additional evidence for the successful ensemble preparation. The Au$_{NCs}$/G-SH thermograph exhibits a 14% mass loss in the temperature range 200–450 ^{o}C, which corresponds mostly to the decomposition of the organic ligand covalently attached onto the thiols of G-SH. Considering that G-SH displayed a mass loss of 10% at the same range, we can have a tentative calculation of the functionalization degree of the G-SH with **1** at ~ 4% (Figure 6.4b). Moving on UV-Vis absorption measurements, the ensemble spectrum displays the characteristics of Au$_{NCs}$; however an obvious 25 nm red shift of the shoulder (from 340 to 365 nm) is recorded attributable to efficient electronic interactions of the hybrid material at the ground state (Figure 6.4c). This was another proof for the successful fabrication of the Au$_{NCs}$/G-SH ensemble. As for interactions at the excited state, the photoluminescence of Au$_{NCs}$ was completely quenched in the Au$_{NCs}$/G-SH, due to the covalent attachment of graphene sheets (Figure 6.4d). Lastly, round nanoclusters with a diameter of 5 nm in average onto the graphene sheets were identified by annular dark-field (ADF) STEM image.

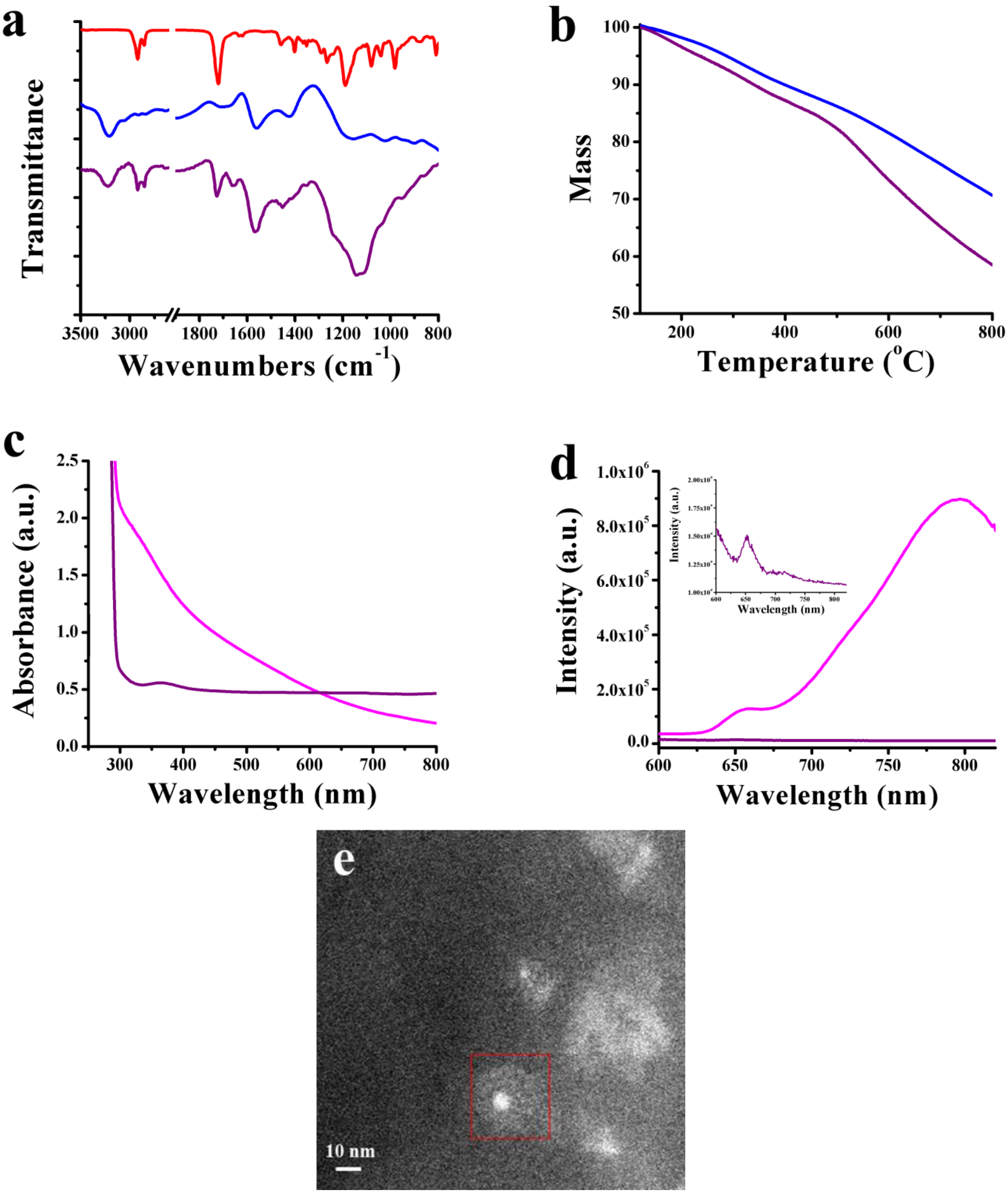

Figure 6.4 (a) ATR-IR spectra for adamantane derivative 1 (red), G-SH (blue), and Au_{NCs}/G-SH (purple). (b) Thermographs for G-SH (blue), and Au_{NCs}/G-SH (purple). (c) UV-Vis spectra for Au_{NCs} (pink), and Au_{NCs}/G-SH (purple). Photoluminescence spectra for Au_{NCs} (pink), and Au_{NCs}/G-SH (purple) (inset: photoluminescence spectrum of Au_{NCs}/G-SH). (e) HADF-STEM image for Au_{NCs}/G-SH.

6.2.6 Characterization of Au_{NCs}/MoS_2-SH

Similar to the graphene-based material, the Au_{NCs}/MoS_2-SH was firstly screened through IR spectroscopy. The hybrid material exhibits the same bands as in case of MoS_2-SH; however the emergence of a new at 1720 cm^{-1} signifies the attachment of adamantane derivative **1** on MoS_2-SH sheets. The TGA of Au_{NCs}/MoS_2-SH exhibits a two-step decomposition process with 27% mass loss in the temperature range 200-600 °C derived from the attachment of the organic functionalities onto MoS_2 sheets.

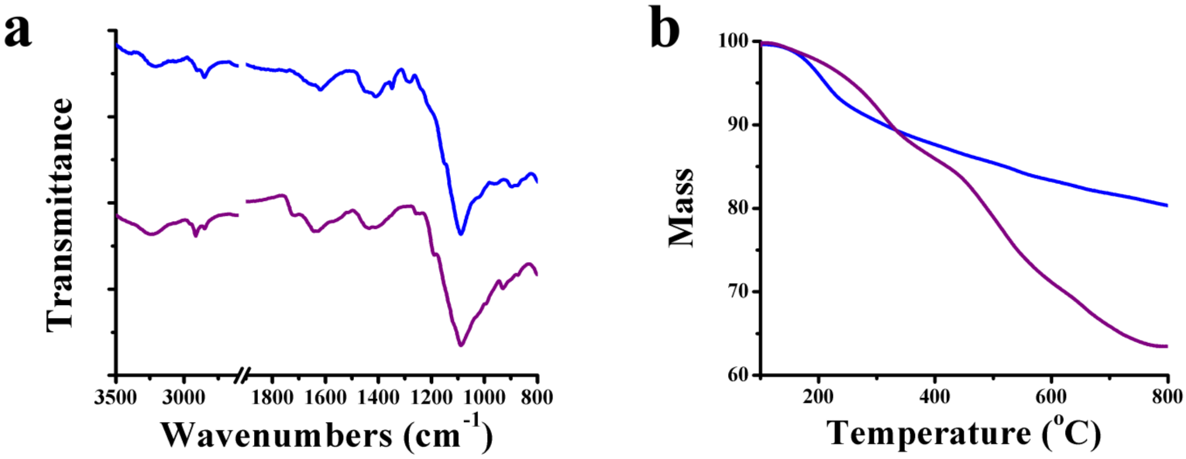

Figure 6.5 (a) ATR-IR spectra for MoS_2-SH (blue), and Au_{NCs}/MoS_2-SH (purple). (b) Thermographs for MoS_2-SH (blue), and Au_{NCs}/MoS_2-SH (purple).

6.3 Conclusions

In summary, this chapter demonstrated a novel protocol for the covalent attachment of metal nanoclusters onto graphene network. We succeeded in the synthesis of an adamantane-based stabilizer with multifunctional features: (a) bulkiness and solubility in organic solvents derived from the adamantane moiety, (b) metal affinity due to the 1,2-dithiolane derivative, and (c) reactivity as the C=C group can participate in “click” reactions. The synthesis of the bulky ligand was based on a well-established esterification process and evaluated through conventional spectroscopy means (NMR, ESI-MS, and ATR-IR). The preparation of NIR fluorescent Au_{NCs} was realized and attributed to the cage-like structure of the adamantane derivative which facilitated the formation of tiny sized and monodispersed particles, suggesting the importance of surface ligands in regulating the shape and physicochemical properties of metal nanocrystals. The chemistry behind the controlled growth of metal nanoparticles with high surface reactivity using bulky ligands is expected to be beneficial in designing atomically precise metal nanoparticles with desirable surface and/or unusual properties targeted for specific applications.

The newly prepared Au_{NCs} were then covalently bonded with pre-functionalized graphene sheets bearing thiol units. The reaction between C=C groups of the adamantane derivative and thiol moieties on graphene and MoS_2 allowed the realization of respective hybrid materials. The successful preparation of Au_{NCs}/G-SH was screened through a series of spectroscopic, thermal, and imaging techniques. With regard to chemical functionalization of graphene, thiol–ene click chemistry overhangs as a very promising route compared to the other usually employed methodologies, due to high efficiency, easy handling and adaptability. The advantages of exploiting graphene’s and TMDs’ properties are largely understood; however the way how to tether them with bizarre entities is limited only to human imagination. The current strategy employed for the preparation of the hybrids constitutes a general tool that is wide in scope and can, in principle, be extended to the modification of other 2D materials and/or compounds for the fabrication of hybrid schemes with tailored characteristics that today is unattainable.

6.4 Experimental section

6.4.1 General

All solvents and reagents were purchased from Aldrich and used without further purification unless otherwise stated. For thin layer chromatography (TLC), Riedel–de Haën silica gel F254 plates were used. For flash column chromatography, silica gel 60 (230–400 mesh, 0.04–0.063 nm) was used. ^{1}H and ^{13}C NMR spectra were recorded on a Varian V300 MHz spectrometer and $CDCl_3$ as solvent (^{1}H, 7.26 ppm; ^{13}C, 77.16 ppm). Mass spectra were recorded on a Waters Acquity ESI-MS system with a Waters 2966 Photodiode Array detector coupled to a Waters Micromass ZQ mass spectrometer. A single-quadrupole Quattro micro mass spectrometer (ACQUITY SQ Detector) equipped with an electrospray ionization (ESI) interface was used for analytical detection. ESI-MS instrument was operated in positive ion mode. All data were acquired and processed using Masslynx 4.1 software (Waters Corp., MA, Milford, USA). Mid-infrared spectra in the region 500−4500 cm^{-1} were obtained on a Fourier transform IR spectrometer (Equinox 55 from Bruker Optics) equipped with a single reflection diamond ATR accessory (DuraSamp1IR II by SensIR Technologies). Micro-Raman scattering measurements were performed at room temperature in the backscattering geometry using a RENISHAW inVia Raman microscope equipped with a CCD camera and a Leica microscope. As an excitation source a 514 nm argon ion laser was used for characterizing the Raman signatures of graphene sheets with and without functionalization. The data were collected and analyzed with Renishaw Wire and Origin software. Thermogravimetric analysis was performed using a TGA Q500 V20.2 Build 27 instrument by TA in a nitrogen (purity >99.999%) inert atmosphere at a heating rate of 10 ^{o}C/min. Steady state electronic absorption spectra were recorded on a Perkin-Elmer (Lambda 19) UV–Vis spectrophotometer. Steady state emission spectra were recorded on a Fluorolog-3 JobinYvon-Spex spectrofluorometer (model GL3-21).

6.4.2 Synthesis of adamantane derivative 1

To a solution of α-lipoic acid (200 mg, 0.97 mmol) and 1-acryloyloxy-3-hydroxyadamantane (215 mg, 0.97 mmol) in 20 mL of dry THF under nitrogen atmosphere at 0 ^{o}C, N,N’ -dicyclohexylcarbodiimide (DCC) (220 mg, 1.07 mmol) and 4-dimethylaminopyridine (DMAP) (11.8 mg, 0.09 mmol) were added and the resulting solution was stirred for 1 h at 0 °C and 18 h at RT. At completion of the reaction, 1 drop of acetic acid was added, and the stirring was continued for 15 min. The precipitate was filtered off, the filtrate was evaporated to dryness, the residual yellow oily fluid was dissolved in ethyl acetate, and the solution was kept at 4 ^{o}C overnight. The separated precipitate was filtered, the filtrate was extracted with brine and water, and then dried over $MgSO_4$. Then, the organic phase was filtered, evaporated to dryness and the crude residue was purified by column chromatography through elution with the mixture of ethyl acetate and hexane (1:10) to afford a yellow oil (20 mg, 5%).

6.4.3 Preparation of thiol-functionalized graphene (G-SH)

The preparation of thiol-functionalized graphene was based on a previously reported method.[22] In a typical experiment, 15 mg of graphene oxide[23] were dispersed in distilled water (15 mL) and bath sonicated for 30 min to enable good dispersibility. Then, HBr (2 mL) was added, and the mixture was stirred at 30 ^oC for 6 h. Thiourea (1 g) was subsequently added and refluxed at 80 ^oC for 24 h. After the completion of the reaction, the suspension was cooled to RT, then aqueous NaOH (4M, 10 mL) was added and stirring continued for 1 h. The dispersion was filtered over a 0.2 μm PTFE membrane, washed with water, and MeOH to remove any unreacted material. The collected solid was stored in vacuum overnight to afford 12 mg of G-SH.

6.4.4 Preparation of thiol-functionalized MoS_2 (MoS_2-SH)

Firstly, the exfoliation of MoS2 sheets was based on a previously applied method.[24] Afterwards, 15 mg of as-exfoliated MoS_2 were dispersed in 3 mL of dry DMF and 3 mL of 2,2′-(ethylenedioxy)diethanethiol and stirred at 50 ^oC for 48 h. The dispersion was filtered over a 0.2 μm PTFE membrane, washed with MeOH and DCM to remove any unreacted material. The collected solid was stored in vacuum overnight to afford 12 mg of MoS_2-SH.

6.4.4 Synthesis of Au nanoclusters

The adamantane derivative **1** (5 mg, 0.012 mmol) in 3 mL of THF was vigorously mixed with $HAuCl_4\cdot 3H_2O$ (0.48 mg, 0.0012 mmol). The reaction mixture was stirred for one hour, during which period the solution became light yellow, and then was cooled to 0 ^oC in an ice bath. Then 125 μL of aqueous $NaBH_4$ (0.65 mg, 0.017 mmol) was added instantaneously under vigorous stirring, turning the solution to the characteristic dark brown color. The stirring continued for one hour at 0 ^oC and overnight at RT during which period the particles turned to pale brown indicating the effective growth of Au_{NCs}. The product was evaporated under reduced pressure to dryness followed by centrifugation with MeOH to remove unreacted stabilizer and $NaBH_4$ impurities. The brown solid material was stored in vacuum overnight to provide Au_{NCs}.

6.4.5 Preparation of Au_{NCs}/G-SH and Au_{NCs}/MoS_2-SH ensembles

For the preparation of the ensemble, 5 mg of G-SH were dispersed in 15 mL of dry DMF/o-DCB (2:1 v/v) under nitrogen atmosphere, and bath sonicated for 30 min to enable good dispersibility. Then, 5 mg of Au_{NCs} were dissolved in 2 mL of dry DMF and immediately added to the graphene-based suspension with simultaneous addition of azobisisobutyronitrile (AIBN) (20 mg, 0.122 mmol). The mixture was heated at 80 °C in nitrogen atmosphere and stirred overnight. The solid product was collected by filtration and washed with of MeOH to remove excess AIBN and unreacted nanoclusters. The produced material was stored in vacuum overnight to provide Au_{NCs}/G-SH ensemble. The same procedure was followed for the Au_{NCs}/MoS_2-SH.

6.5 Appendix

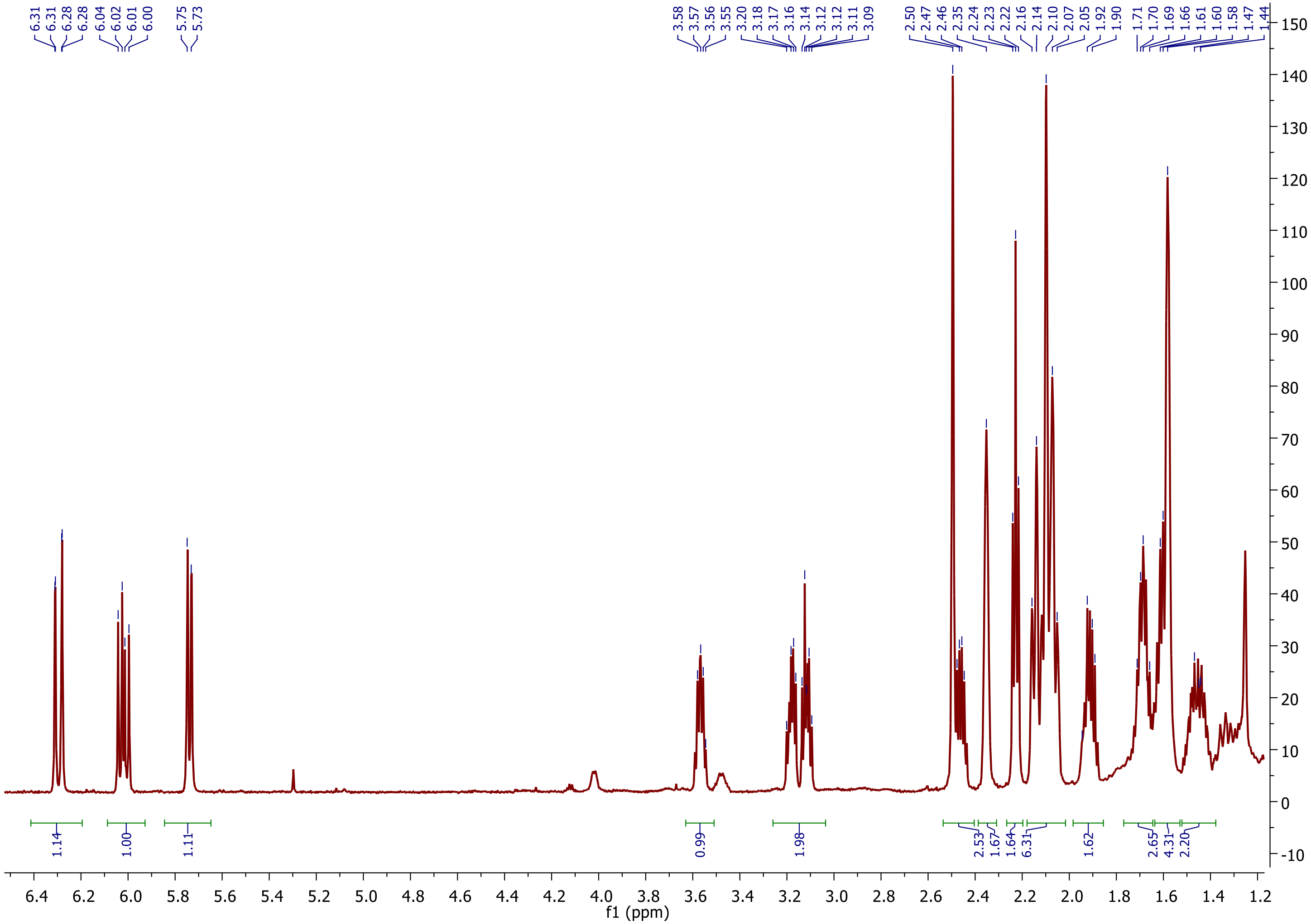

Figure S6.1 ^{1}H NMR spectrum of adamantane derivative 1 in $CDCl_3$.

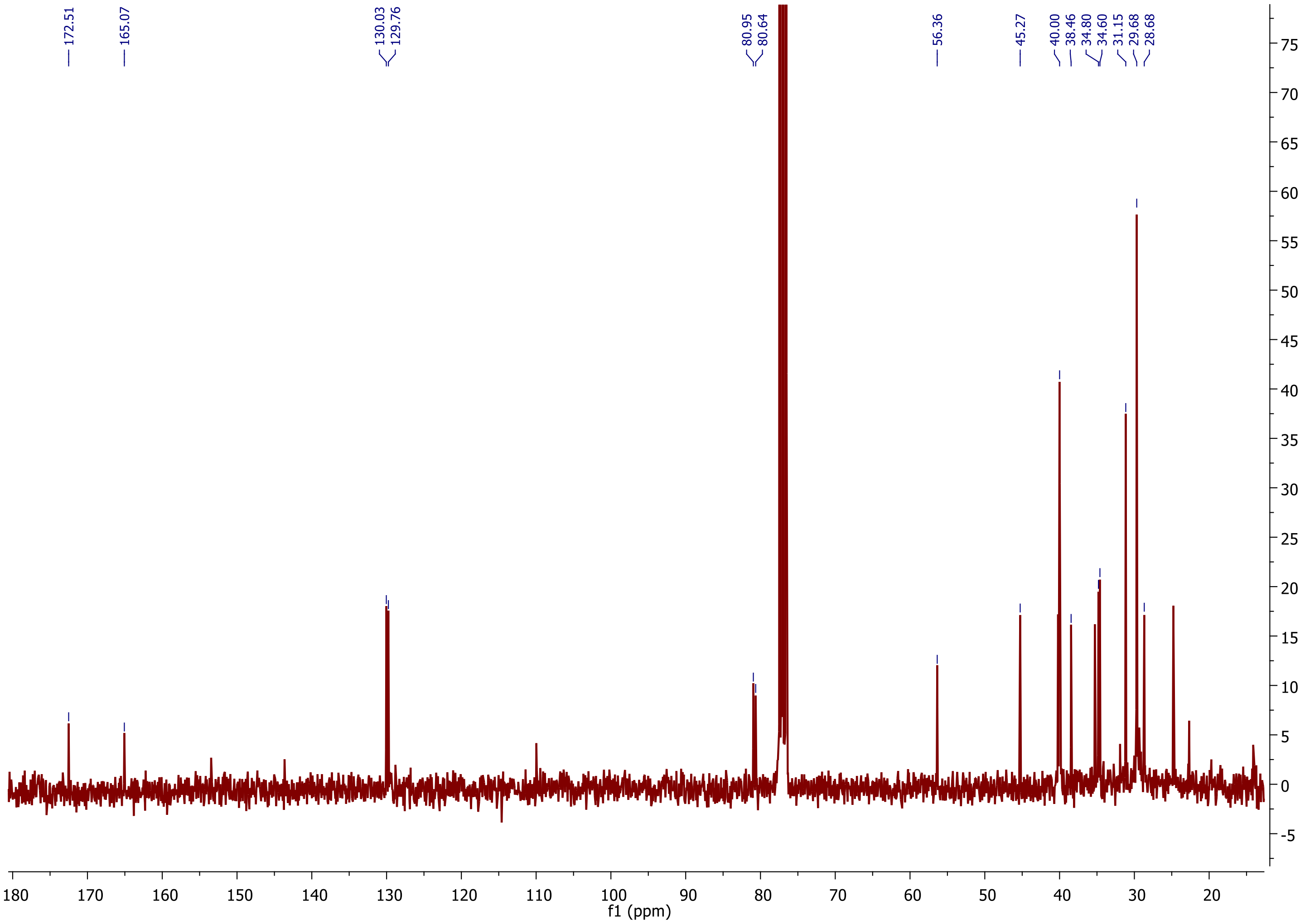

Figure S6.2 ^{13}**C NMR spectrum of adamantane derivative 1 in CDCl$_3$.**

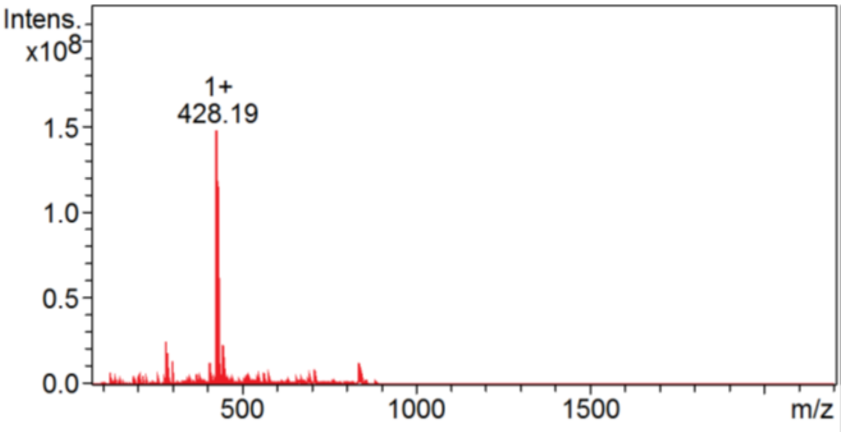

Figure S6.3 ESI-MS of adamantane derivative 1

References

1. Liu, P.; Qin, R.; Fu, G.; Zheng, N., Surface Coordination Chemistry of Metal Nanomaterials. *J. Am. Chem. Soc.* **2017,** *139* (6), 2122-2131.
2. Jin, R.; Zeng, C.; Zhou, M.; Chen, Y., Atomically Precise Colloidal Metal Nanoclusters and Nanoparticles: Fundamentals and Opportunities. *Chem. Rev.* **2016,** *116* (18), 10346-10413.
3. Du, Y.; Sheng, H.; Astruc, D.; Zhu, M., Atomically Precise Noble Metal Nanoclusters as Efficient Catalysts: A Bridge between Structure and Properties. *Chem. Rev.* **2019** (DOI: 10.1021/acs.chemrev.8b00726).
4. Liu, L.; Corma, A., Metal Catalysts for Heterogeneous Catalysis: From Single Atoms to Nanoclusters and Nanoparticles. *Chem. Rev.* **2018,** *118* (10), 4981-5079.
5. Chakraborty, I.; Pradeep, T., Atomically Precise Clusters of Noble Metals: Emerging Link between Atoms and Nanoparticles. *Chem. Rev.* **2017,** *117* (12), 8208-8271.
6. Aikens, C. M., Electronic and Geometric Structure, Optical Properties, and Excited State Behavior in Atomically Precise Thiolate-Stabilized Noble Metal Nanoclusters. *Acc. Chem. Res.* **2018,** *51* (12), 3065-3073.
7. Jin, R., Atomically precise metal nanoclusters: stable sizes and optical properties. *Nanoscale* **2015,** *7* (5), 1549-1565.
8. Yu, Y.; Luo, Z.; Chevrier, D. M.; Leong, D. T.; Zhang, P.; Jiang, D.-e.; Xie, J., Identification of a Highly Luminescent $Au_{22}(SG)_{18}$ Nanocluster. *J. Am. Chem. Soc.* **2014,** *136* (4), 1246-1249.
9. Yu, Y.; Geng, J.; Ong, E. Y. X.; Chellappan, V.; Tan, Y. N., Bovine Serum Albulmin Protein-Templated Silver Nanocluster (BSA-Ag_{13}): An Effective Singlet Oxygen Generator for Photodynamic Cancer Therapy. *Adv. Healthc. Mater.* **2016,** *5* (19), 2528-2535.
10. Krommenhoek, P. J.; Wang, J.; Hentz, N.; Johnston-Peck, A. C.; Kozek, K. A.; Kalyuzhny, G.; Tracy, J. B., Bulky Adamantanethiolate and Cyclohexanethiolate Ligands Favor Smaller Gold Nanoparticles with Altered Discrete Sizes. *ACS Nano* **2012,** *6* (6), 4903-4911.

11. Shevchenko, E. V.; Talapin, D. V.; Rogach, A. L.; Kornowski, A.; Haase, M.; Weller, H., Colloidal Synthesis and Self-Assembly of $CoPt_3$ Nanocrystals. *J. Am. Chem. Soc.* **2002,** *124* (38), 11480-11485.

12. Ye, Y.-S.; Chen, Y.-N.; Wang, J.-S.; Rick, J.; Huang, Y.-J.; Chang, F.-C.; Hwang, B.-J., Versatile Grafting Approaches to Functionalizing Individually Dispersed Graphene Nanosheets Using RAFT Polymerization and Click Chemistry. *Chem. Mater.* **2012,** *24* (15), 2987-2997.

13. Clavé, G.; Campidelli, S., Efficient covalent functionalisation of carbon nanotubes: the use of “click chemistry”. *Chem. Sci.* **2011,** *2* (10), 1887-1896.

14. Castelaín, M.; Martínez, G.; Marco, C.; Ellis, G.; Salavagione, H. J., Effect of Click-Chemistry Approaches for Graphene Modification on the Electrical, Thermal, and Mechanical Properties of Polyethylene/Graphene Nanocomposites. *Macromolecules* **2013,** *46* (22), 8980-8987.

15. Sun, S.; Cao, Y.; Feng, J.; Wu, P., Click chemistry as a route for the immobilization of well-defined polystyrene onto graphene sheets. *J. Mater. Chem.* **2010,** *20* (27), 5605-5607.

16. Jin, Z.; McNicholas, T. P.; Shih, C.-J.; Wang, Q. H.; Paulus, G. L. C.; Hilmer, A. J.; Shimizu, S.; Strano, M. S., Click Chemistry on Solution-Dispersed Graphene and Monolayer CVD Graphene. *Chem. Mater.* **2011,** *23* (14), 3362-3370.

17. Döhler, D.; Michael, P.; Binder, W. H., CuAAC-Based Click Chemistry in Self-Healing Polymers. *Acc. Chem. Res.* **2017,** *50* (10), 2610-2620.

18. Hoyle, C. E.; Lowe, A. B.; Bowman, C. N., Thiol-click chemistry: a multifaceted toolbox for small molecule and polymer synthesis. *Chem. Soc. Rev.* **2010,** *39* (4), 1355-1387.

19. Hoyle, C. E.; Bowman, C. N., Thiol–Ene Click Chemistry. *Angew. Chem.* **2010,** *49* (9), 1540-1573.

20. Castelaín, M.; Martínez, G.; Ellis, G.; Salavagione, H. J., A versatile chemical tool for the preparation of conductive graphene-based polymer nanocomposites. *Chem. Commun.* **2013,** *49* (79), 8967-8969.

21. Lowe, A. B.; Hoyle, C. E.; Bowman, C. N., Thiol-yne click chemistry: A powerful and versatile methodology for materials synthesis. *J. Mater. Chem.* **2010,** *20* (23), 4745-4750.

22. Chua, C. K.; Pumera, M., Monothiolation and Reduction of Graphene Oxide via One-Pot Synthesis: Hybrid Catalyst for Oxygen Reduction. *ACS Nano* **2015,** *9* (4), 4193-4199.

23. Hummers, W. S.; Offeman, R. E., Preparation of Graphitic Oxide. *J. Am. Chem. Soc.* **1958,** *80* (6), 1339-1339.

24. Koklioti, M. A.; Bittencourt, C.; Noirfalise, X.; Saucedo-Orozco, I.; Quintana, M.; Tagmatarchis, N., Nitrogen-Doped Silver-Nanoparticle-Decorated Transition-Metal Dichalcogenides as Surface-Enhanced Raman Scattering Substrates for Sensing Polycyclic Aromatic Hydrocarbons. *ACS Appl. Nano Mater.* **2018,** *1* (7), 3625-3635.

Chapter 7

Conclusions

Since its revolutionary discovery, graphene brought 2D materials into the limelight. Graphene and graphene-like materials, in particular transition metal dichalcogenides (TMDs) with MoS_2 and WS_2 as main flatlanders, have triggered a lot of scientific interest due to their exciting physical and chemical properties. The 2D family is deemed suitable for widespread applications, such as catalysis, electronics, medicine, energy storage, and sensing. However, their chemical inertness handicaps their potential capabilities, thus modification methodologies and combination with other materials should be applied to broaden their application spectrum. The primary purpose of this Thesis was to explore hybrid materials based on 2D materials (graphene, and TMDs) and fluorescent metal nanoclusters and understand their tailor-made properties towards energy conversion applications, i.e. catalytic and sensing activity.

Key findings and contributions

In **Chapter 3**, graphene sheets were covalently functionalized with a suitable organic group bearing positively charged ammonium units, which facilitated the dispersibility of graphene in aqueous media. On the other hand, negatively charged α-lipoic acid-stabilized M_{NCs} (Au and Ag) were prepared and electrostatically tethered to functionalized graphene, realizing the corresponding hybrid materials. The methodology was simple to be applied and its steps were effectively monitored via complementary spectroscopic techniques. Next, the examination of the role of visible light irradiation on the catalytic performance of Au-based ensemble toward the reduction of 4-nitrophenol, shed light on the mechanistic pathways took place upon photoillumination of the hybrid. For the first time, photoinduced hydrogen production was experimentally documented, which was the most valuable conclusion of this research work.

Although research on M_{NCs}/graphene ensembles is in primary stage, the promising results encourage the investigation and further development of these potent materials in the future. The merits to employ M_{NCs} instead of traditional metal nanoparticles or other fluorophores are summarized as follows: (a) the passivation of tiny M_{NCs} by specific ligands to facilitate their growth and the formation of tunable luminescent markers, provide facile pathways to tether them not only to graphene but also to any sensing probe, (b) the photostability and luminescence reveal intrinsic advantages over conventional organic fluorophores, which are susceptible towards photodegradation, and, (c) the ultrasmall size of M_{NCs} as compared to molecular fluorophores or quantum dots, and their non-toxic characteristics provide versatile means to apply them to biological media. As for graphene, it is utilized as a substrate due to its large planar surface area and impressive charge-transport properties. Additionally, its favorable energetics to accept electrons, along with the ease of developing multifunctional hybrids with tailored properties render graphene an exceptionally key mediator for improving the performance of energy conversion devices.

In **Chapter 4**, a facile way to prepare nitrogen doped TMDs (MoS_2 and WS_2) through plasma treatment, while they were simultaneously decorated with silver nanoparticles, was demonstrated. The avoidance of any wet chemistry procedure was among the advantages of the proposed methodology, while X-ray photoelectron spectroscopy proved as the key technique to confirm the success of functionalization. Next, the TMD-based materials functioned as excellent SERS platforms as they could detect RhB at very low concentrations attributable to charge transfer phenomena between TMDs and chromophore. However, the most important finding of this chapter was the sensing of PAHs from the MoS_2-based ensemble. Usually, for their detection sophisticated experimental protocols are employed in the literature to facilitate effective communication between the substrate and analyte, because the aromatic rings exhibit low affinity with metal nanoparticles.

Undoubtedly, the observation of SERS phenomenon employing modified TMDs (i.e. doped with N and featuring immobilized Ag nanoparticles) as substrates is in its infancy; however the generated results are encouraging and offer a variety of information for future explorations, such as: (a) the roughened surface of TMDs due to the plasma treatment gives good Raman enhancements and is considered to facilitate photoinduced charge transfer between the analyte and TMDs, (b) silver nanoparticles were fabricated directly on the solid substrates ensuring chemical stability and homogeneity, in contrast to traditional wet chemistry methods, (c) the sample preparation is essentially limited to the time needed for exfoliation of TMDs from bulk counterparts, as only a few seconds of plasma treatment were sufficient to observe SERS signals, and, (d) good absorption of the analytes on TMD surface was accomplished, even in the case of PAHs which exhibit an inert π-conjugated carbon network. With all those capabilities, we anticipate that such TMD-based SERS platforms could be developed to meet emerging needs in diverse research fields, such as ultrasensitive biological sensing, environmental pollution monitoring, food safety evaluation, and defense applications.

In **Chapter 5**, MoS_2 sheets were covalently functionalized via binding of a 1,2-dithiolane derivative to defected Mo atoms bearing sulfur vacancies. The employed 1,2-dithiolane was bearing an ammonium cation, which was beneficial to drastically improve the admitted difficulty of TMDs to be dispersed in aqueous media. Next, functionalized MoS_2 sheets were electrostatically tethered to negatively charged core – shell $Ag_{NCs}@Au_{NCs}$ labeled with BSA, in a same manner as it was described in Chapter 3. The fabricated hybrid material exhibited high catalytic capabilities towards photodegradation of RhB attributable to the generation of highly reactive species that could decompose the organic chromophore molecules. Despite similar studies being available in the literature, both the functionalization procedure for exfoliated MoS_2 and hybrid's performance in photocatalysis are the key points of consideration in this Chapter.

There is an increasing research interest in chemical functionalization of TMDs, and particularly MoS_2, by exploiting the thiol chemistry at sulfur vacancies located at the edges.

However, in most cases, thiols tend to be converted into the corresponding disulfides in a catalytic reaction activated by the presence of MoS_2, which eventually physisorb – and not covalently attach – onto the basal plane of the nanosheets, rendering the exact nature of MoS_2/thiol interaction unclear. However, we succeeded in the formation of a stable and robust bond between MoS_2 and a 1,2-dithiolane derivative, which was critical for the next steps of fabrication of the respective ensemble. The knowledge generated from the above study would be of great benefit for the functionalization methods of MoS_2 and construction of corresponding nanohybrids with desired structural features. Moreover, MoS_2 capability to interact with fluorescent metal nanoclusters and participate in photocatalytic schemes will open up a new area in the energy conversion field.

In **Chapter 6**, a new bulky organic stabilizer was developed based on an adamantane derivative, which functioned as building block molecule facilitating both nanocluster formation and covalent attachment of 2D materials (graphene, and MoS_2). The choice of this adamantane-based ligand was decisive, as it gathered a lot of virtues: (a) the cage-structure, high metal affinity (derived from the free 1,2-dithiolane group), and improved solubility to facilitate Au_{NC} growth with near-infrared luminescence, and (b) the C=C entity to covalently interact with thiol-modified 2D materials (graphene, and TMDs) through thiol–ene click chemistry means. Thiol–ene reaction possess many desirable features, such as simplicity, high efficiency, no by-products and high yield, and also present an additional advantage since it can be externally-triggered by thermal initiator. Both click chemistry reactions and adamantane derivatives open up an innovative avenue to controllably design hybrid materials that fulfill specific urgent demands. The current strategy employed constitutes a general tool that is wide in scope and can, in principle, be extended to the modification of other 2D materials and/or compounds for the fabrication of hybrid schemes with tailored characteristics that today is unattainable.